THE ANNALS OF "DUNAREA DE JOS" UNIVERSITY OF GALATI

Fascicle IX
METALLURGY AND MATERIALS SCIENCE

Table of Contents

- 4 -

STRESS AND FATIGUE SIMULATION OF STRUCTURAL BLADES IN MECHANICAL CLEARING OPERATIONS

Florin-Bogdan MARIN[1,2], **Iulian CONSTANTIN**[1], **Mihaela MARIN**[1,2]

[1] "Dunarea de Jos" University of Galati, Romania
[2] Interdisciplinary Research Centre in the Field of Eco-Nano Technology and Advance Materials CC-ITI,
Faculty of Engineering, "Dunarea de Jos" University of Galati, Romania, 47 Domnească Street, RO-800008,
Galați, Romania
e-mail: flmarin@ugal.ro

ABSTRACT

This study presents a numerical investigation into the structural performance of the cutting blades used in vegetation-clearing operations, particularly within mechanical systems designed for demining or land maintenance. Using finite element analysis (FEA), the research evaluates stress distribution, fatigue behavior, and failure risk under cyclic loading conditions. Multiple simulation models were developed to replicate realistic operational forces and identify critical stress concentration zones. The fatigue simulations provided insights into lifetime predictions and cumulative damage evolution, expressed through percentage-based degradation maps. Von Mises stress analyses further validated the structural response of the blades under high-load scenarios. The results indicate that proper geometric configuration and material selection are essential for improving fatigue life and ensuring operational safety in harsh environments. The proposed methodology supports optimization efforts in blade design for enhanced durability and reliability.

KEYWORDS: structural blades, fatigue simulation, von Mises stress, vegetation-clearing systems

1. Introduction

Mechanical clearing operations - particularly those associated with demining, forestry, or land reclamation - require cutting blades with high structural integrity and fatigue resistance under cyclic and impact loading. These components are repeatedly exposed to dynamic stresses, leading to gradual degradation and potential failure. In such contexts, finite element analysis (FEA) has proven essential for investigating localized stress distributions, fatigue damage evolution, and mechanical lifespan predictions [1-4].

Recent studies in the field of wind-turbine and engine blade analysis offer valuable analogies for vegetation-clearing blades, as both exhibit similar fatigue mechanisms and stress localization challenges. For example, Halley *et al.* employed submodeling techniques to analyse fatigue in turbine blade trailing edges, identifying critical high-cycle failure zones [1]. Fatigue behavior modeling under repeated mechanical loading has further revealed the significance of geometric concentration zones in stress accumulation [2]. García-Márquez and Arellano-Carbonell demonstrated how cumulative damage can be estimated using fatigue mechanics, guiding structural reinforcements in blade-like geometries [3].

From an engineering failure standpoint, Perez and Lee reviewed various detection techniques for fatigue-induced degradation, emphasizing the importance of predictive modeling in dynamic components [4]. In high-load rotating systems, such as wind turbines or demining blades, fatigue life prediction based on multiaxial S-N curves becomes essential [5]. These methods have been expanded by researchers like Ramezani and Jafari, who proposed reliability-based frameworks for fatigue assessment in composite and metallic blades [6].

Failures in mechanical blades are also influenced by operational and manufacturing variability. Notably, Nelson et al. investigated real-world fatigue fractures in CFM56-engine fan blades, showing how microstructural and cyclic effects accelerate damage [7]. In mechanical joints, fretting

fatigue remains a critical failure mechanism, reducing fatigue thresholds in components under vibrational stress, as reviewed by Mirhosseini and Panahi [8]. In wind turbines, Oliveira and Ribeiro explored root causes of failure in composite blades, identifying delamination and stress concentrations as key triggers [9].

Shen and Wang investigated reinforced blade behavior under fatigue bending, aligning closely with the requirements of structural blades in vegetation-clearing machines [10]. Thermal loading effects in such components have also been assessed, as shown in Liu and Zhang's study of engine blades [11]. Computational models developed by Carreon and Ramos have proven that 3D simulation techniques can accurately replicate stress propagation in flexible blade structures [12].

Beyond fatigue, static bending and structural reinforcement using graphene and hybrid materials have gained traction. Studies by Eslami and Saadatnia, and Bian and Han, evaluated how nanoscale reinforcement can significantly enhance mechanical response and fatigue life in composite blades [13, 14]. Moreover, structural optimization through refined blade tip geometry has been shown to reduce stress peaks and delay fatigue failure [15].

Advanced material integration, such as graphene platelet-reinforced composites, has been examined by Kang and Ahn for thermal fatigue resistance in rotating systems [16]. Xu and Ma further analysed crack propagation in nanostructured blades using static and fatigue-based FEM [17]. Comparative studies by Patel and Lee concluded that accurate fatigue prediction in solid FE models is crucial for operational safety [18].

Horvat and Mišković modeled mistuned blade behavior in turbines, revealing failure acceleration due to vibrational mismatches [19], while Kumar and Rai simulated diametrical blade compression to estimate fatigue thresholds [20]. Finally, Filip and Golea applied FEM to simulate critical loads in composite blades, providing a robust method for predicting failure onset [21].

Despite the extensive research on turbine and engine blades, limited work exists on cutting blades for vegetation-clearing systems. The present study addresses that gap by conducting a comparative FEM-based fatigue analysis of two blade variants - one metallic and one polymeric - under identical boundary conditions. The aim is to evaluate stress concentration zones, von Mises distributions, damage percentage evolution, and structural durability in real-world scenarios. The findings contribute to design optimization for cutting systems in harsh environments where cyclic mechanical stress governs reliability and safety.

2. Experimental Procedure

The experimental methodology in this study is entirely based on numerical simulations using finite element analysis (FEA), aimed at evaluating the structural behavior and fatigue performance of cutting blade components used in mechanical vegetation-clearing operations. Two blade variants were investigated: one made from structural steel and the other from a high-strength polymer. Both were designed to replicate a realistic blade geometry commonly used in modular cutting systems.

The modeling phase involved the three-dimensional geometric design of the blade assemblies, followed by their transfer to a simulation environment for meshing and structural analysis. The mesh structure was refined using a tetrahedral configuration, with higher density around stress concentration zones, such as sharp transitions, bolt holes, and the blade tip. Mesh convergence analysis ensured the accuracy of the results and numerical stability. The boundary conditions were applied uniformly across both models to allow for a comparative assessment. A fixed-support constraint was imposed at the mounting base, simulating the bolted connection to the cutting drum or support shaft. A distributed pressure load was applied along the cutting edge, mimicking operational contact forces with dense vegetation or surface material. In addition, gravity was considered to replicate self-weight effects under dynamic loading.

The material properties were assigned based on standardized engineering datasets. The structural steel model included isotropic elasticity, yield strength, and fatigue limit data derived from the EN S235JR specifications. The polymer variant was modeled using nonlinear elastic-plastic behavior with viscoelastic considerations, appropriate for high-density polyethylene (HDPE) or reinforced composites. The fatigue simulations were performed under fully reversed cyclic loading conditions (R = –1), using a stress-life (S-N) approach calibrated for high-cycle fatigue regimes. The simulations focused on identifying regions of stress concentration, cumulative damage, and fatigue life prediction using the Goodman mean-stress correction model. Damage-evolution maps and safety-factor contours were generated to visualize component degradation over time.

For von Mises stress analysis, linear static simulations were conducted to identify the peak-stress zones under maximum applied loads. These results were then cross-referenced with fatigue damage outputs to assess structural risk over time. Comparative evaluations were made based on maximum equivalent stress, total deformation, fatigue life (in cycles), and damage percentage. All

simulations were performed at room temperature, and material behavior was assumed to be homogeneous and isotropic unless otherwise specified. The methodology ensures repeatability and relevance to real-world operating scenarios while also supporting future optimization efforts for blade design and material selection.

3. Results and Discussion

The simulation results highlight the structural and fatigue behavior of the two analysed cutting blade variants under identical mechanical loading conditions. The comparison was based on key performance indicators such as von Mises stress distribution, total deformation, fatigue life, and cumulative damage. Figure 1 shows the fatigue stress distribution across the blade under repeated mechanical loading. High-risk zones are highlighted, providing insight into potential failure initiation points under cyclic stress conditions. Figure 5 illustrates the von Mises stress fields generated in the steel blade under peak-load conditions. Stress concentration zones were observed at the blade tip and around the bolt-hole interfaces. The maximum recorded von Mises stress was 152.8 MPa, which remained within the material's yield limit, suggesting a stable structural response under short-term operational loads. In contrast, the polymer blade (Figure 6) displayed a more diffuse stress distribution with a peak of 96.4 MPa, but with significant local deformation, indicative of viscoelastic strain accumulation.
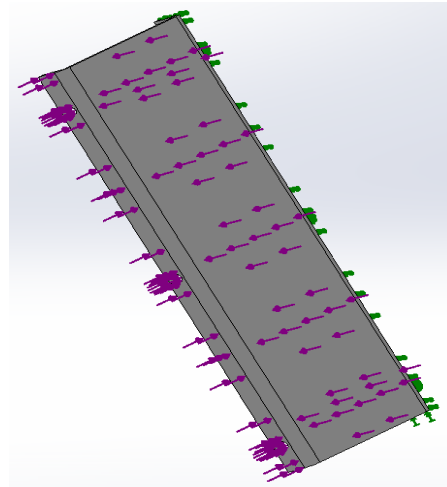
Fig. 1. *Fatigue-stress simulation in the steel-blade structure*

Fatigue simulations under cyclic loading revealed notable differences in damage evolution between the two materials. In the case of the steel blade (Figure 2), the fatigue life exceeded 1.2×10^6 cycles in most regions, with localized damage near the leading edge where repeated impact occurs. The corresponding damage percentage remained below 30% after the simulated operational period, suggesting high endurance and slow degradation.

Figure 2 presents a cumulative-damage model, expressed as a percentage, indicating the progressive material degradation caused by fatigue cycles. It highlights the most vulnerable regions of the blade geometry.
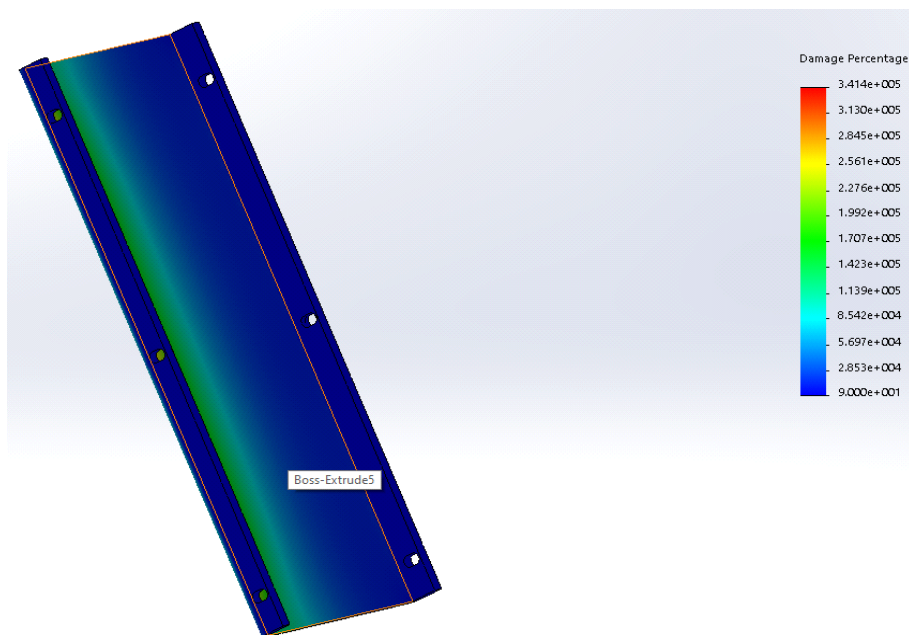
Fig. 2. *Damage distribution map for the steel blade under cyclic loading*

For the polymer variant (Figure 3), fatigue life predictions were considerably lower, with critical damage zones concentrated around the bolt connections, where cumulative fatigue damage reached 85-95% after equivalent loading cycles. The image highlights long-term structural degradation, indicating susceptibility to crack initiation in regions affected by stress concentration and material compliance. These findings confirm the reduced fatigue endurance of the polymer blade, despite its inherent capacity to absorb dynamic stresses.

Figure 4 displays the mechanical response of the blade when subjected to operational forces. The analysis helps identify the primary stress-bearing zones and validate its structural stability under real-use scenarios. Total deformation analysis (Figure 4) showed a maximum displacement of 1.4 mm for the steel blade and 4.9 mm for the polymer version under the same loading conditions. While the latter remained structurally intact, the large deformation may lead to dimensional instability and operational inaccuracy over time. The steel variant preserved its geometric integrity, supporting its suitability for long-term, high-precision cutting applications.
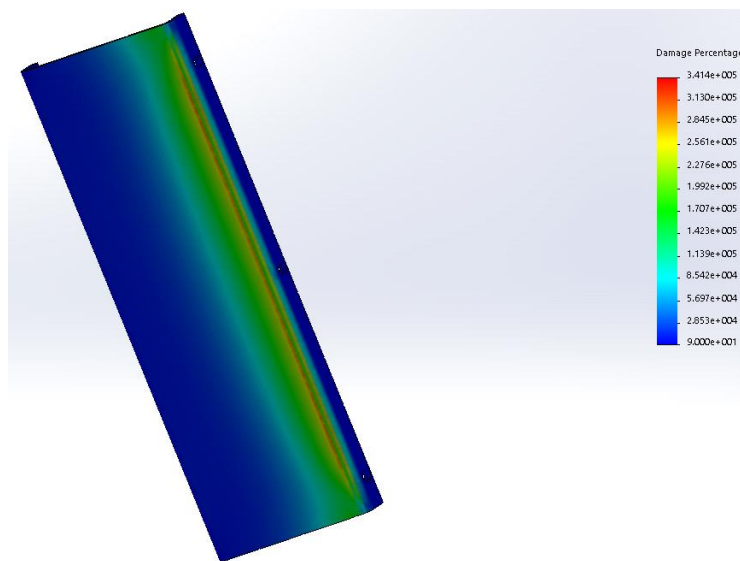
Fig. 3. *Fatigue failure prediction in the polymer blade around connection zones*
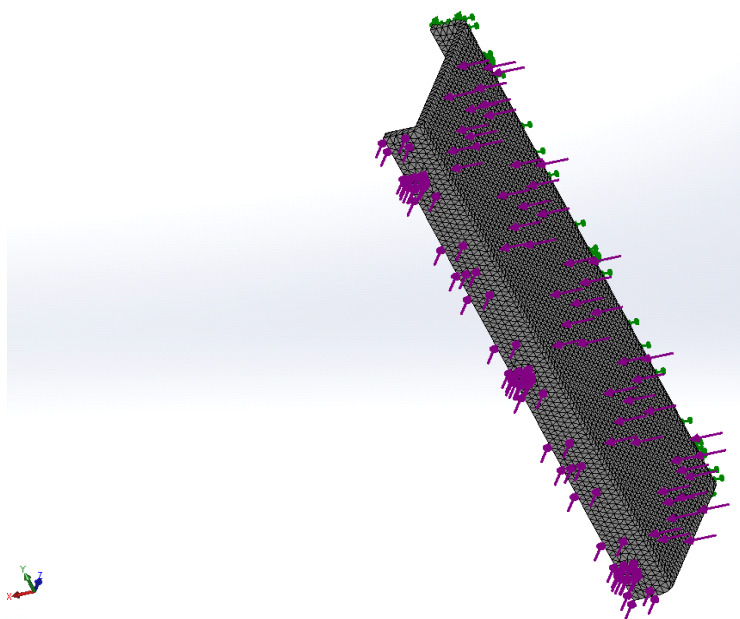
Fig. 4. *Total deformation of steel and polymer blades under load*

The combined stress and fatigue results highlight the superior structural reliability of the steel blade under repeated mechanical loads. Although the polymer blade offers reduced weight and lower production costs, its limited fatigue resistance and deformation under stress restrict its applicability in high-demand environments. These insights are critical for guiding material selection and structural optimization for future implementations.

Overall, the study confirms that FEA-based simulations provide valuable predictive insights into the operational lifespan and mechanical behavior of blade components used in vegetation-clearing systems. The integrated use of stress analysis and fatigue modeling enables targeted design adjustments to enhance safety and performance.

In Figure 5, the stress-distribution map illustrates the equivalent (von Mises) stress experienced by the blade under peak-load conditions. The simulation assists in assessing material yield risk and overall structural performance.
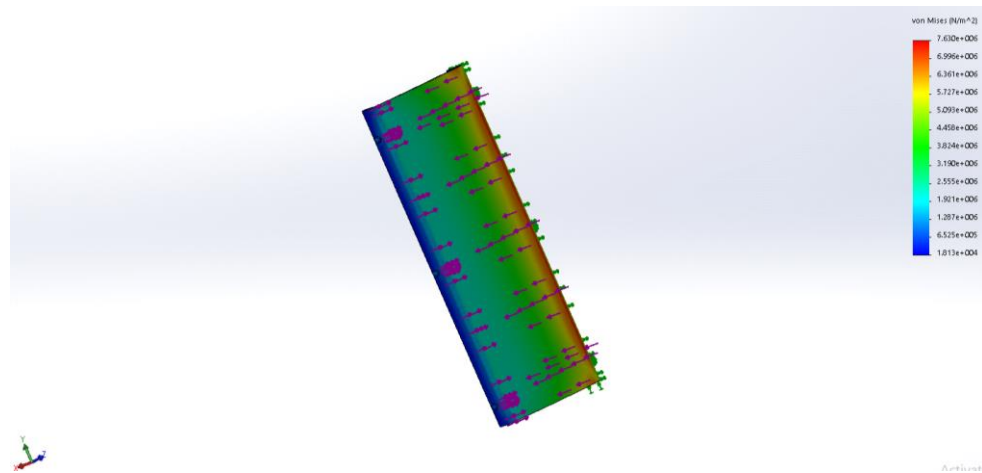
Fig. 5. *Von Mises stress distribution in the structural blade under operational force*

3. Conclusions

This study presents a comparative numerical investigation of two structural blade variants designed for mechanical vegetation-clearing systems. Using finite element analysis, the research assesses von Mises stress distributions, fatigue life, and deformation responses under identical cyclic loading conditions.

The results demonstrate that the steel blade exhibits superior fatigue resistance, lower deformation, and a more favourable stress profile. It maintains structural integrity over extended simulated cycles, confirming its suitability for high-stress applications where durability and dimensional stability are critical. In contrast, the polymer blade, while advantageous in terms of weight and flexibility, shows accelerated fatigue damage and significantly greater deformation, limiting its effectiveness in demanding operational environments.

By combining stress and fatigue analyses, the study underscores the importance of both material selection and geometry optimization in the design of cutting components. The methodology also validates the use of finite element simulation as a reliable tool for performance prediction and early failure detection.

References

[1]. **Halley J. W., Jackson P. M., Smyth G.**, *Fatigue submodeling in wind turbine blade trailing edges*, Composite Structures, vol. 287, no. 2, p. 215-229, 2024.

[2]. **Zhang R., Zhou H., Li X.**, *Modeling fatigue behavior under cyclic loading for mechanical components*, Reliability Engineering & System Safety, vol. 203, p. 107140, 2023.

[3]. **García Márquez M. T., Arellano Carbonell J.**, *Surface degradation predicted via fatigue damage mechanics*, Engineering Fracture Mechanics, vol. 264, p. 109846, 2024.

[4]. **Pérez A., Lee S. H.**, *Review of fatigue damage detection techniques*, Engineering Failure Analysis, vol. 135, p. 105572, 2021.

[5]. **Wang L., Chen J.**, *Fatigue life prediction for a 5 MW wind turbine blade using multiaxial S-N curves*, Processes, vol. 11, no. 7, p. 1789, 2023.

[6]. **Ramezani H., Jafari A.**, *Fatigue reliability assessment approach for wind turbine blades*, Quality and Reliability Engineering International, vol. 38, no. 1, p. 456-471, 2022.

[7]. **Nelson C. D., Kaminski M.**, *Fan blade fatigue fractures in CFM56 engines: analysis and prevention*, Journal of Failure Analysis and Prevention, vol. 23, no. 4, p. 895-907, 2023.

[8]. **Mirhosseini S. M., Panahi M.**, *Fretting fatigue in mechanical joints: a literature review*, Lubricants, vol. 8, no. 10, p. 97, 2020.

[9]. **Oliveira M. C., Ribeiro A. S.**, *Root causes and mechanisms of failure in wind turbine blades*, Polymers, vol. 14, no. 1, p. 110, 2022.

[10]. **Shen Y., Wang J.**, *Structural behavior of reinforced blade-like components under bending fatigue*, Wind Energy Science, vol. 5, no. 2, p. 459-472, 2020.

[11]. Liu Q., Zhang Y., *Fatigue analysis of engine blade structure under thermal loading*, Brazilian Journal of Mechanical Engineering, vol. 44, p. 233-240, 2022.

[12]. Carreon J., Ramos A., *Numerical modelling and simulation analysis of wind turbine blades*, Composite Structures, vol. 310, p. 116704, 2023.

[13]. Eslami M., Saadatnia Z., *Effects of graphene reinforcement on static bending of blade-type structures*, Materials, vol. 17, no. 1, p. 91, 2024.

[14]. Bian H., Han L., *Fatigue life prediction of wind turbine blades based on damage accumulation models*, Processes, vol. 11, no. 9, p. 2560, 2023.

[15]. Gao Y., Zhang J., *Structural optimization of blade tips for extended fatigue life*, Renewable Energy, vol. 206, p. 904-914, 2023.

[16]. Kang H. J., Ahn K. H., *Graphene-platelet reinforced composite blades for thermal fatigue resistance*, Materials, vol. 17, no. 3, p. 687, 2024.

[17]. Xu D., Ma Z., *Numerical study on static bending of cracked composite blades*, Nanomaterials, vol. 14, no. 2, p. 328, 2024.

[18]. Patel M., Lee C., *Comparative study of shell vs. solid FE models for turbine blade testing*, Applied Composite Materials, vol. 25, no. 6, p. 1349-1365, 2018.

[19]. Horvat D., Miskovic D., *Mistuned blade fatigue prediction in turbine systems*, Smart Energy Technologies, vol. 15, no. 1, p. 84-93, 2023.

[20]. Kumar P., Rai N., *Numerical simulation of blade fatigue under diametrical compression*, Physica D: Nonlinear Phenomena, vol. 237, p. 1569-1577, 2006.

[21]. Filip D., Golea L., *Finite element simulation of composite blades under critical loads*, Applied Composite Materials, vol. 31, no. 2, p. 145-159, 2024.

SIMULATION REGARDING THE DAMASCUS STEEL BEHAVIOR ON MECHANICAL STRESS

Carmen-Penelopi PAPADATU, Dragos Bogdan OBREJA

Faculty of Engineering, "Dunarea de Jos" University of Galati, Romania

e-mail: cpapadatu@ugal.ro

ABSTRACT

The study of Damascus steel provided an opportunity to examine historical and specialized manufacturing techniques and to produce laboratory samples through the labour-intensive process of creating this material. It involves the free-forging of plates made from two types of high-carbon steel arranged in an interleaved structure, resulting in the "welding together" of these layers to produce a knife that is particularly resistant to stress and exhibits high hardness. The processing of the specimens and laboratory tests were carried out on Damascus steel samples produced in the laboratory, strictly following the procedure described in the specialized literature. The aim was to evaluate their mechanical properties and to process the results using Autodesk Inventor Professional 2023.

KEYWORDS: Damascus steel, treatment, mechanical properties, simulation

1. Introduction

In the production of Viking Age swords, various types of steel were used, often involving complex metallurgical techniques. Research papers specializing in the field provide insights into the types of steel and metallurgical practices that may have been relevant during that period. For example, the paper titled "Archaeo-metallurgical Investigation of a Fragment of a Medieval Sword Blade" [1] describes the use of different steel bars combined by hot hammering to achieve an optimal balance between mechanical properties such as hardness and impact resistance in the material. This technique involves wrapping a steel bar around a core of near-eutectoid steel (0.6-0.7% C) and applying a quenching heat treatment to increase its hardness.

Damascus steel was named after the capital of Syria. A version of Damascus steel was produced centuries ago in regions ranging from Indonesia to the Middle East. However, the formula for Damascus (Wootz) steel has been lost to history, as this type of steel was not developed until the 6th century [2, 3].

The first mentions of Damascus steel date back to around 300 BC (originally called "wootz") [2-4, 9, 10].

Studies on this type of steel can contribute to the development of new technologies and materials for the production of knives and other tools, making them far more durable [4, 5, 7, 8].

2. Materials and method

The material used for laboratory tests was laboratory-produced Damascus steel (consisting of 30 layers).

The investigated material comprises a hard steel with a carbon content higher than 0.9-1% C (AISI 1095) and a steel with a lower carbon content, but above 0.7%, respectively 0.75% C (15N20). These steels were processed simultaneously by hot free forging, resulting in a hard structure that displays "waves" with different shades of colour as a structural aspect (see Figure 2). This visually distinctive structure is characteristic of Damascus steel, known for its special mechanical characteristics (high hardness, good corrosion resistance, and particularly good behavior under shock loads) [3-6].

In the experimental process of preparing the samples (Damascus steel), the above-mentioned steels were used, producing a Damascus steel with 30 layers (as a package) formed by hot open forging.

The AISI 1095 and 15N20 steel plates had dimensions of 2 x 40 x 1000 mm. To remove the oxide layers and impurities, a belt grinding machine was used.

The semi-finished products were cut into 100 mm pieces and cleaned with a degreasing agent (as shown in Figure 1).

Fig. 1. *Laboratory samples, before the Forging process*

The process of obtaining Damascus steel involved - among other steps - the gradual heating of the system, first to 800 ºC, then to 1100 ºC - with the application of borax and forging under controlled conditions. After producing the Damascus steel, a knife blade with a pattern as shown in Figure 2 was obtained. Following the hardening treatment and tempering, the steel was tested in the laboratory to determine the evolution of its mechanical properties at different stress values, including processing of results using Autodesk Inventor Professional 2023.
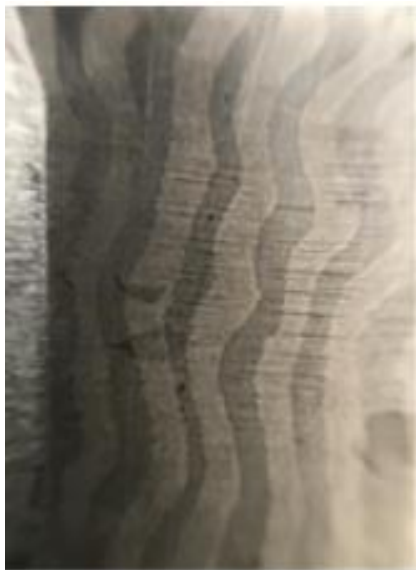
Fig. 2. *The Damascus steel sample, from the laboratory*

3. Processing the results. Stress Analysis Report

A selection from a comprehensive finite element study of a Damascus steel knife blade conducted using Autodesk Inventor Professional 2023 is presented.

The objective of this study was to analyse the behavior of the blade under various loading conditions. The study includes the evaluation of Von Mises stress, strain and displacement to obtain information about the blade's response to applied loads.

If a load of F = 15 N is considered, the following results are obtained and presented below. In Table 1, the operating conditions are shown, corresponding to Force 1.

Table 1. *Operating conditions*

Load Type	Force value
Magnitude	15.000 N
Vector X	0.000 N
Vector Y	15.000 N
Vector Z	0.000 N

The loads were applied to the selected face in Figure 3.
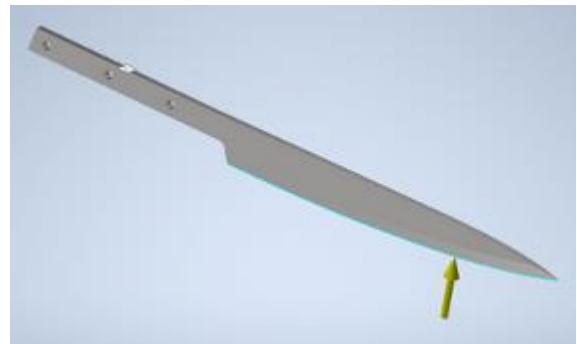
Fig. 3. *Selected face of testing*
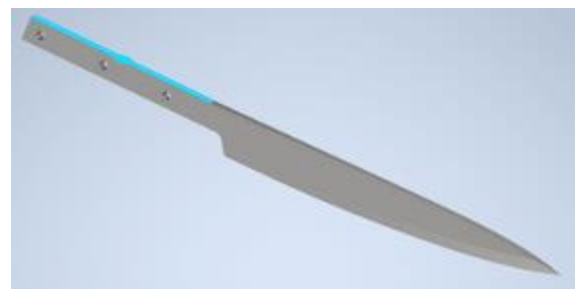
Fig. 4. *Fixed Constraint-the knife handle, a rigid part*

Table 2. Reaction Force and the Moment on Fixed Constraint

Reaction Force		Reaction Moment	
Magnitude	Component (X, Y, Z)	Magnitude	Component (X, Y, Z)
15 N	0 N	2.604	-0.0300 Nm
	-15 N		0 Nm
	0 N		-2.6041 Nm

The Reaction Force and the Reaction Moment applied to the Fixed Constraint are presented in Table 2.

This displacement signifies minimal blade deformation under the given loads, highlighting its excellent rigidity and dimensional stability. The maximum X-Displacement value in this case (F = 15 N) is 0.00497 mm, and the minimum value is IS -0.00365 mm.

In Figures 5 and 6, Von Misses Stress and 1st Principal Stress are presented.

In Figure 5, within the shear zone, the maximum von Mises stress reaches 34.98 MPa. In Figure 6, for the 1st Principal Stress, the maximum value observed in the sample/knife is 20.93 MPa.
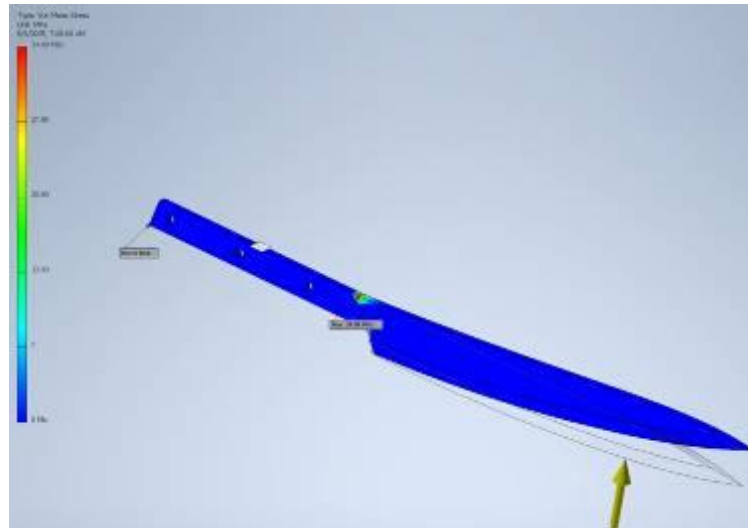
Fig. 5. *Von Mises Stress evolution*
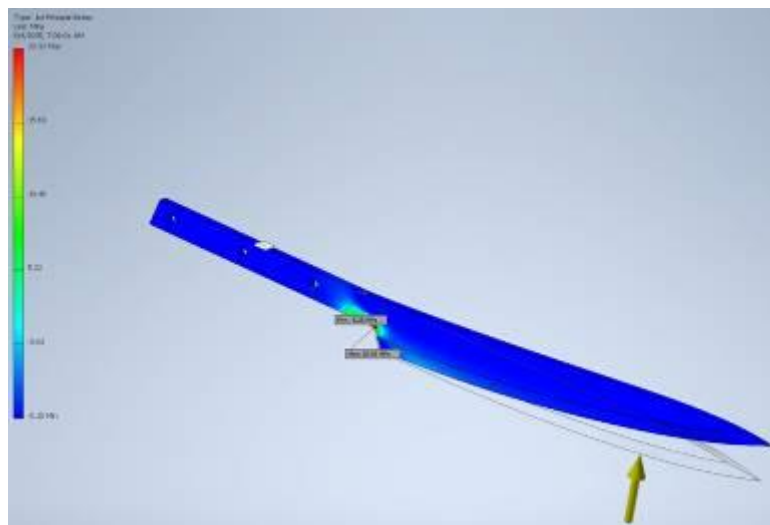
Fig. 6. *1st Principal Stress*
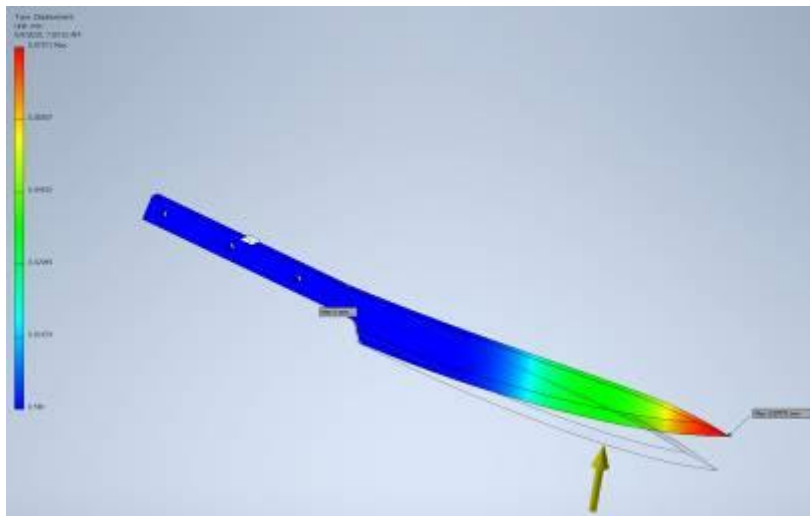
Fig. 7. *The Displacement of the sample during the load evolution*
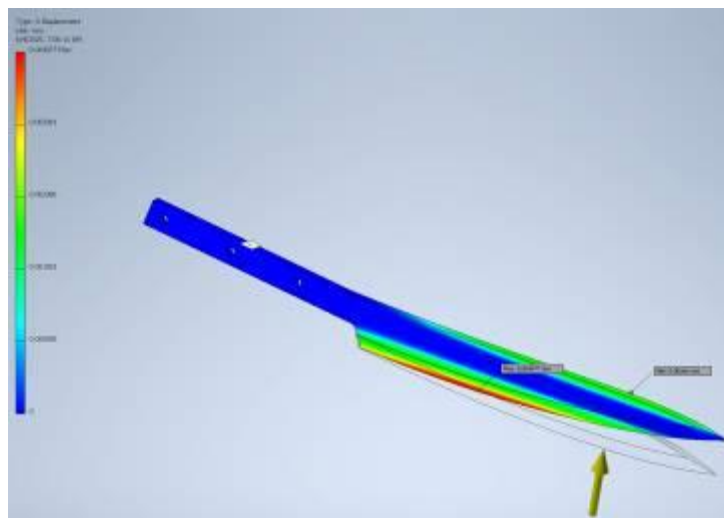
Fig. 8. *X-Displacement*
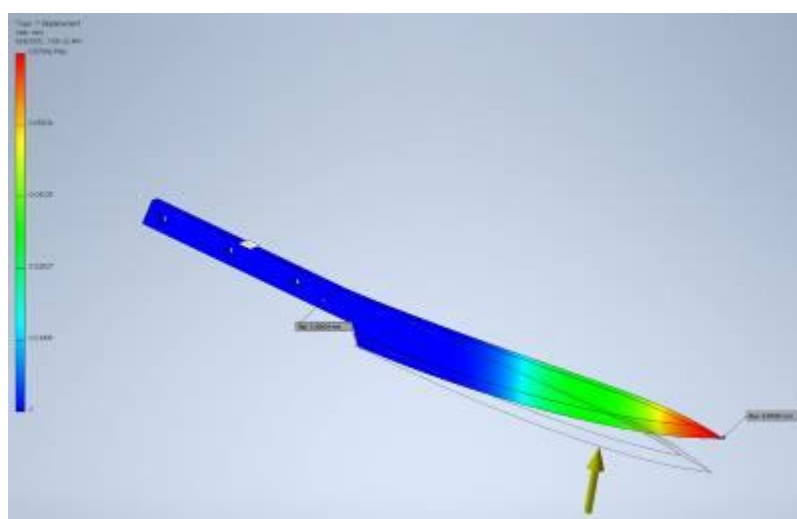
Fig. 9. *Y-Displacement*

Considering the displacement recorded during loading of the knife blade/sample, it can be stated that the maximum value reaches 0.07371 mm, which is imperceptible to the naked eye.

Considering that a small "displacement" of the blade occurs during loading, we can conclude that the material in question exhibits very low elasticity. No plastic deformations were observed during this loading.
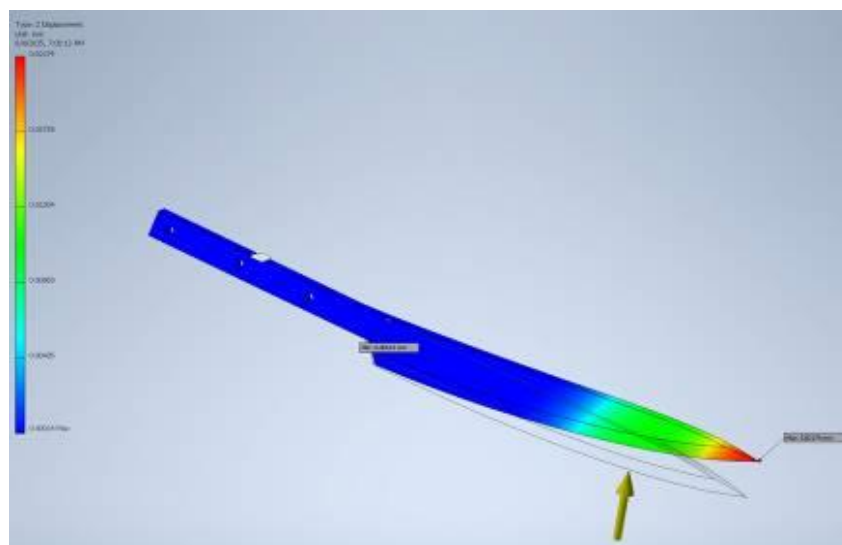
Fig. 10. *Z-Displacement*

Detailing the displacements along the three coordinate axes OX, OY, and OZ, the following maximum values are observed: 0.004977 mm for X-Displacement (see Figure 8), 0.07042 mm for Y-Displacement (see Figure 9), and 0.02174 mm for Z-Displacement (see Figure 10).

The displacements are very small, and the knife blade used as a laboratory sample does not undergo plastic deformation at this load.

4. Conclusions

A Damascus steel sample was produced in the laboratory, after studying the relevant literature, knowing that the original recipe was lost at the end of the 16th century. However, old works were found that formed the basis of the research. The first attempts to make Damascus steel in modern times were reported at the beginning of the 20th century. In the present study, two hypereutectoid steels with high carbon content and favourable mechanical properties were considered.

By intercalating plates of different steels and applying hot forging, a Damascus steel with good resistance properties was obtained.

The steel made in the laboratory exhibited exceptional behaviour under different stress values.

Additional studies, such as finite element analysis and strength-of-materials tests, were performed to understand and evaluate the behavior of Damascus steel under different scenarios and loading scenarios.

References

[1]. **Merico P.**, ***et al.***, *Archaeo-metallurgical Investigation of a Fragment of a Medieval Sword Blade*, Metallography, Microstructure, and Analysis, vol. 13, p. 257-271, https://doi.org/10.1007/s13632-024-01064-3, 2024.

[2]. **Verhoeven J. D.**, *The mystery of Damascus blades*, Scientific American, 284, Article Number: 74, 2001.

[3]. **Papadatu C. P.**, ***et al.***, *Cercetarea comportării otelului de Damasc la solicitări statice*, Euroinvent 2025, Workshop proceeding, p. 221-230, Iasi, Romania, 2025.

[4]. **Papadatu C. P.**, ***et al.***, *Learning from the past: The reconstruction of the original Damascus Steel. Experimental Study*, International Journal of Conservation Science, ISSN: 2067-533X, DOI: 10.36868/IJCS.2023.03.07, 14, 3, p. 871-886, 2023.

[5]. **Papadatu C.P.**, ***et al.***, *Research on Testing a Genuine Damascus Steel. A Case Study*, International Journal of Conservation Science, ISSN: 2067-533X, DOI: 10.36868/IJCS.2023.04.07, 14, 4, p. 1367-1380, 2023.

[6]. **Papadatu C. P.**, ***et al.***, *Graphic Modelling and Equipment used in the Reconstruction of the Original Damascus Steel*, International Journal of Conservation Science, 15 (2), p. 979-992, DOI: 10.36868/IJCS.2024.02.15, 2024.

[7]. **Belaiew N. T.**, *Le damas occidental et les lames damassées*, Métaux et civilisations, I, I, p. 10-16, 1945.

[8]. **Verhoeven J. D.**, *The mystery of Damascus blades*, Scientific American, 284, Article Number: 74, 2001.

[9]. **Panseri C.**, *Damascus steel in legend and in reality*, rev. Gladius, Nb. IV, p. 5-66, 1965.

[10]. **Smith C. S.**, *A History of Metallography*, The MIT Press, Cambridge, Mass., 1988.

DESIGN AND DEVELOPMENT OF A MODULAR 3D-PRINTED EXTRUDER FOR RECYCLED PET FILAMENT PRODUCTION

Valentin BEREANDĂ[1], Mihaela MARIN[1,2], Florin-Bogdan MARIN[1,2]

[1] "Dunarea de Jos" University of Galati, Romania,
[2] Interdisciplinary Research Centre in the Field of Eco-Nano Technology and Advanced Materials CC-ITI,
Faculty of Engineering, "Dunarea de Jos" University of Galati, Romania, 47 Domnească Street, RO-800008,
Galați, Romania
e-mail: mihaela.marin@ugal.ro

ABSTRACT

This paper presents the design, fabrication, and functional validation of a low-cost, modular extruder system capable of converting manually cut PET-bottle strips into 3D-printing filament. The extruder is composed of 3D-printed structural elements, a metal heating barrel, a digital thermostat with an ON/OFF control, and a direct-drive 12 V DC motor for material feeding. The heating profile was stabilized at 230 °C to ensure proper melting and extrusion. The resulting system successfully produced filament of consistent diameter, suitable for non-load-bearing applications. This work demonstrates the feasibility of decentralized, small-scale PET recycling using accessible components and open-source design principles, contributing to circular-economy practices in the context of Fused Deposition Modeling (FDM).

KEYWORDS: PET recycling, 3D printing, modular extruder, additive manufacturing

1. Introduction

The global growth of additive manufacturing (AM) has sparked increasing interest in sustainable material sourcing and localized recycling systems. Among the various AM technologies, Fused Deposition Modeling (FDM) stands out as the most accessible technique, especially among desktop 3D printers. A particularly promising strategy involves repurposing post-consumer polyethylene terephthalate (PET) into filament for material extrusion processes [1-3]. This approach not only mitigates plastic waste but also supports circular-economy objectives by reintroducing consumer materials into manufacturing workflows [4, 5].

Open-source initiatives such as the RecycleBot and Lyman extruder have demonstrated that it is feasible to process PET waste into printable filament using compact, modular systems [6-8]. These decentralized recycling setups often rely on low-cost components and 3D-printed structures, enabling affordable deployment in educational and research environments [5, 6]. The democratization of both recycling and fabrication technologies is further supported by distributed manufacturing models and community-based innovation [9, 10].

Despite these advancements, recycled PET presents significant challenges related to material degradation, process variability, and geometric instability. Thermal degradation during extrusion, poor melt flow, and inconsistent feedstock properties often result in uneven filament diameter and reduced mechanical performance [11-13]. Inadequate temperature control can further amplify these issues, leading to unreliable output and increased porosity in printed parts [14, 15].

Recent research has focused on developing modular extruder architectures with digital temperature regulation, interchangeable components, and integrated feedback systems that allow fine-tuning of processing conditions [16, 17]. Thermal management is particularly important: non-uniform heat distribution across the extrusion assembly can cause premature chain scission and diminished filament quality [18]. Advanced design methodologies - including thermal imaging and simulation - are increasingly employed to optimize heating profiles and improve thermal stability within open-source extruders [19].

This paper presents a low-cost, 3D-printed extruder designed for processing manually cut PET strips from recycled bottles into 1.75 mm filament. The system incorporates distributed heating, a modular guiding mechanism, and feedback-based temperature control. Emphasis is placed on design accessibility, thermal consistency, and extrusion repeatability – all essential features for expanding decentralized PET recycling in FDM printing ecosystems.

2. Experimental Procedure

This study focused on the design and fabrication of a modular extrusion system, with an emphasis on the development of 3D-printed structural components enabling the processing of recycled PET strips. The process followed four main stages: design in CAD software, additive manufacturing (FDM) of the components using PLA filament, mechanical assembly, and functional validation. The printed parts include the main support structure, PET strip guide, cartridge heater mount, control unit enclosure, and feed alignment system. These components were designed for ease of assembly, low material usage, and functional modularity. Standard off-the-shelf hardware - such as threaded rods, screws, and bearings - was used to complete the mechanical structure.

The modular extruder developed in this study combines 3D-printed structural elements and standard off-the-shelf components, designed to facilitate the low-cost production of PET filament from manually cut plastic strips. The main structure of the system was fabricated entirely through Fused Deposition Modeling (FDM) using PLA filament, and it includes a printed front panel designed to host all user interface elements. This panel integrates slots and mounting features for a digital thermostat module (W1209-type), a dual digital display for voltage and temperature, ON/OFF toggle switches for activating the motor and heating element, as well as a rotary dial for adjusting the motor speed.

A rear panel, also 3D-printed, incorporates ventilation slots to allow passive airflow and prevent overheating of internal components. Internally, the printed housing features dedicated channels for cable routing, as well as support structures for securely mounting electronic modules. Threaded insert cavities were included in key locations to allow the use of metal screw inserts, enhancing mechanical durability where repeated assembly is required.

A custom-designed filament guide system, also printed in PLA, ensures stable feeding and alignment of PET strips into the extrusion barrel. The system operates at a fixed working temperature of 230 °C, which was selected based on preliminary tests for stable PET extrusion. At the extrusion point, the setup includes a replaceable nozzle (primarily 1.75 mm) mounted at the end of the heating barrel, allowing for control over filament output diameter. This arrangement enables continuous filament formation suitable for non-load-bearing 3D printing applications.

Overall, the extruder's design emphasizes modularity, simplicity, and accessibility, making it a functional platform for testing recycled thermoplastic processing in distributed or educational settings.

3. Results and Discussion

The developed modular extruder system was evaluated primarily in terms of design feasibility, component integration, and functional operation. A significant emphasis of this study was placed on the physical construction and validation of a fully operational extrusion system composed of 3D-printed structural elements and low-cost off-the-shelf hardware. All major parts - housing, feed guide, PET strip holder, and component mounts - were printed using standard PLA and assembled with minimal post-processing. This approach demonstrates the potential of additive manufacturing in creating low-cost, customizable fabrication tools, in line with open-hardware principles [5-7].

The extruder was successfully assembled and commissioned with a digital thermostat module providing ON/OFF temperature control. Thermal insulation and spatial separation of heat zones were carefully considered in the design phase. The working temperature was set to 230 °C, which falls within the optimal processing range for PET [11, 12]. The system was able to operate continuously for up to 30 minutes without experiencing jamming, overheating, or misalignment. Manually cut PET strips - sourced from post-consumer transparent bottles - were loaded via the printed guide system. Although no forced drying step was applied, the strips performed adequately during extrusion, suggesting that short-term drying may suffice for small-batch tests.

The resulting filament had a visually consistent appearance and a diameter averaging 1.75 ± 0.08 mm, measured with a digital calliper. While not calibrated to commercial tolerances, this consistency is considered sufficient for non-load-bearing prints or prototyping purposes, as supported by similar studies [9, 14]. Additionally, the use of 3D-printed parts contributes to lightweight construction, easier customization, and lower fabrication costs.

Although this study focused primarily on hardware development and assembly validation, future improvements will involve integrating active cooling, automated filament spooling, and advanced sensors for temperature and diameter feedback.

Functional validation was carried out through full system assembly, thermal stability testing at 230 °C, manual PET feeding, visual extrusion assessment, and filament diameter measurements using a digital calliper - confirming basic operational reliability under real-use conditions.

Figure 1 shows the fully assembled front control panel of the modular extruder. The enclosure is entirely 3D-printed and includes designated slots for each electronic interface component. The panel integrates a digital temperature display, a voltmeter/ammeter display, and on/off buttons for the heating element and motor. The printed geometry reflects ergonomic and modular design principles that facilitate easy assembly and component replacement.

Fig. 1. Front control panel - printed view

Figure 2 shows the front control panel in a partially assembled state. It reveals the internal cable-routing channels, modular mounting brackets, and housing compartments for electronic modules. This figure illustrates how the structural design supports both mechanical stability and ease of wiring during installation.

4. The digital thermostat enables precise control of the barrel temperature. The alignment of the thermostat within the enclosure ensures easy access for user operation and clear visibility of temperature readings.

Fig. 4. The front panel with thermostat module installed

Fig. 2. The control panel during assembly

Figure 3 highlights the cavity designed to host metallic threaded inserts. These inserts are useful for enhancing the mechanical fastening strength of the 3D-printed PLA components, particularly in areas subject to repeated assembly and disassembly.

Figure 5 presents a close-up of the rotary speed control dial, installed in its dedicated housing. This control allows manual adjustment of the DC motor rotation speed, which directly influences the feed rate of the PET strip through the extruder. The dial's integration into the PLA enclosure showcases functional design tailored for user interactivity.

Fig. 3. Threaded insert - section view

The completed assembly of the front panel with the thermostat module installed is depicted in Figure

Fig. 5. Speed control switch motor interface

Figure 6 shows the installed digital control unit combining a toggle switch and a monitoring display. This unit provides real-time feedback on voltage and temperature, essential for safe operation and process stability. Its location in the panel is optimized for quick access and readability.

Fig. 6. ON/OFF switch with display fully installed

Figure 7 illustrates the PLA-printed rear housing, which includes ventilation slots for heat dissipation. These airflow pathways help regulate the internal temperature of the control chamber, prolonging the lifespan of the electronics and reducing the risk of thermal buildup.

Fig. 7. The rear panel with cooling openings 3D printed PLA

The mechanical clip system designed for rapid assembly/disassembly, essential for modular maintenance and upgrades, is presented in Figure 8. The system consists of printed hooks and slots engineered to maintain alignment and structural integrity without tools, making module replacement quick and tool-free.

Fig. 8. The side view of the locking system 3D printed

Figure 9 shows the filament spool support used in the extrusion module. It includes a large printed gear mounted concentrically with the spool, allowing optional coupling with rotation monitoring or assisted feeding mechanisms. The support structure was custom-designed and fabricated using PLA to ensure strength and stability.

Fig. 9. 3D-printed spool holder with integrated gear ring

A custom bracket for securing axial fans near the heated zone, ensuring stable thermal control during operation is presented in Figure 10. This bracket ensures proper airflow over the extrusion barrel, maintaining temperature stability and preventing overheating during continuous filament production.

Fig. 10. The ventilation fan support 3D printed

A 3D-printed alignment bracket designed to guide manually cut PET strips into the extruder intake is presented in Figure 11. The component ensures proper positioning and stability of the feed material during operation, reducing the risk of misalignment or jamming at the input stage.
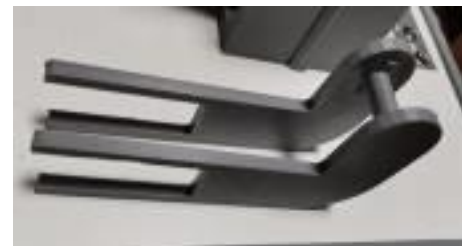
Fig. 11. PET strip guide bracket

Figure 12 illustrates the large gear blank used in the extrusion drive module. This component was 3D printed using PLA and features a flat circular profile with a central bore, intended to be mounted on a keyed shaft. Although shown before finishing and integration, the gear is designed to transmit torque from the motor to the feeder mechanism, working in conjunction with a smaller interlocking gear within the gearbox assembly. The printed geometry reflects the custom adaptability provided by additive manufacturing in creating functional transmission parts with tight dimensional tolerances.

Fig. 12. *3D-printed large gear blank for the extrusion drive assembly*

Figure 13 shows the interface fully mounted and wired. It features a temperature display, adjustment buttons, and a power switch. The figure emphasizes ergonomic layout and visibility, ensuring intuitive use and quick operator feedback.

Fig. 13. *The display interface and switch installed*

A detailed close-up of the digital panel is shown in Figure 14, displaying real-time temperature and voltage data. This visual feedback is essential for maintaining consistent operating parameters and for detecting any system faults promptly.

Fig. 14. *The digital monitoring panel close-up*

A complete perspective of the extruder system in its operational configuration is depicted in Figure 15. All subsystems, including the control panel, extrusion barrel, drive system, and filament guiding module, are integrated. The modular design facilitates component swapping and compact desktop use.

Fig. 15. *The extruder system assembled view*

4. Conclusions

This paper presented the design, fabrication, and functional validation of a modular extrusion system capable of processing manually cut PET strips into 3D printing filament. Emphasis was placed on mechanical modularity, ease of assembly, and the use of 3D-printed structural components alongside low-cost electronics and hardware.

Functional testing demonstrated that the extruder could operate continuously at a working temperature of 230 °C without jamming or thermal instability. The resulting filament showed stable diameter and surface quality, suitable for further evaluation in non-critical 3D printing applications. The findings support the feasibility of repurposing PET waste into usable filament using open-source, low-cost extruder designs.

The modular system provides a scalable and replicable platform for small-scale recycling, making it appropriate for academic, research, and community-based settings. In the educational domain, this extruder can serve as a hands-on tool for learning about material processing, thermal management, and digital manufacturing. Its customizable, open design encourages adaptation for various experimental and eco-design projects aligned with circular economy principles.

References

[1]. Baechler C., Garcia D. C., Pearce J. M., *Distributed recycling of waste polymer into RepRap feedstock*, Rapid Prototyping Journal, vol. 19, no. 2, p. 118-125, 2013.
[2]. Kreiger M. A., Pearce J. M., *Environmental Life Cycle Analysis of Distributed 3D Printing and Conventional Manufacturing of Polymer Products*, ACS Sustainable Chemistry & Engineering, 1(12), p. 1511-1519, 2013.

[3]. Woern A. L., Pearce J. M., *Distributed Manufacturing of Flexible Products: Technical Feasibility and Economic Viability*, Technologies, 5(4), 71, 2017.

[4]. Cruz Sanchez F. A., Boudaoud H., Hoppe S., Camargo M., *Polymer recycling in an open source additive manufacturing context: mechanical issues*, Additive Manufacturing, 17, p. 87-105, 2017.

[5]. Pearce J. M., *Building Research Equipment with Free, Open Source Hardware*. Science, 337(6100), p. 1303-1304, 2012.

[6]. Zhang C., et al., *Open Source 3D Printable Optics Equipment*, PLoS ONE, 8(3), 2013.

[7]. Lee D., et al., *Thermal and Mechanical Degradation of Recycled Polylactic Acid Filaments for Three Dimensional Printing Applications*, Polymers, 14(24), 2022.

[8]. Chopade S., et al., *Conversion of Waste PET Bottles into 3D Printing Filament: A Sustainable Approach*, Journal of Neonatal Surgery, 14(31s), p. 732-741, 2025.

[9]. Van de Voorde B., et al., *Effect of extrusion and fused filament fabrication processing parameters of recycled poly(ethylene terephthalate) on the crystallinity and mechanical properties*, Additive Manufacturing, 50, 102518, 2022.

[10]. Pepek E. S., Hanan J. C., *3D Printing with Recycled PET as a Sustainable Thermoplastic Alternative: Comparing Printed and Filament Material Properties*, Polymer Plastics Technology and Materials, p. 1-15, 2025.

[11]. Nguyen P. Q. K., et al., *Influences of printing parameters on mechanical properties of recycled PET and PETG using fused granular fabrication technique*, Polymer Testing, 132, 108390, 2024.

[12]. Robbika F., et al., *Recycled PET Plastics Filament: Characteristics and Cost Opportunity*, Semesta Teknika, 27(2), p. 148-158, 2024.

[13]. Seibert M., et al., *Manufacturing of a PET filament from recycled material for material extrusion (MEX)*, Recycling, 7(5), 69, 2022.

[14]. Morales Mendez G., et al., *Prototype Pultrusion of Recycled Polyethylene Terephthalate Plastic Bottles into Filament for 3D Eco Printing: Education for a Sustainable Development Project*, Sustainability, 16(19), 8347, 2024.

[15]. Voorde B. van de, et al., *The effect of carbon fiber content on physico-mechanical properties of recycled polyethylene terephthalate composites additively manufactured with fused filament fabrication*, Additive Manufacturing, 60, 103246, p. 583-600, 2022.

[16]. Woern A. L., et al., *RepRapable Recyclebot: Open source 3 D printable extruder for converting plastic to 3 D printing filament*, HardwareX, 4, e00026, 2018.

[17]. Moretti M., Rossi A., *Closed Loop Filament Feed Control in Fused Filament Fabrication*, 3D Printing and Additive Manufacturing, 10(3), p. 500-513, 2023.

[18]. Rashwan O., et al., *Extrusion and characterization of recycled polyethylene terephthalate (rPET) filaments compounded with chain extender and impact modifiers for material extrusion additive manufacturing*, Scientific Reports, 13, 16041, 2023.

[19]. Chien Y.-C., et al., *Closed Loop Recycling of 3D Printed Wood–PLA Composite Parts: Effects on Mechanical and Structural Properties via Fused Filament Fabrication*, Polymers, 16(21), 3002, 2024.

INVESTIGATION OF THERMAL CONDUCTIVITY IN ADVANCED METALLIC MATERIALS VIA COMPUTATIONAL FLUID DYNAMICS

Rareş AVĂDANEI[1], Florin-Bogdan MARIN[1,2], Mihaela MARIN[1,2]

[1] "Dunarea de Jos" University of Galati, Romania
[2] Interdisciplinary Research Centre in the Field of Eco-Nano Technology and Advanced Materials CC-ITI,
Faculty of Engineering, "Dunarea de Jos" University of Galati, Romania, 47 Domnească Street, RO-800008,
Galaţi, Romania
e-mail: flmarin@ugal.ro

ABSTRACT

This study investigates the transient thermal behavior of Ti6Al4V alloy using computational fluid dynamics (CFD) simulations. The primary objective is to characterize the alloy's heat-conduction performance under controlled thermal-loading conditions. A dual-scale modeling approach was employed, combining a simplified body-centered cubic (BCC) lattice structure to represent the β-phase and a macroscopic solid domain to simulate the bulk material response. The simulations were performed over a 10-minute interval, with thermal data extracted at 1-, 3-, 5-, and 10-minute time steps. The results indicate delayed, uneven heat propagation in Ti6Al4V, attributed to its intrinsically low thermal conductivity (6.5 W/m·K). The findings provide insight into the alloy's thermal limitations, particularly in applications requiring efficient heat dissipation. The study demonstrates the potential of CFD as a predictive tool for evaluating thermal performance in advanced metallic materials.

KEYWORDS: thermal conductivity, Ti6Al4V, CFD, transient heat transfer

1. Introduction

Ti6Al4V is one of the most widely used titanium alloys in high-performance engineering sectors such as aerospace, biomedical implants, and additive manufacturing, due to its excellent strength-to-weight ratio, corrosion resistance, and biocompatibility [1-4]. However, its relatively low thermal conductivity - typically between 5 and 7 W/m·K - poses challenges in applications requiring efficient heat dissipation [5-7]. This limitation becomes critical in processes like laser powder bed fusion (LPBF), where high thermal gradients can lead to undesirable microstructures, residual stresses, and thermal distortion [8-10]. Notably, experimental studies have revealed significant discrepancies in thermal conductivity between bulk and powder forms of Ti6Al4V. For example, Saeidi *et al.* reported ~0.13 W/m·K for powder, compared to ~5.4 W/m·K for bulk material, emphasizing the effects of porosity and contact resistance [3, 11, 12]. The influence of phase composition is also important, as Ti6Al4V exhibits a dual-phase (α + β) structure. The β-phase, typically

modeled using a BCC lattice, shows directional heat transfer behavior, which can be impacted by grain morphology and crystallographic orientation [6, 13]. Such microstructural factors play a significant role in thermal anisotropy.

Computational fluid dynamics (CFD) has emerged as a valuable tool for modeling the thermal response of Ti6Al4V under various boundary conditions. CFD DEM semi-coupled simulations have been employed to model powder–build interactions, melt pool formation, and porosity development in LPBF processes [6, 14-16]. These models help in optimizing process parameters such as scan speed and preheating temperature, ultimately enhancing component quality [9, 6, 17]. Furthermore, powder properties such as particle size, shape, and packing density significantly affect the effective thermal conductivity, especially in electron beam powder bed fusion (EB-PBF) processes [18].

Despite the growing body of literature, most studies integrate convective and radiative effects, which obscure the alloy's intrinsic conductive properties. To bridge this gap, the present study

employs CFD simulations to investigate transient thermal conduction in Ti6Al4V under strictly conduction-dominated conditions. A dual-scale modeling approach is used: a macroscopic solid domain for bulk behavior, and a microstructural BCC lattice for directional heat transfer in the β-phase. This framework aims to isolate material-specific effects and provide insights for the design of thermally optimized components using Ti6Al4V. The implementation of computational fluid dynamics (CFD) in this study is justified by its demonstrated capability to accurately model transient heat conduction phenomena in metallic materials. As a numerical technique, CFD offers a rigorous and flexible framework for solving the governing heat transfer equations under well-defined boundary conditions, thus enabling detailed simulation of thermal diffusion across both macroscopic domains and microstructural representations.

In the specific case of Ti-6Al-4V, a dual-phase alloy characterized by notable thermal anisotropy, CFD facilitates the quantitative assessment of directional heat conduction as influenced by crystallographic architecture and phase morphology. This is particularly relevant when analysing idealized body-centered cubic (BCC) lattice configurations that approximate the behavior of the β-phase. Unlike analytical or empirical approaches, CFD provides enhanced spatial and temporal resolution, which is important for capturing multi-scale thermal transport phenomena. Furthermore, it allows the explicit isolation of conduction mechanisms by excluding convective and radiative contributions - thereby offering a more intrinsic evaluation of the material's conductive properties. Considering the inherent difficulties associated with experimental characterization of heat flow in complex microstructures, CFD emerges as a powerful predictive tool for advancing both scientific insight and thermally optimized component design.

2. Experimental Procedure

To investigate the transient thermal conduction behavior of Ti6Al4V, a series of computational fluid dynamics (CFD) simulations was performed using two complementary geometric models: a macroscopic solid block and a microstructural lattice structure representing the β-phase. This dual-scale approach was designed to capture both global and directional thermal diffusion phenomena specific to the alloy. The macroscopic model consisted of a solid rectangular domain with dimensions 100 mm × 300 mm × 10 mm, intended to approximate bulk material behavior under thermal loading. In parallel, a simplified body-centered cubic (BCC) lattice with dimensions 4 mm × 4 mm × 3 mm was constructed to

mimic heat transfer pathways within the β-phase of the alloy. This structure was used to explore localized anisotropic conduction effects resulting from the crystallographic configuration of the β-phase.

Material properties were defined based on literature values validated by experimental measurements. Ti6Al4V was assigned a density of 4410 kg/m^3, a thermal conductivity of 6.5 W/m·K, and a specific heat capacity of 326 J/kg·K. These values ensured realistic thermal behavior within the simulation environment and enabled time-accurate transient analysis.

The simulation domain was initialized with an ambient temperature of 20 °C. A thermal load was applied to the bottom surface of the model by imposing a fixed temperature of 100 °C, while the remaining surfaces were considered adiabatic. This configuration allowed the observation of one-dimensional heat flow without interference from convective or radiative effects, which were intentionally excluded to focus solely on conductive mechanisms.

Transient simulations were executed over a duration of 10 minutes, with thermal data extracted at time intervals of 1, 3, 5, and 10 minutes. A structured mesh was employed for both models, with higher node density near the heat source to capture steep thermal gradients. Mesh convergence testing was performed to ensure numerical stability and independence of results from mesh resolution.

Post-processing of simulation data included the extraction of temperature contours and thermal flux distributions at each time interval. These outputs enabled detailed observation of heat propagation dynamics and thermal gradient evolution within the two geometries. The microstructural BCC model was particularly instrumental in identifying anisotropic heat transfer pathways and delayed temperature equalization, providing insights into the role of microstructure in limiting the thermal conductivity in Ti6Al4V.

3. Results and Discussion

The CFD simulations conducted on Ti6Al4V under conduction-dominated conditions reveal distinct transient thermal behavior at both macro and microstructural scales. In the macroscopic simulation, where heat was applied uniformly to the bottom surface of a solid block, temperature evolution over a 10-minute period showed a delayed and highly non-uniform thermal response. As illustrated in Figure 1, the highest temperatures remained concentrated near the heat source, while the upper surface exhibited only modest increases. This confirms the limited thermal conductivity of Ti6Al4V, which inhibits efficient heat transfer along the vertical axis.
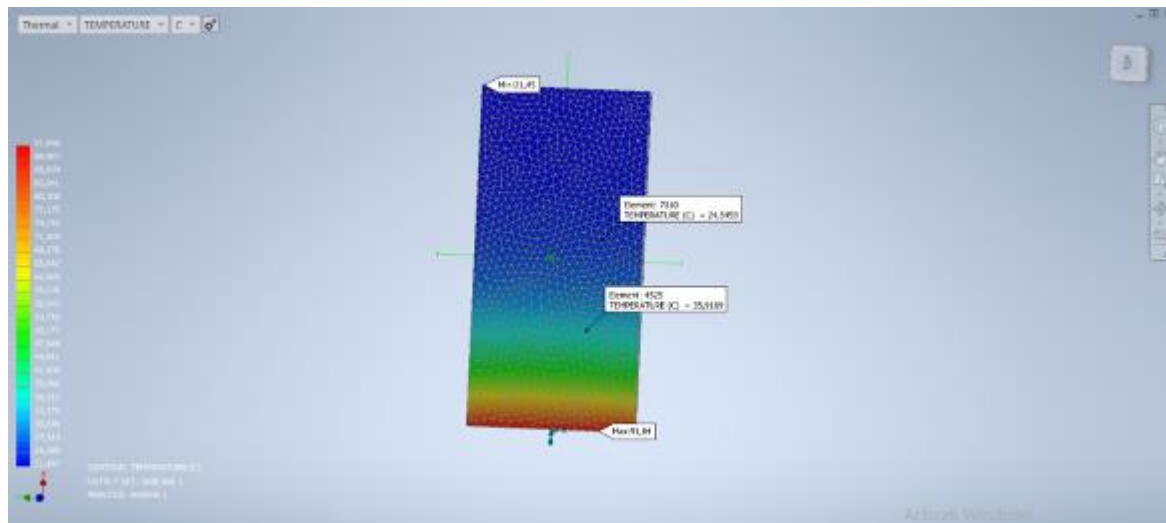
Fig. 1. Simulated temperature field in a macroscopic Ti6Al4V block after 10 minutes of conduction-driven heating

To better understand heat diffusion within the β-phase, a body-centered cubic (BCC) lattice model was employed (Figure 2). The simplified structure enabled the capture of directional conduction through the microstructure. Temperature snapshots taken at 1, 3, 5, and 10 minutes (Figures 3-6) show progressive, yet delayed, thermal diffusion from the base upward.

At 1 minute, the temperature remained highly localized at the base, with minimal change in the upper lattice region. As heating continued, thermal propagation advanced slowly, becoming more uniform at 5 and 10 minutes, though vertical gradients persisted.
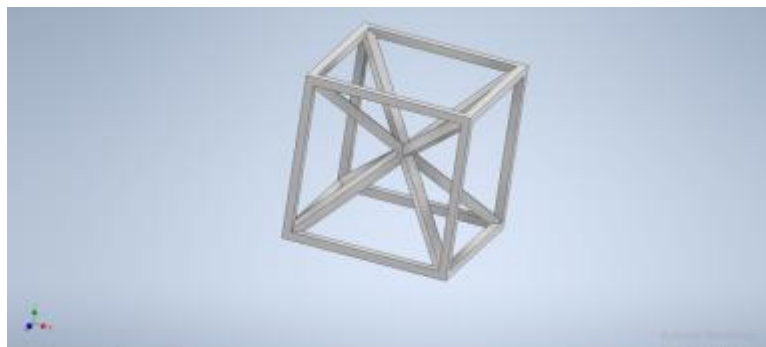
Fig. 2. CAD-based geometric representation of a BCC lattice unit used to model the β-phase in Ti6Al4V

These results reflect the alloy's intrinsic thermal resistance, governed by its low thermal diffusivity. Ti6Al4V yields a thermal diffusivity of 4.47×10^{-6} m²/s, calculated via $\alpha = k / (\rho \cdot c_p)$.

This low α value supports the simulation findings of slow heat penetration and persistent temperature gradients.

In practical applications, these findings underscore the importance of accounting for Ti6Al4V's slow heat conduction, particularly in designs involving passive thermal management or transient thermal loads. While the material's mechanical and corrosion-resistant properties remain advantageous, its thermal limitations may necessitate the use of auxiliary cooling methods or hybrid material solutions in temperature-sensitive components. The CFD-based methodology used in this study has proven effective in isolating and analysing these material-specific thermal behaviours, offering a predictive framework for optimizing Ti6Al4V in thermally constrained environments.

This crystallographic arrangement contributes to the alloy's thermal behavior. The tightly packed atomic structure and directional bonding influence heat transfer, supporting the observed anisotropy in thermal distribution during simulation.
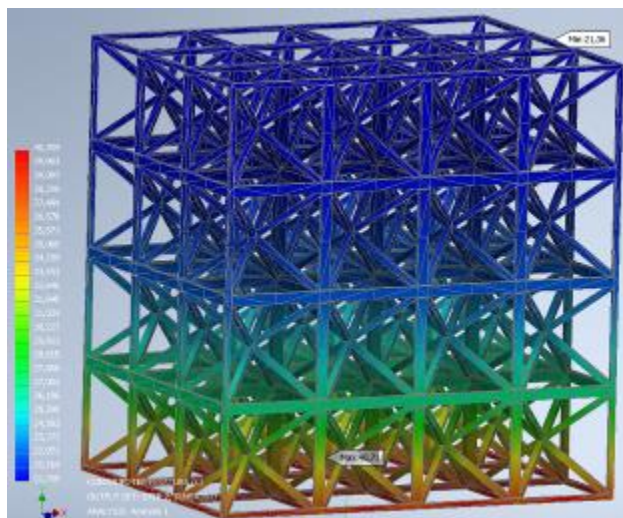
Fig. 3. *Simulated initial thermal propagation in the BCC lattice model of Ti6Al4V at t = 1 minute*
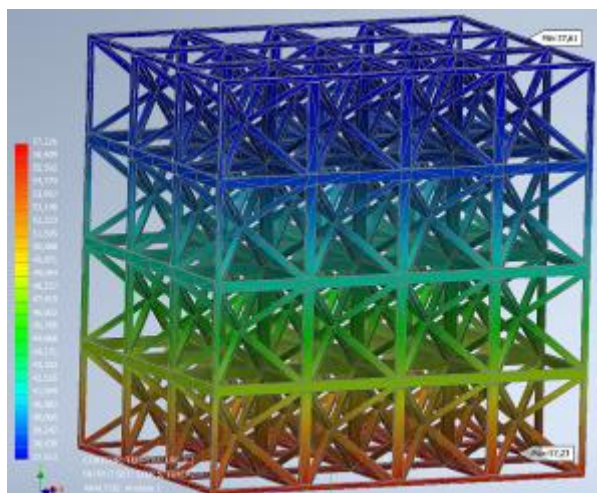
Fig. 4. *Simulated intermediate thermal propagation in the BCC lattice model of Ti6Al4V at t = 3 minutes*
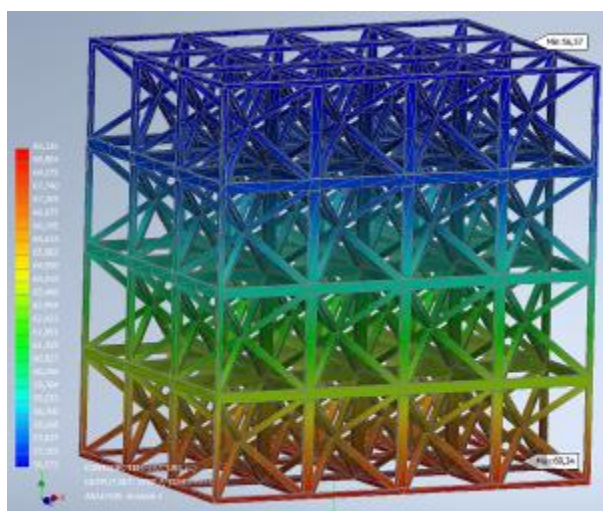
Fig. 5. *Simulated advanced thermal propagation in the BCC lattice model of Ti6Al4V at t = 5 minutes*
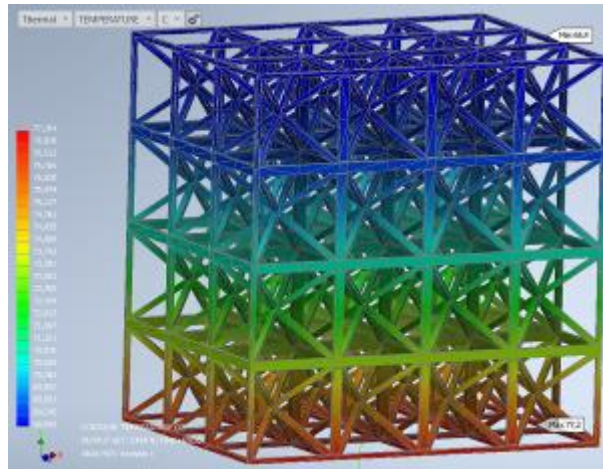
Fig. 6. *Quasi-steady-state thermal distribution in the BCC lattice model of Ti6Al4V at t = 10 minutes*

The thermal resistance observed in both simulations reflects the material's intrinsic properties. Based on the thermal diffusivity relation $\alpha = k / (\rho \cdot c_p)$, and using values of 6.5 W/m·K for conductivity, 4410 kg/m^3 for density, and 326 J/kg·K for specific heat, Ti6Al4V exhibits low α. This theoretical result aligns with the delayed thermal response in both the bulk and lattice domains. At the end of the simulation period (t = 10 min), the temperature at the base reached approximately 240 °C, while the top surface remained below 137 °C. This temperature gradient reinforces the slow thermal response and poor vertical conduction efficiency of Ti6Al4V.

The combined findings reinforce the conclusion that Ti6Al4V - although mechanically robust and corrosion resistant - is limited in its ability to quickly or uniformly dissipate heat. The thermal gradients persist well into the simulation period, indicating that the alloy is more suitable for applications where structural integrity is critical, but passive thermal management must be supplemented or reconsidered. CFD has proven to be a reliable tool in capturing both macroscopic heat flow and localized anisotropic behavior, providing a predictive framework for optimizing Ti6Al4V in thermally constrained environments.

4. Conclusions

This paper employed computational fluid dynamics (CFD) simulations to investigate the transient thermal behavior of the titanium alloy Ti6Al4V under conduction-dominated conditions. By combining macro-scale and microstructural models, the simulations provided valuable insights into both bulk and directional heat transfer characteristics of the material. The results consistently demonstrated a slow and non-uniform thermal response, with significant vertical gradients persisting throughout the simulation period. This behavior was evident in both the solid block and the BCC lattice models, indicating that the alloy's low thermal conductivity and thermal diffusivity fundamentally limit its ability to rapidly dissipate heat.

The microstructural simulations highlighted the influence of lattice structure on thermal propagation, particularly within the β-phase of Ti6Al4V. The BCC geometry revealed delayed and anisotropic heat conduction, with thermal gradients diminishing only gradually over time. These findings underscore the material's limitations in applications that require efficient and rapid thermal equalization, such as those involving cyclic thermal loading, high-power electronics, or additive manufacturing processes where thermal control is important to part integrity.

Despite these thermal constraints, Ti6Al4V remains a highly valuable material due to its exceptional mechanical properties, corrosion resistance, and biocompatibility. However, its use in thermally sensitive designs must be carefully considered. These findings suggest that while Ti6Al4V is structurally ideal, its thermal constraints demand strategic adaptations in design when used in temperature-sensitive environments.

References

[1]. **Bartsch K.,** *et al.*, *Thermal Conductivity of Ti 6Al 4V in Laser Powder Bed Fusion*, Frontiers in Mechanical Engineering, 8, 830104, 2022.
[2]. **Taha Tijerina J. J., Edinbarough I. A.**, *Comparative Cutting Fluid Study on Optimum Grinding Parameters of Ti6Al4V Alloy Using Flood, Minimum Quantity Lubrication (MQL), and Nanofluid MQL (NMQL)*, Lubricants, 11(6), art. 250, 2023.
[3]. **Mukherjee T.,** *et al.*, *Heat and fluid flow in additive manufacturing – Part II: Powder bed fusion of stainless steel, and titanium, nickel and aluminum base alloys*, Computational Materials Science, 150, p. 369-380, 2018.
[4]. **Kollmannsberger S.,** *et al.*, *Accurate prediction of melt pool shapes in laser powder bed fusion by the non-linear temperature*

equation including phase changes – isotropic versus anisotropic conductivity, arXiv preprint arXiv:1903.09076, 2019.

[5]. Shanbhag G., Vlasea M., Effect of varying preheating temperatures in electron beam powder bed fusion: Part I – Assessment of the effective powder cake thermal conductivity, arXiv preprint arXiv:2107.14684, 2021.

[6]. Yu T., Zhao J., Semi coupled resolved CFD–DEM simulation of powder based selective laser melting for additive manufacturing: a case study on Ti6Al4V, Computers & Mathematics with Applications, 81, p. 259-273, 2021.

[7]. Gong H., et al., Influence of Defects on Mechanical Properties of Ti 6Al 4V Components Produced by Selective Laser Melting and Electron Beam Melting, Materials & Design, 86, p. 545-554, 2015.

[8]. Calta N. P., et al., Cooling dynamics of two titanium alloys during laser powder bed fusion probed with in situ X ray imaging and diffraction, Materials & Design, 195, 108987, 2020.

[9]. Boccardo A. D., et al., Martensite decomposition kinetics in additively manufactured Ti 6Al 4V alloy: in situ characterisation and phase field modelling, arXiv preprint arXiv:2404.09806, 2024.

[10]. Bai H. J., et al., Effect of Heat Treatment on the Microstructure and Mechanical Properties of Selective Laser Melted Ti64 and Ti 5Al 5Mo 5V 1Cr 1Fe, Metals, 11(4), 534, 2021.

[11]. Khairallah S. A., et al., Laser powder-bed fusion additive manufacturing: physics of complex melt flow and formation mechanisms of pores, spatter, and denudation, Acta Materialia, 108, p. 36-45, 2016.

[12]. Halder R., et al., The Effect of Interlayer Delay on the Heat Accumulation, Microstructures, and Properties in Laser Hot Wire Directed Energy Deposition of Ti 6Al 4V Single Wall, Materials, 17(13), 3307, 2024.

[13]. Mao Y., et al., Quantitative Analysis of the Physical Properties of Ti6Al4V Powders Used in a Powder Bed Fusion Based on 3D X ray Computed Tomography Images, Materials, 17(4), 952, 2024.

[14]. Azadi Tinat M. R., et al., Numerical Simulations to Predict the Melt Pool Dynamics and Heat Transfer during Single Track Laser Melting of Ni Based Superalloy (CMSX 4), Metals, 13(6), art. 1091, 2023.

[15]. Ransenigo C., et al., Evolution of Melt Pool and Porosity During Laser Powder Bed Fusion of Ti6Al4V Alloy: Numerical Modelling and Experimental Validation, Lasers Manuf. Mater. Process. 9, p. 481-502, 2022.

[16]. Bayat Mohamad, et al., A review of multi-scale and multi-physics simulations of metal additive manufacturing processes with focus on modeling strategies, Additive Manufacturing, 47, 102278, 2021.

[17]. Wang X., et al., CFD Simulation of Heat Transfer and Fluid Flow in Laser Wire Deposition of Ti 6Al 4V Alloy, 3D Printing and Additive Manufacturing, PMCID PMC10440678, 2023.

[18]. Brika S. E., et al., Influence of particle morphology and size distribution on the powder flowability and laser powder bed fusion manufacturability of Ti 6Al 4V alloy, Journal of Manufacturing Processes, 57, p. 746-758, 2020.

MATHEMATICAL MODELING AND DEVELOPMENT OF A GRAPHICAL INTERFACE (GUI) FOR SIMULATING THE ORBITAL FORGING PROCESS

Marian-Iulian NEACȘU[1], Elisabeta ȚANU-LUPU[1]

[1] "Dunarea de Jos" University of Galati, Faculty of Engineering, Department of Materials and Environmental Engineering

e-mail: marian.neacsu@ugal.ro

ABSTRACT

The main objective of this work was to develop a theoretical and practical tool for understanding and simulating the orbital forging process, using mathematical modeling and GUI-based graphical interfaces developed with MATLAB. This interface represents a link between theoretical analysis and practical applicability.

KEYWORDS: orbital forging, mathematical modeling, interpolation, graphical interface

1. Introduction

In the field of metal working by plastic deformation, current trends are moving towards processing methods with minimal metal and energy consumption, in particular, cold plastic deformation. A number of economic, technical and organizational considerations argue in favour of cold plastic deformation. However, in cold plastic deformation processes, high forces are required, due to the resistance of the material in the cold state, as a result of work hardening during deformation and friction on the contact surfaces between the material and the tools. These have limited the industrial use of cold working [1].

The reconsideration of conventional cold forming presses led to the adoption of different kinematics, more complex tool movements, and a focus on parts of a specific shape [1, 2].

The orbital forging process is based on the fact that the axial force acting to deform a metallic material is considerably reduced if, in the area where the tools act, the contact surface between the tools and the semi-finished product is reduced, so the pressure exerted during pressing is not applied to the entire surface of the semi-finished product, but only to an area of it, which represents approximately 20-30% of the related frontal surface [3, 4].

The terminology used in the specialized literature to define this process varies from one country to another: thus, in Great Britain the term "rotary forging" and "rocking die" are used, in the

USA the process is called "orbital forging", and in Russia "stampovka obkatîvaniem" and "tsartsovoi prokatka" (a process similar in principle and developed especially in this country) [1, 4].

Mathematical modeling is the process of formulating an abstract model in terms of mathematical language to describe the complex behavior of a real system. Mathematical models are quantitative models and are often expressed in terms of ordinary differential equations and partial differential equations. Mathematical models can also be statistical models, fuzzy logic models, and empirical relationships. In fact, any description of a model that uses mathematical language can be called a mathematical model [5].

Mathematical modeling is a principled activity that has principles behind it and methods that can be successfully applied. Principles can be general principles or meta-principles formulated as questions about the intentions and goals of mathematical modeling [6].

A system of interactive visual components for a computer or system software is called a GUI (graphical user interface). GUI is the interface that uses graphical elements to allow people to interact with electronic devices, including computers, laptops, tablets, and smartphones, as required [7, 8]. In terms of human-computer interaction systems or technology, it is a very important component of software application programming, as it replaces actions with text-based commands in the system. Whether it is a text file, an object, an image, or a

video, GUI displays all types of necessary content that a user can imagine in the system [9-11].

2. Experimental conditions

In the experiments carried out on the orbital forging machine, we used lead specimens, with dimensions Ø 15 x 40 mm.

Of the total length, 10 mm constitutes the part fixed in the mould, and the remaining 20 mm is the free end, subject to deformation.

The lead specimens were deformed with reductions per rotation, of 1 mm, 2 mm, and 3 mm.

Both the height after deformation and the characteristic diameters, D_1, D_2 and D_3, were measured (Figure 1).
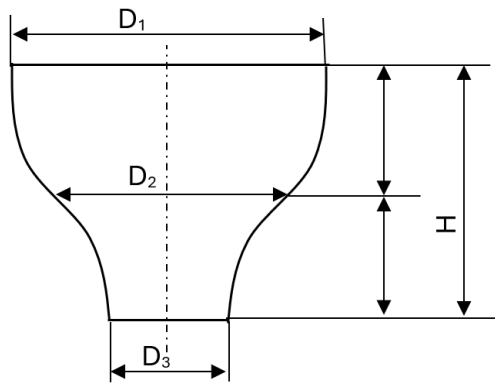
Fig. 1. *Characteristic dimensions of the part: D_1 - diameter measured at the interface of the blank - forming tool; D_2 - diameter measured at the middle of the height of the blank; D_3 - diameter measured at the base of the blank; H - Height of the blank*

The measurement results were listed in Tables 1, 2, 3.

Table 1. *Specific diameters for 1 mm/revolution reduction*

Nr. crt.	Do	Ho	D_1	D_2	D_3
1	15	30	15	15	15
2	15	30	18	16	15.5
3	15	30	23	18	17
4	15	30	30	23	20
5	15	30	40	30	25

Based on these measured data, the mathematical model equations for the experimental orbital forging were developed.

Table 2. *Specific diameters for 2 mm/revolution reduction*

Nr. crt.	Do	Ho	D_1	D_2	D_3
1	15	30	15	15	15
2	15	30	17	16.5	15
3	15	30	22	20	19
4	15	30	28	25	24
5	15	30	38	33	30

Table 3. *Specific diameters for 3 mm/revolution reduction*

Nr. crt.	Do	Ho	D_1	D_2	D_3
1	15	30	15	15	15
2	15	30	17	16.5	15
3	15	30	21	20	19
4	15	30	27	25	24
5	15	30	35	33	30

Independent parameters of the orbital forging process were considered:

- x_1 is the current height;
- x_2 is the pressing speed.

The dependent process parameters are D_1, D_2, D_3.

- D_1 represents the diameter measured at the interface of the blank and the deformation tool;
- D_2 represents the diameter measured at the middle of the height of the blank;
- D_3 represents the diameter measured at the base of the blank;

The mathematical model equations obtained for D_1, D_2, D_3 are

$$D_1 = 56.25 - 1.375 * x_1 - 3.75 * x_2 + 0.125 * x_1 * x_2$$
$$D_2 = 27.5 - 0.45 * x_1 - 4.5 * x_2 + 0.15 * x_1 * x_2$$
$$D_3 = 26.25 - 0.375 * x_1 - 3.75 * x_2 + 0.125 * x_1 * x_2$$

3. Creating a graphical interface in MatLab

MatLab is a program that works with numerical data represented by fields or matrices.

To create this GUI in MatLab, we used the "uimenu" and "uicontrol" functions for elements of the "slider", "button" and "display fields" types, which help us create a GUI in which we can modify the input parameters of the process without modifying the source code each time [12].

The graphical representations were made using the "plot", "plot3" and "surf" functions, for the 2D and 3D visualization of the diameter variation depending on the deformation height [12, 13].

As an example, Figure 2 is a schematic representation of the orbital forging process and this

image is an integral part of the graphical interface created.

The interpolated values were calculated using the "interp1" function, and the differences from the modeled values were displayed in real time. Interactivity was ensured by using callbacks associated with each control element.

To create an interface in MatLab, we used measured data obtained from the orbital forging experiment as well as the mathematical model equations for the 3 diameters D_1, D_2, D_3.

In the case of this experiment, the input parameters are the pressing speed and the desired final height for the semi-finished product.

Three different pressing speeds were used, namely 1 mm, 2 mm, and 3 mm per rotation, and the initial height of the semi-finished product subjected to forging was 30 mm.
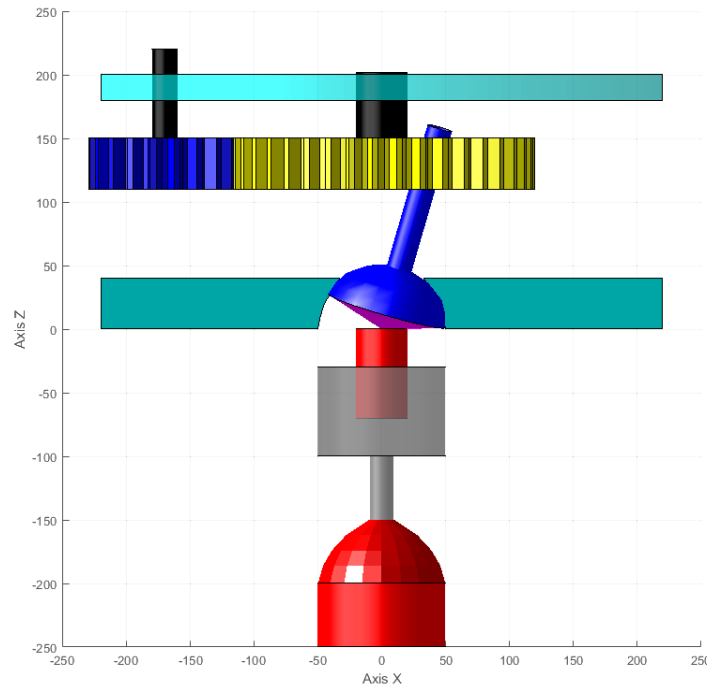
Fig. 2. *Schematic representation of the orbital forging process*

Figure 3 shows the calculated values for the specific dimensions D_1, D_2 and D_3 following a simulation of the orbital forging process, at a current height H = 29 mm. For each diameter, three types of values are displayed:

• Interpolated values - results from interpolation of experimental data, using the "spline (interp1(..., 'spline'))" method;

• Modeled values - calculated based on the process-specific regressive mathematical model (polynomial);

• Difference - represents the deviation between the interpolated and modeled value (Difference = Interpolated - Modeled).

Fig. 3. *Specific dimensions D_1, D_2 and D_3*

Figure 4 illustrates the variation of the values for D_1, D_2, D_3 as a function of the semi-finished product height values, as obtained by simulation using the GUI graphical interface. This variation is the same as the variation of the measured values.

In Figure 5 we have an overview of the graphical interface created in MatLab that displays the results of the orbital forging process simulation (the values of the diameters D_1, D_2, D_3 obtained both by interpolation and by calculation using the equations of the mathematical model) for a semi-finished product height of 29 mm.
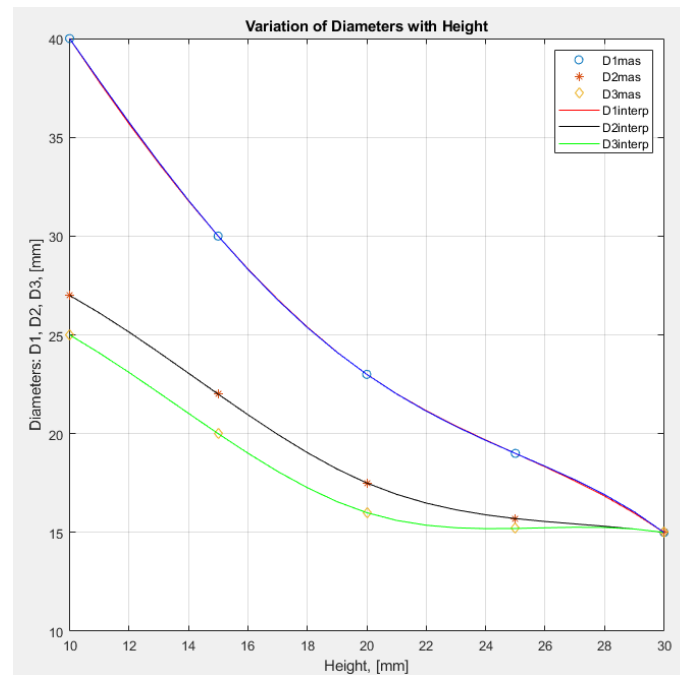
Fig. 4. *Variation of values for D_1, D_2, D_3 depending on the height values of the semi-finished product, values obtained through simulation using the GUI graphical interface*
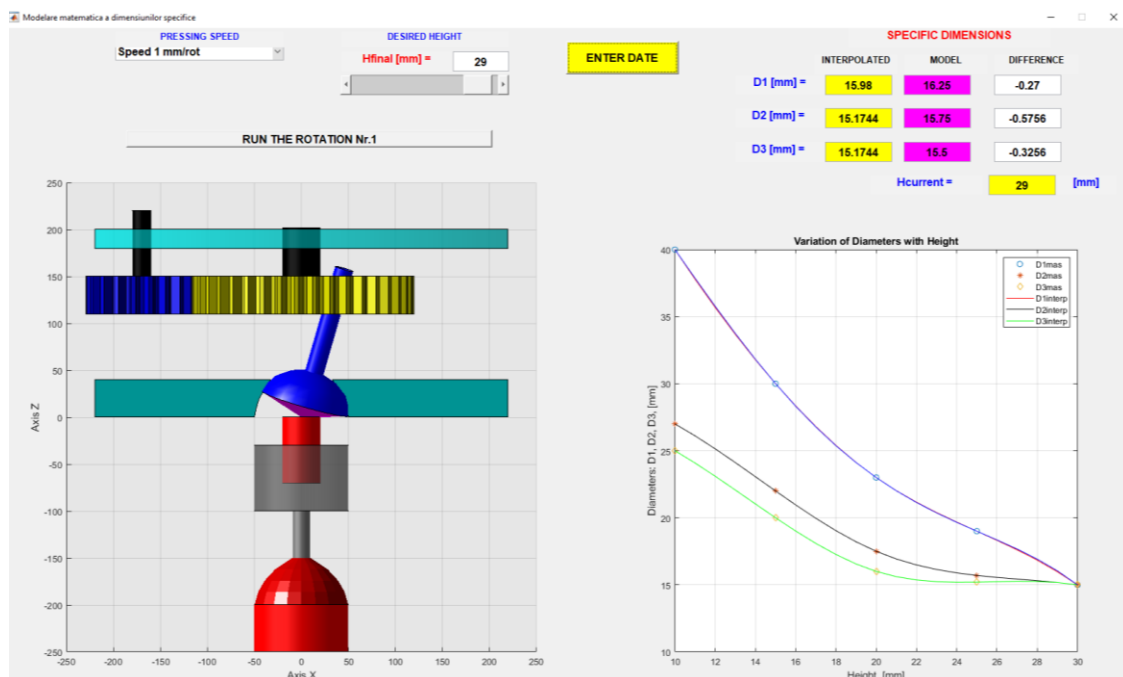
Fig. 5. *Overview of the graphical interface made in Matlab*

4. Conclusions

The main objective of this paper was to develop a theoretical and practical tool for understanding and simulating the orbital forging process, using mathematical modeling and GUI graphical interfaces. This integrated approach reflects the current trend of modern engineering, in which numerical analysis, simulation and visual interaction become essential for optimizing technological processes and for making decisions in a fundamental way.

During the paper, a review of the main characteristics of the orbital forging process was carried out, highlighting the advantages it offers compared to conventional forging, such as: reducing deformation forces, improving the surface quality of the finished part, increasing tool durability and the possibility of cold and semi-hot processing of materials. At the same time, the complex nature of the kinematics of this process was emphasized.

In this context, mathematical modeling has proven to be an indispensable tool for describing and understanding the mechanical behavior of the semi-finished product during forging.

Another significant contribution of the work consists of the development of an interactive graphical interface in MatLab, which integrates the formulated mathematical models and allows the visual simulation of the orbital forging process. This interface represents a connecting point between theoretical analysis and practical applicability. Through it, the user can enter different input parameters and visualize in real time the effects of the changes, being able to interpret the results intuitively. The interface thus becomes not only an educational tool, but also one for industrial research and development.

In conclusion, the work reflects a relevant contribution in the field of simulation of plastic deformation processes, by combining theory with practical application in a coherent and applicable manner.

References

[1]. **Madej L., et al.**, *Recent development in orbital forging technology*, 2008.

[2]. **Zaharia L.**, *Studii privind curgerea materialului la forjare orbitală*, Lucrare sesiunea "Contribuţia învăţământului politehnic la dezvoltarea ramurilor de vârf din România", Iaşi l988.

[3]. **Leonid B. Aksenov, Sergey N. Kunkin**, *Hot Orbital Forging by Tool with Variable Angle of Inclination*, Advances in Mechanical Engineering, 2018.

[4]. **Andrzej Kocańda**, *Development of Orbital Forging Processes by Using Marciniak Rocking-Die Solutions*, 60 Excellent Inventions in Metal Forming, 2015.

[5]. **Nowak, et al.**, *The Material Flow Analysis in the Modified Orbital Forging Technology*, Materials Science Forum, volumes 654-656, 2010.

[6]. **Xin-She Yang**, *Engineering Mathematics with Examples and Applications*, 2017.

[7]. **Cha D., et al.**, *Fundamentals of Modeling and Analyzing Engineering Systems*, Cambridge University Press, New York, 2000.

[8]. **Nowak J., et al.**, *Recent development in orbital forging technology*, Int J Mater Form 1 (Suppl 1), p. 387-390, https://doi.org/10.1007/s12289-008-0076-2, 2008.

[9]. **Clive L. Dym**, *Principles of Mathematical Modeling*, Cambridge University Press, New York, 1994.

[10]. **Carson and C. Cobelli**, *Modelling Methodology for Physiology and Medicine*, Academic Press, San Diego, CA, 2001.

[11]. ***, https://www.geeksforgeeks.org/computer-graphics/what-is-graphical-user-interface/.

[12]. **Eshkabilov S.**, *Graphical User Interface Model Development*, Beginning MATLAB and Simulink, Apress, Berkeley, CA, https://doi.org/10.1007/978-1-4842-5061-7_3, 2019.

[13]. **Ghinea M., Fireţeanu V.**, *MatLab, calcul numeric, grafică, aplicaţii*, Teora, Bucureşti, l997.

[14]. **Nasiruzzaman A. B. M.**, *Using MatLab to develop standalone graphical user interface (GUI) software packages for educational purposes*, MatLab - Modelling, Programming and Simulations, Edited by Emilson Pereira Leite, 2010.

SMART METALLURGY: THE IMPACT OF INDUSTRY 4.0 ON MATERIALS PROCESSING AND INNOVATION

Patricia Isabela BRĂILEANU

National University of Science and Technology POLITEHNICA Bucharest, Faculty of Industrial Engineering
and Robotics, Department of Robots and Manufacturing Systems, Romania
e-mail: patricia.braileanu@upb.ro

ABSTRACT

This paper analyses the revolutionary effect of Industry 4.0 technologies on materials processing and innovation in the metallurgical industry. It extensively analyses how this new industrial revolution, defined by the widespread interconnection of digital systems, is systematically re-designing conventional processes into smart, networked and highly efficient systems. The study highlights the function of enabling technologies such as Internet of Things (IoT), Artificial Intelligence (AI) and Machine Learning (ML), Cyber-Physical Systems (CPS), Additive Manufacturing (AM) and Big Data analytics, revealing their cumulative ability to enhance energy efficiency, resource allocation, quality control, and predictive maintenance along the whole metallurgical value chain. While recognizing the industry's current mid-term period of digital adoption, this analysis highlights how Industry 4.0 is already providing dramatic gains in efficiency, productivity, and sustainability, critically meeting both challenges of digitalization and decarbonization. Practical implementation highlighted includes real-time process monitoring, creation of digital twin prototypes for simulation, and the enablement of very high customization of manufacture. Theoretically, this research enriches the heavy industry discourse on digitalization by outlining technological adoption and industry-maturity interaction and discussing the novel concept of the "metallurgical Internet of Things" (m-IoT) of a globally networked, resource-efficient materials world.

KEYWORDS: smart metallurgy, Industry 4.0, materials processing, advanced manufacturing, digital transformation

1. Introduction

Nowadays, we are witnessing a new industrial revolution, known as Industry 4.0, which represents a significant shift in production methodology, driven by the extensive integration of digital technology into production systems [1-4]. Primarily, this technological transformation is supported by the expansion of cyber-physical systems that monitor physical processes, create virtual models and subsequently make decentralized decisions [1, 2, 5].

Typically, these technologies may include the Internet of Things (IoT), Artificial Intelligence (AI), Big Data analytics, cloud computing, automation and advanced manufacturing processes such as additive manufacturing (AM) [1, 2, 4-9].

The metallurgy and materials processing sector forms the foundation for many other industries, such as automotive, construction and machinery [6], and is increasingly subject to these transformative changes aimed at improving production processes [4, 10]. Although historically regarded as a mature sector, it is now evolving into a smart industry through the adoption of Industry 4.0 technologies [4, 10].

Digitalization plays a key role at the core of this evolution, as it has the potential to transform manufacturing models, enabling the development of more efficient and creative processes and products [4, 10]. This includes the digitalization of sub-processes such as melting, casting, rolling and finishing, which are vital to numerous industrial sectors. Digital technologies are now considered essential for optimizing production chains and supporting the development of low-carbon and sustainable steel

production methods, thus addressing the dual challenges of digitalization and decarbonization faced by the global industry [8, 11-13].

Although it can be stated that Industry 4.0 concepts and technologies are being increasingly adopted in metallurgy, the sector is still observed to be at an intermediate stage between Industry 3.0 and 4.0 [4]. Even though improvements in efficiency, productivity and sustainability are becoming increasingly evident, the specific impact and full integration of these technologies across all areas of metallurgy require time and deeper analysis [4, 8].

This paper aims to analyse the impact of Industry 4.0 technologies on materials processing and innovation within the metallurgical sector, exploring the opportunities, challenges, and transformative potential of this digital revolution on traditional practices and future developments.

## 2. Industry 4.0 Technologies in Metallurgy

Industry 4.0 can be viewed as a significant transformation, especially in the manufacturing industry, driven primarily by the adoption of advanced digital technologies shown in Fig. 1. These technologies are aimed at transforming traditional industrial processes into intelligent, smart, networked and highly productive systems. For example, in the metallurgical and material processing sector, their adoption of these Key Enabling Technologies (KET) is a key step toward the achievement of the concept of smart metallurgy [4, 7]. These technologies form the foundation for improved process control, data-informed decision-making, increased productivity and the development of new materials and novel manufacturing approaches [4, 7-9, 14]. The next section presents the most important Industry 4.0 technologies and considers their specific applications and impact on metallurgy.
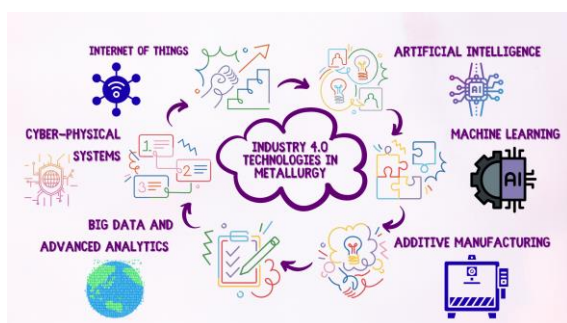
Fig. 1. *Core Digital Technologies Driving the Transformation of Metallurgy in Industry 4.0*

Internet of Things (IoT) in Metallurgy. As described by U. M. Dilberoglu *et. al.*, the Internet of Things (IoT) refers to a network of interconnected physical devices embedded with sensors, software and connectivity, enabling them to collect, exchange and act upon data [2, 8]. This can facilitate the machine-to-machine (M2M) communication and system-wide data flow [1, 9]. In metallurgical processes, the deployment of sensors and connected devices throughout the production chain, from raw material handling to finished product, represents the foundation of the digital transformation, as shown in Fig. 2 [4, 6, 13]. This network, often referred to as the Industrial Internet of Things or IIoT, allows for the real-time collection of vast amounts of data on important process parameters such as temperature, vibration, pressure, chemical composition and energy consumption [4, 13].

Most of the applications are diverse and impactful. For example, in the study conducted by Gajdzik B. on steel mills, IoT sensors monitor processes like melting, casting, rolling and finishing, providing continuous data streams for analysis and control [4, 10]. Therefore, this real-time data is essential for optimizing process efficiency, resource management and energy consumption, particularly in energy-intensive operations like electric steelmaking [4, 8, 9, 13].
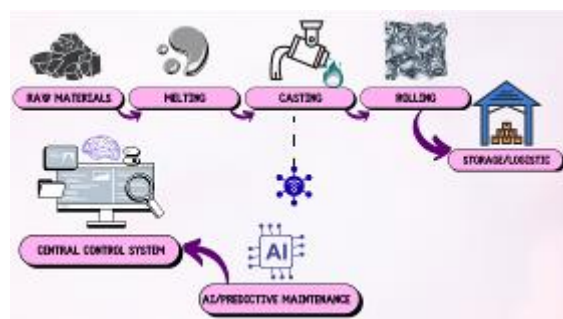
Fig. 2. *IoT Applications and Data Flow in Metallurgical Processes*

IoT networks also support predictive maintenance by identifying anomalies and predicting equipment failures before they occur, thereby increasing reliability and reducing downtime [4, 7-9]. Moreover, IoT enables enhanced material tracking throughout the plant and supply chain, improves logistics management and supports remote monitoring and control of operations [3, 4, 7, 9]. In AM, IoT integration can be used to automate processes, improve efficiency and enable the mass production of customized parts and smart materials [1]. Hence, by providing the foundational connectivity and data infrastructure, IoT makes metallurgical operations significantly smarter, more

responsive and more adaptive to changing conditions and demands [4, 9, 13].

Artificial Intelligence and Machine Learning in Metallurgy. Artificial Intelligence (AI) and Machine Learning (ML) are advanced computational techniques that enable systems to learn from data, identify patterns, make predictions and automate decision-making processes (Fig. 3) [1, 5, 6, 9]. These technologies allow shifting from purely reactive data analysis to predictive and prescriptive analytics, offering more profound understanding of complex processes [15]. Within metallurgy, AI/ML applications are rapidly expanding, driving significant improvements across various functional areas.

One example of its implementation is the process optimization, where AI algorithms analyse large datasets from IoT sensors to identify efficiencies, predict optimal operating parameters, and continuously improve production workflows [14, 15]. AI and ML are also important for quality control and defect detection, enabling real-time monitoring, automated inspection, prediction of imperfections in AM [4] and automated surface defect detection in materials like steel [3, 16].
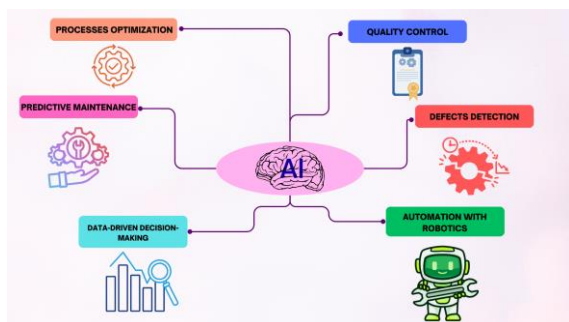
Fig. 3. *Applications for AI/ML in Metallurgy*

These systems can learn from historical data to automatically grade products and suggest corrective actions. Thus, AI highlights predictive maintenance strategies, by using ML models to forecast equipment needs based on operational data, thereby increasing machine reliability [4, 7, 8, 14]. AI, which is also often integrated with robotics, can automate repetitive and hazardous tasks, improving safety and consistency [14, 15]. This synergy of AI with IoT or AIIoT, transforms decision-making, allowing for more qualified, data-driven choices in molten metal processing and manufacturing [15, 17]. AI/ML also contributes to making metallurgical operations smarter by enabling automated learning, complex data analysis and proactive decision-making, leading to improved quality, efficiency and adaptability [14].

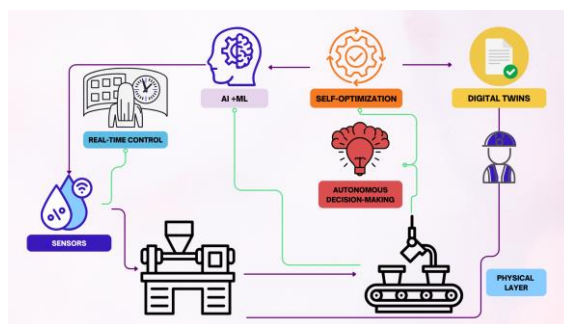*Cyber-Physical Systems (CPS) in Metallurgy.* Cyber-Physical Systems are the foundational framework of Industry 4.0, representing the seamless integration of computational and physical processes (Fig. 4) [1, 3, 4, 18]. CPS consists of cyber components that monitor and control physical processes, create virtual representations of the physical world and communicate and cooperate with each other, also with humans, in real time [1, 2, 9]. These systems enable decentralized decision-making and self-optimization [1, 9]. Particularly, in metallurgy, the transition to Industry 4.0 is fundamentally marked by the development and implementation of Cyber-Physical Production Systems or CPPS, often referred to as "smart factories" or "smart mills" [4, 6, 7, 9].

Specific applications include the creation of integrated manufacturing systems where physical production facilities, storage systems and IT networks are connected and communicate autonomously [1, 2, 6]. CPS allows for real-time monitoring and control of complex metallurgical processes, enabling instantaneous adjustments based on live data feedback [2]. By creating virtual copies (digital twins, as discussed later) of physical systems, CPS facilitates simulation, analysis and prediction of process behavior, allowing for proactive identification and resolution of potential issues [2, 9].

The implementation of CPS, for example in steel mills, aims to achieve deep automation, integrated process management and autonomous operations where machines can adapt their behavior to changing conditions through self-optimization and reconfiguration [4, 14]. This transition from traditional hierarchical automation structures to more flexible, integrated architecture is mandatory for the adaptive and efficient operation of modern metallurgical plants [14].

**Fig. 4.** *Cyber-Physical Systems in Smart Metallurgy*

CPS significantly enhances the ability of metallurgical facilities to operate as intelligent, self-regulating entities, improving overall efficiency, reliability and responsiveness [2, 4, 14].

Additive Manufacturing in Metallurgy. AM known as 3D printing is an innovative technology that builds three-dimensional parts layer by layer

from computer aided design (CAD) models [1, 2]. Unlike the traditional subtractive manufacturing technologies, AM focuses on material addition (Fig. 5), enabling the creation of particular geometries and highly customized parts [2]. Although explored initially for prototyping, AM has become an essential industrial technique for both product innovation and development, particularly with metallic materials [1, 2].

Metal Additive Manufacturing or MAM is an important subset of AM in metallurgy, focusing on producing metallic components from powders or wires [2]. Most MAM processes include powder bed fusion (e.g., Selective Laser Sintering/Melting - SLS/SLM, Electron Beam Melting - EBM), direct energy deposition (e.g., Laser Engineering Net Shaping - LENS), material jetting, and binder jetting, as well as Wire and Arc Additive Manufacturing (WAAM) [2]. MAM allows the creation of complex metallic structures with specific microstructures and mechanical properties [2]. A significant advantage is the ability to produce parts with greater customization and complex designs that are difficult or impossible with conventional methods [1, 2]. AM also maximizes material utilization by building only where material is needed, thereby reducing waste [1, 15].
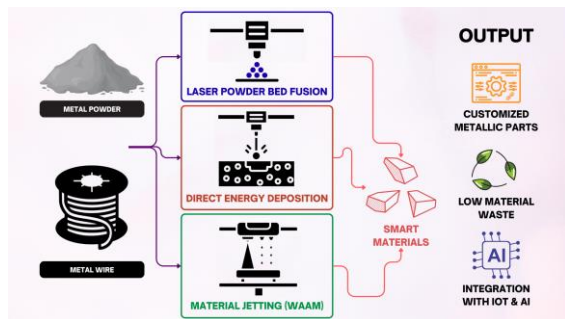
Fig. 5. *Metal Additive Manufacturing (MAM) in Metallurgy*

Beyond traditional metals, AM can be used to print programmable or smart materials that can change their functional properties in response to environmental stimuli and to fabricate multi-material components [1]. Applications range from manufacturing powders of metals and ceramics [18, 19] to producing customized biomedical implants [1, 18, 19].

Although challenges remain regarding cost, production speed and achieving desired mechanical properties consistently [2], the integration of AM with Industry 4.0 technologies like IoT and AI enhances its efficiency and reliability [1]. AM contributes to smarter and more adaptive metallurgy by enabling on-demand manufacturing of complex and customized parts, fostering rapid innovation and supporting the development of novel materials [1, 2, 14].

Big Data and Advanced Analytics in Metallurgy. Big Data is large amounts of heterogeneous data produced by current industrial processes, ranging from sensor measurements and machine logs to design parameters, customer orders and supply chains, as indicated in Figure 6 [2]. Advanced Analytics is sophisticated methods, such as ML and AI, employed to process, analyse and draw meaningful conclusions about this data [1, 5, 6]. In Industry 4.0, it's the capacity to gather, process and review Big Data that's vital in converting raw information into useful knowledge [2].
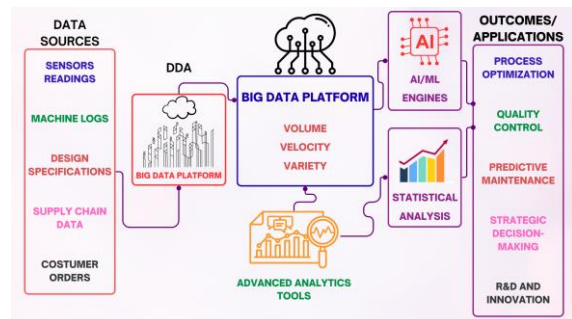
Fig. 6. *Big Data Analytics Workflow in Metallurgical Processes*

In metallurgical processes the Big Data and Advanced Analytics are essential for monitoring, controlling and optimizing complex operations in real time [4, 15]. Analysing data streams from interconnected systems, companies can gain deep insights into process performance, identify bottlenecks and predict outcomes [14, 15]. The method enables greater process efficiency, more efficient resources and energy utilization that helps minimize production costs and waste [3, 8, 9]. Advanced analytics is strongest in quality assurance, where it allows for the automatic examination of product data for defect discovery, characterization and forecasting [3, 8, 10]. This allows for stricter quality control and proactive interventions to prevent defects [14]. Predictive maintenance is also heavily reliant on Big Data analytics to analyse historical and real-time machine data to predict maintenance needs accurately [8, 9, 15].

Beyond operational improvements, Big Data and analytics support qualified decision-making at various levels, from shop floor adjustments to strategic planning [15, 17]. They are also vital for driving research and development activities, identifying areas for innovation and understanding the impact of new technologies [7]. By providing tools to process and understand complex information,

Big Data and Advanced Analytics enable metallurgical operations to become significantly smarter by facilitating informed, data-driven optimization and predictive capabilities [7, 15].

3. Future Metallurgy Trends and Research Directions

Incorporation of Industry 4.0 innovations into metallurgy and materials processing is introducing a significant shift, but it's somewhat new with ongoing research and development. Current research focuses largely on theoretical potential, with further practical implementation required to fully understand impact and benefit. The direction in the future involves the use of advanced digital technology to overcome significant challenges such as boosting process efficiency, boosting the quality of products, reducing environmentally detrimental effects, and facilitating human-technology collaboration.

Major areas with great promise in the future are the increased use of Artificial Intelligence and Machine Learning. These are increasingly becoming key to predictive maintenance, optimization of processes, quality control by defect identification and extraction of deeper insights from large amounts of data accumulated during manufacture. AI has great suitability in assuming repetitive jobs in metal manufacture, hence boosting efficiency and consistency.

Next-gen digital twins will become increasingly sophisticated, with dynamic, real-time virtual replicas of metallurgy processes, as well as complete plants. The digital twins will enable ongoing monitoring, simulation, fault detection and predictive analytics, enabling proactive adjustments to maximize process reliability while minimizing waste.

Smart sensor, IIoT device development and mass deployment are key enablers of real-time sensing in harsh metallurgical conditions, such as extreme temperature or corrosive environments. The flood of new data is essential in supporting advanced analytics, process control, energy effectiveness and resource management in smart steel mills and foundries. The "metallurgical Internet of Things" (m-IoT) concept [20] is evolving, with an intention to network the worldwide metal processing equipment digitally in order to measure resource efficiency and sustainability in interconnected material loops.

A major future direction involves moving toward an energy-efficient, sustainable metallurgical system. Advanced analytics and digital transformation technology are key enablers to energy and resource reduction, minimization of by-products and waste, and enabling decarbonization, toward the aims of the circular economy. The digital technologies are equally important in optimizing the recycling and reuse of materials, while monitoring the properties throughout the lifecycle.

Evolution into Industry 5.0 refers to an industrial future emphasis on flexible and human-oriented industrial systems, with an integration of technological innovation with human needs and societal challenges. It includes advancement in human-machine communication, with the potential use of technology like Augmented Reality and Virtual Reality in teleoperation, assistance and training of hazardous or difficult tasks. Future research is, nonetheless, imperative in facilitating the full interaction between robot and human capabilities. Edge computing could, in addition, be involved in processing vast amounts of in-situ data for real-time decisions.

Achieving these advancements requires increased interdisciplinary collaboration among materials scientists, data scientists, automation engineers, IT experts and other stakeholders.

4. Conclusions

This review effectively highlights the revolutionary path of the metallurgical industry under the drive of Industry 4.0. The review carefully integrates the ubiquitous imprint of important enabling technologies like IoT, AI/ML, CPS, AM and Big Data analytics, through exemplifications of their synergistic capabilities to reimagine conventional materials processing as networked and highly efficient systems of intelligence. This transformation is shown not as an operational enhancement but as a very essential re-architecture of industrial models enabling unprecedented efficiency, precision and adaptability all along the whole metallurgical value chain.

This examination enriches the discussion of heavy industry digitalization, specifically through defining the intricate technological adoption and industry-maturity interplay. This places it within current industrial epochs, and more significantly the twin pressure for decarbonizations and sustainable innovation, through an emphasis on the central role of digital technologies in meeting energy efficiency, waste reduction and circular economy aims within metallurgy. Identifying the industry being at an "intermediate phase" delivers a sophisticated understanding of industrial development, an acceptance of technological integration as an iterative process.

Anticipatory understandings, such as the prospective "metallurgical Internet of Things" (m-IoT) idea, also point towards future research avenues towards an internationally networked, resource-efficient materials system. In conclusion, this research

explains that the current digital revolution represents an overall driver of sustainable innovation in metallurgy and drives the industry toward an intelligent, resource-efficient and environmentally aware future.

References

[1]. **Ashima R.,** *et al.*, *Automation and manufacturing of smart materials in Additive Manufacturing technologies using Internet of Things towards the adoption of Industry 4.0*, Materials Today: Proceedings, 45, p. 5081-5088, 2021.

[2]. **Dilberoglu U. M.,** *et al.*, *The role of additive manufacturing in the era of industry 4.0*, Procedia manufacturing 11, p. 545-554, 2017.

[3]. **Stroud D.,** *et al.*, *Industry 4.0 and the road to sustainable steelmaking in Europe: Recasting the future*, Springer Nature, p. 230, 2024.

[4]. **Gajdzik B., Wolniak R.,** *Transitioning of steel producers to the steelworks 4.0—Literature review with case studies*, Energies, 14(14), 4109, 2021.

[5]. **Biały W.,** *et al.*, *Engineer 4.0 in a metallurgical enterprise, Multidisciplinary Aspects of Production Engineering*, 2, 2019.

[6]. **Gajdzik B.,** *How steel mills transform into smart mills: Digital changes and development determinants in the Polish steel industry*, 2022.

[7] **Gajdzik B., Wolniak R.,** *Framework for R&D&I activities in the steel industry in popularizing the idea of industry 4.0*, Journal of Open Innovation: Technology, Market, and Complexity, 8(3), 133, 2022.

[8]. **Tolettini L., Di Maria E.,** *The impact of industry 4.0 on the steel sector: paving the way for a disruptive digital and ecological transformation*, Recycling, 8(4), 55, 2023.

[9]. **Miśkiewicz R., Wolniak R.,** *Practical application of the Industry 4.0 concept in a steel company*, Sustainability, 12(14), 5776, 2020.

[10]. **Akyazi T.,** *et al.*, *The Effects of Industry 4.0 on Steel Workforce: Identifying the Current and Future Skills Requirements of the Steel Sector and Developing a Sectorial Database*, In Industry 4.0 and the Road to Sustainable Steelmaking in Europe: Recasting the Future, Cham: Springer International Publishing, p. 183-201, 2024.

[11]. **Stroud D.,** *et al.*, *The technological and social transformation of the European steel industry: Towards decarbonisation and digitalization*, In Industry 4.0 and the Road to Sustainable Steelmaking in Europe: Recasting the Future, Cham: Springer International Publishing, p. 17-34, 2024.

[12]. **Weinel M.,** *et al.*, *Introduction: The historic importance and continued relevance of steel-making in Europe*, In Industry 4.0 and the Road to Sustainable Steelmaking in Europe: Recasting the Future, Cham: Springer International Publishing, p. 1-14, 2024.

[13]. **Gajdzik B.,** *et al.*, *Electricity and heat demand in steel industry technological processes in Industry 4.0 conditions*, Energies, 16(2), 787, 2023.

[14]. **Branca T. A.,** *et al.*, *The impact of the new technologies and the EU climate objectives on the steel industry*, In Industry 4.0 and the Road to Sustainable Steelmaking in Europe: Recasting the Future, Cham: Springer International Publishing, p. 53-75, 2024.

[15]. **Ďurčo R.,** *et al.*, *Aiming for Industry 4.0: The Case of the Czech Republic*, In Industry 4.0 and the Road to Sustainable Steelmaking in Europe: Recasting the Future, Cham: Springer International Publishing, p. 113-127, 2024.

[16]. **Antonazzo L.,** *et al.*, *Preparing for a digital steel industry: What challenge for skills formation systems?*, In Industry 4.0 and the Road to Sustainable Steelmaking in Europe: Recasting the Future, Cham: Springer International Publishing, p. 167-181, 2024.

[17]. **Mishra S. B., Liyakat K. K. S.,** *AI-Driven-IoT (AIIoT) Based Decision-Making in Molten Metal Processing*, Journal of Industrial Mechanics, 9(2), p. 45-56, 2024.

[18]. **Dobrzański L. A.,** *et al.*, *Manufacturing powders of metals, their alloys and ceramics and the importance of conventional and additive technologies for products manufacturing in Industry 4.0 stage*, Archives of Materials Science and Engineering, 102(1), 2020.

[19]. **Dobrzański L. A.,** *et al.*, *Overview of conventional technologies using the powders of metals, their alloys and ceramics in Industry 4.0 stage*, Journal of Achievements in Materials and Manufacturing Engineering, 98(2), p. 56-85, 2020.

[20]. **Reuter M. A.,** *Digitalizing the circular economy: Circular economy engineering defined by the metallurgical internet of things*, Metallurgical and Materials transactions B, 47(6), p. 3194-3220, 2016.

STUDIES AND RESEARCH ON THE CORROSION BEHAVIOUR IN A 3.5% NaCl SOLUTION OF SINTERED 316 STAINLESS STEELS

Simona BOICIUC

"Dunarea de Jos" University of Galati, Romania
e-mail: simona_boiciuc@yahoo.com

ABSTRACT

Products made from austenitic 316 stainless steels obtained through powder metallurgy technologies are used in many applications across various industrial fields due to their resistance to corrosion from air, water, and different acids. They are also non-magnetic, possess good mechanical properties at both low and high temperatures, offer good creep resistance, and have good weldability. This paper presents a series of experimental studies on the corrosion behaviour of sintered austenitic 316 stainless steels in a 3.5% NaCl solution. The different behaviours observed can be attributed to varying compaction pressures and can be improved by reducing surface roughness, increasing chemical and structural homogeneity, and by alloying.

KEYWORDS: stainless steel 316, electrochemical corrosion, open-circuit potential (OCP), potentiodynamic polarization, polarization resistance, Rp, corrosion rate

1. Introduction

The use of stainless steels in various fields must take into account the conditions under which the material is to operate, namely the working environment, its temperature, and the nature and level of stress. Considering these aspects and other possible criteria (processing conditions and cost-effectiveness, availability), the set of operating properties required for the steel used is determined [1].

The chemical composition of austenitic stainless steel 316 can influence the mechanical properties and corrosion behaviour. Thus, chromium increases corrosion resistance, nickel, a gamma-forming element, stabilises the austenitic structure, ensures repassivation especially in reducing environments, and improves toughness at low temperatures. Molybdenum stabilises the resulting passive film, especially in combination with chromium, and improves resistance to pitting and crevice corrosion. It also improves oxidation resistance at high temperatures and mechanical properties at both low and high temperatures [2].

Since austenitic stainless-steel powders are obtained by water atomisation, they may have a carbon content higher than 0.03%. This improves high-temperature resistance but may lead to the development of pitting corrosion or intergranular corrosion (caused by the precipitation of chromium carbides at the grain boundaries) [2, 3].

The presence of manganese can influence pitting corrosion behaviour, as it forms manganese sulphide in the presence of sulphur.

The presence of nitrogen in the structure of these steels increases strength and hardness, reduces ductility, but increases susceptibility to intergranular corrosion (as a result of the formation of chromium nitrides).

The presence of iron particles incorporated into stainless alloys can negatively affect corrosion resistance. These may originate from the supplier, during mixing with additives, from the die during pressing, from inadequate cleaning of the sintering furnace, or from processing or storage [2, 3].

The austenitic structure specific to stainless steel 316 provides resistance to the corrosive action of air, water, concentrated nitric, sulphuric, and phosphoric acids, and to creep. These steels are non-magnetic, have good weldability, but their machinability deteriorates due to work hardening [4, 5].

They are used in the chemical, petrochemical, food, aerospace, medical, transport industries, and household items [4].

The mechanical characteristics of stainless steel 316, according to MPIF, [3] are: tensile strength 280 MPa, yield strength 230 MPa, Young's modulus 105

GPa, Poisson's ratio 0.25, hardness 59 HRB, density 6.4 g/cm³.

The porous nature of sintered steels increases the tendency to corrosion (pitting, crevice corrosion, and their propagation). Thus, increasing the compaction pressure increases density and improves corrosion behaviour.

Also, increasing the sintering temperature from 1149 ºC to 1316 ºC results in increased sintering rate and densification, which leads to increased tensile strength, yield strength, hardness, impact resistance, and corrosion resistance. Sintering in a hydrogen atmosphere can increase densification and ductility as a result of oxide reduction [3].

The corrosion behaviour of sintered stainless steel 316 in various environments can be characterised using electrochemical tests. In this way, the electrochemical conditions present on the surface of stainless steel exposed to a certain corrosive environment can be studied, the stability of passivity can be assessed, the types of corrosion and especially the danger caused by macroscopic and microscopic electrochemical cells due to differences in physical or chemical states between two points on the surface of a steel.

The purpose of the paper is to characterise the corrosion behaviour, in a 3.5% NaCl solution of sintered austenitic stainless steel 316.

2. Experimental conditions

The chemical composition of the austenitic stainless steel 316 powder used in the experimental research is shown in Table 1. It complies with the Metal Powder Industries Federation standards [3].

Table 1. Chemical composition of 316 powder

Steel brand	Chemical composition, %								
	C	**Cr**	**Ni**	**Mo**	**Si**	**Mn**	**S**	**P**	**Fe**
316	max 0.08	16 - 18	10 - 14	2 - 3	max 1	max 2	max 0.03	max 0.045	remaining
	0.03	17.1	12.09	2.5	0.51	0.84	0.012	0.03	remaining

The powder was obtained by water atomisation and has an irregular shape.

The powder had a measured hardness of $HV_{0.05}$ = 939.6 MPa [6].

Pressing was carried out at ambient temperature. The compaction pressures were: for sample P1, F1 = 540 MPa; for sample P2, F2 = 628 MPa; for sample P3, F3 = 726 MPa; and for sample P4, F4 = 863 MPa [6].

Sintering was carried out at 1150 ºC, with a holding time of 1 hour, followed by slow cooling. The microhardness after sintering was $HV_{0.05}$ = 3120.2 MPa [6].

The microstructure of the obtained samples consisted of austenite. The average porosity of the stainless steel 316 compacts was determined using the line-intercept method and had the following values: sample P1 – 0.3178%, sample P2 – 0.2821%, sample P3 – 0.2153%, and sample P4 – 0.1272% [6].

Before the corrosion tests, the samples were mechanically polished to obtain lower surface roughness. This reduces deposits of solid materials, dust, rust, ferrous or other particles resulting from grinding or machining.

The metallographic analysis of the sintered stainless steel 316 samples subjected to corrosion in 3.5% NaCl solution was carried out using a Neophot 2 microscope with computer data acquisition.

Electrochemical studies were performed using a multi-channel electrochemical device, potentiostat/galvanostat system, OrigaLys France, OrigaFlex – model OGF+01A, and data acquisition was done using its OrigaMaster OM5 software. The electrochemical cell used was a classical three-electrode cell (working electrode – the tested material, reference electrode – Ag/AgCl with saturated KCl solution, potential versus NHE = +199 mV, against which all recorded potentials were measured, and counter electrode – a platinum electrode).

The samples subjected to corrosion tests were connected to a copper wire and then embedded in epoxy resin to obtain an active surface of approximately 1.6 cm².

The characterisation of corrosion behaviour was carried out using the following methods:
- monitoring the open-circuit potential (OCP) for 120 minutes, with a measurement interval of 0.6 s;
- potentiodynamic polarization testing, with measurement from -1.5 V to +1.5 V and a scan rate 1 mV/s;

3. Results and discussions
3.1. Metallographic analysis

In Figure 1 the microstructures of the sintered stainless steel 316 samples subjected to corrosion in

3.5% NaCl solution are shown, in both the unetched and electrolytically etched state with 50% HNO_3.

Analysing Figure 1, the presence of pitting corrosion can be observed. This is a form of localised attack, characteristic of passivable alloys, caused by the breakdown of the protective film due to the presence of aggressive anionic species, such as chloride ions. The chloride anion has high diffusivity, interferes with passivation, and is ubiquitous as a contaminant. A characteristic feature of this type of corrosion is that, on the surface of the alloy, along with intact passive areas, active points may appear simultaneously, without a protective film—meaning some areas with very low anodic current density (broad cathodic zones) and other smaller areas with higher current density (anodic zones).
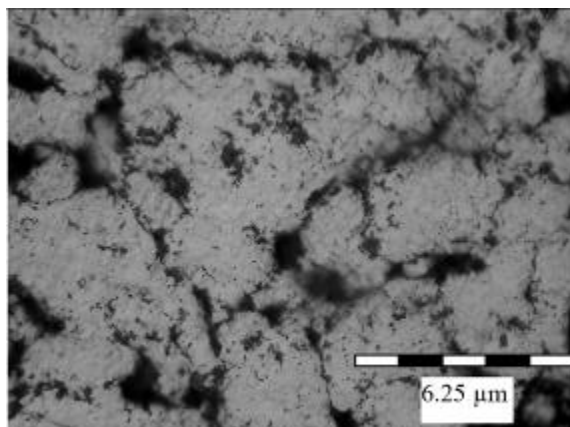
a - F1
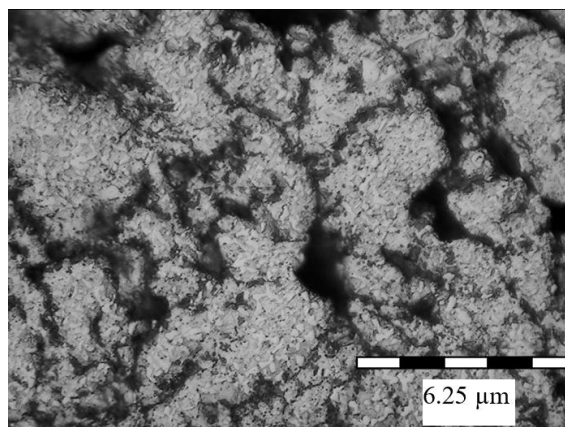
b - F1
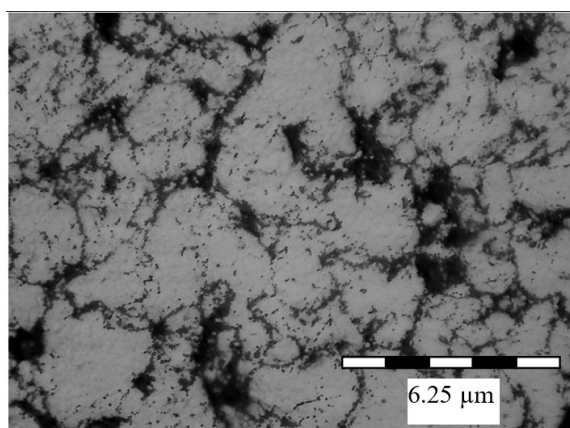
a - F2

b - F2

a - F3

b - F3

Fig. 1. Microstructure of sintered austenitic stainless steel 316 samples subjected to corrosion in 3.5% NaCl solution: a – unetched state; b – etched state, electrolytic etching with 50% HNO₃
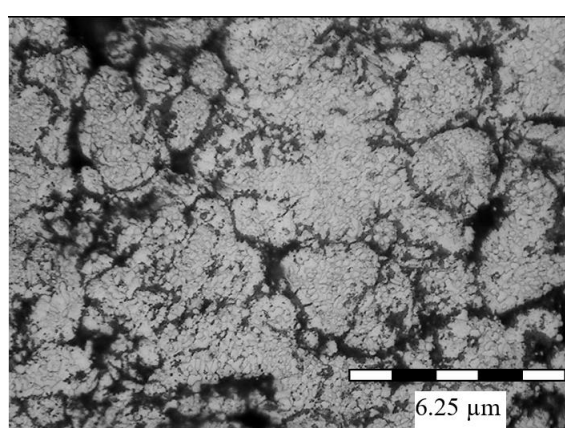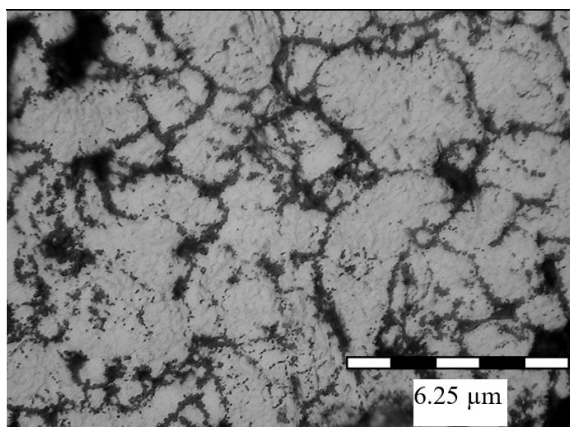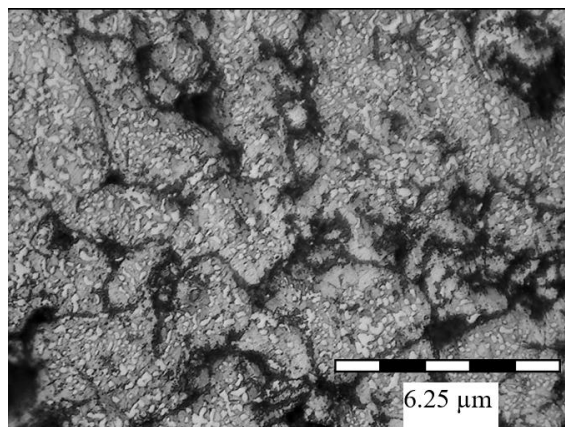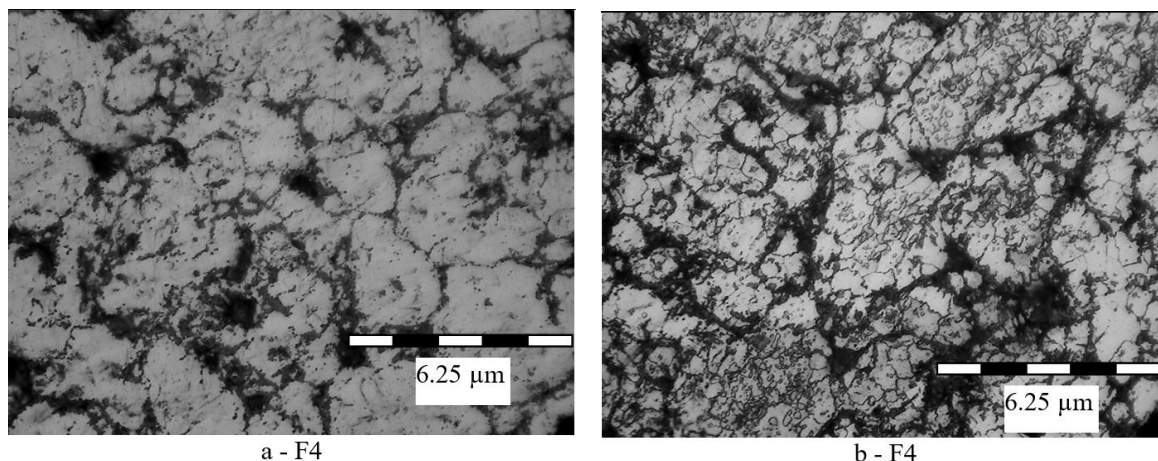
Pitting corrosion is initiated at a certain chemical or physical heterogeneity on the surface, such as inclusions, secondary phase particles, precipitates segregated at grain boundaries, defects caused by mechanical processing, or dislocations.

Also, increasing the degree of surface processing through mechanical polishing enhances pitting corrosion resistance and ensures the formation of more compact, and therefore more protective films.

It is estimated that the tendency for pitting corrosion decreases with increasing chromium and nickel content in the alloy and by the inclusion of 2-5% molybdenum [1, 9].

By analysing Figure 1, intergranular corrosion can also be observed in certain areas. This manifests at grain boundaries where chromium carbides have precipitated, depleting the adjacent zones. It appears around the grains, develops in depth, and may sometimes lead to the disintegration of the steel.

Since carbon content plays an essential role in the occurrence of intergranular corrosion (due to carbide precipitation), it is estimated that reducing it to values lower than 0.03% decreases the steel's sensitivity to this type of corrosion. Also, adding stabilising elements to the steel that have a higher affinity for carbon than chromium such as titanium (in the ratio Ti/C $\geq$ 4) or niobium (in the ratio Nb/C $\geq$ 8) reduces susceptibility to intergranular corrosion [1].

3.2. Monitoring of open-circuit potential (OCP)

This is an electrochemical method that provides information on the corrosion behaviour of a material after immersion in a corrosive solution. It indicates the tendency of the material to interact with the corrosive environment.

Corrosion tests for each stainless steel 316 sample began with the monitoring of the open-circuit corrosion potential after immersion in the 3.5% NaCl solution, until a steady-state value was reached.

The duration of OCP monitoring was 120 minutes, to reach a steady-state value versus the Ag/AgCl reference electrode.

Figure 2 shows the time evolution of the open-circuit potential.

For sample P1 pressed with F1 = 540 MPa, an instability of the curve can be observed, specifically a decrease in the corrosion potential over the monitored interval, which can be attributed to the presence of chloride ions in the solution. This behaviour indicates a more active electrochemical state, caused by the infiltration of the solution into the open pores of the sample and the degradation of the passive film formed on the surface. A tendency towards stabilisation of the potential can be observed at a value of -412 mV, approximately 100 minutes after immersion.

For samples P2, P3, P4 pressed with forces F2 = 628 MPa, F3 = 726 MPa, F4 = 863 MPa, a stabilisation of the corrosion potential is observed after approximately 50 minutes of immersion. This indicates that a passive layer has formed on the analysed surfaces, which protects them from the action of the aggressive chloride ions in the electrolyte.

It can be noted that higher compaction pressures, around 863 MPa, ensure more noble (more positive) values of open-circuit potential, of -294.29 mV compared to the open-circuit potential values recorded for samples compacted at lower pressures, approximately -352.97 mV for a pressure of 628 MPa, and -393.48 mV for a pressure of 726 MPa.

The shift of the potential to more positive values with increasing compaction pressure shows the ability

of stainless steel 316 to develop a passive layer on its surface that reduces the corrosion process in the saline solution. The most positive potential, with a high tendency to stabilise over time, corresponds to the sample compacted at 863 MPa.
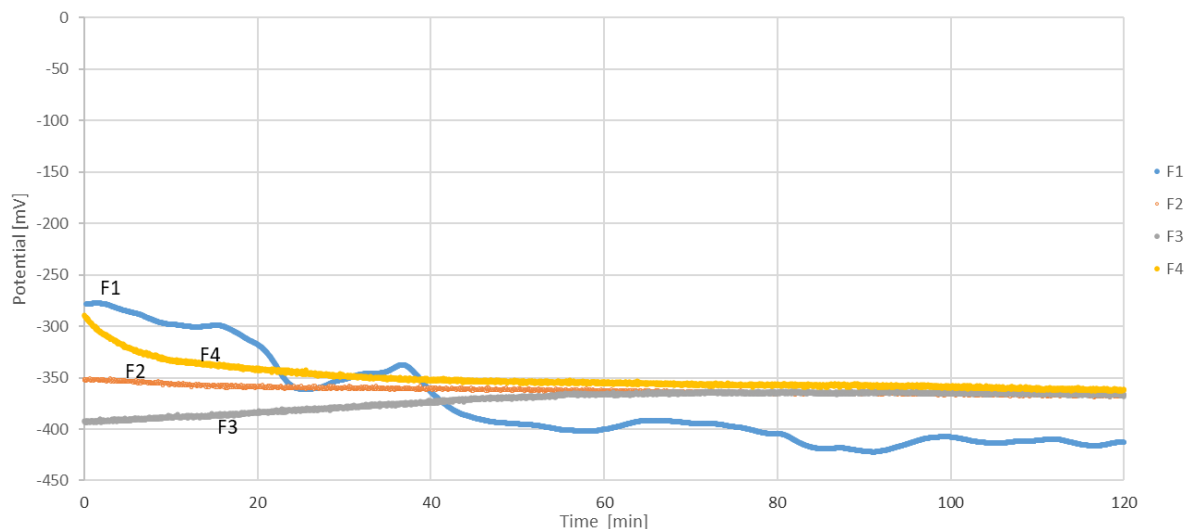
Fig. 2. *Time evolution of open-circuit potential (OCP)*

To increase the electrode potential and improve the passivity of the analysed samples, alloying with platinum and palladium can be carried out [3].

3.3. Potentiodynamic method – PD

For the successful use of a stainless steel, it is decisive whether in a certain corrosive environment it reaches the passive state, meaning whether the corrosion potential in an electrolyte decreases or not over a long period under these conditions. The shape of the current density – potential curves, Fig. 3 (depending on the steel grade and the corrosive environment), provides information about the corrosion kinetics.

From the analysis of the potentiodynamic polarization curves, especially from the analysis of the passivation domains, the anticorrosive performance of stainless steel 316 tested in contact with the corrosive environment consisting of 3.5% NaCl can be evaluated.

Passivity is the state of high corrosion resistance of stainless steels, under conditions in which they are thermodynamically active. This state is determined by the kinetic inhibition of the anodic metal dissolution process, through the shift of the potential to more electropositive values, accompanied by the formation of protective films. For each alloy and for each working condition, there is a current density value at which passivation occurs. Thus, the higher the current density, the shorter the time required to passivate the surface.
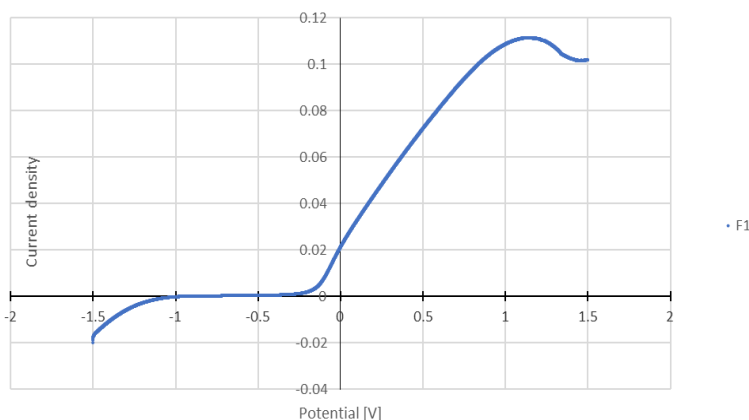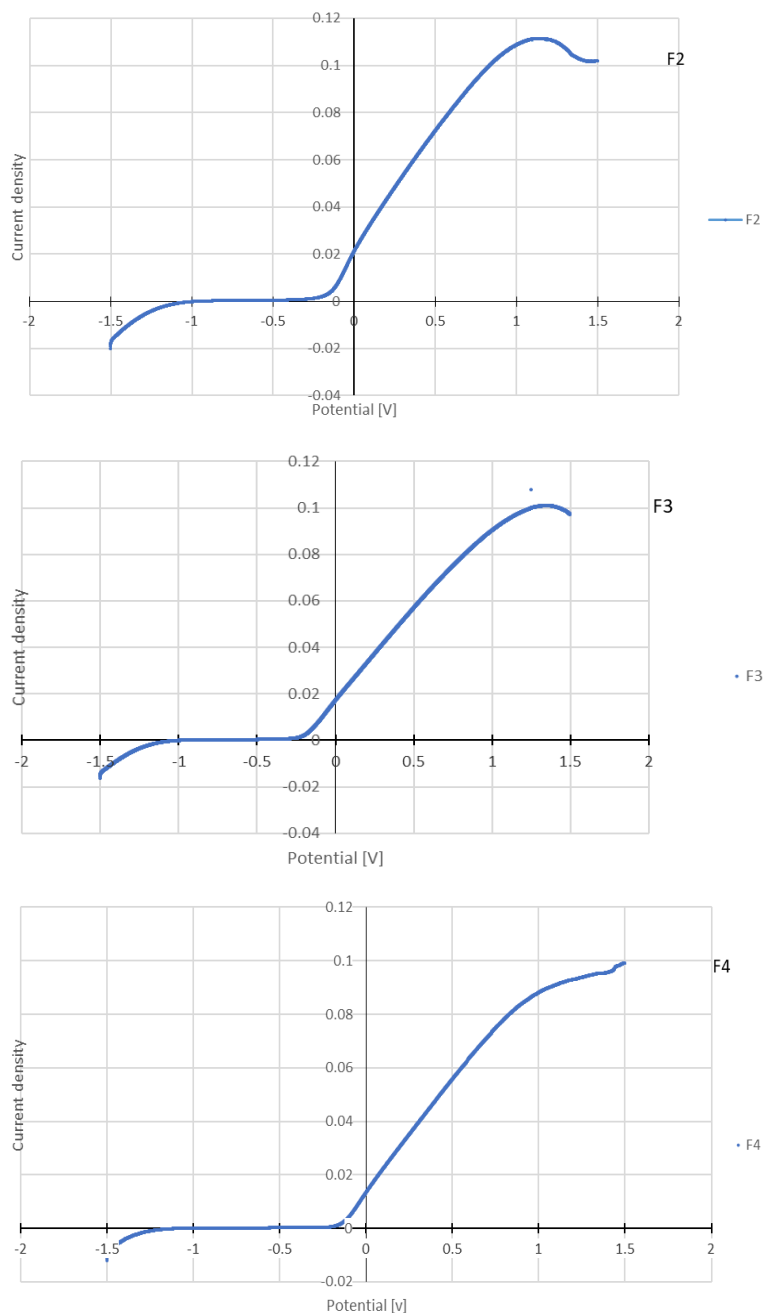
***Fig. 3.** Potentiodynamic curves*

By analysing Figure 3, it can be observed that the highest current density of 0.0013 µA/cm² corresponds to compaction with force F1, and the lowest current density of 0.0011 µA/cm² corresponds to compaction with force F4. Thus, sample P1 with higher porosity passivates more quickly, while sample P4 with higher compactness passivates over a longer period.

By analysing Fig. 3, the presence of passivation plateaus can be observed, ranging from -1.0950 V to -0.2422 V for the sample compacted at a pressure of 540 MPa, and from -1.2448 V to -0.1459 V for the sample compacted at a pressure of 863 MPa. Thus, it can be concluded that the stainless steel 316 samples resist corrosion over a wide potential range, which improves with increasing compactness. This aspect is due to the microstructure composed of austenite, a homogeneous solid solution that exhibits high stability in the saline environment.

Monitoring the temperature at which the corrosion process takes place is important because it can influence the corrosion rate. Thus, increasing temperature can intensify the electrochemical reactions of the corrosion process and reduce the

concentration polarization of the cathodic reaction, which leads to the acceleration of the diffusion of the depolarizing agent and ions in the solution. The presence of Cl^- ions lead to the breakdown of the passivation films.

Monitoring polarization resistance is an electrochemical method for measuring corrosion, which provides information about the corrosion rate. Therefore, the higher the polarization resistance, the lower the corrosion current, and the more resistant the alloy is to corrosion.

By analysing Figure 4, it can be observed that with the increase in compaction pressure from 540 MPa for sample P1 to 863 MPa for sample P4, the polarization resistance increases from 513.82 Ωcm^2 to 7119.22 Ωcm^2, which leads to an increase in corrosion resistance.
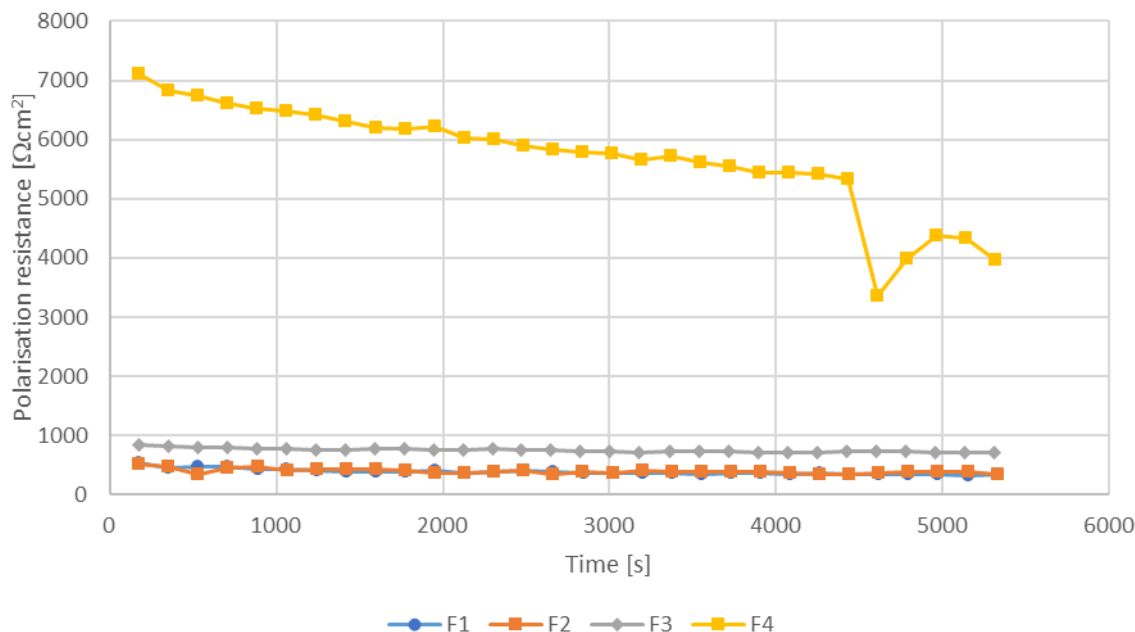
Fig. 4. *Evolution of polarization resistance over time*

Regarding the evolution of corrosion rate over time, shown in Figure 5, it can be seen that the corrosion rate is higher for samples P1 and P2, compacted at pressures of 540 MPa and 628 MPa, and then begins to decrease with the increase in compaction pressure to 726 MPa for sample P3, and more significantly for sample P4 compacted at a pressure of 863 MPa.
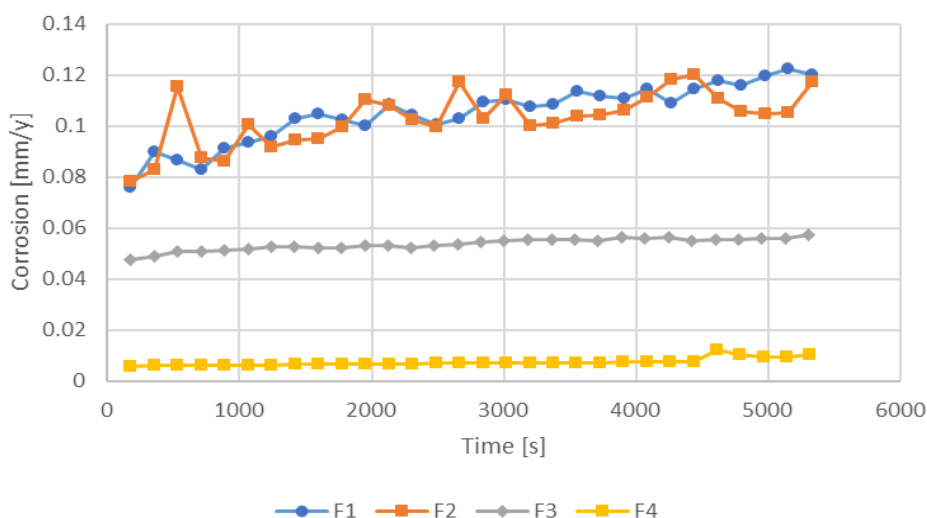
Fig. 5. *Evolution of corrosion rate over time*

Thus, with the increase in compactness of the samples, the corrosion rate decreases from 0.078 mm/year for sample P1 to 0.0056 mm/year for sample P4.

An improvement in the corrosion resistance of the analysed stainless steel 316 can be achieved by reducing open porosity and increasing compactness. Thus, chemical passivation treatments, sintering with the presence of a liquid phase, double pressing and double sintering, injection moulding, the addition of alloying elements such as molybdenum up to 5%, alloying with titanium and niobium or with copper and tin up to 1.5% can significantly improve corrosion resistance.

In liquid-phase sintering, the use of additives such as 0.2% B, 1% BN, 1% NiB, 1% CrB with particle sizes of 38 µm leads to the formation of dense microstructures, thus improving corrosion resistance [9].

Increasing the sintering temperature from 1150 ºC to 1250 ºC, as well as the sintering time from 30 minutes to 240 minutes, results in the reduction of open pores and the content of carbon, oxygen, and nitrogen, thereby improving corrosion resistance. Increasing cooling rates up to values of about 200 ºC can ensure a reduction in corrosion rates due to the formation of homogeneous structures [9].

If high porosity is required, as in the case of filters, it has been found that infiltration with copper and bronze can lead to an improvement in corrosion resistance [9].

4. Conclusions

When assessing corrosion behaviour, one must take into account the influence of crystalline defects, as well as the fact that in industrial processes the surface contains impurities that become cathodic zones and is mechanically and structurally altered, thus creating areas with higher energy that will tend to corrode, becoming anodic zones, thereby affecting and reducing corrosion resistance.

Following the conducted research, the following conclusions can be formulated:

- the metallographic analysis performed on the sintered stainless steel 316 samples subjected to corrosion in 3.5% NaCl solution reveals both pitting and intergranular corrosion; pitting corrosion is reduced by lowering surface roughness through mechanical polishing, thus also limiting contamination and improving the chemical and structural homogeneity of the alloy; increasing the

chromium, nickel, and molybdenum content improves resistance to pitting corrosion;

- intergranular corrosion is limited by reducing the carbon content in the steel below 0.03% and by introducing alloying elements such as titanium or niobium, which prevent the formation of chromium carbides at the grain boundaries;

- as the compaction pressure increases, the electrode potential and its tendency to stabilise over time also increase;

- from the analysis of the passivation domains, it can be concluded that the stainless steel 316 samples resist corrosion in 3.5% NaCl solution over a wide potential range, which improves with increasing compactness; this is due to the passive layer formed on the surface of the samples, which reduces corrosion in the saline solution;

- samples with higher porosity passivate over a shorter time but over a smaller potential range;

- with the increase in compaction pressure from 540 MPa for sample P1 to 863 MPa for sample P4, the polarization resistance increases from 513.82 Ωcm^2 to 7119.22 Ωcm^2, which leads to increased corrosion resistance;

- with the increase in compactness of the samples, the corrosion rate decreases from 0.078 mm/year for sample P1 to 0.0056 mm/year for sample P4;

- the corrosion resistance of stainless steel 316 samples in 3.5% NaCl solution can be improved by reducing open porosity, increasing compactness, and alloying.

References

[1]. **Constantinescu A., Constantinescu G.**, *Guide for the rational use of stainless and refractory steels (Îndrumar pentru utilizarea raţională a oţelurilor inoxidabile şi refractare)*, Bucharest, 1989.
[2]. ***, *ASM Handbook, Volume 5 - Surface Engineering*, 1994.
[3]. ***, *ASM Handbook, Volume 7 - Powder Metal Technologies and Applications*, 1998.
[4]. **Colan H., et al.**, *Study of metals (Studiul metalelor)*, Cluj Napoca, 1983.
[5]. **Schwartz M.**, *Practical elements of physical metallurgy (Elemente practice de metalurgie fizică)*, Editura tehnică, 1956.
[6]. **Boiciuc S., Potecasu F.**, *Research on the production of sintered powder 316*, The Annals of Dunărea de Jos" University of Galati, Fascicle IX, Metalurgy and Materials Science, no. 4, ISSN 1453-083X, 2012.
[7]. **Cheşa I., et al.**, *Steel trademarks and products (Mărci şi produse din otel)*, Editura tehnică, 1989.
[8]. **Cârâc G., Stefan C.**, *Electrochemistry – fundamental principles and applications (Electrochimie – principii fundamentale şi aplicaţii)*, Editura GUP, 2012.
[9]. ***, *ASM Metals Handbook, Volume 13 A - Corrosion: Fundamentals, Testing, and Protection*, 2003.

FINITE ELEMENT SIMULATION OF THERMOPLASTIC POLYURETHANE COMPONENTS FOR NVH TRANSFER PATH ANALYSIS

Florin Bogdan MARIN[1,2], **Gheorghe GURĂU**[1,2], **Iurie DRUMOV**[1], **Mihaela MARIN**[1,2]

[1] "Dunarea de Jos" University of Galati, Romania,
[2] Interdisciplinary Research Centre in the Field of Eco-Nano Technology and Advanced Materials CC-ITI,
Faculty of Engineering, "Dunarea de Jos" University of Galati, Romania, 47 Domnească Street, RO-800008,
Galați, Romania
e-mail: flmarin@ugal.ro

ABSTRACT

Thermoplastic polyurethane (TPU) has emerged as a versatile material for noise, vibration, and harshness (NVH) control due to its tuneable viscoelastic properties and compatibility with additive manufacturing. This study presents a finite element-based modeling framework for the characterization and evaluation of TPU in transfer path analysis (TPA). Nonlinear stiffness and damping functions were implemented based on literature data, while frequency-dependent viscoelastic behavior was introduced through storage and loss modulus functions. Contact interactions were modeled with nonlinear springs incorporating frictional effects to capture realistic interface dynamics. Vibro-acoustic coupling was investigated using a FEM-based approach, and further assessed using hybrid FEM–BEM methods. The results showed close agreement between predicted mode shapes and analytical expectations. Displacement fields were reproduced with high fidelity, and higher-order modes highlighted the importance of including frequency-dependent damping and friction models. Hybrid FEM–BEM coupling improved acoustic predictions while reducing computational cost. Parametric optimization further demonstrated that small modifications in TPU thickness and support positioning can reduce sound pressure levels by up to 15%. Overall, the simulations suggest that TPU has significant potential for application as both a structural decoupler and acoustic absorber in NVH engineering, providing a numerical framework that can guide lightweight and multifunctional designs in automotive and related engineering fields.

KEYWORDS: Thermoplastic Polyurethane (TPU), Finite Element Method (FEM), Noise, Vibration, and Harshness (NVH), Transfer Path Analysis (TPA), vibro-acoustic coupling

1. Introduction

Noise, vibration, and harshness (NVH) continue to be major challenges in automotive engineering and related industries, where comfort, safety, and lightweight construction must be balanced. Thermoplastic polyurethane (TPU) has emerged as a promising material in this context due to its tuneable viscoelasticity, wide processing flexibility, and capacity to function both as a structural decoupler and as an acoustic absorber [1-3].

Accurate assessment of TPU in NVH applications requires approaches that account for preload-dependent stiffness, frequency-dependent damping, and nonlinear contact effects. Finite element modeling (FEM) has proven effective in capturing these behaviours and in supporting transfer path analysis (TPA) [4, 15-17]. Recent studies have also integrated data-driven strategies with classical TPA, such as neural network–based methods for noise source diagnosis [4].

Vibro-acoustic coupling is another critical aspect. While FEM–FEM approaches deliver high

fidelity at the expense of computational cost, hybrid FEM–BEM methods provide efficiency without compromising accuracy [14, 15]. These strategies have been successfully applied to porous foams, lattice structures, and mechanical metamaterials [2, 20].

In parallel, TPU-based metamaterials and lattices have attracted increasing attention. Research has demonstrated multistable architectures with proprioceptive capabilities [6], torque-transmitting designs combining rigidity and compliance [7], modular "SoftSnap" units for rapid prototyping [8], and pneumatic grippers fabricated through additive manufacturing [9]. Beyond robotics, TPU has been employed in multifunctional metamaterials for energy absorption, programmability, and reconfigurability [10-13, 18]. Other works highlight the integration into soft actuators [19], flexible strain sensors [21], and lightweight lattice geometries [20].

These advances emphasize the importance of combining reliable numerical modeling with optimization routines. Parametric FEM studies have shown that adjusting TPU thickness, hardness, or support positioning can significantly reduce sound pressure levels without increasing mass [3].

Building on these developments, the present work applies FEM-based methodologies to TPU structures, focusing on modal analysis, vibro-acoustic coupling, and parametric optimization. The goal is to establish a robust framework to integrate TPU into NVH engineering, particularly for transfer path analysis in automotive and related applications.

2. Experimental Procedure

The analysis of TPU components in NVH applications was performed entirely using finite element simulations. The studied structure was an enclosure, modeled to evaluate the global modal behaviour and transfer path characteristics.

The geometry was discretized using 3D solid elements, with mesh refinement applied in regions of high stress and displacement gradients. A mesh convergence study was conducted to ensure numerical stability and accuracy of the obtained results.

The viscoelastic behavior of TPU was implemented as frequency-dependent storage and loss modulus functions, allowing the model to capture both stiffness and damping effects across the relevant frequency range. Contact interactions between TPU layers and rigid components were modeled using nonlinear spring elements, including tangential stiffness, damping, and frictional effects, which ensured realistic representation of interface dynamics.

Modal analyses were performed to extract natural frequencies and displacement fields. The first four significant mode shapes of the enclosure are reported in Figures 1-4, with amplitudes expressed in mm. These simulations illustrate the influence of TPU properties on the vibrational response of the structure.

Vibro-acoustic coupling was further investigated by applying both FEM–FEM and FEM–BEM approaches, which enabled efficient prediction of structural–acoustic interactions. Finally, parametric optimization was implemented, by varying TPU thickness, stiffness, and support positioning to assess their effects on the reduction of transmitted vibration and sound pressure levels.

3. Results and Discussions

The first step in validating the TPU-based NVH framework was the modal analysis of the enclosure. Figure 1 shows the displacement distribution of the first vibration mode obtained from the FEM analysis. The maximum displacement amplitude was approximately 10.2 mm, concentrated at the center of the plate, while the boundary regions remained fully constrained.
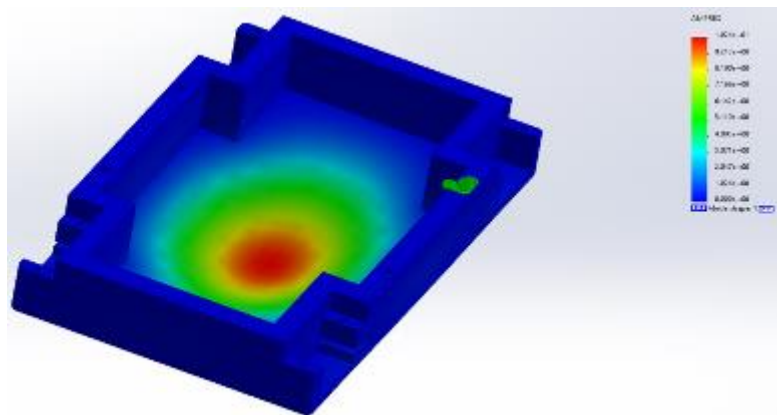
Fig. 1. *FEM displacement distribution analysis of the first vibration mode*

As frequency increased, the enclosure exhibited its second vibration mode, shown in Figure 2, with two distinct displacement peaks. The maximum amplitude was about 9.57 mm, located on opposite sides of the enclosure. This mode shape demonstrates the redistribution of vibrational energy across symmetric paths and validates the inclusion of preload-dependent stiffness and calibrated friction parameters in the contact model.
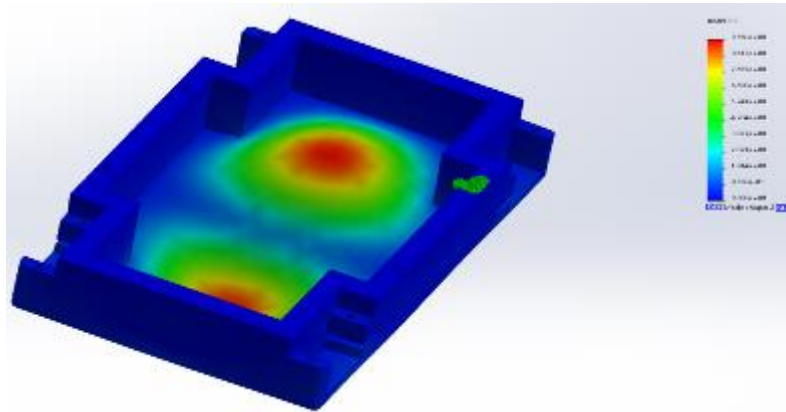
Fig. 2. FEM mode shape distribution corresponding to the second vibration mode of the enclosure

At intermediate frequencies, the third vibration mode was identified. Figure 3 illustrates this mode, where the maximum displacement amplitude was around 5.55 mm, concentrated in a central lobe with secondary amplification along the edges. This result emphasizes the need for frequency-dependent viscoelastic data, as simplified elastic assumptions would underestimate damping and shift the modal response.
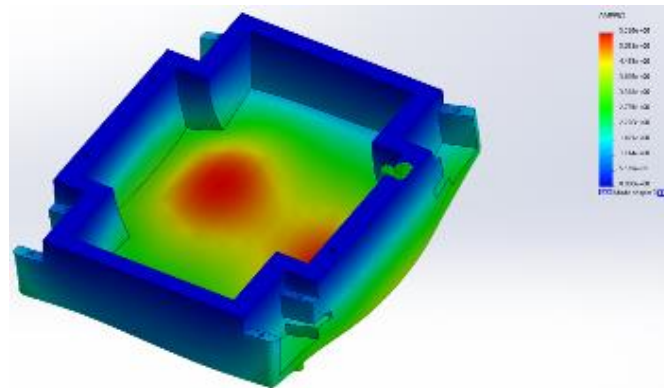
Fig. 3. FEM mode shape distribution corresponding to the third vibration mode of the enclosure

Higher-order responses became evident in Figure 4, which corresponds to the fourth vibration mode of the enclosure. Two dominant lobes appear, with a maximum displacement of approximately 9.79 mm. This distribution highlights the complexity of the enclosure's dynamic behavior at higher frequencies and underlines the importance of vibro-acoustic coupling models for predicting radiated noise.

The results in Figures 1-4 confirm that TPU, when modeled with viscoelastic and interfacial parameters, can reproduce modal responses within realistic amplitude ranges (5-10 mm in these cases). The close agreement between numerical predictions and theoretical expectations can be explained by the fact that the obtained modal frequencies and shapes match the classical thin-plate vibration theory: the first mode corresponds to a global bending deflection, the second to a symmetric double-peak mode, while the third and fourth exhibit higher-order lobes consistent with analytical solutions for rectangular plates. This agreement also is consistent with previous studies on TPU-based damping elements [1-3, 15].

This indicates that TPU correctly captures the global flexibility of the structure under low-frequency excitation.
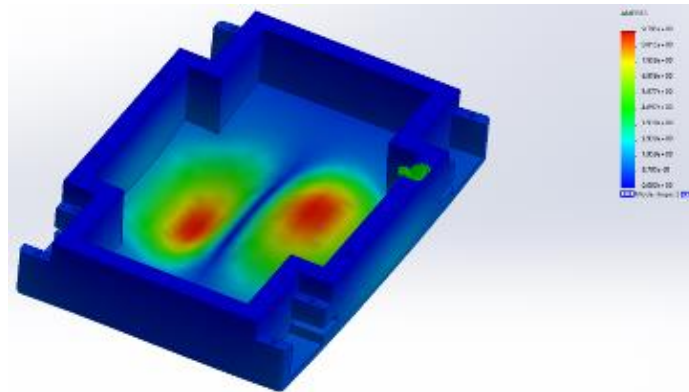
Fig. 4. *FEM mode shape distribution corresponding to the fourth vibration mode of the enclosure, highlighting two dominant displacement regions*

4. Conclusions

The finite element simulations suggest that thermoplastic polyurethane (TPU) has strong potential for use in NVH engineering as a structural decoupler and acoustic absorber. The modal analysis of the enclosure demonstrated that the first vibration mode reached a displacement amplitude of about 10.2 mm (Figure 1), while higher-order modes such as the second and third exhibited amplitudes of 9.57 mm and 5.55 mm, respectively (Figures 2-3). At higher frequencies, the fourth mode reached 9.79 mm (Figure 4), which underlines the complexity of vibro-acoustic interactions and the importance of accounting for realistic damping and friction effects.

The FEM analyses further indicated that preload-dependent stiffness, frequency-dependent viscoelasticity, and nonlinear friction models are essential for accurately predicting TPU behavior. Incorporating these parameters enabled accurate modal simulations and provided a foundation for optimizing TPU components in NVH applications.

In conclusion, this research demonstrates that TPU, when modeled with appropriate viscoelastic and interfacial properties, offers strong modal and acoustic performance potential. These findings support the integration of TPU into automotive NVH solutions and highlight important directions toward lightweight and multifunctional applications in engineering.

References

[1]. Zheng Y., Shangguan W.-B., Liu X.-A., *Modeling of a quasi-zero static stiffness mount fabricated with TPU materials using fractional derivative model*, Mechanical Systems and Signal Processing, 177:109258, 2022.

[2]. Yun D., Kim J., *Acoustic performance of flexible polyurethane composite foams filled with melamine particles*, Korean Journal of Chemical Engineering, 40, p. 3052-3058, 2023.

[3]. Zu R., *et al.*, *Tailor-made 3D printing TPU/PLA composites for damping and energy absorption*, Materials & Design, 252, 113752, 2025.

[4]. Huang Y., *et al.*, *Noise source diagnosis via transfer path analysis and neural networks*, Applied Sciences, 13(22), 12244, 2023.

[5]. Rafsanjani A., *et al.*, *Programming soft robots with flexible mechanical metamaterials*, Science Robotics, 4, eaav7874, 2019.

[6]. Oliveira H. S., *et al.*, *Proprioceptive multistable mechanical metamaterial via soft capacitive sensors*, Smart Materials & Structures, 34, 035002, 2025.

[7]. Carton M., *et al.*, *Bridging hard and soft: torque-transmitting mechanical metamaterials*, Advanced Intelligent Systems, 6(7), 2400123, 2024.

[8]. Zhao L., *et al.*, *SoftSnap: rapid prototyping of untethered soft robots*, Soft Robotics, 11(5), p. 823-835, 2024.

[9]. Hiremath S., *3D-printed TPU pneumatic actuators for soft grippers*, Robomech Journal, 12:55, 2025.

[10]. Pishvar M., Harne R. L., *Active mechanical metamaterials for smart matter*, Advanced Science, 8(22), 2101440, 2021.

[11]. Liu C., *et al.*, *Programmable mechanical metamaterials: a review*, Frontiers in Materials, 11, 1452396, 2024.

[12]. Gregg C. E., *Ultralight, strong, and self-reprogrammable mechanical metamaterials*, Science Robotics, 9, eadi2746, 2024.

[13]. Surjadi J., *et al.*, *Double-network-inspired mechanical metamaterials*, Nature Materials, 24, p. 945-954, 2025.

[14]. Armentani E., *et al.*, *Vibro-Acoustic Numerical Analysis for the Chain Cover of a Car Engine*, Applied Sciences, 7(6), 2017.

[15]. Sakhaei B., *et al.*, *Vibration transfer path analysis for vehicle interiors*, Journal of Sound and Vibration, 482, 115472, 2020.

[16]. Wienen K., *et al.*, *Robust NVH engineering using experimental methods—source characterization techniques for component transfer path analysis and virtual acoustic prototyping*, SAE Technical Paper, 1, 2019-01-1542, 2019.

[17]. ***, *Altair Engineering, Transfer Path Analysis documentation*, OptiStruct User Guide, 2021.

[18]. Vasconcelos A. C. A., *et al.*, *Hybrid mechanical metamaterials: Advances of multi-functional mechanical metamaterials with simultaneous static and dynamic properties*, Heliyon, 11(3), e41985, 2025.

[19]. Hu Y., *et al.*, *Shape estimation for a TPU-based multi-material 3D printed soft pneumatic actuator using deep learning models*, Science China Technological Sciences, 67(5), p. 1470-1481, 2024.

[20]. de la Rosa S., *et al.*, *Design of customized TPU lattice structures for additive manufacturing: Influence on the functional properties in elastic products*, Polymers, 13(24), 4341, 2021.

[21]. Zhou Z., *et al.*, *Flexible strain sensors based on thermoplastic polyurethane fabricated by electrospinning: A review*, Sensors, 24, 4793, 2024.

TOPOLOGY OPTIMIZATION FOR MASS REDUCTION OF A STRUCTURAL COMPONENT IN A SURGICAL ROBOTIC ARM

Florin Bogdan MARIN[1,2]**, Daniela Laura BURUIANĂ**[1,2]**,
Larisa IONICĂ**[1]**, Mihaela MARIN**[1,2]

[1] "Dunarea de Jos" University of Galati, Romania,
[2] Interdisciplinary Research Centre in the Field of Eco-Nano Technology and Advanced Materials CC-ITI,
Faculty of Engineering, "Dunarea de Jos" University of Galati, Romania, 47 Domnească Street, RO-800008,
Galaţi, Romania
e-mail: flmarin@ugal.ro

ABSTRACT

This paper presents a case study on the topology optimization of a structural component in a surgical robotic arm, aiming to reduce mass while maintaining mechanical performance. The component, made of aluminium alloy Al7075-T6, was subjected to finite element analysis and topology optimization using Altair OptiStruct. The objective of the study was to minimize mass under the imposed constraints of maximum displacement (≤ 0.2 mm) and von Mises stress (≤ 250 MPa). The stress limit was selected as 50% of the alloy's yield strength (≈ 503 MPa), to ensure an additional safety margin. Finite element analysis (FEA) was employed to evaluate and validate the optimized geometry. The initial design exhibited a displacement of 0.21 mm and a maximum stress of 240 MPa, which corresponds to a safety factor of 1.04. After optimization, the final design achieved a displacement of 0.18 mm and a maximum stress of 227 MPa, which results in a safety factor of 1.3. These results demonstrate that the adopted topology optimization strategy can effectively reduce structural mass (≈34%) while maintaining compliance with displacement and stress constraints, ensuring reliability for robotic applications.

KEYWORDS: topology optimization; surgical robot; Altair OptiStruct; structural analysis; Al7075-T6; robotic arm component

1. Introduction

Minimally invasive surgery (MIS) has led to a significant demand for lightweight, high-precision robotic systems with excellent dynamic response and structural integrity. In such systems, each component must be optimized for mass efficiency without compromising stiffness or strength [1-2]. Topology optimization (TO) has become a well-established strategy for designing lightweight components, with numerous studies applying it successfully in robotic systems, including manipulators, grippers, and arms [3-5].

The use of topology optimization has expanded with the integration of Computer-Aided Design (CAD) and Finite Element Analysis (FEA) tools, such as HyperMesh and Altair OptiStruct [6-7]. Recent comparative analyses of TO platforms emphasize the importance of solver capabilities, stress-based constraints, and integration with additive manufacturing (AM) workflows [2, 8]. Moreover, lattice-based design methods tailored for AM have shown promising results, enabling further weight reduction through geometric complexity that is not achievable with traditional manufacturing [1, 9-10].

The structural efficiency of robotic components can also be enhanced by combining TO with multi-material optimization [11-12], and by incorporating fabrication constraints like symmetry, minimum member size, and extrusion directions, which ensure manufacturability without sacrificing performance [4, 13-14]. Such comparative reviews highlight that fabrication-aware approaches remain essential for bridging theoretical topology optimization and practical engineering applications [13]. Advanced techniques, such as robustness-based and manufacturing-tolerant topology optimization, have been implemented to handle uncertainty in load cases

and material properties [15-17]. More recent studies have proposed stress-constrained approaches under uncertain load positions [16], generalized frameworks based on first-order second-moment formulations [18], reliability-based methods incorporating additive manufacturing constraints [19], robust continuum optimization schemes [20], and strategies with local stress constraints and variable load directions. These contributions highlight the continuous evolution of TO toward more realistic and application-oriented design strategies. Studies also show that compliant mechanisms and soft robotic structures benefit from TO methods that consider nonlinear deformation and fatigue life [5, 21]. In this context, novel optimization schemes such as level-set methods, topological sensitivity, and fatigue-driven constraints are gaining traction [14, 21]. Material selection is another key factor. Aluminum alloy Al7075-T6 is widely used in robotic and aerospace structures because of its excellent strength-to-weight ratio, good machinability, and corrosion resistance. With a Young's modulus of about 71.7 GPa, yield strength near 503 MPa, and density of 2,810 kg/m^3, this alloy provides high mechanical performance for lightweight components. It is particularly effective for internal, non-biological-contact parts of medical devices, where biocompatibility is not a primary requirement but stiffness and strength remain essential [22-23, 25].

This paper presents a complete design and optimization workflow for a surgical robotic component, starting from CAD modeling, followed by meshing and structural simulation in HyperMesh, and final-stage topology optimization in Altair OptiStruct. The objective is to achieve maximum mass reduction while ensuring that key mechanical constraints - such as displacement and von Mises stress - remain within safety limits. The approach aligns with recent trends in robotic engineering and

contributes to more efficient, precise, and manufacturable designs.

2. Experimental Procedure

The objective of the research was to optimize the structural design of a robotic arm component used in minimally invasive surgery. The experimental procedure included CAD modeling, meshing, topology optimization, and finite element analysis (FEA) validation.

The initial geometry of the robotic arm component was created as a simplified, hollow rectangular structure made of Al7075-T6 aluminium alloy. With overall dimensions of 200 mm in length, 50 mm in width, and 30 mm in height, and a wall thickness of 4 mm, the model represented a typical load-bearing element used in surgical robotic systems. The material selected for the design was Al7075-T6, chosen for its excellent strength-to-weight ratio, high stiffness, and suitability for lightweight structural applications. Its mechanical properties include a Young's modulus of 71.7 GPa, yield strength of about 503 MPa, and density of 2,810 kg/m^3. In addition, this alloy offers good machinability and corrosion resistance, which explains its widespread use in aerospace and robotic components where high mechanical performance is required without biocompatibility constraints.

The CAD model was transferred to Altair HyperMesh for mesh generation and the application of boundary conditions. A first-order tetrahedral mesh with an average element size of 2 mm was created to ensure adequate resolution for structural analysis. To replicate real operational conditions, the component was fully fixed at one end, while a concentrated load of 50 N was applied to the opposite extremity. This simulation setup reflected the mechanical stresses typically encountered by the robotic arm during surgical procedures.

Fig. 1. Initial 3D CAD model of the robotic component

Fig. 2. *Boundary conditions and applied load on the model*

3. Results and Discussions

After 30 iterations, the topology optimization process produced a geometry with substantial material redistribution. The initial model exhibited a maximum displacement of 0.21 mm and a maximum stress of 240 MPa, values close to the imposed thresholds, which corresponded to a safety factor of 1.04. After optimization, the final design achieved a maximum displacement of 0.18 mm and a maximum stress of 227 MPa, which increased the safety factor to 1.3. The final optimized model achieved a 34% reduction in mass, while fully meeting all mechanical performance criteria. The initial output from the optimization featured irregular surfaces and sharp transitions, which could hinder manufacturability. To address this, the geometry was reimported into a CAD environment and refined using surface smoothing techniques. The final post-processed model preserved the essential structural features of the optimized design while significantly enhancing surface quality, making it suitable for additive manufacturing and practical implementation.

Figure 3 shows the optimized structure, emphasizing its efficient internal layout that ensures stiffness with minimal material use. Figure 4 provides a top-down view, highlighting the non-intuitive load paths and material patterns that emerged through the optimization, specifically adapted to the applied mechanical constraints.

Fig. 3. *Topologically optimized 3D model*

Fig. 4. *Top view of the optimized structure showing material distribution*

The maximum displacement recorded was 0.18 mm, and the peak von Mises stress reached 227 MPa, remaining well below the 250 MPa allowable limit.

In a related study, Batista *et al.* [1] reported a 31% mass reduction in a robotic arm component using lattice-based optimization techniques specifically tailored for additive manufacturing. By contrast, the present study achieves a slightly higher reduction using a classical topology optimization approach, without relying on predefined lattice structures. These findings underscore the potential of conventional TO algorithms to deliver high-efficiency structural designs, even before incorporating AM-specific enhancements. Table 1 summarizes the improvements obtained through topology optimization compared to the initial design.

Table 1. *Comparison of mechanical performance before and after topology optimization*

Design Stage	Mass Reduction	Max Displacement (mm)	Max Von Mises Stress (MPa)	Safety Factor
Initial Model	-	0.21	240	1.04
Optimized Model	-34%	0.18	227	1.3

As shown in Figure 5, the side view of the model with superimposed stress distribution confirms that the structural integrity of the component remains intact under the applied loading conditions. Figure 6 illustrates the redistribution of stresses and the continuity of load paths along the optimized ribs. These results collectively demonstrate that the optimized geometry achieves an effective balance between rigidity and lightweight design, validating its suitability for surgical robotic applications.

Fig. 5. *The side view of the optimized model showing stress distribution*

Fig. 6. *The optimized structure from an alternate viewing angle*

The initial output from the topology optimization process featured irregular surfaces and sharp transitions, which could hinder manufacturability and introduce potential stress concentrators. To address this, the geometry was reimported into a CAD environment and refined using surface smoothing techniques. As shown in Figure 7, the final post-processed model preserves the essential structural features of the optimized design while significantly enhancing surface quality, making it suitable for additive manufacturing and practical implementation.
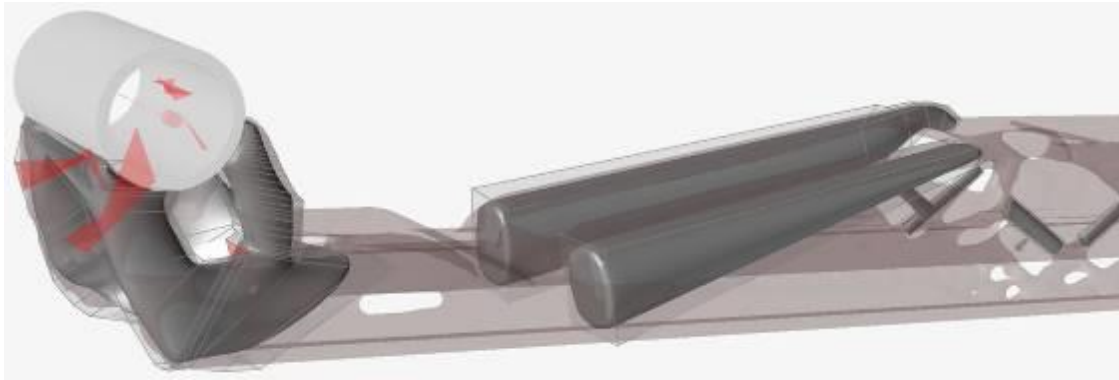
Fig. 7. *The smoothed and post-processed version of the optimized model*

A final FEM simulation was conducted on the refined model to verify its structural integrity. The results confirmed that all constraints were met, with a safety factor of 1.3, validating the design for surgical robotic applications.

The internal structure of the component resembles trabecular bone, a naturally optimized geometry for stiffness and weight. This result underscores the biomimetic potential of topology optimization in medical device engineering. Moreover, the compatibility of the final geometry with metal 3D printing technologies supports its practical manufacturability, minimizing waste and production time, which are key advantages in customized biomedical device fabrication.

4. Conclusions

This paper demonstrated the effectiveness of applying topology optimization to reduce the mass of a structural component intended for a surgical robotic arm, while ensuring mechanical integrity under realistic operational loads. By employing a CAD-integrated workflow and the Altair OptiStruct solver, a mass reduction of approximately 34% was achieved compared to the original design. The optimization process preserved the required mechanical performance, with a maximum displacement of 0.18 mm and a peak von Mises stress of 227 MPa - both remaining within the defined design limits. The resulting geometry exhibited a non-intuitive, lattice-like internal structure that efficiently redirected stress to critical load-bearing regions, mirroring the efficiency of natural bone structures. To ensure manufacturability, the optimized model was refined through CAD-based post-processing, addressing surface quality and eliminating geometric irregularities. This step rendered the design suitable for fabrication via metal additive manufacturing. The FEM simulations validated that the optimized structure complies with the imposed constraints of maximum displacement ($\leq$ 0.2 mm) and von Mises

stress ($\leq$ 250 MPa). The initial configuration exhibited a displacement of 0.21 mm and a maximum stress of 240 MPa, while the final optimized design achieved 0.18 mm displacement and 227 MPa stress, both remaining below the limits. The calculated safety factor was 1.3, indicating adequate structural reliability while achieving mass reduction. These results demonstrate that topology optimization can be effectively applied to robotic arm components, enabling lightweight design without compromising structural integrity. Furthermore, the findings provide a solid numerical foundation for future developments, including experimental validation and the integration of advanced optimization methods into robotic system design.

References

[1]. Batista R. C., ***et al.***, *Lattice-based topology optimization of robot arm components for additive manufacturing*, Front. Mech. Eng, 10, 1422539, 2024.

[2]. Curkovic P., *Comparative Analysis of Topology Optimization Platforms for Additive Manufacturing of Robot Arms*, Designs, 8, 98, 2024.

[3]. Sha L., ***et al.***, *A topology optimization method of robot lightweight design based on the finite element model of assembly and its applications*, Sci. Prog, 103(3), p. 36850420936482, 2020.

[4]. Langelaar M., *Topology optimization of 3D self-supporting structures for additive manufacturing*, Addit. Manuf, 12(Part A), p. 60-70, 2016.

[5]. Jia J., Sun X., *Structural Optimization Design of a Six Degrees of Freedom Serial Robot with Integrated Topology and Dimensional Parameters*, Sensors, 23(16), p. 7183, 2023.

[6]. Chen J., Chen Q., Yang H., *Additive manufacturing of a continuum topology-optimized palletizing manipulator arm*, Mech. Sci, 12, p. 289-304, 2021.

[7]. Dammer G., ***et al.***, *Design, topology optimization, and additive manufacturing of a pneumatically actuated lightweight robot*, Actuators, 12(7), p. 266, 2023.

[8]. El Khadiri I., ***et al.***, *Topology optimization methods for additive manufacturing: A review*, Int. J. Simul. Multidisci. Des. Optim, 14, p. 12, 2023.

[9]. Fernandez E., ***et al.***, *Topology optimisation for large-scale additive manufacturing: generating designs tailored to the deposition nozzle size*, Virtual Phys. Prototyping, 16(2), p. 196-220, 2021.

[10]. Pinskier J., ***et al.***, *Automated design of pneumatic soft grippers through design-dependent multi-material topology*

optimization, Proc. IEEE Int. Conf. Soft Robotics (RoboSoft), 2023.

[11]. Silva G. A., Beck A. T., Sigmund O., *Stress-constrained topology optimization considering uniform manufacturing uncertainties*, Comput. Methods Appl. Mech. Eng, 344, p. 512-537, 2019.

[12]. Suresh S., *et al.*, *Topology optimization for transversely isotropic materials with high-cycle fatigue as a constraint*, Struct. Multidiscip. Optim, 63, p. 161-172, 2021.

[13]. Sigmund O., Maute K., *Topology optimization approaches: A comparative review*, Structural and Multidisciplinary Optimization, 48(6), p. 1031-1055, 2013.

[14]. Suresh S., *et al.*, *Topology optimization using a continuous-time high-cycle fatigue model*, Struct. Multidiscip. Optim, 61, p. 1011-1025, 2020.

[15]. Liu K., Tovar A., *An efficient 3D topology optimization code written in Matlab*, Structural and Multidisciplinary Optimization, 50(6) p. 1175-1196, 2014.

[16]. Oh M. K., Lee D. S., Yoo J., *Stress-constrained topology optimization simultaneously considering the uncertainty of load positions*, International Journal for Numerical Methods in Engineering, 123(3), p. 339-365, 2022.

[17]. Granlund G., *et al.*, *Stress-constrained topology optimization of structures subjected to non-proportional loading*, Int. J. Numer. Methods Eng, 124(12), p. 2818-2836, 2023.

[18]. Kranz M., Lüdeker J. K., Kriegesmann B., *A generalized approach for robust topology optimization using the first-order second-moment method for arbitrary response functions*, Structural and Multidisciplinary Optimization, 66, 98, 2023.

[19]. Murat F., Kaymaz I., Şensoy A. T., *Reliability-Based Topology Optimization Considering Overhang Constraints for Additive Manufacturing Design*, Applied Sciences, 15(11), 6250, 2025.

[20]. Martínez-Frutos J., Herrero-Pérez D., *Robust topology optimization of continuum structures*, Computers & Structures, 257, 106677, p. 1-15, 2021.

[21]. Yun G. H., *Topology optimization considering the fatigue constraint of variable amplitude load based on the equivalent static load approach*, Appl. Math. Model, 56, p. 626-647, 2018.

[22]. Hermansen S. M., Lund E., *Multi-material and thickness optimization of laminated composite structures subject to high-cycle fatigue*, Struct. Multidisc. Optim, 66, p. 259, 2023.

[23]. Tang H., *et al.*, *Numerical Prediction of Fatigue Life for Landing Gear Considering the Shock Absorber Travel*, Aerospace, 12(1), p. 42, 2025.

[24]. Senhora F. V., *Topology optimization with local stress constraints and continuously varying load direction*, Proceedings of the Royal Society A: Mathematical, Physical and Engineering Sciences, 478(2260), 20220436, 2023.

[25]. Venkatesh S., *et al.*, *A review on aluminium 7075 alloy: Micro structure, mechanical properties and application*, AIP Conf. Proc, 3221, p. 020001, 2024.

SIMULATION WITH THE HELP OF MATLAB OF THE FORGING TECHNOLOGY FOR THE ROTOR SHAFT REFERENCE OF A WIND TURBINE INSTALLATION

Marian-Iulian NEACSU

"Dunarea de Jos" University of Galati, Romania
e-mail: mneacsu@ugal.ro

ABSTRACT

In this paper, a simulation of the forging process was carried out to obtain the rotor shaft of a wind turbine.

The simulation program used for the forging process in the referenced work is based on the mathematical formulations specific to plastic deformation during forging, integrated into a computational model that faithfully reproduces the real technological conditions.

KEYWORDS: forging, simulation, rotor shaft, wind turbines

1. Introduction

For millennia, the art of forging iron and other metals has played a crucial role in the evolution of human civilizations. Since the Bronze and Iron Ages, the ability to process and shape metals through forging has marked a major step in technological progress [1-3]. Even today, this process continues to be crucial for the production of basic materials and equipment used in strategic industries such as energy, oil and gas, construction, and the chemical and petrochemical industries [4-7]. Forging is often considered the "heart" of the metallurgical industry, due to its ability to provide a wide variety of indispensable products, such as metal pipes, fittings, sheets and profiles used in multiple industrial fields. Components obtained by plastic deformation of metals are recognized for their strength and durability, and they constitute key elements in modern industrial infrastructure.

The materials used in forging are mainly carbon steel and alloy steels, in various chemical compositions, followed by metals such as aluminium, magnesium, copper, titanium and their alloys. The raw material can have various forms, such as metal bars, ingots, metal powders or liquid metal. An important indicator in the forging process is the forging ratio, defined as the ratio between the cross-section of the material before deformation and that after deformation. The correct choice of this ratio, together with an appropriate heating temperature, an optimal holding time, the start and end temperatures of forging, as well as a well-controlled deformation

and deformation rate, contribute significantly to improving the quality of the final product and reducing production costs [8-13].

Fig. 1. *Wind turbine installation* [9]

The component known as the "Wind turbine rotor shaft" is a component part of the WTG 2000 kW wind turbine rotor, used for the production of electricity from wind energy (wind energy). This way of obtaining electricity is free of polluting technological processes, is cost-effective, but is only applicable in areas of the world where the wind blows almost constantly throughout the year [14].

The primary shaft is the rotor shaft of the wind turbine; it is also called the slow shaft, because it

rotates at speeds of approximately 20-40 rpm. Through the multiplier, it transmits the movement to the secondary shaft.

Simulation of technological processes in general consists of reproducing their evolution based on mathematical models that describe the respective process, with the aim of highlighting the evolution of the factors that characterize the final products and the technological process [15, 16].

Simulation of technological processes can be classified into several categories, depending on the nature and purpose of the study [15, 16]:

a) Real simulation – involves reproducing the analysed process through another process of a similar nature but carried out at a different scale.

b) Physical simulation – consists in reproducing the technological process using physical phenomena, preserving the characteristic interdependencies between factors. For example, the solidification process of a cast part can be simulated using electrical or hydraulic phenomena.

c) Analytical simulation – involves modelling the technological process using mathematical relationships, expressing the evolution of characteristic parameters through numerical values. This method allows analysing the behaviour of the process under different conditions through calculations.

d) Virtual simulation – is a modern simulation method that consists in representing and visualizing the technological process through computers, by transposing mathematical and physical models into software environments, in the form of image sequences.

In recent years, virtual simulation has developed rapidly, due to the numerous advantages it offers, including reduced material costs, eliminating the need to use tools, devices, installations and measuring equipment, lack of energy consumption and absence of negative impact on the environment.

2. Simulation in MATLAB of the end flange forging process by horizontal extrusion

Among the shortcomings that were identified during the design of the pair forging technology, the following can be noted:
• It is necessary to use large ingots (48000 kg);
• Handling the part during forging is cumbersome;
• Large ingots imply more pronounced segregation effects.

Since the forging of the rotor shaft in pairs (two parts in a single forged part) also has certain limitations, a new technological variant is proposed for forging this type of part.

This technology is based on the upsetting of the free end of the stretched semi-finished product in order to forge (form) the flange, with the semi-finished product in a horizontal position. To obtain the flange by retraction, the vertical movement of the upper anvil of the hydraulic press is transformed into a horizontal movement of the lower anvil.
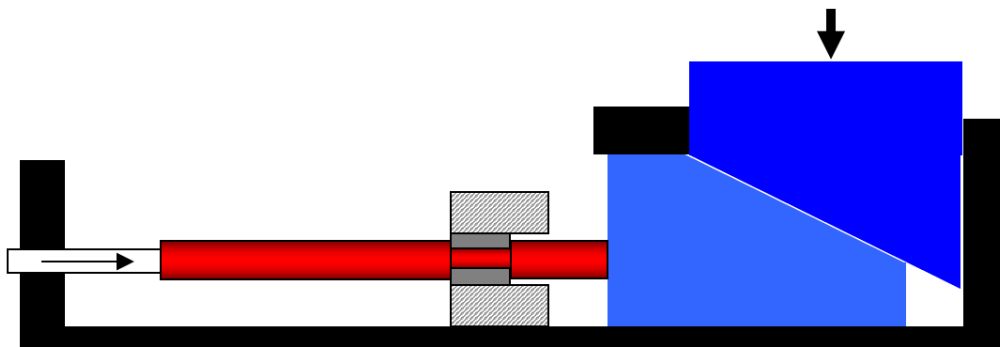
Fig. 2. Schematic diagram of horizontal end flange retraction

According to the website www.thefreedictionary.com [18], MATLAB is described as "an interactive program, developed by the MathWorks company, intended for performing high-performance numerical calculations and graphical representations. It integrates numerical analysis, matrix calculation, signal processing and graphics, in an intuitive and accessible working environment. MATLAB is based on an advanced numerical calculation core for the analysis of linear equations. Its applications cover a wide range of fields such as: applied mathematics, physics, chemistry, engineering, finance, but also other areas that involve complex numerical modelling and calculations."

From the perspective of a computer scientist, MATLAB may be viewed as a programming language, namely an interpreter dedicated to

implementing and running complex numerical calculations.

In this paper, a simulation of the forging process used to obtain the rotor shaft of a wind turbine was carried out.

The simulation program used for the forging process is based on the mathematical relationships specific to plastic deformation through forging, integrated into a computational model that faithfully reproduces the real technological conditions.

The simulation of the process includes the following stages:

Stage I - Initiation of the program developed in MATLAB (Figure 3).

Stage II - Bringing and Placing the Semi-finished Product on the Lower Half-Mold (Figures 4-5).

Stage III - Bringing the upper half-mould onto the semi-finished product (Figure 6).

Stage IV - Forming the flange by pressing the vertical anvil onto the horizontal anvil (Figure 7).
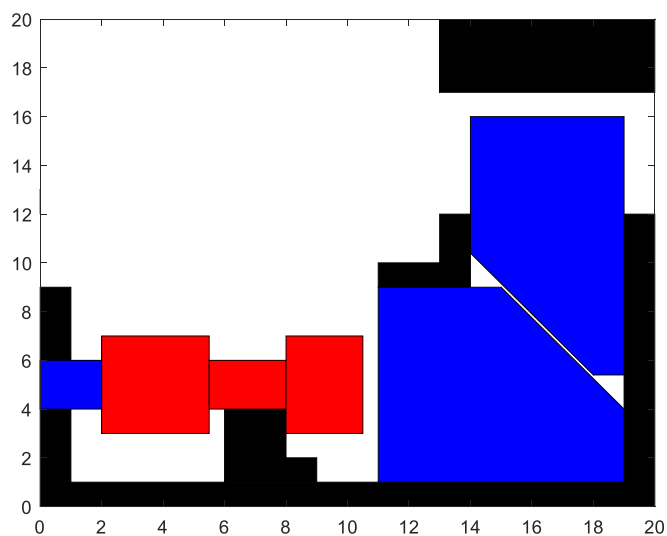
Stage V - Withdrawing the anvils to extract the parts (Figure 8).
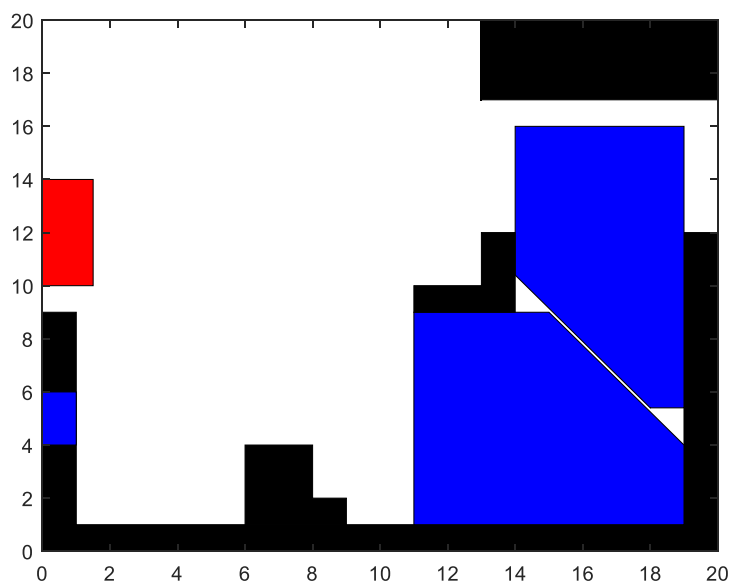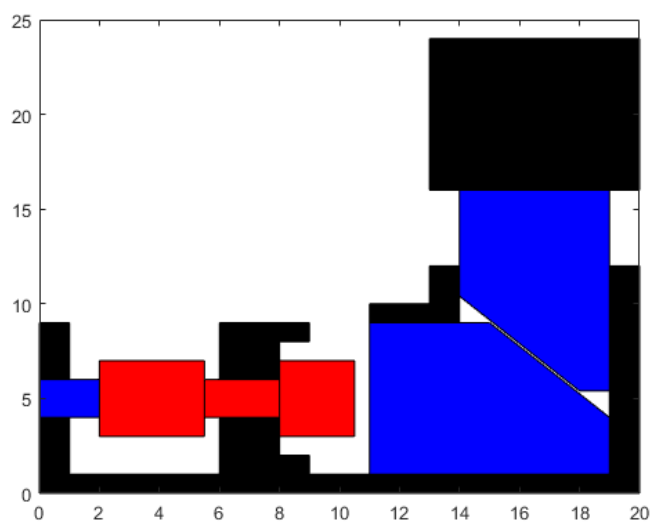

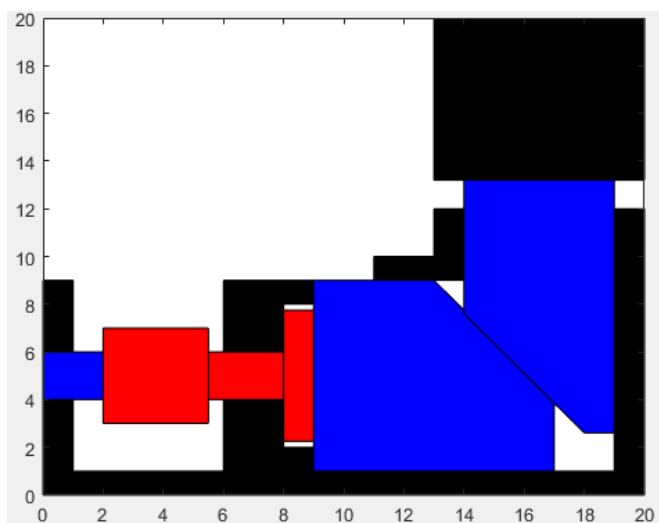**Fig. 3.** *Initiating the simulation program made in MATLAB*
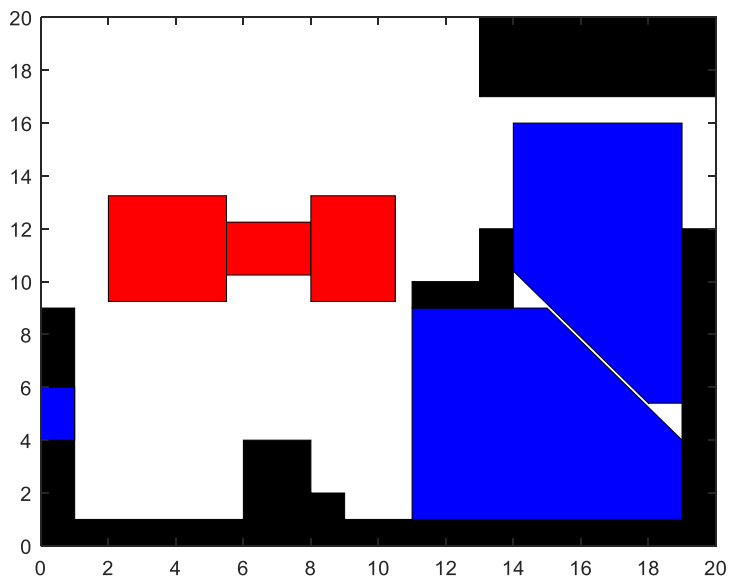
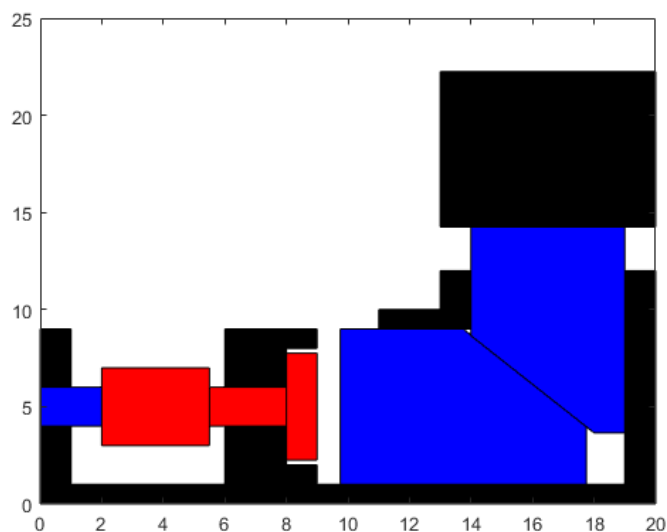**Fig. 4.** *Bringing the blank onto the lower half-die*

Fig. 5. *Placing the blank on the lower half-die*

Fig. 6. *Bringing the upper half-mould onto the blank*

Fig. 7. *Flange retraction by pressing the vertical anvil onto the horizontal anvil*

Fig. 8. *Retracting the anvils to extract the parts*

The semi-finished product subjected to reflow on this device must continue to follow the next operation plan described in Table 1, in order to achieve the proposed objectives.

Table 1. *Operation plan of end flange forging by pushing*

Nr. Crt.	Surgery	Operation outline	Equipment and S.D.V.s	Instructions
1	Forging the section		PH 31500 KN; Mixed anvils; Handling sleeve Compass, tape measure	-
2	Cutting the piece to size		PH 31500 KN; Mixed anvils; Handling sleeve Compass, tape measure Hot cutting axe	-
3	C.T.C., Marking Delivery		-	The external appearance is checked dimensionally and organoleptically.

3. Conclusions

From the analysis of the design of the open pair forging technology and horizontal extrusion of the wind turbine rotor shaft, it can be stated that each of the processes has both advantages and disadvantages. Among them, the following are identified:

FREE FORGING (a piece from an ingot)
Advantages:
• Ingots of relatively small size and mass are used.
• Handling of ingots during forging is easy.

• Segregation is less pronounced.
Disadvantages:
• From small ingots, the part can only be made by introducing in the operations plan, the ingot push-back, an operation that requires prior reheating and is the most energy-consuming, as it requires the greatest force (12000 tf) of all forging operations.
• The technological allowance in the flange area is large, due to the small length of the flange (160 mm) which also leads to appreciable metal consumption.

• The technological allowance is eliminated by machining, which is also a low-productivity and energy-consuming operation.

• Can only be performed on hydraulic presses with nominal forces greater than 12,000 tf = 120,000 kN;

FREE PAIR FORGING

Advantages:

• The ingot pressing operation is eliminated.

• The ingot stretching operation is eliminated.

• The metal utilization coefficient is better than when forging a part from an ingot;

• Due to the large mass of the ingots used, a large amount of heat is stored, which makes reheating unnecessary.

Disadvantages:

• It is necessary to use large ingots (48 t);

• Handling the ingots during forging is more difficult.

• Segregation is more pronounced in large ingots.

• Separating the two parts from the forged piece is difficult.

• The heating rate for forging is slow.

FORGING BY HORIZONTAL FLANGE PRESSURE

Advantages:

• Ingots of relatively small size and mass are used.

• Handling of ingots during forging is easy.

• Segregation is less pronounced.

• The metal utilization coefficient is better than when forging apart from an ingot;

• The pressure force is acceptable, since the pressure is performed with the successive rotation of the punch, which has a small width.

• A corresponding (continuous) fiber is created.

Disadvantages:

• It requires a dedicated special device.

As a general conclusion, it can be said that horizontal pressure of the end flange combines the vast majority of the advantages of the other processes but has the disadvantage of requiring a special device.

References

[1]. ***, https://www.steelforging.org/the-history-of-forging-process/.

[2]. ***, https://www.wasatchsteel.com/the-history-of-steel-and-metal-forging-part-1/.

[3]. ***, https://www.steelavailable.com/en/history-steel-forging/.

[4]. ***, https://en.m.wikipedia.org/wiki/Forging.

[5]. ***, https://www.scribd.com/doc/90995816/Forjarea-Metalelor.

[6]. ***, https://www.zxhydraulic.com/news/free-forging-and-die-forging/.

[7]. ***, https://forgedsteelfs.com/free-forging/.

[8]. ***, https://zxhydraulicpress.com/blog/difference-between-die-forging-and-free-forging/.

[9]. ***, International Journal of Scientific and Research Publications, vol. 4, issue 6, ISSN 2250-3153, June 2014.

[10]. ***, https://www.iqsdirectory.com/articles/forging/what-is-forging.html.

[11]. ***, https://www.generalkinematics.com/blog/cold-forging-vs-hot-forging/.

[12]. ***, https://en.wikipedia.org/wiki/Strain_rate.

[13]. ***, Journal of Materials Processing Technology, vol. 210, nr. 8, p. 998-1007, 1 June 2010.

[14]. ***, https://www.lpelectric.ro/ro/products/wind_ro.html.

[15]. Zahariea D., Simularea sistemelor fizice în MATLAB, Ed. PIM, Iași, 2010.

[16]. ***, MathWorks, MATLAB, Desktop Tools and Development Environment, 2017.

[17]. Ghinea M., Firețeanu V., MATLAB. Calcul numeric, grafică, aplicații, Editura Teora, București, 2003.

[18]. ***, www.thefreedictionary.com.

MODERNISATION OF IRRIGATION SYSTEMS – A SUSTAINABLE SOLUTION FOR EFFICIENT WATER RESOURCE MANAGEMENT IN AGRICULTURE

Daniela-Felicia BABENCU[2], Gina Genoveva ISTRATE[1,2]

[1] Interdisciplinary Research Center in the Field of Eco-Nano Technology and Advanced Materials (CC-ITI)
[2] Faculty of Engineering, "Dunarea de Jos" University of Galati, 111 Domneasca Str., 800008, Galati, Romania
e-mail: gina.istrate@ugal.ro

ABSTRACT

In the current context, marked by accelerated climate change, population growth, and the development of anthropogenic activities, pressure on water resources is increasing. Therefore, the need to develop efficient and sustainable agriculture through effective water resource management is becoming a priority at both global and national levels. Romania is increasingly facing challenges in adapting the agricultural sector to new climatic conditions. These conditions are characterized by increasingly pronounced fluctuations in precipitation and a rising frequency of drought years – characteristics that negatively affect crop productivity and stability.

This article aims to analyse the benefits of modernizing irrigation technologies, focusing on innovative, smart, and environmentally friendly solutions, such as precision irrigation. An innovative alternative solution is examined, namely the use of fog collectors as a complementary method of passive water collection, with potential for application in favourable microclimates, including the hilly areas of Romania.

KEYWORDS: irrigation, water stress, fog collectors

1. Introduction

Although 71% of the Earth's surface is covered with water, only 2.53% is freshwater. Of this percentage, 68.7% is in solid form at the two poles and in high mountains, 30.1% is groundwater, meaning that only 1.2% of the planet's freshwater volume actively participates in sustaining and prospering human life and civilization [1].

It is well known that no organism on our planet can survive without water. People's biological needs include drinking water and basic hygiene, but in today's society, water is also necessary for industry, agriculture, hydroelectric power, etc. In addition to this, water is an indispensable element of the landscape for recreation, navigation, fishing, and other activities.

Romania's hydrographic network is 78,905 km long and evenly distributed, with 98% of the rivers in Romania originating in the Carpathian Mountains [2]. An important network of rivers crosses the state border, and the Tisa, Prut, and Danube form part of Romania's border. The main rivers are the Mureș

(761 km), Prut (742 km), Olt (615 km), Siret (559 km), Ialomița (417 km), Someș (376 km), and Argeș (350 km) [2, 3].

The Danube River is by far the most important source of fresh water in Romania, ranking 23rd in the world with a flow rate of approximately 6,450 m3/s and a total length of 2860 km, of which 1075 km lie within Romania [1].

Romania has a significant amount of groundwater, approximately 9.6 billion m^3, of which 4.66 billion m^3 is usable and 4.9 billion m^3 represents the deep reserves [4].

According to the Environmental Report of the National Strategy for Preventing and Combating Desertification and Land Degradation, in 2021, there were 143 groundwater bodies, divided as follows:
- 115 groundwater bodies;
- 28 deep groundwater bodies.

Water quality, determined by its organoleptic, physical, chemical, biological, and bacteriological characteristics, is continuously monitored at input points (natural waters) and output/effluent points (discharges from various outlets).

With Romania's accession to the European Union, it was necessary to implement 18 Directives and 2 Decisions on integrated water monitoring.

Three types of monitoring programs are applied to surface waters:
• Surveillance monitoring assesses the status of all water bodies in river basins.
• Operational monitoring is an integral part of surveillance monitoring and is intended for water bodies at risk of not meeting protection objectives.
• Investigative monitoring aims to identify the causes of exceedances of the limits set in the quality standards.

Two types of monitoring programs are implemented for groundwater:
• Quantitative monitoring.
• Qualitative monitoring, which may be surveillance and/or operational [5].

According to the assessment carried out within the Updated National Management Plan for the National Portion of the Danube River Basin, the ecological status of surface waters is good in terms of chemical quality. The assessment was carried out on 3025 water bodies and found that 97.65% are in good chemical status, while the remaining 2.35% do not achieve good chemical status [2].

Figure 1 shows the ecological status and ecological potential of surface water bodies at the national level. The green lines represent water bodies in good condition, the yellow lines represent water bodies in moderate chemical condition, and the red lines represent water bodies that do not achieve good chemical status.
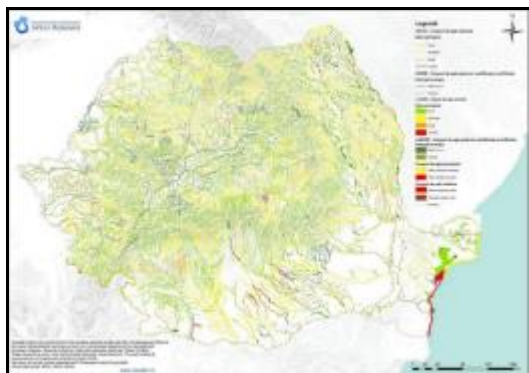
Fig. 1. *Ecological status and ecological potential of surface waters in Romania* [2]

2. The importance of water

2.1. Use of water resources

Since ancient times, humans have understood that without water, their bodies cannot function, and that without it, neither animal nor plant food can be obtained. Therefore, waterways have been used to provide the necessary water, but also for transportation (navigation). Historical data confirms that the great ancient civilizations developed on the banks of the Nile, Tigris, Euphrates, Indus, and other rivers. The links between humans, society, and water are extremely complex and, as society developed, humans were compelled to intervene in waterways, thus causing changes in both riverbed processes and water quality.

Conclusive evidence of water collection and use systems remains in various parts of the world. Wells, aqueducts, navigation channels, dams, drainage, and irrigation systems are just some examples, and they prove that in order to obtain water, people throughout history have used all their intellectual capacity in conjunction with the technical means available at the time.

In modern society, the need for water is directly linked to human actions that transform the environment in order to easily obtain what is necessary for life, for urbanization and industrialization, or for more intensive agriculture.

In Europe, approximately 75% of the water extracted comes from surface water (rivers and reservoirs), and the remaining 25% from groundwater. The highest quantities are extracted during the growing season [2].

The main source of water in Romania comes from inland rivers. Although there are quite many natural lakes, they have small volumes, except Lake Razelm and Sinoe.

At the European level, large quantities of water are used in activities such as agriculture (58%), cooling in energy processes (18%), mining (11%), and households (10%). It follows that agriculture is the economic sector with the highest consumption of water resources [5].

Although at the European level, the largest volume of water collected from surface sources is used in agriculture. In Romania, the industry uses the largest proportion of water resources, followed by agriculture. Between 2015 and 2020, water requirements were analysed for three sectors: industry, agriculture, and population. The data obtained from the analysis are presented in Figure 2 and shows that the industry has the highest water consumption. It can also be seen that demand is higher than the available withdrawal level for all three categories analysed, except for 2020, in which the amount of water withdrawn for agriculture was higher than demand, indicating water loss in this area.
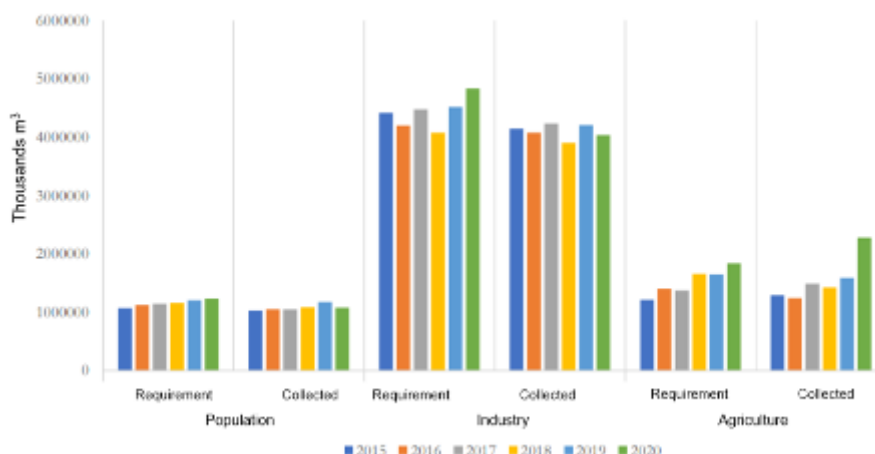
Fig. 2. Surface water requirements/quantity sampling [2]

Regarding groundwater, in Romania, the largest amount captured is used to supply water to the population, followed by industry, agriculture, and other activities. Figure 3 shows the distribution of the volume of groundwater abstracted and its use at the level of river basins. The colours in the figure indicate each category analysed: blue for the population, green for industry, and yellow for agriculture and other activities. It should be noted that the Dobrogea-Litoral basin has the largest amount used by the population, and the Olt River basin uses the entire volume of groundwater extracted only for the population and industry.
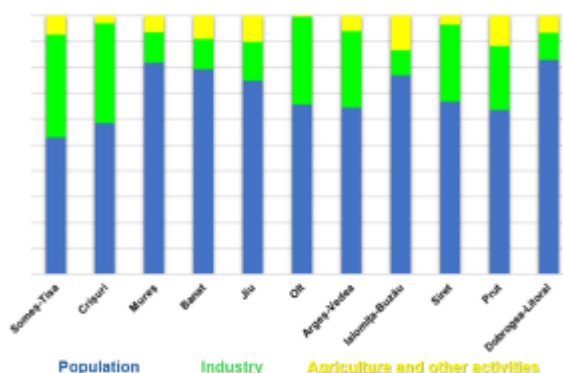

Fig. 3. Groundwater use at the level of watersheds in Romania [3]

2.2. Pressure on water bodies

Factors such as climate change, reflected in rising average temperatures and the frequent occurrence of extreme weather events (including drought), population growth, and economic development are amplifying water shortages around the world, both seasonally and over extended periods.

In the European Union, a large part of the territory is already affected by water abstraction exceeding available reserves, leading to increasing water stress. Water stress is the ratio between total water abstraction and available renewable surface and groundwater reserves [2].

According to a study conducted by the World Bank, over the last 55 years, there has been a 17% decrease in renewable water reserves per capita at the European level [2]. This phenomenon is partly caused by population growth, but economic pressures and climate change also significantly contribute to the intensification of water shortages, which are felt seasonally or throughout the year in certain regions of the European Union. Forecasts for 2030 show a significant increase in the areas of Europe where water stress will intensify. Figure 4 shows the situation in European regions in 2021 as a reference for the 2030 forecasts. It can be seen that in Romania, there are regions with high and very high-water stress, especially in the northeast, east, and southeast. In the northwest, there are areas with low to medium and medium to high water pressure, but these occupy smaller areas.
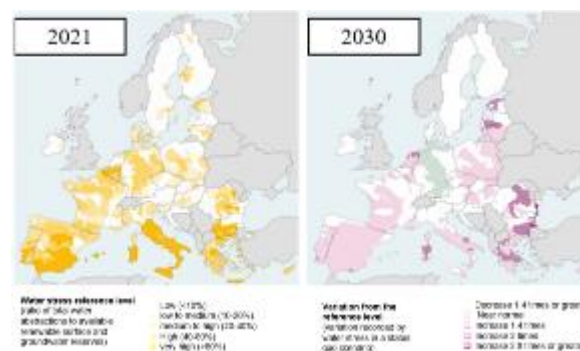
Fig. 4. Water stress in the EU in 2021 and projections for 2030 [6]

Agriculture is closely linked to water availability. Irrigation provides farmers with protection against rainfall variability, promoting increased productivity, yield, and crop quality. However, it also puts significant pressure on water reserves. Research shows that the greatest pressure is generated in Spain (20-40%), followed by France and Bulgaria with 10-20% for surface water. In the case of groundwater, Hungary ranks first with a percentage of more than 40%, followed by Spain and Greece (20-40%). In Romania, there are no water bodies under pressure, but as mentioned above, most of the water collected in our country is used in industry.

Therefore, water is an important resource for life, ecological balance, and economic development, which is why its management must be efficient for the future of our planet. The primary source of fresh water is surface water and groundwater, but their quality and availability are threatened by overuse and poor management.

Forecasts for 2030 highlight the worrying reality that freshwater reserves are declining, and urgent measures are therefore needed to conserve and use this resource sustainably.

Investments in modern technologies can help optimise excessive consumption in agriculture and protect water resources for future generations, which is in line with the principle of sustainable development. Therefore, it is very important that every individual and every government adopt a responsible attitude to ensure a balance between current needs and the protection of this essential resource for life, namely water.

3. Efficient water management in irrigation

Water is an indispensable resource for life, but it is also one of the most vulnerable elements to climate instability. Globally, agriculture uses over 70% of available water (rivers, lakes, groundwater, etc.) Conventional irrigation methods are inefficient and generate high losses, contributing to soil degradation and water resource depletion. In Romania, most of the irrigation systems built during the communist regime have been abandoned or have suffered major damage. Moreover, the lack of functional infrastructure seriously affects agricultural production, especially in the southern and eastern regions of the country.

Water management in irrigation involves the application of practices and technologies designed to reduce water consumption and losses through evaporation, runoff, and uncontrolled infiltration, as well as to improve the efficiency of irrigation systems. Measuring soil moisture and water flow,

rational irrigation scheduling, and the use of modern technologies are important in the development of sustainable and efficient irrigation systems [7].

Irrigation efficiency is a fundamental concept in irrigation engineering, used to characterise irrigation performance, evaluate water use in irrigation, and promote more efficient use of water resources, especially those used in agriculture and green space management [8].

Irrigation efficiency is defined by the following elements:
- irrigation system performance;
- uniformity of water application;
- crop response to irrigation.

Each element of irrigation efficiency can vary in scale and time.

The spatial scale can range from very small units, such as a single irrigation application device (e.g., a siphon tube, pipe valve, sprinkler, or micro-irrigation emitter) to somewhat larger units, such as an irrigation set (a basin plot, a group of furrows, a sprinkler line, or a micro-irrigation lateral). On an even larger scale, it can include extensive areas such as an agricultural field, an entire farm, or an irrigation lateral [8].

3.1. Fog collectors – an alternative water source in arid areas

Climate change poses a major challenge for agriculture. Water resources and crop stability are key priorities in policies to prevent and mitigate extreme events.

Unconventional water resources are considered viable solutions to meet or supplement irrigation water demand in water-scarce regions. Technologies for collecting water from the atmosphere must be efficient, affordable, and stable to ensure long-term irrigation, even in seasons with low rainfall.

Although the quantities of water obtained by methods such as dew collection or condensation are relatively small, they can be a valuable source of water, especially in arid and semi-arid areas where traditional water resources are limited or difficult to access. Condensation irrigation systems rely on atmospheric moisture and are specifically designed for regions with water shortages.

Below are some fog collectors that use atmospheric moisture to irrigate high-value crops, such as vegetables for processing and fresh consumption (peppers, bell peppers, early tomatoes, etc.) or aromatic and medicinal plants (lavender, basil, mint etc.).

3.1.1. How it works

Fog collectors are passive systems, generally constructed from polyethylene or nylon nets, mounted vertically on a support structure (metal or wood). They work by intercepting water droplets from the fog, which condense on the mesh threads, accumulate, and then drain into a collection trough, from which they are directed by gravity to a storage tank [9].

Research suggests that these fog collectors work best in coastal areas, where water can be collected as fog is pushed inland by the wind.

But they can also be adapted to hilly areas, such as the Vrancea region, where frequent fog formation is favoured by low nighttime temperatures, which cause water vapor to condense, as well as by the thermal inversions characteristic of the terrain. These conditions are suitable for the implementation of fog collectors, which can harness atmospheric humidity as an additional source of water for irrigation, especially during periods of water shortage.

A standard fog collector consists of the structural and functional elements shown in Figure 5, each of which plays an important role in the efficiency of the process of water collection from the atmosphere.
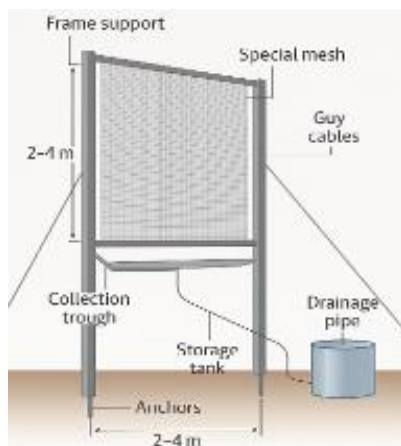
Fig. 5. *Schematic of a standard fog collector*

Support frame – is the basic structure on which the collection net is mounted. It can be made of galvanized metal profiles or treated wood for outdoor use. The dimensions of the frame may vary depending on the needs, but the standard one, shown in Figure 5, has a height between 2 and 4 meters and a width between 2 and 4 meters. The frame ensures the stability of the system in strong wind conditions and positions the net so that it captures fog currents as efficiently as possible.

Special net – generally, the net used in collectors is the Raschel type or other variants of high-density net (HDPE), with 1-2 mm mesh, to easily retain fine water droplets. The surface area of a collector's net varies, depending on the application, between 4 and 8 m2 (for individual or experimental use) and 40 m^2 (for community or agricultural systems).

Collection gutter – mounted at the base of the net, at a slight angle of approximately 5-7° from the horizontal, it collects the water that drains from the net. It is made of PVC, stainless steel, or plastic, all of which is corrosion-resistant, and the width of the gutter can be 10-15 cm.

The drainage pipe, with a diameter of DN32-DN50 mm, transports water from the gutter to the storage tank. In the case of an assembly containing several collectors, these pipes are joined together in a main collector pipe (spine-type system), which descends gravitationally from the slope to the storage tank.

Storage tank – this can be a plastic container approved for water or a semi-buried cistern with a volume of between 200 and 1000 litres/collector, depending on the estimated yield and local needs. For collective networks, larger modular tanks can be used.

Anchors and tension cables – for the safety of the collector in strong wind conditions, the frame is secured with metal anchors or concrete stakes and further stabilized with galvanized steel tension cables anchored in the ground at a distance of 1-2 meters from the base.

Optionally, the collector can be equipped with a simple filtration system (screen or pre-filter at the tank inlet) to prevent contamination with particles or debris from the net, and overflow valves or taps for water collection [9].

Research on fog water harvesting has focused on developing more efficient and durable mesh materials. The standard Raschel mesh (Figure 6 A) recorded a daily average water collection of 1.235 L/m^2 and is considered the benchmark in the field. The Aluminet mesh, made of high-density polyethylene with an aluminium coating, achieved an average of 96% of the volume collected by the Raschel mesh and was preferred due to its good performance at low wind speeds. In areas with very strong winds, such as South Africa, special nets made of polymers woven with stainless steel (Figure 6 B) have been developed, which, although less efficient at collection, offer superior durability and lower maintenance costs, demonstrating that, under certain conditions, the reliability of the material can be more important than maximum efficiency in collecting fog water. Figure 6 C shows another type of material, namely a prototype 3D polymer net – an experimental design that uses a three-dimensional structure to improve fog capture performance [10].
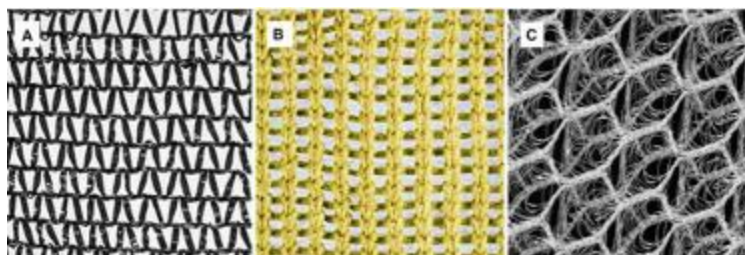
Fig. 6. *Types of mesh for mist catcher: A) Single layer Raschel mesh; B) Stainless steel reinforced poly-yarn mesh; C) 3D polymer mesh prototype*

3.1.2. Optimal operating conditions for fog collectors

The efficient operation of fog collectors largely depends on the climate and terrain of the region where they are installed. The hilly area of Vrancea county, where the Pufești-Ruginești agricultural area analysed in this case study is located, has climatic (fog, wind, etc.) and terrain characteristics that are favourable for the adoption of this technology.

According to data provided by Direcția Silvică Vrancea (the Vrancea Forestry Directorate), the hilly area of Vrancea experiences between 100 and 120 days of fog per year, with a higher incidence during the cold season (autumn, winter, and early spring) [11]. The local microclimate, influenced by the relief and the proximity of forests, maintains a high relative humidity, favouring the formation of fog, especially in depressions and valleys. The fog observed in this area is generally dense and rich in fine water droplets, with an estimated diameter of 0.005-0.05 mm, which is considered optimal for fog collectors [11]. Persistent fog provides an additional supply of water, which is especially useful during dry periods or when precipitation is below average.

Meteorological statistics for the area of interest (Pufești-Ruginești) show that the average wind speed ranges between 1.2 and 3.8 m/s in autumn and spring. These are ideal values for collecting fog with special nets, without significant losses due to strong currents [11].

In the hilly region of Vrancea, there is a marked temperature contrast between day and night, especially in April-May and September-November, which favours condensation and the maintenance of fog during the night and morning.

Taking into account these climatic data (number of days with persistent fog, wind speed etc.), it is estimated that a fog collector with an area of 40 m² installed on a ridge exposed to prevailing winds could collect between 160 and 280 L of water/day during favourable periods. This contribution does not cover the entire irrigation needs for large areas, but it can effectively be used to supplement irrigation in nurseries or to maintain soil moisture during the emergence of the main crops.

The integration of a fog collector in the Pufești-Ruginești agricultural perimeter, as an auxiliary system, can contribute to the diversification of water sources and increase the resilience of local farms to drought. This can reduce pressure on conventional resources and lower the operating costs of the irrigation system.

3.1.3 Maintenance, operation, and costs of fog collectors

Once correctly installed, fog collection systems require simple operation and minimal maintenance, especially if users have been directly involved in the installation. Long-term success depends on a routine maintenance program and quality control of collected water. Some of the activities included in the maintenance program are:

• Periodic checking of cable tension and fasteners to prevent structural damage;

• Inspection and repair of nets, which can be affected by tears or dust accumulation reducing efficiency and affect water quality;

• Cleaning the gutters, screens, and pipes to prevent blockages and biological contamination;

• Sanitizing storage tanks with disinfectant solutions and preventing the entry of insects or other impurities;

• Monitoring the chlorine level in the water as a method of controlling microbiological risks [12].

The installation costs of fog collector systems vary considerably depending on the location, climatic conditions, and technical specifications of the project. For example, in a project carried out in the Antofagasta region of Chile, the installation cost of a fog collector was estimated at approximately 83 EUR/m² of net. In another project in northern Chile, a 40 m² collector had a total cost of around 348 EUR (of which 207 EUR was for materials, 58 EUR for labour, and 36 EUR for contingencies). This system had an average yield of 3.0 L/m²/day [12].

Both capital and operating costs are influenced by several factors, including the efficiency of the

collection system, the length of the pipes, and the volume of the storage tanks. For example, for a system with an efficiency of 2.0 $L/m^2/day$, the unit cost of water production was estimated at 4.40 EUR/1000 L, while an increase in efficiency to 5.0 $L/m^2/day$ would reduce this cost to just 1.75 EUR/1000 L [12].

3.1.4. Application possibilities in Romania

Although Romania does not have microclimates identical to those in desert regions, there are hilly and mountainous areas where fog collectors can be beneficial, such as the sub-Carpathian regions (Vrancea, Buzău, Vâlcea, etc.), mountain depressions (Apuseni, Făgăraș, etc.), or the Black Sea coast (where fog is frequent in winter and spring).

The Pufești-Ruginești area (Vrancea county) has a number of geographical and climatic characteristics that are favourable for the implementation of fog collectors:

• hilly terrain with altitudes ranging from 200 to 500 m,

• frequent fog (estimated at 100 – 120 days/year),

• the orientation of the valleys, which favours the accumulation of moisture-laden air currents and creates a favourable environment for the condensation of water vapor on the surfaces of the collectors.

Based on these factors and analysing the yields observed in international projects, a potential collection of 4 - 7 $L/m^2/day$ is estimated during the active season. Therefore, a system consisting of 40 m2 collectors could provide a constant supply of water to supplement the irrigation system. This can help to reduce pressure on conventional sources and increase the resilience of local agriculture in the face of water shortages.

The role of fog collectors is complementary in mixed irrigation systems. They can supply water for greenhouses and nurseries by feeding buffer tanks in drip systems, or they can partially cover precision watering and replenishment needs during dry periods.

### 3.2. Pilot project: Fog collection system - Pufești-Ruginești area, Vrancea

Considering both the climatic conditions in the Pufești-Ruginești area and the need to supplement water resources for irrigating sensitive crops with added value, a pilot project is proposed to collect water from fog for a 5-hectare plot dedicated to growing peppers, irrigated by drip irrigation.

3.2.1. Estimation of water requirements and collector efficiency

According to specialised studies, in peppers, daily evapotranspiration (ETc) is 4 - 6 mm/day during peak periods, which corresponds to 4 - 6 $L/m^2/day$ in a well-managed system [13]. Therefore, if we estimate an average daily water consumption during the growing season of 5 $L/m^2/day$ for an area of 5 hectares (50.000 m^2), this results in a requirement of 250.000 L/day. Taking into account the estimated values for the efficiency of fog collectors in the analysed area (between 4 and 7 $L/m^2/day$, on average 5.5 $L/m^2/day$), a 40 m^2 panel can collect between 160 and 280 litters daily (average 220 L/day).

To ensure an additional flow of at least 12.500 L/day (representing a minimum contribution of 5% of the total daily requirement), it is proposed to install 80 collectors, each with an area of 40 m^2 (4 m wide and 10 m high), i.e., a collection area of 3.200 m^2. The distance between collectors, both parallel and in line, is 5 m. This space allows for adequate air and fog flow, easy access for maintenance, and structural stability (for anchoring and tensioning).

Taking all this data into account, the total area occupied on the ground by the entire collector system will be approximately 0.5 ha, which can be integrated into the areas adjacent to the plot or on sloping, low-yield land. Figure 7 shows a model layout of fog collectors on the slope of an uncultivated hill.
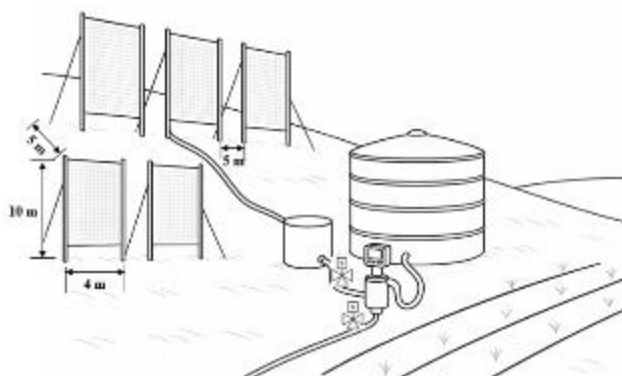
Fig. 7. *Example of fog collector layout on a hill*

The collectors will provide a daily contribution of an estimated flow rate between:
• 12.800 L/day (at a minimum yield of 4 L/m²/day);
• 22.400 L/day (at a maximum yield of 7 L/m²/day).

This amount of water is equivalent to covering 5.1% to 9% of daily needs, thus reducing the pressure on the irrigation network during dry periods. The supply obtained can fully cover the water needs for 0.6 - 1.1 ha of the total soil, reducing water stress during critical periods of plant development.

3.2.2. Estimated implementation costs

The total estimated cost for one collector (purchase + transport + anchoring) is between 400 EUR and 600 EUR, depending on the materials used and the complexity of the installation [12]. For the 80 units proposed:
• Total cost of the collectors: between 32000 EUR and 48000 EUR;
• Additional infrastructure costs are estimated as follows:
o Connection pipes and gutters: 2500 EUR;
o Semi-buried tank (capacity 100 m³): 2000 EUR;
o Labour and installation work: 6000 EUR.

Therefore, the total cost of the pilot project is estimated at 42500 EUR and 58500 EUR, or approximately 530-730 EUR per collector unit installed (including infrastructure).

Even though the initial investment is quite high for a complementary solution, it is offset by savings in water consumption from conventional sources, reduced water stress, and increased productivity in drip-irrigated plots. Furthermore, the lack of operating costs (the collectors are passive) and the high durability of the equipment (over 10 years) result in medium-term amortization (estimated at 4 – 5 years) if the system is correctly integrated into an intensive production chain.

4. Conclusions

The pilot project for the use of fog collectors as a complementary water source, applicable to a 5-hectare plot with a value-added crop, is an additional proposal for improving the irrigation system. The gravity-fed system, with 40 m² vertical panels arranged on a slope and connected to a collection tank, was designed using actual flow and cost calculations and has been shown to provide a significant portion of the water needed for drip irrigation during dry periods, thus reducing dependence on conventional sources.

This article demonstrated that the modernisation of irrigation systems is not only feasible but necessary. The combination of precision technologies with digitization and alternative water sources offers a sustainable solution for adapting agriculture to new climatic conditions. The proposed model can serve as a basis for the regional expansion of smart irrigation systems, contributing both to the resilience of agricultural production and to the sustainable conservation of water resources.

References

[1]. **Zăvoianu I.**, *Râurile- bogăția Terrei (Rivers - the wealth of the Earth)*, Editura Albatros, Colecția Cristal, București, 284 pag., 1998.

[2]. **Ministerul Mediului Apelor şi Pădurilor - Direcția Generală Păduri și Strategii în Silvicultură**, *Raport de mediu: Strategia națională privind prevenirea și combaterea deșertificării și degradării terenurilor (Environmental report: National strategy to prevent and combat desertification and land degradation)*, 2019-2030.

[3]. **Ministerul Mediului**, *Planul Național de Management actualizat (2021) aferent porțiunii naționale a bazinului hidrografic internațional al fluviului Dunărea (Updated National Management Plan (2021) for the national portion of the international river basin of the Danube River)*, 2021.

[4]. **Ministerul Mediului Apelor şi Pădurilor**, *România şi apele subterane (Romania and groundwater)*, martie 2022.

[5]. ***, https://water.europa.eu/freshwater/europe-freshwater/freshwater-themes/water-resources-europe.

[6]. ***, https://www.wri.org/data/aqueduct-water-risk-atlas.

[7]. ***, https://search.app/cJT1bLS2y1oAiYe1A.

[8]. **Howell T. A.**, *Irrigation-Efficiency*, United States Department of Agriculture (USDA), Bushland, Texas, U.S.A, 2003.

[9]. **Regalado C. M., *et al.***, *A bioinspired ladder-like harp fog water collector. II. Construction, simulations and field testing*, Journal of Water Process Engineering, vol. 75, https://doi.org/10.1016/j.jwpe.2025.107902, June 2025.

[10]. **Domen J. K., *et al.***, *Fog water as an alternative and sustainable water resource*, Clean Techonologies and Environmental Policy, 16(2), DOI:10.1007/s10098-013-0645-z, 2013.

[11]. **Direcția Silvică Vrancea**, *Raport de Mediu (Environmental Report)*, 2024.

[12]. ***, https://www.oas.org/usde/publications/unit/oea59e/ch12.htm#TopOfPage.

[13]. **Allen R. G., *et al.***, *Crop evapotranspiration: Guidelines for computing crop water requirements*, FAO Irrigation and Drainage Paper 56, Rome, 1998.

ASPECTS OF DYNAMIC MODELLING OF MOTOR VEHICLES WITH EMPHASIS ON THE INFLUENCE OF THE NONLINEAR CHARACTER OF ELASTIC FORCES IN TYRES

Adrian LEOPA

"Dunarea de Jos" University of Galati, Engineering and Agronomy Faculty of Braila,
Research Centre for Mechanics of Machines and Technological Equipments - MECMET
e-mail: adrian.leopa@ugal.ro

ABSTRACT

The study of oscillatory motions in vehicles is of particular interest from the perspective of improving their dynamic performance. This aspect has been highlighted in the present work by emphasizing the scientific interest that has been identified in the specialized literature, with several representative studies brought to the forefront. The study proceeds with the presentation of a four-degree-of-freedom dynamic model capable of characterizing the oscillatory regime of a vehicle when passing over an obstacle. Based on this dynamic model, the kinematic parameters of the oscillatory motion of a vehicle as it passes over an obstacle were investigated, highlighting the influence of the nonlinear nature of the elastic forces in the tires on these parameters. The conclusions of the study indicate that accounting for the nonlinear characteristics of the tire elastic forces is necessary to achieve a more realistic characterization of the dynamic behavior of the analysed phenomenon; however, for the numerical values considered, the amplitudes of the displacements and velocities of the analysed masses do not differ significantly from those predicted by the linear model.

KEYWORDS: dynamics, vehicles, dynamic modeling, nonlinear elastic forces, obstacle crossing

1. Introduction

The issue of dynamic vehicle modeling during motion has attracted considerable interest in the scientific community, driven by efforts to improve comfort, maneuverability, and stability. In this regard, numerous research studies have extensively addressed this subject, with dynamic models continuously evolving in complexity to more accurately reflect real-world conditions.

In this context, Untaru and Tabacu (1981) proposed various dynamic models for characterizing the oscillatory motion of a vehicle: simple models with one degree of freedom, models with two degrees of freedom, and a more comprehensive four-degree-of-freedom model.

Jazar (2008) provides a classical approach to vehicle dynamics, presenting the general theory of oscillatory motions and emphasizing the fundamental mathematical models used to describe vehicle behavior. His work addresses essential aspects such as suspension modeling, the influence of unsprung masses, and the analysis of lateral stability.

Rajamani (2012) investigates control strategies aimed at improving vehicle dynamic performance, with a focus on advanced stability control and the optimization of tire–road interaction. The study highlights the importance of control algorithms and sensors in ensuring improved maneuverability, while underscoring the necessity of precise modeling of the mechanical systems involved.

Azadi, Vaziri, and Shahhoseini (2010) present a comprehensive model of a vehicle with a flexible body, simulated in MSC.ADAMS and MSC. NASTRAN for directional stability analysis. An optimized control strategy is proposed for the Vehicle Dynamics Control (VDC) system, combined with ABS, in order to maintain wheel slip within optimal limits. The comparative study between rigid and flexible models reveals significant differences in both vehicle dynamics and the control efforts required.

The present study analyses the dynamic behavior of a passenger car as it passes over

obstacles, under the assumption that the vehicle can be modelled as a four-degree-of-freedom system (Fig. 1). Based on this model, vertical and pitch oscillations of the vehicle were studied comparatively, separately considering the cases in which tire elastic forces were modeled as linear or nonlinear.

2. Dynamic modeling of a vehicle passing over an obstacle

The dynamic study addressed in this work is based on the physical and mathematical models presented by Untaru and Tabacu (1981), which describe the vehicle as a rigid system with four degrees of freedom. Although this model includes four degrees of freedom, it introduces the assumption that the wheels of the same axle traverse an obstacle on the road surface simultaneously. In other words, the system is perturbed only when passing over obstacles whose length is at least equal to the width of the vehicle (Figure 1).

The mathematical model (Untaru & Tabacu, 1981) is a system of four second-order differential equations, given in equation (1).
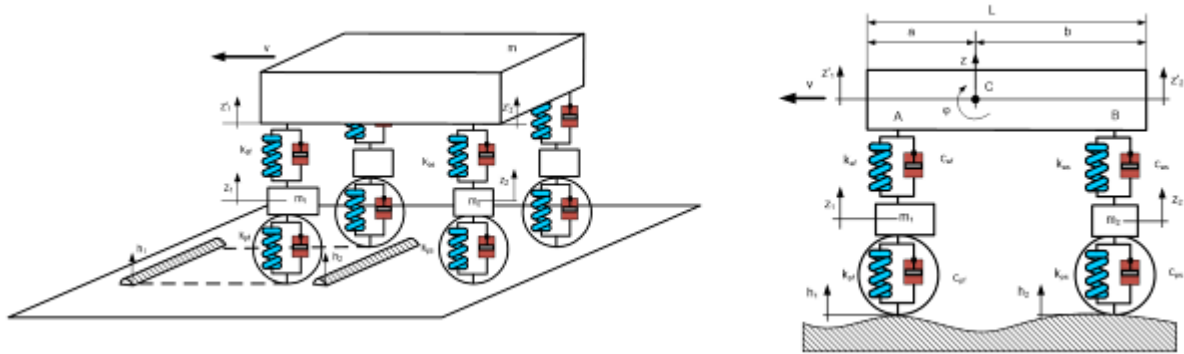

Fig. 1. Physical model of vehicle with four degrees of freedom

$$\begin{cases} m \cdot \ddot{z} + c_{af} \cdot (\dot{z}'_1 - \dot{z}_1) + c_{as}(\dot{z}'_2 - \dot{z}_2) + k_{af}(z'_1 - z_1) + k_{as}(z'_2 - z_2) = 0 \\ m \cdot \rho^2 \cdot \ddot{\varphi} + a \cdot c_{af} \cdot (\dot{z}'_1 - \dot{z}_1) - b \cdot c_{as}(\dot{z}'_2 - \dot{z}_2) + a \cdot k_{af}(z'_1 - z_1) - b \cdot k_{as}(z'_2 - z_2) = 0 \\ m_1 \cdot \ddot{z}_1 + c_{af} \cdot (\dot{z}'_1 - \dot{z}_1) - k_{af}(z'_1 - z_1) + c_{pf}(\dot{z}_1 - \dot{h}_1) + F_{nzf}) = 0 \\ m_2 \cdot \ddot{z}_2 - c_{as} \cdot (\dot{z}'_2 - \dot{z}_2) - k_{as}(z'_2 - z_2) + c_{ps}(\dot{z}_2 - \dot{h}_2) + F_{nzs}) = 0 \end{cases} \tag{1}$$

where the following notations are used:

m – suspended mass of the vehicle;

m_1, m_2 – unsprung masses at the front and rear, respectively;

z_1, z_2 – vertical displacements of the front (m_1) and rear (m_2) unsprung masses, respectively;

k_{af} – equivalent stiffness constant of the front axle springs;

k_{as} – equivalent stiffness constant of the rear axle springs;

k_{pf} – equivalent stiffness constant of the front axle tires;

k_{ps} – equivalent stiffness constant of the rear axle tires;

c_{af} – equivalent damping coefficient of the front axle springs;

c_{as} – equivalent damping coefficient of the rear axle springs;

c_{pf} – equivalent damping coefficient of the front axle tires;

c_{ps} – equivalent damping coefficient of the rear axle tires;

h_1, h_2 – heights of the road surface irregularities;

h – amplitude of the irregularities;

z_a, z_p – vertical displacements of the masses m_1 and m_2;

z'_a, z'_p – vertical displacements of points A and B;

z – displacement of mass m;

φ – angular displacement of the suspended mass;

a – distance from the centre of gravity to the front axle;

b – distance from the centre of gravity to the rear axle;

F_{nzf} – front axle nonlinear tire force;

F_{nzs} – rear axle nonlinear tire force.

and

$$F_{nz}f = k_{2f}(z_1 - h_1)$$

$$F_{nz}s = k_{2s}(z_2 - h_2)$$

where:

k_{2f} – nonlinear stiffness coefficient of the front tire;

k_{2s} – nonlinear stiffness coefficient of the rear tire.

In the monograph by Jazar (2008), for the case of nonlinear elastic forces arising from tire deformation, it is assumed that this force is the superposition of two components, static and dynamic, as expressed in equation (2).

$$F_{nz} = F_{nzs} + F_{nzd} \qquad (2)$$

where:

F_{nz} – nonlinear elastic force due to vertical deformation z of the tires;

F_{nzs} – static component of the nonlinear elastic force;

F_{nzd} – dynamic component of the nonlinear elastic force.

For the model under consideration, the static and dynamic components of the nonlinear elastic tire force may be written analytically as shown in equations (3) and (4).

$$
\begin{aligned}
F_{nzf} &= F_{nzsf} + F_{nzdf} \\
F_{nzsf} &= k_{1pfn} \cdot (z_1 - h_1) + k_{2pfn} \cdot (z_1 - h_1)^2 \\
F_{nzdf} &= k_{3pfn} \cdot (\dot{z}_1 - \dot{h}_1) \\
F_{nzf} &= k_{1pfn} \cdot (z_1 - h_1) + k_{2pfn} \cdot (z_1 - h_1)^2 + k_{3pfn} \cdot (\dot{z}_1 - \dot{h}_1)
\end{aligned}
\qquad (3)
$$

$$
\begin{aligned}
F_{nzs} &= F_{nzss} + F_{nzds} \\
F_{nzss} &= k_{1psn} \cdot (z_2 - h_2) + k_{2psn} \cdot (z_2 - h_2)^2 \\
F_{nzds} &= k_{3psn} \cdot (\dot{z}_2 - \dot{h}_2) \\
F_{nzs} &= k_{1psn} \cdot (z_2 - h_2) + k_{2psn} \cdot (z_2 - h_2)^2 + k_{3psn} \cdot (\dot{z}_2 - \dot{h}_2)
\end{aligned}
\qquad (4)
$$

where:

F_{nzd} – static elastic force of nonlinear type in vertical direction for the tires of both axles;

F_{nzsf} – nonlinear static elastic force in the vertical direction for the front axle tires;

F_{nzsf} – nonlinear static elastic force in the vertical direction for the rear axle tires;

F_{nzsf} – nonlinear dynamic elastic force in the vertical direction for the front axle tires;

F_{nzds} – vertical direction nonlinear dynamic elastic force for rear axle tires;

k_{1pfn} – coefficient of nonlinear equivalent stiffness for front axle tires;

k_{1psn} – coefficient of nonlinear equivalent stiffness for rear axle tires;

k_{2pfn} – quadratic nonlinear equivalent stiffness coefficient of the front axle tires;

k_{2psn} – quadratic nonlinear equivalent stiffness coefficient of the rear axle tires;

k_{3pfn} – the equivalent stiffness coefficient for the dynamic component of the front axle tires;

k_{3psn} – the equivalent stiffness coefficient for the dynamic component of the rear axle tires.

According to the previously presented relations, the system of differential equations (1), which characterizes the considered physical model, can be written in the following form:

$$
\begin{cases}
m \cdot \ddot{z} + c_{1f} \cdot (\dot{z}'_1 - \dot{z}_1) + c_{1s}(\dot{z}'_2 - \dot{z}_2) + F_{nz} = 0 \\
m \cdot \rho^2 \cdot \ddot{\varphi} + a \cdot c_{1f} \cdot (\dot{z}'_1 - \dot{z}_1) - b \cdot c_{1s}(\dot{z}'_2 - \dot{z}_2) + a \cdot F_{nzsf} - b \cdot F_{nzss} = 0 \\
m_1 \cdot \ddot{z}_1 + c_{1f} \cdot (\dot{z}'_1 - \dot{z}_1) - F_{nzsf} + c_{2f}(\dot{z}_1 - \dot{h}_1) + k_{2f}(z_1 - h_1) = 0 \\
m_2 \cdot \ddot{z}_2 - c_{1s} \cdot (\dot{z}'_2 - \dot{z}_2) - F_{nzss} + c_{2s}(\dot{z}_2 - \dot{h}_2) + k_{2s}(z_2 - h_2) = 0
\end{cases}
\qquad (5)
$$

In classical dynamic models, the nonlinear elastic forces generated by tire deformation were often neglected to simplify the solution of systems of differential equations, due to limited computational resources. However, this simplification does not fully represent reality, as tires dissipate part of the energy resulting from deformation as heat.

3. Effect of Nonlinear Elastic Forces Tire

For the theoretical investigation of the influence of tire nonlinear behavior, it was assumed that the vehicle passes over an obstacle such as the one shown in Figure 1, at a speed of 50 km/h. Under this assumption, the dynamic excitation produced by the obstacle was modeled as a sinusoidal function (Figure 2).
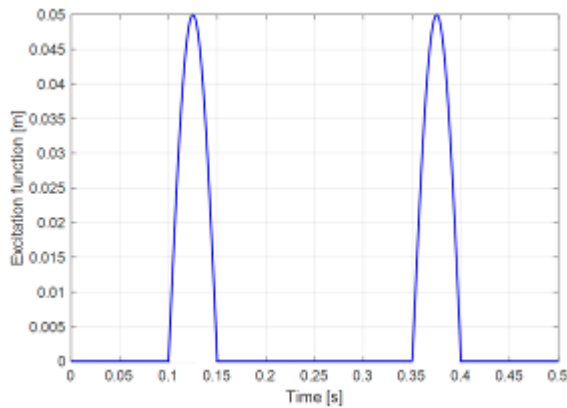
Fig. 2. Excitation function

The solution of the system of differential equations was carried out using the numerical values from Table 1, corresponding to a road vehicle of category M1 The solution of the system of differential equations was carried out with the numerical values listed in Table 1, corresponding to a category M1 road vehicle.

Table 1. *Numerical values of geometric, mass, and rheological parameters*

m, m_1, m_2	1500 kg, 70 kg, 70 kg
$k_{af}, k_{as}, k_{pf}, k_{ps}$	$25 \cdot 10^3$ N/m, $20 \cdot 10^3$ N/m, $200 \cdot 10^3$ N/m, $150 \cdot 10^3$ N/m
k_{1pfn}, k_{1psn} k_{2pfn}, k_{2pfn} k_{3psn}, k_{3pfn}	200000, 150000, N/m 100000, 80000, N/m² 50000, 40000 Ns/m
$c_{af}, c_{as}, c_{pf}, c_{ps}$	2000 Ns/m, 2500 Ns/m, 2500 Ns/m, 2500 Ns/m
h_1, h_2	$h_1 = h \cdot \sin(\omega \cdot t)$ m, h=0,1 m, ω=62,8 rad/s $h_2 = h \cdot \sin(\omega \cdot t)$ m, ω=62,8 rad/s
a, b	1.07 m, 1.61 m

Using these numerical values, the system of second-order differential equations was solved in MATLAB R2021b, obtaining graphical representations of the kinematic parameters of the vehicle's oscillatory motion for two scenarios:
• the elastic forces resulting from tire deformation are linear;
• the elastic forces resulting from tire deformation are nonlinear.

For ease of highlighting the differences between the two cases, the graphs of the analysed parameters have been presented in parallel.

4. Interpretation of the Results

For the masses m, m_1, and m_2, the variations of displacements and velocities were graphically represented in both the time and frequency domains, as well as in the phase plane, Figures 3-9.

In the time domain, the displacements and velocities of the suspended mass exhibit similar values for both models. The maximum oscillation amplitudes are not significantly affected by the inclusion of nonlinear terms in the tire model. In the phase plane, the resulting trajectories are nearly identical, reflecting system stability and the predominantly linear nature of the vehicle body's response.

The spectral representations of the displacement indicate a clearly defined dominant frequency, without significant harmonics appearing in the nonlinear model. This suggests that, at the body level, the nonlinear characteristics of the tire forces have a limited effect under moderate dynamic conditions.

In both models, the trajectories of the suspended mass in the phase plane are elliptical and well-defined, indicating stable and lightly damped oscillations, characteristic of quasi-harmonic response systems. The differences between the linear and nonlinear trajectories are negligible, confirming the minor influence of tire nonlinearities on the vehicle body under the simulated conditions.
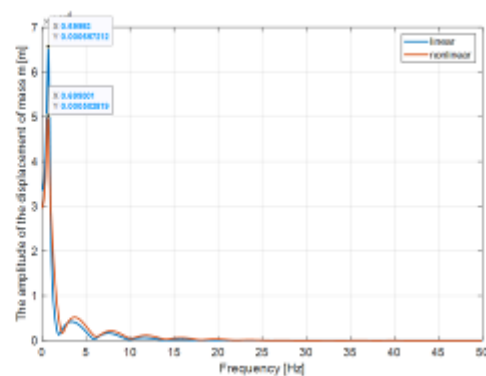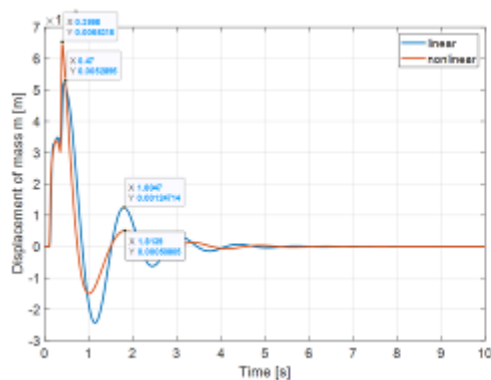
Fig. 3. Displacement of mass m [m]: left – linear; right nonlinear
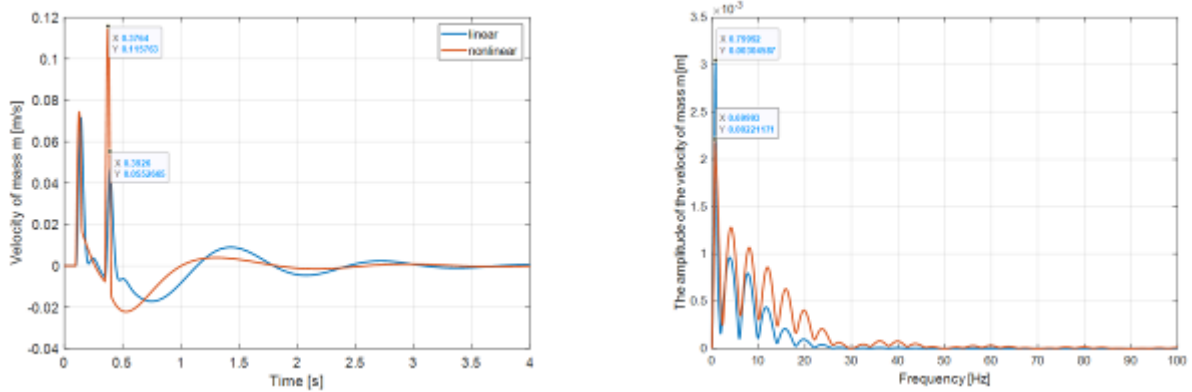
Fig. 4. *Velocity of mass m [m/s]: left – linear; right - nonlinear*
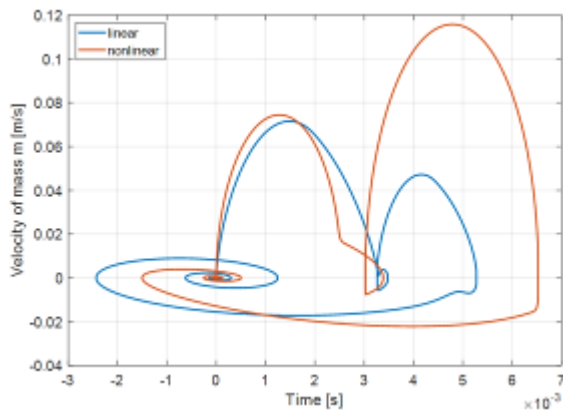

Fig. 5. *Motion of mass m in the phase plane*

The front unsprung mass exhibits larger oscillations, being directly influenced by contact with surface irregularities and the rheological characteristics of the tires. In the case of nonlinear modeling, a slight attenuation of the peak amplitudes is observed, reflecting the capacity of the quadratic and dynamic terms to introduce additional energy dissipation.

The phase plane shows a slight dispersion of the trajectory in the nonlinear case, indicating more complex behavior with slightly increased variability in kinetic energy. The frequency spectrum reveals, in addition to the fundamental frequency, the appearance of higher-order harmonics in the nonlinear model, characteristic of the higher-order nonlinear effects of the tire–road system.

For mass m_1, the trajectories in the phase plane are wider and more asymmetric, reflecting more complex dynamic behavior. In the nonlinear model, a slight thickening of the trajectory is observed, signalling the presence of additional frequency components and an irregular damping effect. This phenomenon indicates a possible transition from harmonic oscillations to responses with multiple frequency content, typical of nonlinear systems.
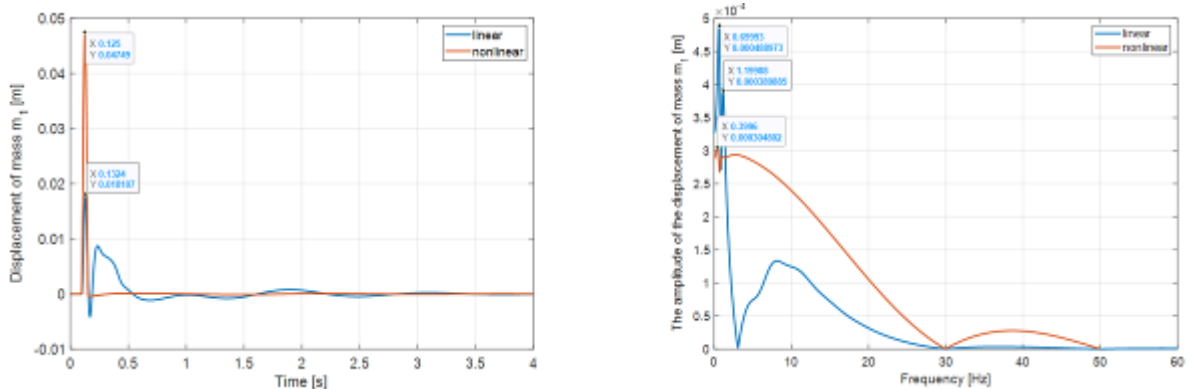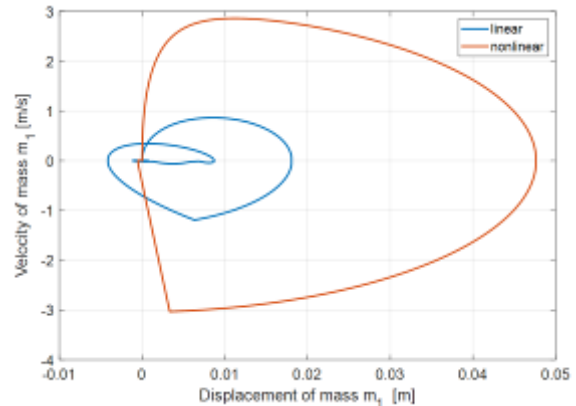

Fig. 6. *Displacement of mass m_1 [m]*

The behavior of the rear unsprung mass is similar to that of mass m_1, but with slightly smaller amplitudes due to the lower stiffness constants of the rear axle. A slight modification of the oscillation profile is observed in the nonlinear model, indicating a more damped response during the initial phase of motion.

The phase-plane trajectories are more dispersed in the nonlinear model, particularly in the transient regime, suggesting more efficient energy dissipation. The frequency spectrum of the displacement of mass m_2 shows a slightly broader energy distribution in the nonlinear case, confirming the influence of the quadratic terms on the response spectrum.

Like mass m_1, the phase-plane trajectories of mass m_2 are slightly more dispersed in the nonlinear model, with a noticeable tendency for the curves to close more rapidly due to a better-damped response. This behavior confirms the role of different rheological coefficients on the rear axle and highlights the influence of nonlinearities in dissipating mechanical energy at the tire–bump contact.

Fig. 7. *Motion of mass m_1 in the phase plane [m/s]*
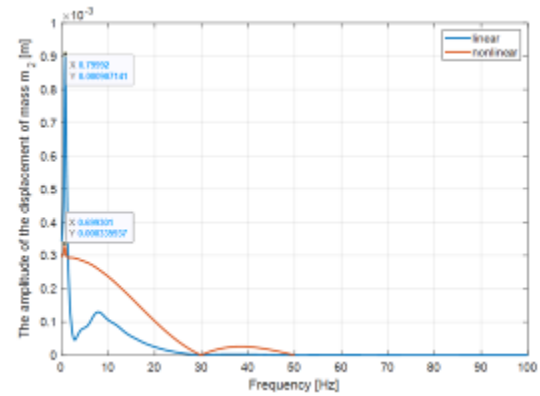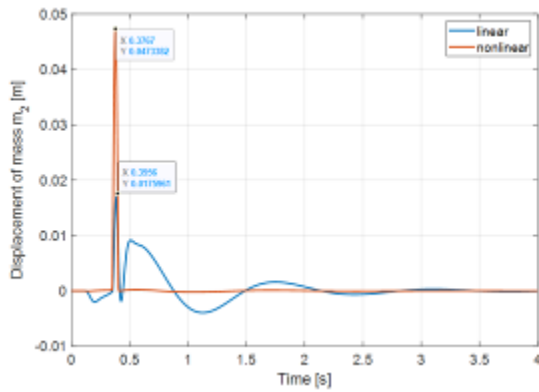
Fig. 8. *Displacement of mass m_2 [m]*
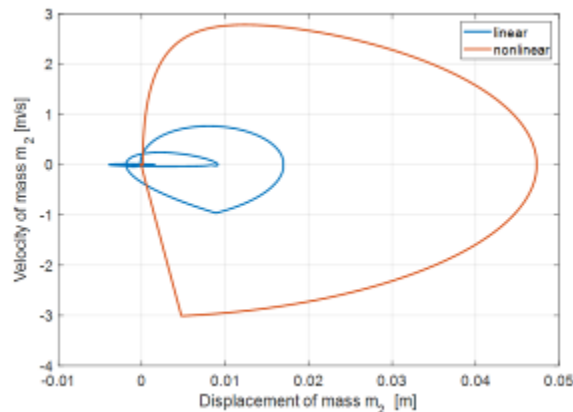
Fig. 9. *Motion of mass m_2 in the phase plane*

5. Conclusions

The present study analysed the oscillatory behavior of vehicle passing over road irregularities, using a four-degree-of-freedom model that considers both the sprung and unsprung components. The focus was placed on the influence of the nonlinear elastic forces developed by the tires compared to the classical linear model.

The results show that, under the simulated conditions, the amplitudes of the displacements and velocities of the analysed masses do not differ significantly between the two models. Nevertheless, nonlinear modeling is essential for realistically

describing vehicle behavior under demanding dynamic conditions, where internal damping and energy dissipation effects become significant.

Moreover, the nonlinear formulation of the elastic forces allows for a natural extension of the study to transient simulations, testing advanced active suspension control strategies, as well as integrating complex tire–road interaction models.

As directions for future research, the development of a full spatial vehicle model is proposed, incorporating lateral and roll effects, as well as validating the theoretical model through experimental tests using sensors mounted on real vehicles, to correlate simulated results with real-world data.

References

[1]. **Untaru M.,** *et al.*, *Dinamica autovehiculelor pe roţi*, Bucureşti, Editura Didactică şi Pedagogică, 1981.

[2]. **Jazar R. N.**, *Vehicle dynamics: Theory and applications*, New York, NY: Springer, https://doi.org/10.1007/978-0-387-74244-1, 2008.

[3]. **Rajamani R.**, *Vehicle dynamics and control (2nd ed.)*, New York, Springer, Available at: https://ftp.idu.ac.id/wp-content/uploads/ebook/tdg/TERRAMECHANICS%20AND%20MOBILITY/epdf.pub_vehicle-dynamics-and-control-2nd-edition.pdf, 2012.

[4]. **Azadi S.,** *et al.*, *Vehicle dynamic control of a passenger car applying flexible body model*, Vehicle System Dynamics, 48(5), p. 613-632, https://doi.org/10.1080/00423110902974092, 2010.

[5]. **Azadi S.,** *et al.*, *Chapter 2 - Vehicle dynamics control using a flexible body model*, Elsevier, p. 29-75, https://doi.org/10.1016/B978-0-323-85659-1.00005-7, 2021.

[6]. Ghinea M., Fireteanu V., *MATLAB: Calcul numeric, grafică, aplicaţii*, Bucureşti: Editura Teora, 1999.

AIR EMISSIONS AND ENVIRONMENTAL CHALLENGES IN THE ENERGY INDUSTRY: A REVIEW

Nicoleta CIOBOTARU

"Dunarea de Jos" University of Galati, Faculty of Engineering and Agronomy,
Calarasi Street, 29, RO-810017, Braila, Romania
e-mail: nicoleta.ciobotaru@ugal.ro

ABSTRACT

The global energy sector, owing to the high complexity of its installations, technological processes, and the waste streams it generates, has a profound and multifaceted impact on the environment. Electric power generation influences ecosystems, alters local microclimatic conditions, and poses risks to human health. Conventional thermal energy production based on fossil fuels remains the most polluting source, whereas renewable energy technologies and nuclear power generally exhibit lower environmental footprints, though they may still involve indirect or long-term ecological effects. Pollutants originating from the energy sector contribute to the degradation of air, soil, and water quality, as well as to climate change and broader ecological imbalances. Patterns of energy production and consumption differ significantly among countries, reflecting disparities in resource availability, geographic characteristics, and policy frameworks. Despite the accelerating deployment of renewable energy, fossil fuels continue to dominate the energy mix in many regions of the world.

KEYWORDS: *energy industry, pollution, climate change, fossil fuels, combustion*

1. Introduction

In recent decades, environmental issues have become increasingly severe and urgent. Pollution, climate change, soil degradation, and biodiversity loss are among the most pressing challenges facing our planet today [1]. Nevertheless, there is hope in technological innovations that can contribute to environmental remediation and the mitigation of these adverse effects [2].

One of the most critical environmental challenges is air pollution. Industrial emissions, transportation activities, and the combustion of fossil fuels constitute some of the major sources of atmospheric contaminants. To address this issue, a wide range of innovative technologies has been developed, including air filtration systems, air purifiers, and air quality monitoring networks [3]. These technologies facilitate the removal of particulate pollutants from the atmosphere and enable the measurement and tracking of pollution levels to identify the primary sources of emissions.

Addressing environmental challenges is a shared responsibility. Nevertheless, technological innovation can play a pivotal role in accelerating environmental remediation and reducing pollutant emissions. It is therefore essential to continue developing and implementing advanced environmental technologies in order to protect natural ecosystems and ensure a sustainable future for future generations [4].

Anthropogenic sources of pollution are more numerous and emit more concentrated pollutants than natural sources, while also undergoing continuous development - thus representing a significant ecological threat that must not be overlooked [5]. Unfortunately, there are still many polluting industrial plants operating with obsolete technologies, often situated in areas lacking favourable meteorological or topographical conditions that would support natural self-purification [6]. Figure 1 schematically presents various technological systems characterized by different levels of environmental impact, classified as follows [7]:

- Polluting plants with outdated technology, which fall under the Passive type of ecological approach, where pollution is largely ignored;
- Plants that take into account atmospheric protection through measures such as land-use

planning, meteorological and topographical studies, and the dilution–dispersion principle, generally categorized as Reactive type systems.
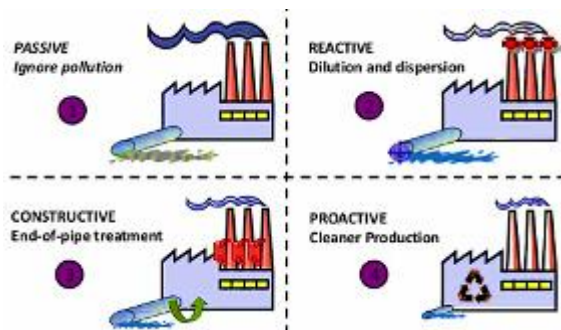
Fig. 1. *Technologies with different types of environmental impact* [7]

Product design under the motto "cleaner production" can be approached in two main ways from the perspective of material selection based on ecological criteria [8], namely:

- The "reactive" approach, which applies end-of-pipe technologies and provides solutions for transforming pollutants generated during the production process into less harmful forms. This type of approach does not actually reduce the number of pollutants but rather converts or even increases it in certain cases.

- The "preventive" approach, which involves modifying the production process itself so that pollution is minimized from the very beginning. The preventive strategy seeks to eliminate the causes of pollution at the source through practical measures such as product redesign or technological modifications.

2. Energy Sources and Impact

Regarding air pollution originating from industrial activities, the categories of materials that can act as pollutants include [9]:

- Raw materials (e.g., coal, minerals, etc.);
- Impurities in raw materials (e.g., sulphur, arsenic, lead, mercury, fluorine, etc.);
- Intermediate substances, generated at specific stages of the technological process (e.g., SO_2 in the sulfuric acid industry, carbon disulfide (CS_2), hydrocarbons in the petrochemical industry, etc.);
- Final products (e.g., cement, carbon black, chlorine, nitric acid (HNO_3), sulfuric acid (H_2SO_4), etc.).

At the global level, the energy sector, due to the complexity of its installations and technological processes, the characteristics of the raw materials involved, and the waste generated, as well as the number and extent of land areas occupied, is one of the most significant industrial sectors, with a major environmental impact [10, 11]. Electric power generation is not a technologically efficient process [11], particularly when environmental impact considerations are taken into account. Consequently, any method of electricity production involves a varying degree of environmental burden.

Hydropower developments, during their operational phase, cause localized modifications of the microclimate, affecting both flora and fauna [12]. However, a major disruption of ecosystems occurs primarily during the construction phase of hydropower projects [13]. Deforestation, large-scale excavations, and dam construction produce substantial environmental impacts that affect all environmental components [12, 13]. Nevertheless, modern hydropower turbines can convert up to 90% of the available energy into electricity, whereas even the most efficient fossil fuel-based installations achieve an efficiency of only 50% [14].

At nuclear power plants, radioactive pollution is minimal, typically not exceeding the natural background radiation [11]. Nevertheless, this type of facility carries the risk of major radioactive contamination, as the devastating effects of potential accidents can affect large areas [15]. Therefore, all possible measures must be implemented to ensure the safe operation of nuclear reactors. Another perspective on nuclear energy, in terms of its potential pollution, concerns the entire technological chain, from nuclear fuel extraction to radioactive waste disposal [16]. Even under these conditions, nuclear energy remains far less polluting and safer than conventional thermal power generation [17].

Electricity generation from wind or solar installations is considered clean technologies. However, changes in airflow distribution and evaporation volumes, with subsequent effects on the local microclimate, cannot be neglected [11]. Additionally, it may be of interest to analyse the pollution associated with the production of electricity required for the construction of unconventional installations, particularly since almost all materials used are energy-intensive.

The exploitation of geothermal resources (dry and hot rocks) remains prohibitively expensive at present. Biomass incineration (municipal and industrial solid waste) emits harmful substances, as many of these residues are toxic [18]. Due to the high moisture content and low calorific value of biomass, combustion typically requires a support fuel, which can also be used for ignition [19].

The last category refers to conventional thermal power generation, based on the combustion of fossil fuels, which has a major impact on all environmental components. The environmental burden arises not

only from the combustion process itself but also from all associated processes, including extraction and waste storage. It is also noteworthy that this highly polluting process accounts for a substantial share of the total energy produced globally. Consequently, fossil fuel combustion processes worldwide generate the following pollutants, with quantities expressed as a percentage of the total anthropogenic emissions within each pollutant category [11]: Sulphur oxides (SOx): 90%, Carbon monoxide (CO): 30–50%, Suspended particulate matter: 40%, Volatile organic compounds (VOCs): 55%, Methane (CH_4): 15-40%, Carbon dioxide (CO_2): 55–80%. In addition, other pollutants are released in varying proportions [11], including nitrogen oxides (NOx), hydrogen sulphide (H_2S), arsenic (As), fluorides (F_2), phenols, hydrocarbons, aldehydes, ketones, inorganic and organic acids, among others.
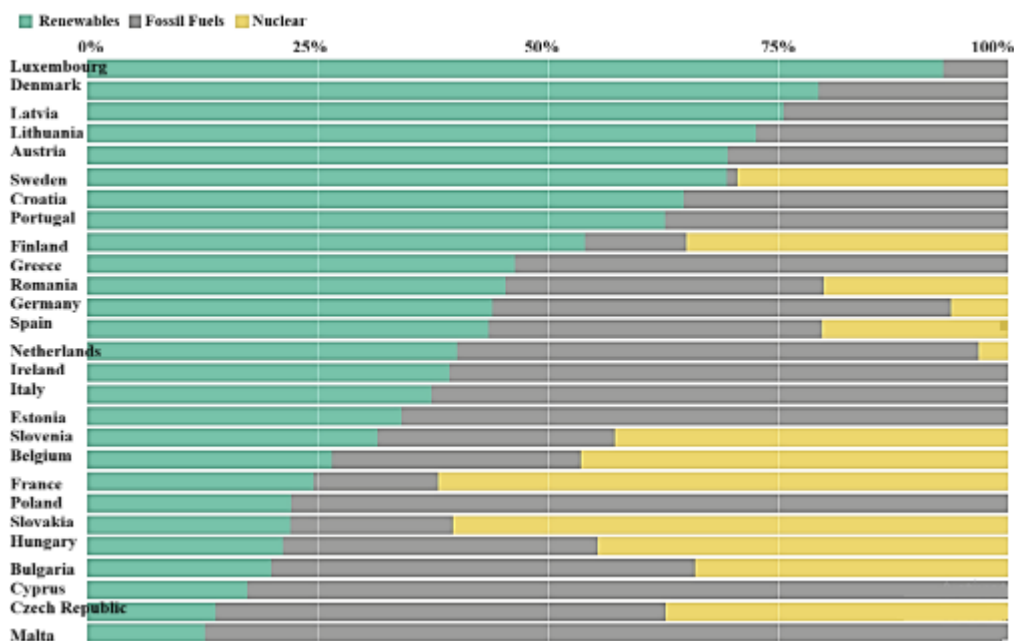
***Fig. 2.** Electricity production in European countries (2022)* [21]

3. Proportion of Thermal Energy in Romania and Globally

The share of electricity consumption in each country varies depending on [20]: geographical conditions, availability of natural resources (coal or gas deposits), economic structure and political decisions (such as whether to develop nuclear power generation capacity). In 2022, the European Union (EU) produced 2,641 TWh of electricity, distributed as follows [21] (Figure 2):

- Approximately 40% - renewable energy sources;
- Fossil fuels accounted for 38.6%;
- Nuclear power contributed more than 20%.

Among fossil fuels, natural gas was the primary source for electricity generation (19.6%), followed by coal (15.8%) [21]. Figure 3 shows the net electricity production in the EU by fuel type in 2022. Data over the past 20 years indicate that the share of renewables in electricity production has increased from 20% to over 45% (Figure 4). Consequently, in the last 2–3 years, within Europe, several countries such as

Poland, Estonia, Italy, and Greece still lack nuclear power generation capacity, and renewable energy sources do not yet represent a significant share. In these countries, fossil fuel combustion remains the predominant method of electricity generation.
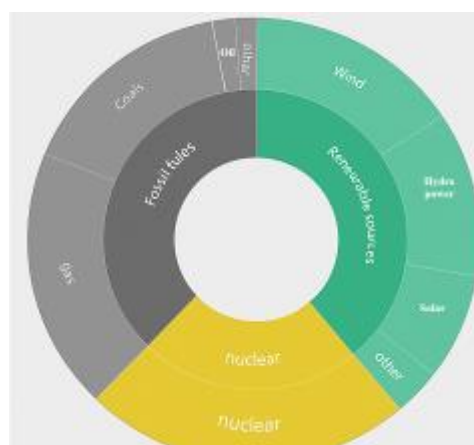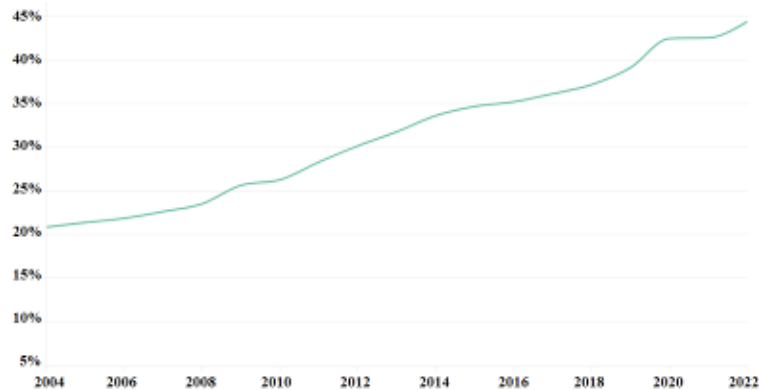

***Fig. 3.** Net electricity production in the EU by fuel type (2022)* [21]

In Romania, renewable energy sources have experienced significant growth; however, the thermal power industry still accounts for approximately half of electricity production in winter (Figure 5) and about one-third in autumn (Figure 6).

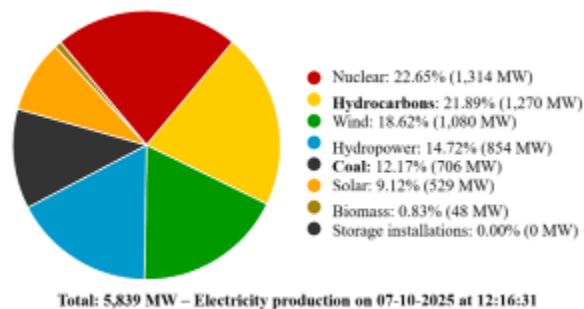Electricity production and consumption in Romania over a single day in January 2025 [22] show that, out of a total production exceeding 6,600 MW, more than 3,000 MW are generated by hydrocarbons (yellow line) and coal (black middle line) — i.e., fossil fuels. Nuclear power contributes approximately 1,400 MW, and hydropower provides over 1,500 MW. Other sources, including wind, solar, and biomass, account for approximately 600 MW.

Fig. 4. *Share of renewable energy in electricity production in the EU (2004–2022)* [21]
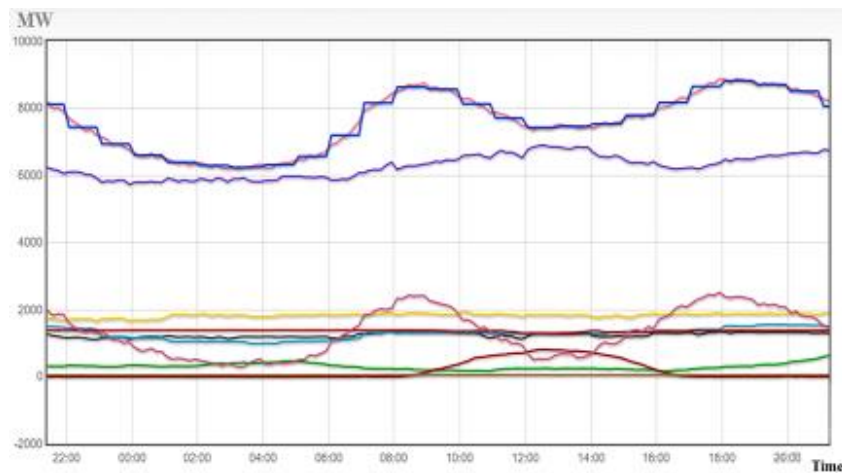
Fig. 5. *Electricity production and consumption in Romania in January 2025* [22]*:* ■ *Consumption: 8342 MW* ■ *Hourly average consumption: 8504 MW* ■ *Production: 6668 MW* ■ *Coil: 1297 MW* ■ *Hydrocarbons: 1855 MW* ■ *Hydropower: 1534 MW* ■ *Nuclear: 1380 MW* ■ *Wind: 545 MW* ■ *Solar: -2 MW* ■ *Biomass: 56 MW* ■ *Sold: 1674 MW*

Fig. 6. *Electricity production and consumption in Romania in October 2025* [22]

Thermal power plants therefore produce approximately 80% of the global electricity demand, relying on fossil fuels (solid, liquid, or gaseous) [9].

4. Key Gaseous Emissions in Thermal Power Generation

The pollution resulting from combustion is closely linked to the composition of the fuel [23]. In the case of complete combustion, the resulting particulate pollutants consist primarily of ash.

In high-rank coals, ash content ranges from 5-10%, whereas in low-rank coals it reaches 40-50%, representing one of the quantitative criteria for assessing coal quality; the higher the ash content, the lower the calorific value, and the greater the amount of coal required to achieve the same energy output [23]. This not only contributes to atmospheric pollution but also interrupts the carbon cycle by halting the natural carbonization process [9]. In the case of incomplete coal combustion, the emitted gases are rich in ash, soot, and unburned coal particles [24]. The largest quantity of soot is released during the initial ignition phase, when not all the fuel has reached the combustion temperature ($\sim$750 °C) [9]. Therefore, interruptions in operation and temperature fluctuations during combustion are undesirable, both from an environmental and economic perspective [23, 24]. Accordingly, it is recommended that fast-igniting fuels (e.g., natural gas or petroleum products) be used at boiler start-up, as they burn without producing soot, so that once the system reaches normal operating temperature, coal can be introduced [9].

4.1. Carbon-Based Compounds

Carbon oxides (CO and CO_2) are produced during the combustion of carbon, from any type of fuel. Incomplete combustion of carbon (in the presence of insufficient air), which produces CO, has the following disadvantages: it releases approximately 3.5 times less heat than complete combustion and generates a toxic gas [25]. The higher the CO_2/CO ratio, the better the combustion efficiency [26]. In modern installations, the CO_2/CO ratio is continuously monitored, and by adjusting the fuel-to-air ratio, the CO concentration is reduced to near zero. In cities with developed industry, CO_2 concentrations, expressed as a volume percentage, range between 0.03–0.05% [27]. While this level is not significant from a toxicological perspective, it is important in terms of indoor air quality deterioration and intensifying the greenhouse effect on a global scale [27].

Table 1 compares the various amounts of major pollutants released into the atmosphere by different technological sources with those produced naturally within their respective cycles. It has been observed that for carbon, sulphur, and nitrogen derivatives, human activity is significantly altering their circulation rates in the biosphere. In fact, the magnitude of anthropogenic H_2S, SO_2, and sulphate (aerosol) emissions is comparable to that released naturally through biogeochemical processes (113×10^6 t/year versus 130×10^6 t/year). A similar situation is observed for carbon, due to excessive fossil fuel consumption.

Table 1. Comparison between the amounts of gaseous substances produced by humans and those released into the atmosphere through natural biogeochemical processes [9]

Compound	Quantities Produced (x 10^6 tonnes/year)	
	of natural origin	of industrial origin
O_2	$1.8 \cdot 10^3$	small
CO_2	$7.2 \cdot 10^4$	$1.95 \cdot 10^4$
CO	>70	>$3 \cdot 10^2$
H_2O	$4.5 \cdot 10^8$	$1.5 \cdot 10^3$
Sulfur Compounds	130	113
Nitrogen Compounds	1400	<93

The carbon cycle (Figure 7) is one of the most efficient biogeochemical cycles, due to the rapid rate at which carbon circulates among inorganic reservoirs and within the living community, through trophic chains. The carbon cycle operates on a timescale of approximately 300 years, and human activity has disrupted this cycle, primarily through the increasing consumption of fossil fuels [28], which enriches the atmosphere with CO_2 (Figure 7). It has been calculated that fossil fuels are consumed thousands of

times faster than the rate at which carbon naturally fossilizes [30].
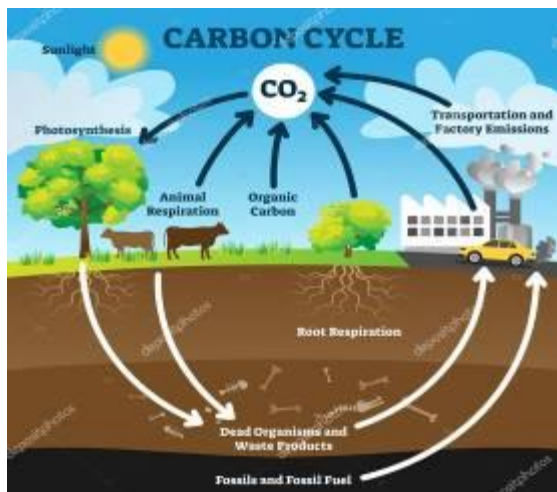
***Fig. 7.*** *The Carbon Cycle* [29]

Data from Table 2 present a comparison of the quantities of CO_2 circulating in the biosphere from different sources. Analysis of these data shows that CO_2 consumed through photosynthesis is lower than the quantities released into the atmosphere through respiration, fermentation, combustion, and deforestation, resulting in a continuous increase in atmospheric CO_2 levels. Vegetal biomass also acts as a balancing factor, consuming a significant portion of CO_2 via photosynthesis. Human-driven deforestation of tropical areas results in increased atmospheric CO_2, which is no longer absorbed through photosynthesis, while a considerable amount of dead organic matter is introduced into the soil. The oceanic reservoir plays a crucial role in regulating the cycle by dissolving CO_2 from the air and transferring it to the ocean floor as sediments in deep layers. Experiments indicate that only 49% of the CO_2 produced through combustion since 1950 has been deposited in the deep ocean layers [28]. Therefore, as fossil fuel use and accelerated exploitation of forest ecosystems continue, the atmospheric concentration of CO_2 is steadily increasing, which in turn enhances the greenhouse effect [30].
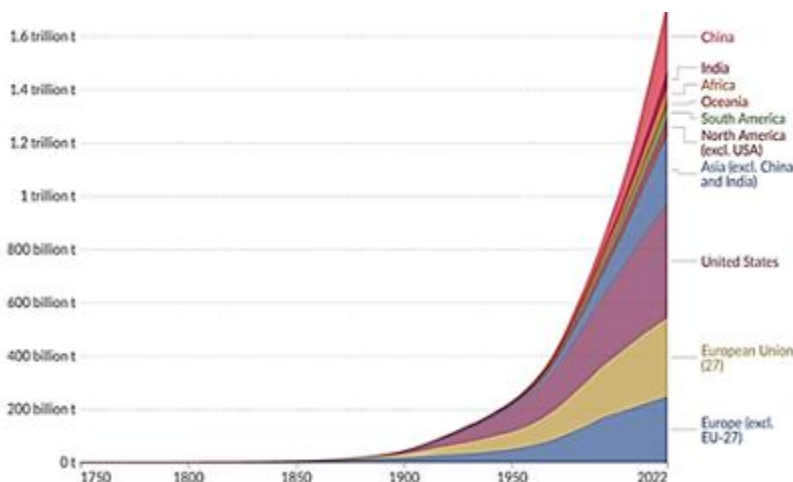
The global distribution of CO_2 emissions from industrial sources shows a concentration in the heavily industrialized Northern Hemisphere, with major contributors including China and the USA, followed by Russia, India, and Europe (Figure 8).

Table 2. *CO₂ circulation in the biosphere* [9]

The process	Quantity (t/year)	Recovery time (years)
Atmospheric Content	$2.6 \cdot 10^{12}$	-
Photosynthesis	$2.2 \cdot 10^{11}$	<12
Respiration and Fermentation	$2.3 \cdot 10^{11}$	-
Combustion	$1.95 \cdot 10^{10}$	143
Deforestation	$1.2 \cdot 10^{10}$	219
Fossilization	10^7	$2.8 \cdot 10^5$
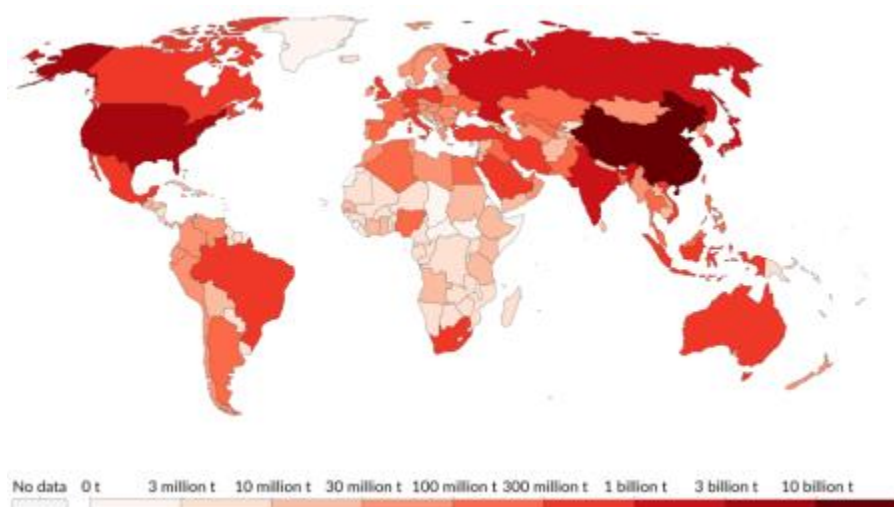
Fig. 8. *The global distribution of CO₂ emissions from industrial sources* [31]

Fig. 9. *The global CO_2 emissions from fossil fuel combustion, solely from industrial sources, 1750–2022* [31]

Quantitatively, the same global distribution of annual CO_2 emissions highlights that China alone, as the leading emitter, releases 1,600 million tons of CO_2 annually. Compared to previous centuries, beginning in the 20th century, CO_2 emissions have been on a continuous upward trend (Figure 9).

Hydrocarbons are present in combustion gases, either due to their formation and release from fuels during combustion (through processes such as cracking, dehydrogenation, polymerization, decarboxylation, and dealkylation) or as a result of incomplete combustion due to insufficient air supply [28]. Emissions are higher for liquid fuels, where hydrocarbons are already present prior to combustion.

4.2. Sulphur-Based Compounds

Coal contains sulphur in proportions of 0.6–6%, crude oil 0.1-4%, while natural gas contains negligible amounts [32]. In Romania, lower-rank lignite contains on average 1% sulphur, and bitumen around 2%. Consequently, bitumen-fired thermal power plants emit more SO_2 into the atmosphere than lignite-fired plants [9]. In coal, sulphur occurs in both organic and inorganic forms (sulphides and sulphates). Sulphur in sulphates remains in the ash, while organic sulphur and sulphides are converted into SO_2 and SO_3 [32]. Approximately 80–90% of atmospheric SO_2 originates from the combustion of fuels [33].

To date, the problem of atmospheric sulphur acid pollution has been only partially addressed, primarily through coal washing and/or increasing chimney heights to 200 m [34]. These measures are insufficient, as SO_2 pollution can be detected up to 8–10 km around a thermal power plant equipped with outdated technology. When released into the atmosphere, SO_2 reacts with oxygen at a rate of approximately 1–2‰ per hour under ultraviolet radiation, forming SO_3 [34]. This gas subsequently reacts with water vapor to form sulfuric acid. During foggy or highly humid conditions, the conversion rate can reach up to 15.7%.

SO_2 is a colourless gas with a pungent, suffocating odour. Its environmental and health impacts include the exacerbation of chronic respiratory diseases. At low concentrations, it causes spasms and constriction of the upper respiratory muscles, whereas at high concentrations, it can cause burns of the respiratory and conjunctival mucosa, breathing difficulties, and a sensation of suffocation. The presence of sulphur oxides in the environment affects plants directly and also alters the composition of water and soil. High concentrations of SO_2 destroy chlorophyll, an effect that is amplified synergistically with NO_2 [35]. Sulphur oxides, and the resulting sulphurous and sulfuric acids produced through hydration, cause corrosion, material discoloration, and reductions in the strength and elasticity of organic compounds [36].

The odour of SO_2 can be detected at 2–5 mg/m³, depending on individual sensitivity. Respiratory irritation begins at 6-13 mg/m³, poisoning occurs around 50 mg/m³, and concentrations of 1 g/m³ or higher can be fatal [37].

4.3. Nitrogen-Based Compounds

Nitrogen oxides (NOx) are formed from the reaction between oxygen and nitrogen in the air at combustion temperatures, with the reaction rate increasing at higher temperatures. It is estimated that

the thermoelectric industry is responsible for approximately 50% of atmospheric NOx, with the remainder originating from transportation sources [38]. Numerous industries emit NOx. Figure 10 presents the sources of NOx emissions in the USA, measured in 2017. "Mobile sources" - including road vehicles, boats, aircraft, and agricultural machinery - are the largest contributors. In both the USA and Europe, road vehicles are the primary type of mobile NOx source. In areas where vehicles dominate NOx emissions, higher concentrations of NO_2 are often observed during peak traffic hours.

The global distribution of nitrogen oxides emissions indicates that the largest contributors to global N_2 compound emissions are East Asia, South Asia, Africa, and South America. Emissions from synthetic fertilizers dominate in China, India, and the USA, whereas emissions resulting from the application of manure-based fertilizers dominate in Africa and South America. The highest growth rates occur in emerging economies, particularly in Brazil, China, and India, where both crop production and livestock numbers have increased (Figure 11).
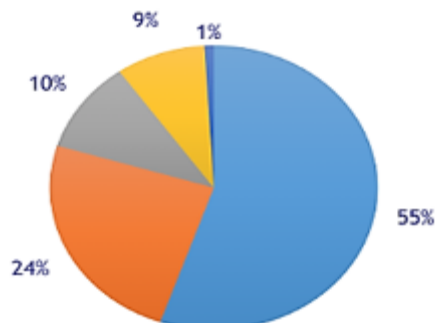
Fig. 10. *Sources that emit NO_2 into the atmosphere* [39]: ● *Mobile sources* ● *Other sources* ● *Industrial processes* ● *Fossil Fuels combustion* ● *Natural sources*
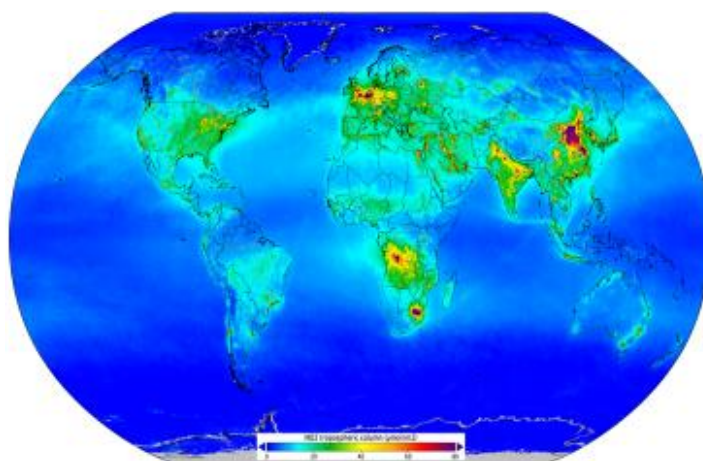

Fig. 11. *The global distribution of NOx emissions* [39]

Due to their aggressiveness and toxicity, nitrogen oxides and nitric acid are extremely hazardous to humans [40]. They attack mucous membranes and respiratory tracts and convert oxyhemoglobin into methemoglobin, which can lead to paralysis. Prolonged exposure to nitrogen oxides, even at very low concentrations (0.5 ppm), weakens the human body, increasing susceptibility to bacterial infections - a risk especially pronounced in children. Additionally, the toxicity of nitrogen oxides is amplified synergistically by the presence of other toxic substances.

Nitric acid, formed by the reaction of NO_2 with H_2O, causes various types of corrosion, severely affecting metal structures. HNO_3 reacts with different atmospheric cations to form nitrates, which are corrosive to copper, brass, aluminium, nickel, and

may also damage electrical and telecommunications networks [38]. These processes can occur even at very low NOx concentrations in the atmosphere (0.08 ppm).
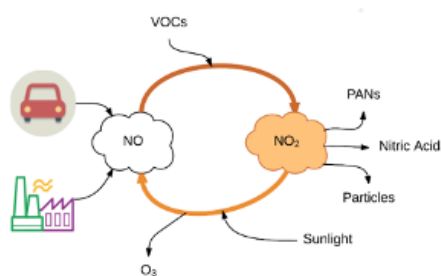
Fig. 12. *NO_2 life cycle* [39]

As shown in Figure 12, at the emission point (i.e., the exhaust pipe), NOx consists of

approximately 90% NO and 10% NO_2. After several hours in the atmosphere, and in the presence of volatile organic compounds (VOCs), NO is converted into NO_2. This reaction may occur over timescales ranging from seconds to several hours.

NO_2 further reacts with other atmospheric substances to form nitric acid, particulate matter, and peroxyacyl nitrates (PANs). Additionally, under sunlight, NO_2 can revert to NO and produce ozone (O_3) as a secondary pollutant. Due to the potential to form these secondary pollutants, its monitoring and regulation are essential.

Primary and secondary measures for reducing nitrogen oxide emissions are always accompanied by the formation of secondary emissions of CO, N_2O, and NH_3. This may result it to an increase of up to 10% in annual N_2O concentrations in the troposphere.

The harmful effects of N_2O are twofold [40]: first, it contributes to the enhancement of the greenhouse effect; second, and more importantly, N_2O destroys the protective ozone layer. While inert in the troposphere, N_2O is harmful in the stratosphere due to its catalytic role in photochemical reactions, generating active radicals that deplete ozone. This phenomenon is intensified by N_2O's long atmospheric lifetime, which can reach up to 180 years [40].

Atmospheric pollution arguably has the most severe impact on the environment, not only due to the quantity and diversity of pollutants but also because of its effects on vast geographic areas. For this reason, atmospheric pollution is no longer a local problem but has acquired a global character. Based on both its effects and their spatial and temporal extent, atmospheric pollution can be classified into the following categories:

- Proximity (local) pollution: occurring on a time scale of hours, where the main atmospheric pollutants (SO_2, NOx, CO, O_3, Pb, particulate matter) have immediate effects on human health and ecosystems.

- Distributed (regional) pollution: occurring on a time scale of days, with primary effects including acidification, eutrophication, and photochemical pollution.

- Global pollution: occurring on a time scale of years, leading to outcomes such as intensification of the greenhouse effect and destruction of the stratospheric ozone layer.

5. Conclusions

Thermal power plants, which rely predominantly on fossil fuels, remain the largest contributors to global electricity production, providing approximately 80% of the world's energy demand. The combustion of solid, liquid, and gaseous fuels generates significant emissions of pollutants, including particulate matter, sulphur oxides (SO_2, SO_3), nitrogen oxides (NOx), carbon oxides (CO, CO_2), and volatile organic compounds, with both direct and indirect effects on air quality, human health, and the environment.

The generation and release of pollutants depend on fuel composition, combustion efficiency, and technological processes. Incomplete combustion increases the emission of soot, unburned hydrocarbons, and CO, while modern plants monitor CO_2/CO ratios and apply combustion control to minimize harmful emissions. Sulphur content in fuels leads to SO_2 and SO_3 emissions, which cause acid rain, corrosion, and respiratory problems, whereas nitrogen oxides contribute to smog formation, ozone generation, and nitric acid deposition, with severe toxicological effects even at low concentrations.

Renewable energy sources (solar, wind, hydro) and nuclear power exhibit lower direct pollution compared to conventional fossil fuel-based thermoelectric plants. Nuclear energy, while low in routine emissions, poses potential risks from radioactive contamination if accidents occur. Renewable energy technologies, although cleaner, can still affect local microclimates and require energy-intensive production of equipment, highlighting the need for life-cycle assessments of all energy sources.

Air pollution has evolved from a local to a global problem, affecting human health, ecosystems, and climate systems across large geographic areas. Atmospheric pollution can be classified as local (proximity), regional (distributed), or global, depending on spatial extent and temporal scale. The continued increase in greenhouse gases, particularly CO_2 and N_2O, due to fossil fuel consumption and deforestation, contributes to climate change and ozone depletion.

Mitigating the environmental impacts of energy production requires innovative technologies, including cleaner combustion, emissions-scrubbing technologies, and renewable energy deployment, combined with policy measures that promote sustainable energy production and efficient resource use. Preventive approaches, which modify production processes and fuel selection to reduce pollution at the source, are generally more effective than end-of-pipe solutions, which transform rather than eliminate pollutants.

The data reviewed indicate that global energy systems must transition toward low-emission, high-efficiency technologies to protect the environment, ensure public health, and secure a sustainable energy future. While progress has been made in renewable energy adoption and emission control, the dominance of fossil fuels, particularly in certain regions,

continues to pose significant ecological and climatic challenges.

References

[1]. Singh V., *Environmental Disruptions: Planet Earth in the Vicious Cycle of Pollution*, Global Warming, and Climate Change, DOI: 10.59317/9788119002665, 2023.

[2]. Osheyor J., *et al.*, *A review of technological innovations and environmental impact mitigation*, World Journal of Advanced Research and Reviews, 21, (01), p. 75-82, DOI: 10.30574/wjarr.2024.21.1.2687, 2024.

[3]. Imarhiagbe O., *et al.*, *Air Pollution Control Technologies and Strategies*, in book: Evaluating Environmental Processes and Technologies, DOI: 10.1007/978-3-031-85327-2_8, 2025.

[4]. Husainy A. S. N., *et al.*, *Ingale, Innovation Ecosystems and Green Building Techniques for a Sustainable Future: Leveraging Advanced Technologies*, The Asian Review of Civil Engineering 13(2), p. 1-10, DOI: 10.70112/tarce-2024.13.2.4233, 2024.

[5]. Singh V., *et al.*, *Sources of Air Pollution*, in book: Battling Air and Water Pollution, DOI: 10.1007/978-981-96-4375-2_2, 2025.

[6]. Kozhagulov S., Salnikov V., *The Impact of Meteorological and Climatic Conditions on the Potential for Self-Purification of Atmosphere on the Industrial Region*, Journal of Geography and Environmental Management 74(3), p. 63-80, DOI: 10.26577/JGEM.2024.v74.i3-06, 2024.

[7]. ***, https://www.ggspdt.com/24-clean-technology.html.

[8]. Vasilescu E., *Eco-Proiectarea Proceselor în Ingineria Materialelor*, Universitatea „Dunărea de Jos" din Galați, România, Buletinul AGIR, nr. 1, p. 166-171, 2017.

[9]. Popescu M., *Ecologie aplicată*, Ed. Matrix Rom, București, 2000.

[10]. Alola A., Rahko J., *The Effects of Environmental Innovations and International Technology Spillovers on Industrial and Energy Sector Emissions – Evidence from Small Open Economies*, Technological Forecasting and Social Change 198(1):123024, DOI: 10.1016/j.techfore.2023.123024, 2023.

[11]. Istrate M., *Tehnologii şi instalaţii pentru reducerea emisiilor poluante – Controlul poluării în termoenergetică*, Editura Setis, Iaşi, ISBN: 973-86764-0-1, 2004.

[12]. Dhadse S., Kardbhajne A., *Biodiversity Loss Due to Construction of Dams and Hydropower Projects and Its Impact on Aquatic Ecosystems*, In book: Impact of Societal Development and Infrastructure on Biodiversity Decline, DOI: 10.4018/979-8-3693-6950-0.ch008, 2024.

[13]. Basooma A., *et al.*, *Spatiotemporal changes in river network connectivity in the Nile River Basin due to hydropower dams*, PLOS One, 20(4), DOI: 10.1371/journal.pone.0322338, 2025.

[14]. Wenno L. A., *et al.*, *Improvement Potential Hydroelectric Power (Hydropower) Supports Global Sustainability*, Cerdika Jurnal Ilmiah Indonesia, 5(8), p. 2516-2522, DOI: 10.59141/cerdikav5i8.2797, 2025.

[15]. Lelieveld J., *et al.*, *Global risk of radioactive fallout after major nuclear reactor accidents*, Atmospheric Chemistry and Physics, 12(9), p. 4245-4258, DOI: 10.5194/acp-12-4245-2012, 2012.

[16]. Ibrahim N. M., *et al.*, *Influencing factors for spent nuclear fuel from research reactor on radioactive waste management plan*, IOP Conference Series: Materials Science and Engineering 1326(1):012007, DOI: 10.1088/1757-899X/1326/1/012007, 2025.

[17]. Papazis S. A., *Nuclear-Thermal Power Generation: Multicriteria Optimization of the Economic Sustainability*, Sustainability 17(11):4781, DOI: 10.3390/su17114781, 2025.

[18]. Chen D., *et al.*, *Municipal solid waste incineration residues recycled for typical construction materials-a review*, RSC Advances 12(10), p. 6279-6291, DOI: 10.1039/D1RA08050D, 2022.

[19]. Zhuikov A. V., *et al.*, *Research on Co-Combustion of High-Calorific Biomass Obtained Using Gasification and Lignite for Sustainable Utilisation of Resources*, Sustainability 17(7):2845, DOI: 10.3390/su17072845, 2025.

[20]. Cometto M., Keppler J. H., *Nuclear Energy and Renewables. System Effects in Low-carbon Electricity Systems*, OECD Nuclear Energy Agency, Report no. 7056, DOI: 10.13140/RG.2.2.34255.79524, 2012.

[21]. ***, https://www.consilium.europa.eu/ro/infographics/how-is-eu-electricity-produced-and-sold/.

[22]. ***, https://www.transelectrica.ro/ro/web/tel/home.

[23]. Kurniansyah M. H., *et al.*, *The Effects of Raw Material Ratio and Calorific Value on Gasification Rate from Co-Gasification of Coal and Biomass*, Jurnal Bahan Alam Terbarukan 12(2), p. 105-111, DOI: 10.15294/jbatv12i2.44257, 2023.

[24]. Veranth J., *et al.*, *Sources of unburned carbon in the fly ash produced from low-NOx pulverized coal combustion*, Symposium (International) on Combustion, 27(2), p. 1737-1744, DOI: 10.1016/S0082-0784(98)80014-3, 1998.

[25]. Lahiri S. S., *Fly ash: safety and health issues*, in: Handbook of Fly Ash, Elsevier, DOI: 10.1016/C2018-0-01655-2, 2021.

[26]. Ramos M. A., *et al.*, *Effect of Total Combustion Flow and Combustion Ratio on the Cavitation Resistance of Hydrogen HVOF-Sprayed WC-Co-Cr Coatings*, Journal of Thermal Spray Technology, DOI: 10.1007/s11666-025-02025-0, 2025.

[27]. Shafiq A., *et al.*, *Climate Change Mitigation Strategies: Evaluating the Effectiveness of Renewable Energy Policies in Urban Environments*, Bulletin of Business and Economics (BBE), DOI: 10.61506/01.00499, 2024.

[28]. Kirchman D. L., *The Natural Carbon Cycle and Fossil Fuels*, Microbes, DOI: 10.1093/oso/9780197688564.003.0002, 2024.

[29]. ***, https://www.pnnl.gov.

[30]. Alagoz E., Alghawi Y., *The Future of Fossil Fuels: Challenges and Opportunities in a Low-Carbon World*, International Journal of Earth Sciences Knowledge and Applications, e-ISSN: 2687-5993, 2024.

[31]. ***, https://www.OurWorldinData.org(co2-and-greenhouse-gas-emissions).

[32]. Chen L., *et al.*, *The Dynamic Cointegration Relationship between International Crude Oil, Natural Gas, and Coal Price*, Energies, 17, 3126, DOI: 10.3390/en17133126, 2024.

[33]. Kim J.-W., Lee T.-H., *A Comparative Study of Combustion Characteristics for the Evaluation of the Feasibility of Crude Bioethanol as a Substitute for Marine Fuel Oil*, Journal of Marine Science and Engineering, 13(3), 433, DOI: 10.3390/jmse13030433, 2025.

[34]. Shi Q., Wu J., *Review on Sulfur Compounds in Petroleum and Its Products: State-of-the-Art and Perspectives*, Energy & Fuels, 35(18), p. 14445-14461, DOI: 10.1021/acs.energyfuels.1c02229, 2021.

[35]. Baghaie A., *Effect of Sulfur Granular Municipal Solid Waste, Humic Acid, and Nano Fe-Oxide on Lead Uptake by Plants in a Calcareous Soil in the Presence of Thiobacillus*, Avicenna Journal of Environmental Health Engineering, 10(1), p. 10-17, DOI: 10.34172/ajehe.2023.5284, 2023.

[36]. Cheng X. L., *et al.*, *Corrosion of Stainless Steels in Acid Solutions with Organic Sulfur-Containing Compounds*, Corrosion Science, 41(2), p. 321-333, DOI: 10.1016/S0010-938X(98)00125-5, 1998.

[37]. Li W., *et al.*, *Effect of SO_2 and SO_3 on the Distribution of Na/S/Cl and Ash Characteristics of Zhundong Coal during Circulating Fluidized Bed O_2/CO_2 Combustion*, Journal of the Energy Institute, 96(7), DOI: 10.1016/j.joei.2021.03.016, 2021.

[38]. Elliott E. M., *et al.*, *Nitrate Isotopes in Precipitation to Distinguish NO_x Sources, Atmospheric Processes, and Source Areas in the United States*, Environmental Science & Technology, 41 (22), p. 7661-7667, DOI: 10.1021/es070898t, 2007.

[39]. ***, https://aqicn.org/faq/2017-01-10/nitrogen-dioxide-no2-in-our-atmosphere/ro/.

[40]. Dammeier J., *et al.*, *Nitric Acid, 2. Uses, Nitrous Acid, and Nitrogen Oxides*, Ullmann's Encyclopedia of Industrial Chemistry, DOI: 10.1002/14356007.w17_w01, 2025.

A CURRENT MINIREVIEW ON THE AQUATIC ENVIRONMENT: IMPACT OF SOME IONS FROM THE FOOD AND METALLURGICAL INDUSTRIES

Romică CREȚU*, Liviu Cătălin ȘOLEA, Nicolae ȚIGĂU
"Dunarea de Jos" University of Galati, Romania
e-mail: romica.cretu@ugal.ro

ABSTRACT

Recent research has shown the high degree of pollution that the metallurgical and food industries can cause to the environment. In this minireview, the impact that various polluting ions, emitted as a result of technological processes specific to the metallurgical and food industries, can have on the aquatic environment was analysed. Our research also provides an assessment of the potential interactions and the most likely transformations of these chemical forms once they are released into the aquatic environment, as well as the likely impact on the ecosystem.

1. Introduction

A significant part of the atmospheric emissions and residues originating from the food and metallurgical industries ultimately end up in aquatic ecosystems.

Ammonia (NH_3), nitrogen oxides (NOx), sulphur oxides (SOx), volatile organic compounds (VOCs), particulate matter (PM), etc. generated by various food, agricultural, and metallurgical processes, can be deposited through precipitation, transforming into soluble compounds that alter the chemistry of surface and groundwater. Other industries, such as pulp and paper, also have a significant contribution.

Thus, industrial processes can have a significant indirect contribution to the pollution of the aquatic environment.

This occurs not only through direct discharges (effluents), but also through atmospheric transport and the deposition of reactive species.

Agriculture also has a significant impact on the aquatic environment, polluting rivers, lakes and oceans by releasing nutrients.

In this context, while certain pollutants such as NOx and SOx have started to decrease in the last decade as a result of strict controls carried out by the authorities, there is currently increasing emphasis on optimizing technologies to reduce CO_2 emissions.

On the other hand, polluting oxides and the chemical compounds resulting from their transformations, generated by various industrial processes, such as those in the food and metallurgical industries, affect the aquatic environment indirectly.

However, this impact is substantial, manifesting itself through significant changes in several environmental parameters, namely including eutrophication, acidification, increased biochemical oxygen demand (BOD), as well as the bioaccumulation of various metals [1-6].

Although there are studies [2, 7-10] that show how polluting oxides are formed and that monitor CO_2 emissions and Volatile Organic Compounds (VOCs) from the steel and food industries, we believe that there is still currently relatively little research on the evaluation of emissions of other gases, such as SOx and NOx.

This is in the context where the impact of these oxides on the aquatic environment is significant [2, 5].

In general, research on SO_2 and NOx emissions focuses on the main production process, which is sintering. Various pollutants are generated during this process, with most SO_2 and NOx emissions originating from the raw materials used in the sintering material. Nitrogen oxides originate from thermal reactions and sulphur dioxide from the sulphur content of the fuel [11].

The presence in the aquatic environment of nitrogen and sulphur compounds resulting from the transformation of oxides produced in technological processes, to which the agri-food sector has a major

contribution, is certainly a major cause of damage to aquatic ecosystems.

Through the novel elements provided by the specialized literature from the last decade, this minireview presents a perspective on the fundamental processes in which the main types of ions with a polluting character in aquatic systems are involved.

Particular attention is paid to the influence of these chemical species on the biota inhabiting the environments.

2. Bonded nitrogen technology – ammonia synthesis

The technology of bound nitrogen encompasses several fundamental sectors of basic inorganic chemical technology: the synthesis of ammonia, nitric acid and nitrogen fertilizers (simple and complex nitrates, urea, cyanamide, etc.).

Although agriculture is the main global source of NH_3, industrial processes contribute significantly to the increase in the concentration of this chemical compound in industrialized areas. Ammonia production belongs to the basic chemical industry. In nitrogen fertilizer plants, ammonia is produced by the Haber–Bosch process. It is produced exclusively through the synthesis of its constituent elements according to the reaction:

$$N_2 + 3H_2 \rightleftharpoons 2NH_{3\,(g)} \qquad (1)$$
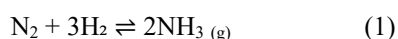
This reaction appears as a strongly exothermic process with a large volume contraction, compounded by the chemical inertness of the nitrogen molecule.

According to the ammonia synthesis plant (Figure 1) the gases resulting from the technological process are recirculated, and after the accumulation of

about 5% CH_4 and noble gases in the recycle, purging into the atmosphere is performed [12].

During technological processes, NH_3 losses amounting to 0.5–2% of total production can occur through leaks from reactors, pipelines, tanks or during cooling and compression stages. They are released into the atmosphere as a gas. NH_3 can also occur as a by-product in nitrogen oxide reduction technologies in thermal power plants when coal or biomass is used.

Although less intuitive, the food industry contributes to NH_3 emissions through fermentation processes, food-wastewater treatment, and food-waste composting [13, 14]. The ammonia molecule plays a central role in the biogeochemical cycle of nitrogen and in the biology of organisms (Figure 2) [15].
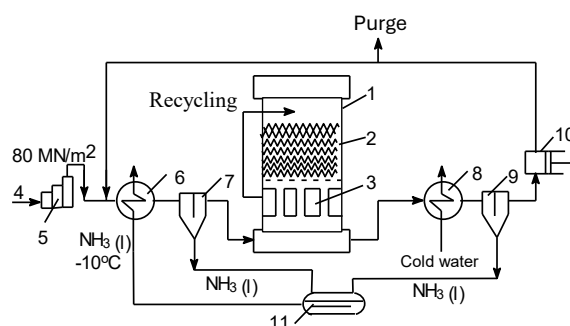

Fig. 1. *Schematic diagram of the ammonia synthesis installation: (1) reactor with catalytic zone (2) and heat exchanger (3); (4) fresh gases; (5) - stage compressor; (6) and (8) NH_3 coolers and water, respectively; (7) and (9) - liquid ammonia separators; (10) – recirculation pump; (11) - NH_3 tank; (reproduction after* [12]*)*
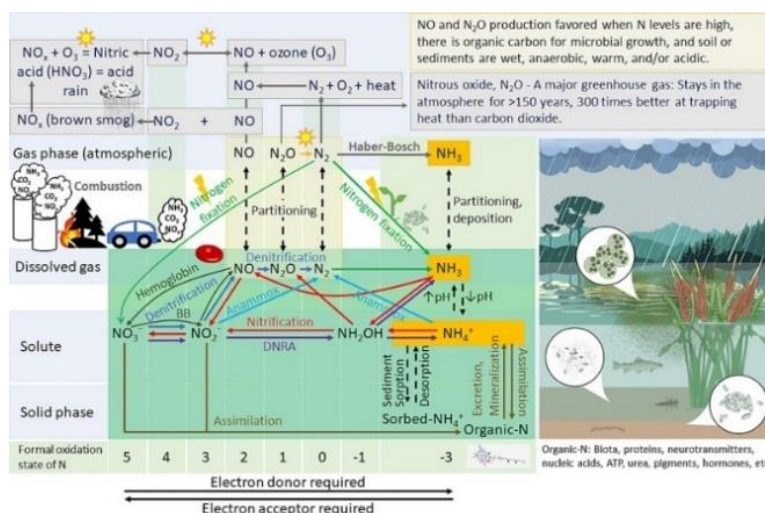

Fig. 2. *The nitrogen (N) cycle (reproduction after* [15]*)*

Due to excess NH_3 from agricultural and industrial activities, the mechanism of transformation of atmospheric ammonia into ammonium ion (reactions 1 and 2) in aquatic environments becomes problematic.

$$NH_3(g) \leftrightarrow NH_3(aq) \qquad (1)$$

$$NH_3(aq) + H_2O(l) \rightleftharpoons NH_4^+(aq) + OH^-(aq) \qquad (2)$$
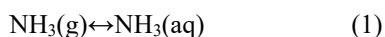
In alkaline waters, the proportion of free NH_3 increases, thereby increasing its toxicity to aquatic organisms [16]. Atmospheric deposition of ammonia from processes specific to the metallurgical and food industries can lead to increased nitrate concentrations in the aquatic environment (Figure 3).
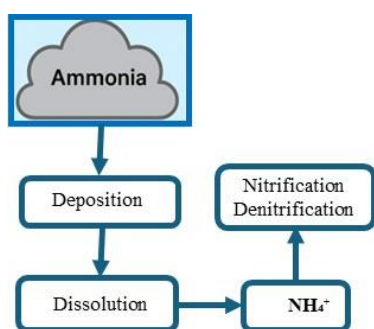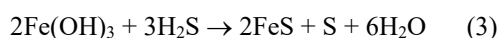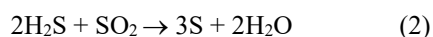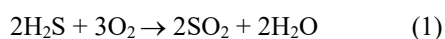
Fig. 3. *Illustrative scheme regarding the atmospheric NH_3 transformation in the aquatic ecosystem*

3. Processing of sulphur ores

Sulphur occurs in nature both in its native state and in minerals. Sulphur present in its native state is extracted after preliminary smelting, either by burning a small amount of sulphur or by injecting steam into the deposit.

A large part of elemental sulphur is recovered from natural gas, water gas, and coal synthesis gas, and from various fractions of crude oil distillation. In principle, in these processes, sulphur compounds are converted to H_2S, which is converted to S by combustion under controlled conditions or absorbed on $Fe(OH)_3$.

$$2H_2S + 3O_2 \rightarrow 2SO_2 + 2H_2O \qquad (1)$$

$$2H_2S + SO_2 \rightarrow 3S + 2H_2O \qquad (2)$$

$$2Fe(OH)_3 + 3H_2S \rightarrow 2FeS + S + 6H_2O \qquad (3)$$

In the manufacture of sulfuric acid, the first technological stage is the production of sulphurous gases (SO_2), which in the second stage are catalytically oxidized (contact process on a Pt or V_2O_5 catalyst) to SO_3, which in the final stage is absorbed in oleum and/or concentrated sulfuric acid (H_2SO_4 98%). According to the technology for obtaining sulfuric acid, its manufacture is based on a double oxidation process of sulphur or metal sulphides [12].

In the first stage, sulphur or metal sulphides, especially pyrite, are thermally oxidized, producing SO_2; in the second stage, SO_2 is oxidized to SO_3. By absorbing and combining SO_3 with water, H_2SO_4 of different concentrations is obtained.

One of the important stages of the sulfuric acid manufacturing technology involves the purification, oxidation and absorption of sulphurous gases (Figure 4).
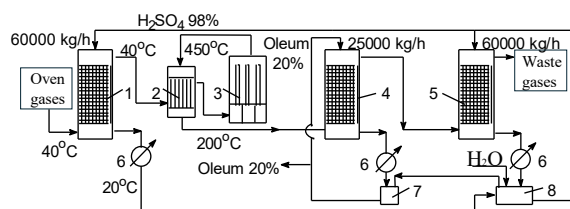
Fig. 4. *Schematic diagram of the purification, oxidation and absorption installation for sulphurous gases in the H_2SO_4 production: 1 - drying tower; 2 - gas heater; 3 - contact stove; 4 - SO_3 absorption tower with 20% oleum; 5 - absorption tower with 98% H_2SO_4; 6 - coolers; 7 and 8 - oleum and 98% H_2SO_4 tanks, respectively. Flow rates of the acid solutions are indicated on the diagram (reproduction after [12])*

On the other hand, while the steel industry remains a major source of air pollutants on a regional and global scale, the food industry generates a complex set of emissions: greenhouse gases (CO_2, CH_4, N_2O), NH_3, NOx and SOx from combustion, VOCs particularly during cooking and frying, PM from thermal processes, etc.

The main sources of NOx/SOx/PM in the food processing sector are steam and heat generation equipment (boilers/boilers) and incineration or auxiliary combustion; these emit NOx, SOx (depending on the sulphur content of the fuel) and particulate matter from combustion. In addition, frying, grilling, baking and deep-frying processes emit VOCs and PM [17].

4. Technological valorisation of phosphorus ores

Phosphate rocks: phosphorites, $Ca_3(PO_4)_2$, fluorapatites ($3Ca_3(PO_4)_2CaF_2$), chlorapatites and
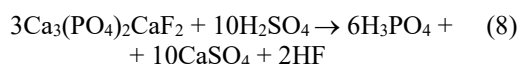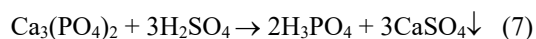
hydroxyapatites $(3Ca_3(PO_4)_2Ca(OH)_2$, are technologically exploited for:

1. Production of phosphorus and phosphoric acid by the thermal method (dry process).

2. Production of phosphoric acid and phosphate fertilizers by the wet process.

The resulting phosphoric acid is purified by distillation and is used in the fertilizer industry, for the manufacture of phosphorus salts, as well as in the pharmaceutical and food industries [12].

Wet processes take place in aqueous solutions. On an industrial scale, the reaction of apatites and phosphorites with H_2SO_4 is used.

Treating phosphates with H_2SO_4 results in an impure phosphoric acid, with 20-40% P_2O_5 before purification and concentration, according to the reactions for the two ores (7, 8).

$$Ca_3(PO_4)_2 + 3H_2SO_4 \rightarrow 2H_3PO_4 + 3CaSO_4\downarrow \quad (7)$$

$$3Ca_3(PO_4)_2CaF_2 + 10H_2SO_4 \rightarrow 6H_3PO_4 + \quad (8)$$
$$+ 10CaSO_4 + 2HF$$

Among the types of emissions resulting from the phosphate fertilizer industry, we can list solid particles ($CaHPO_4$, $Ca_3(PO_4)_2$, etc.) and acidic aerosols such as H_3PO_4 and HF.

On the other hand, in the process of smelting the ores, phosphorus (present as an impurity) is partially released by volatilization in the form of oxides (P_2O_5).

Phosphorus oxide subsequently reacts with water vapor, forming phosphoric acid.

The phosphate ion is also emitted from processes that take place in the food industry, such as the processing and preservation of food, from the combustion of food residues or from the treatment of food wastewater. The mineral aerosols are the dominant source of atmospheric total phosphorus (TP) on a global scale, with primary biogenic particles and combustion sources [18].

Although atmospheric phosphorus emissions are relatively small compared to nitrogen or sulphur, they have a significant ecological impact.

This is due to the fact that phosphate particles can be transported over long distances and subsequently deposited in soils and, implicitly, in waters, promoting secondary eutrophication.

5. Sodium chloride product technology

The production of sodium chloride products is mainly based on the chemical and electrochemical valorisation of salt deposits.

Salt is extracted from deposits by mining and drilling. Before technological use, the extracted product is purified by specific methods [12].

The main stages of treatment and technological valorisation of salt from deposits with the two main directions of chemical processing are presented in Figure 5.
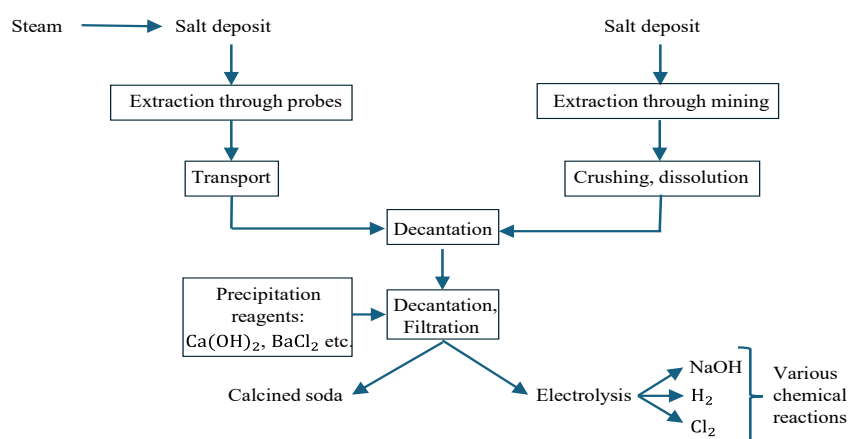
Fig. 5. Scheme of extraction, primary treatment and technological recovery of NaCl (reproduction after [12])

6. The implications of some ions on the aquatic environment

6.1. NO²⁻

Monitoring the presence of nitrites (NO_2^-) in river waters is vital, as they are very toxic to the environment at certain concentrations. NO_2^- ions greatly affect water quality, posing a significant risk to the ecosystem and human health [19]. According to studies, high concentrations of nitrites have been noted in certain research regions. This is an important element concerning the toxicity of these oxides for the environment, given that their impact, from a

biochemical point of view, can have major effects, since nitrites easily pass into the blood of fish and other aquatic creatures, where they react with haemoglobin, forming methaemoglobin (MetHb). Thus, nitrites prevent erythrocytes from delivering oxygen to the cell (methemoglobinemia or brown blood disease), with sensitivity to nitrites varying by species [20].

Therefore, the high content of nitrites present in water samples analysed in certain geographical regions may be associated with an increased risk of developing methemoglobinemia in those people who consume affected fish or who eventually use this water for consumption. Depending on the level of MetHb, negative effects on the living organism may occur, such as cardiac arrhythmias and destructive effects on the central nervous system [21].

Analysing the data obtained through rigorous monitoring of the nitrite ion, a lower amount of nitrite can be noted in one research area compared to another, which may indicate a more intense oxidative process. Also, this higher amount of nitrite present in the other study area may come from the reduction of nitrates in the presence of a reducing flora, as well as a higher water temperature at the time of sampling.

6.2. NO_3^-

Nitrates, salts of major importance for protein synthesis, are the products most used by plants, being found in large quantities in surface waters. Therefore, the presence of nitrates in the aquatic environment is an indication of environmental stability with respect to nitrogen transformation. Nitrates can represent one of the most important factors for the development of algae and other aquatic plants. However, their presence above certain limits in the water of rivers and streams can lead to a harmful effect due to the fact that excessive nitrogen compounds can become toxic. Nitrates present in the analysed waters can have a toxic effect primarily through direct action on living organisms: through in vivo conversion into nitrites and through their ability to oxidize haemoglobin (Figure 2), transforming it into methaemoglobin, which cannot bind oxygen [22]. This process leads to haemoglobin inactivation. This toxicity of nitrates and, implicitly, nitrites, varies in aquatic organisms depending on a series of factors, among which their species and water salinity stand out. The degree of absorption of nitrites depends on the nitrite-chloride ratio present in the analysed water, the toxic effect of NO_2^- decreasing with increasing salinity levels [23, 24].

At the same time, nitrates can have an indirect effect by decreasing the resistance of living organisms to stress factors, thereby favouring the development of various diseases. Also, the presence of high concentrations of nitrates in the aquatic environment can contribute to the uncontrolled development of some aquatic plants.

The analysis of experimental data obtained from analysing samples collected in the aquatic environment leads to the clarification of the implications of nitrates on the pollution of surface waters, deeper waters, and the sediments of the monitored region. In this context, the presence of nitrates determined in a location in higher quantities compared to another region subject to monitoring may be the result of the mineralization of protein-based organic pollutants, as well as fertilizers and pesticides with nitrogen content in the chemical composition. Thus, the higher concentration of nitrates present in the water samples analysed from the respective location may be due to the more abundant presence of bacteria, such as nitrifying bacteria. These oxidize nitrites to nitrates using molecular oxygen (electron acceptor) to produce energy and reducing power. Bacteria such as those belonging to the genera Nitrobacter, Nitrococcus and Nitrospira are present everywhere in freshwater [25-28].

On the other hand, the decrease in nitrate and nitrite concentrations in water samples taken from the aquatic environment is probably the result of the dissimilatory reduction of both ionic nitrogen oxides to gaseous oxides, such as NO and N_2O. Such oxides can be further reduced and eliminated as gaseous nitrogen in the atmosphere. Also, the lower concentration of nitrites/nitrates is probably due to the same biological process carried out exclusively by various bacteria. We consider such research to be especially important. The results obtained in the case of water samples taken from a region of interest may show that a major loss of nitrogen compounds for water and soil fertilization occurs in that location.

6.3. NH_4^+

A series of studies conducted on the aquatic environment several decades ago [29, 30] have shown that there are two forms of ammonium in water: non-ionized (NH_3) and ionized (NH_4^+) ammonia. According to in-depth studies [31] for many aquatic organisms, toxicity is primarily attributed to non-ionized species, with NH_4^+ being relatively less toxic. However, monitoring the NH_4^+ ion in this study is important because ammonium is easily transformed into toxic substances (nitrites, nitrates, etc.).

Increased concentrations of ammonia in water samples taken from a region of the aquatic environment may indicate the existence of an advanced degree of pollution due to the presence of organic substances. This may be due to the action of putrefactive bacteria on proteins present in the body

of dead hydrobionts. Such results show that, due to the presence of ammonia nitrogen in surface waters, there is, in the respective region, a high risk of toxicity for most animal organisms in aquatic ecosystems.

If comparative results indicate much lower concentrations of ammonia nitrogen in the region analysed, then this indcates that, following the various catabolic processes through which protein deamination occurs, hydrobionts eliminate products with lower toxicity in the respective region (urea, uric acid, ammonia salts, etc.).

6.4. Total nitrogen

The nitrogen fraction dosed by total nitrogen is given by the totality of nitrogen-containing compounds. In water, nitrogen exists as inorganic and organic species. Inorganic nitrogen is present in oxidized form (e.g., nitrites and nitrates) and reduced form (e.g., ammonia/ammonium and dinitrogen gas). Organic nitrogen is found in water either in colloidal form or in the form of amino acid molecules. These can originate from the corpses of aquatic organisms. Through their metabolic activity, organisms excrete nitrogen compounds, such as amino acids, polypeptides, urea, hydroxyl amines, etc. In the nitrogen fraction, proteins are dominant, constituting the protein fraction. The difference between total and protein nitrogen represents non-protein or amine nitrogen.

N pollution (total nitrogen represents the sum of all forms of nitrogen in a water sample) also causes eutrophication of water, which disrupts ecology and leads, among other effects, to oxygen depletion and loss of biodiversity [32].

Recent research shows that in some regions, excessive nitrogen inputs can lead to serious pollution problems in aquatic environments. Examples include eutrophication and degradation of water quality parameters that are directly associated with excess total nitrogen [33].

6.5. PO_4^{3-}

Phosphorus, the second most important nutrient for plants after nitrogen [34], is present in water in organic form bound to certain radicals, within complex substances, or in the form of salts of phosphoric acid. Mineral phosphorus is indispensable for biochemical processes, as it is the carrier of energy taken from the sun in photosynthesis and stored in macroergic phosphate groups. The main macroergic substances of metabolism are the organic phosphorus compounds ADP and ATP. Phosphorus also enters the structure of the body's skeleton and the composition of nucleic acids [35]. Phosphorus oxides are toxic. Phosphates also become toxic in high concentrations. In elemental form, phosphorus is toxic and subject to bioaccumulation. For fish, white phosphorus is toxic.

Phosphates are major nutrients for plants, contributing to their growth and productivity. Phosphates enter watercourses from several sources: agricultural soil drainage, stormwater, industrial wastewater discharges, excretory products, variations in temperature and bacterial activity, etc. [36].

High phosphate concentrations determined in the aquatic environment at great depths indicate that in such a location, due to the greater depth of the water in the area where the samples were taken, dissolved oxygen is minimal and, therefore, these regions tend to accumulate higher concentrations of organic substances.

Phosphates, chemical compounds containing the phosphate ion (PO_4^{3-}), actively participate in many complex biochemical processes. At the same time, they are chemical compounds widely used in agricultural fertilizers.
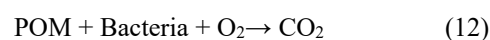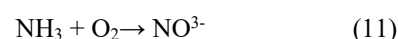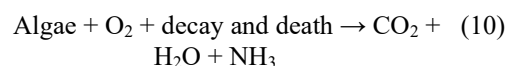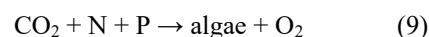
However, the influx of phosphates into aquatic ecosystems can have a significant impact on the aquatic environment.

Phosphate is an important factor affecting the growth rate of organisms, acting as a limiting nutrient for plant growth in freshwater environments [37].

An increase in the phosphate content in the aquatic environment above the permissible limits indicates that pollution processes are taking place in the respective location, likely caused by pesticides, fertilizers or detergents.

The results of our research show that the identification of high phosphate concentrations in certain regions of the aquatic environment is an indication that eutrophication of the aquatic environment is probably favoured in the presence of sunlight and nitrogen.

The sequence of chemical reactions that occur during water eutrophication [38] can be represented by equations (9-12).

$$CO_2 + N + P \rightarrow \text{algae} + O_2 \qquad (9)$$

$$\text{Algae} + O_2 + \text{decay and death} \rightarrow CO_2 + H_2O + NH_3 \qquad (10)$$

$$NH_3 + O_2 \rightarrow NO^{3-} \qquad (11)$$

$$POM + \text{Bacteria} + O_2 \rightarrow CO_2 \qquad (12)$$

where POM - particulate organic matter.

Consequently, the dissolution in water is reduced, which can cause the death or decomposition of animal organisms in aquatic ecosystems.

In addition, the concentrations of phosphates identified in this environment may stimulate the growth of plant species that are accidentally introduced into the ecosystem.

Therefore, we consider that this situation poses a risk of altering plant distribution patterns in these areas.

On the other hand, we can conclude that, in general, the total concentration of phosphorus (including phosphate) in aquatic samples reaches values of only a few ppm. This suggests that phosphate is unlikely to exert direct toxic effects in this region.

However, the excessive influx of phosphate identified in water samples collected from the aquatic environment has the potential to cause eutrophication in the respective ecosystems [39].

This potential of phosphates to stimulate plant overgrowth in freshwater environments may be attributed to the essential nutrient function of phosphate in plant metabolism.

Based on the N/P ratio, a good assessment of the chemical fertility of the water in the analysed areas can be made. Such a ratio is relatively constant in the aquatic environment. Any deviation from this ratio represents a direct indicator of the alteration of the normal metabolism of the ecosystem by various organic pollution phenomena or natural geochemical phenomena [40].

6.6. SO_4^{2-}

Sulphates are widely distributed in nature and can be present in freshwater environments, representing an important source of sulphur for plants and bacteria. Sulphates are typically found in low concentrations in most freshwater systems, although substantial concentrations can be found in areas where sulphate-containing minerals (including barite, epsomite, and gypsum) or anthropogenic activities exist [41].

Sulphates can have various adverse effects on the aquatic environment. Among the most important is their transformation. The process is known as bacterial sulphate reduction. In this process, the sulphate ion is converted to hydrogen sulphide [42] according to equation (13).

$$SO_4^{2-} + 2CH_2O = H_2S + 2HCO_3^{-} \qquad (13)$$
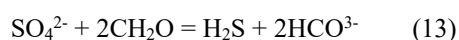
In addition to terrestrial plants, high concentrations of sulphur compounds are produced by marine algae. They accumulate high concentrations of sulphur compounds because the habitats in which they live contain abundant sulphur (from various sources, such as underground volcanoes).

Once in the cells, sulphur is metabolized in various ways: it is incorporated either as organic sulphate or as a thiol group of cysteine. Such metabolites are involved in various cellular processes [42]. The high concentrations of inorganic sulphates identified in water samples taken from the aquatic environment may favour the formation of H_2S in the water (by their reduction under the action of sulphide-reducing bacteria), along with its formation following anaerobic degradation of organic sulphur compounds.

This can affect invertebrates in the aquatic environment, as well as fish eggs and fry. Furthermore, in certain situations conditioned by the pH of the water, sulphides may result.

The toxic nature of sulphides is determined predominantly by the undissociated form (H_2S) and to a lesser extent by the HS^- or S^{2-} ions, which are pH-dependent.

Therefore, from the analysis of water samples, a high concentration of sulphates can be noted, which can result in a major impact on the aquatic environment, as they are toxic to organisms. High concentrations of sulphates in such water samples can facilitate the formation of hydrogen sulphide, which is toxic to most aquatic organisms, lethal doses being very low. The toxic effect can be correlated with the mechanism of action on haemoglobin, forming sulphmethaemoglobin. In addition, poor water circulation can be an important factor the favours the formation of hydrogen sulphide.

On the other hand, if lower concentrations of sulphates are noted, these results can most likely be attributed to the formation of Ca^{2+} and SO_4^{2-} ion pairs which increase the total water hardness in the respective area of the aquatic environment.

6.7. Cl^-

In the case of the analysis of samples taken from the aquatic environment, an increase in the concentration of chlorine ions can be observed, which can directly lead, according to Wu *et al.*, to a reduction of water self-purification processes in the respective area. Such phenomena can make the detection of Cl^- in water very important [43].

In addition, these results are associated with a decrease in aquatic biodiversity [44] compared to the other regions analysed. Chlorine reacts with amino groups in proteins forming hydrochloric acid. Furthermore, the reaction of chlorine with water in tissues results in hydrochloric acid which can cause stomach hyperacidity, followed by ulceration.

When chloride, phosphate, and sulphate anions participate in the metabolic stages of aquatic plants in

high concentrations, they alter the acid-base balance. In this way, acidic conditions are created, a process that can lead to acidosis [45].

6.8. Chemical oxygen demand (COD)

An important indication of the presence of germs in water samples taken from the aquatic environment is the increase or sudden appearance of organic substances. Usually, organic substances are accompanied by such germs.

Therefore, those compounds that can be oxidized under the action of an oxidant constitute the oxidizable organic fraction in water. These are assessed by chemical oxygen demand (COD). However, according to Wojnárovits. *et al.* [46] in recent years, COD has been increasingly replaced by the total organic carbon (TOC) parameter. However, the results obtained regarding the COD parameter may indicate that in the region from which the samples subjected to subsequent analyses were taken, water pollution due to the content of organic substances is significant.

These results are probably due to high concentrations of autochthonous organic substances originating from the body of hydrobionts, such as proteins, cellulose, etc. or from the metabolic activity of hydrobionts, during which various ectocrine substances result. Once eliminated in the aquatic environment, exocrine substances can inhibit certain processes that occur in water. Also, such substances resulting from metabolism can inhibit or stimulate the metabolism of other species.

On the other hand, when the results obtained indicate that, through much lower COD values, the water samples taken are characterized by a lower degree of pollution, this is due to the presence of oxidizable organic substances in a lower percentage.

7. Conclusions

The metallurgical industry produces a wide range of polluting oxides, both non-metallic and metallic, with significant effects on the aquatic environment. The specialized literature of the last decade offers both the mapping of sources and the degree of pollution of the aquatic environment, as well as efficient technical solutions.

Our studies show that all the information accessed from the literature on chemical oxygen demand confirms that this parameter is of major importance for assessing the degree of pollution with organic compounds of the aquatic environment.

Where increases in the degree of pollution of the aquatic environment are identified as a result of technological processes in the metallurgical and food

industries, as well as in agriculture, the modernization of the respective technologies is required. This is necessary to achieve the water protection objectives established by directives of regulatory bodies on aquatic pollution. We believe that the results presented in this minireview are crucial for the development of new environmental policies by regulatory bodies.

References

[1] Zhang J., *et al.*, *Iron and steel industry emissions: A global analysis of trends and drivers*, Environ. Sci. Technol, vol. 57, p. 16477-16488, 2023.

[2]. Zolotova E., *et al.*, *Monitoring of Air Pollution from the Iron and Steel Industry: A Global Bibliometric Review*, Atmosphere, vol. 16(8), p. 992, 2025.

[3]. Ritchie H., *et al.*, *Environmental Impacts of Food Production*, https://ourworldindata.org/environmental-impacts-of-food, accessed: Oct. 10, 2025.

[4]. Liu L., *et al.*, *Exploring global changes in agricultural ammonia emissions and their contribution to nitrogen deposition since 1980*, PNAS, vol. 119(14), p. 1-9, 2022.

[5]. Harrison D. M., *et al.*, *Review of the Aquatic Environmental Transformations of Engineered*, Nanomaterials, vol. 13(14), p. 2098, 2023.

[6]. Bhander G., Jozewicz W., *Analysis of emission reduction strategies for power boilers in the US pulp and paper industry*, Energy Emiss Control Technol, vol. 5, p. 27-37, 2017.

[7]. Zhang C., *et al.*, *An Approach to CO_2 Emission Reduction in the Iron and Steel Industry: Research Status and Development Trends of Integrated Absorption-Mineralization Technologies*, Sustainability, vol. 17(2), p. 702, 2025.

[8]. Wang D., *et al.*, *Global Iron and Steel Plant CO_2 Emissions and Carbon-Neutrality Pathways*, Nature, vol. 622, p. 514-520, 2023.

[9]. Șolea L. C., Crețu R., *Oxidation and Flammability Tests for Grape (Vitis vinifera L.) Seed Oil*, Lubricants, vol. 12(8), p. 26, 2024.

[10]. Tao C., *et al.*, *Review of Emission Characteristics and Purification Methods of Volatile Organic Compounds (VOCs) in Cooking Oil Fume*, Processes, vol. 11(3), p. 705, 2023.

[11]. Ren Z. P., *et al.*, *NOx and SO_2 formation in the sintering process and influence of sintering material composition on NOx emissions*, Huan Jing Ke Xue, vol. 35(10), p. 3669-3673, 2014.

[12]. Florea T., Crețu R., *Tehnologie Chimică Generală. Aplicaţii de Calcul şi Lucrări Practice*, Editura Academica, Galaţi, ISBN 973–8316–81–2, p. 311, 2005.

[13]. Pagans E., *et al.*, *Ammonia Emissions from the Composting of Different Organic Wastes, Dependency on Process Temperature*, Chemosphere, vol. 62(9), p. 1534-1542, 2006.

[14]. Hussain A., *et al.*, *Mitigation of ammonia emissions during food waste composting through acetic acid addition: A promising strategy for sustainable waste management*, Sustainable Chemistry and Pharmacy, vol. 36, p. 101324, 2023.

[15]. Edwards T. M., *et al.*, *Ammonia and aquatic ecosystems – A review of global sources, biogeochemical cycling, and effects on fish*, Science of the Total Environment, vol. 907, p. 167911, 2024, https://doi.org/10.1016/j.scitotenv.2023.167911.

[16]. Wurts A. W., *Daily pH Cycle and Ammonia Toxicity*, World Aquaculture, vol. 34, p. 20-21, 2023.

[17]. Coggon M. M., *et al.*, *Contribution of cooking emissions to the urban volatile organic compounds in Las Vegas*, NV, Atmos. Chem. Phys, vol. 24, p. 4289-4304, 2024.

[18]. Mahowald N., *et al.*, *Global distribution of atmospheric phosphorus sources, concentrations and deposition rates, and anthropogenic impacts*, Global Biogeochemical Cycles, vol. 22(4), 2008.

[19]. Kamel R. M., *et al.*, *Efficient toxic nitrite monitoring and removal from aqueous media with ligand based conjugate materials*, Journal of Molecular Liquids, vol. 285, p. 20-26, 2019.

[20]. Stamper M. A., Semmen K. J., *Chapter 23 - Basic Water Quality Evaluation for Zoo Veterinarians*, Editor(s): R. Eric Miller, Murray Fowler, Fowler's Zoo and Wild Animal Medicine, W.B. Saunders, p. 177-186, https://doi.org/10.1016/B978-1-4377-1986-4.00023-8), accessed: Oct. 10, 2025.

[21]. Skold A., *et al.*, *Methemoglobinemia: Pathogenesis, Diagnosis, and Management*, Southern Medical Journal, vol. 104 (11), p. 757-761, 2011.

[22]. Manassaram D. M., *et al.*, *A review of nitrates in drinking water: maternal exposure and adverse reproductive and developmental outcomes*, Environmental Health Perspectives, vol. 114 (3), p. 320-327, 2026.

[23]. Gutiérrez X. A., *et al.*, *Effects of chronic sub-lethal nitrite exposure at high water chloride concentration on Atlantic salmon (Salmo salar, Linnaeus 1758) parr*, Aquaculture Research, vol. 50 (2), p. 2687-2697, 2019.

[24]. Kir M., Sunar M. C., *Acute Toxicity of Ammonia and Nitrite to Sea Bream, Sparus aurata (Linnaeus, 1758), in Relation to Salinity*, Journal of the World Aquaculture Society, vol. 49(3), p. 516-522, 2018.

[25]. Cébron A., Garnier J., *Nitrobacter and Nitrospira genera as representatives of nitrite-oxidizing bacteria: Detection, quantification and growth along the lower Seine River (France)*, Water research, vol. 39 (20), p. 4979-4992, 2006.

[26]. Eck M., *et al.*, *Exploring Bacterial Communities in Aquaponic Systems*, Water, vol. 11(2), p. 260, 2019.

[27]. Rurangwa E., Verdegem M. C. J., *Microorganisms in recirculating aquaculture systems and their management*, Rev. Aquac, vol. 7, p. 117-130, 2015.

[28]. Itoi S., *et al.*, *Nitrite-oxidizing bacteria, Nitrospira, distribution in the outer layer of the biofilm from filter materials of a recirculating water system for the goldfish Carassius auratus*, Aquaculture, vol. 264 (1-4), p. 297-308, 2007.

[29]. Williams K. A., *et al.*, *Studies on the acute toxicity of pollutants to freshwater macroinvertebrates. Ammonia*, Archiv fur Hydrobiologie, vol. 106(1), p. 61-70, 1986.

[30]. Borgmann U., *Chronic toxicity of ammonia to the amphipod Hyalella azteca, importance of ammonium ion and water hardness*, Environ Pollution, vol. 86(3), p. 329-335, 1994.

[31]. Kater B. J., *et al.*, *Ammonium toxicity at high pH in a marine bioassay using Corophium volutator*, Arch. Environ. Contam. Toxicol, vol. 51(3), p. 347-351, 2006.

[32]. Xu Z., *et al.*, *Total Nitrogen Concentrations in Surface Water of Typical Agro- and Forest Ecosystems in China, 2004-2009*, PLoS ONE, vol. 9(3), 2014.

[33]. Peng H., *et al.*, *Study on Total Control of Total Nitrogen in the Laizhou Bay*, Water, vol. 13(17), p. 2439, 2021.

[34]. Aipova R., *et al.*, *Assessment of biotechnological potential of phosphate solubilizing bacteria isolated from soils of Southern Kazakhstan*, Natural Science, vol. 2(8), p. 841-845, 2010.

[35]. Malhotra H., *et al.*, *Phosphorus Nutrition: Plant Growth in Response to Deficiency and Excess*, Plant Nutrients and Abiotic Stress Tolerance, Springer Nature Singapore, p. 171-190, 2018.

[36]. Holt R. F., *et al.*, *Accumulation of phosphates in water*, Journal of Agricultural and Food Chemistry, vol. 18(5), p. 781-784, 1970.

[37]. Nieder R., *et al.*, *Reactive Water-Soluble Forms of Nitrogen and Phosphorus and Their Impacts on Environment and Human Health*, Soil Components and Human Health, p. 223-255, 2018.

[38]. Badamasi H., *et al.*, *Impacts of Phosphates on Water Quality and Aquatic Life*, Chemistry Research Journal, vol. 4(3), p. 124-133, 2019.

[39]. Kim E., *et al.*, *Aquatic Toxicity Assessment of Phosphate Compounds*, Environmental Health and Toxicology, vol.28, 2013.

[40]. Barnea M., Papadopol C., *Poluarea și protecția mediului*, Editura Științifică și Enciclopedică, București, 1975.

[41]. Davies T. D., *Sulphate toxicity to the aquatic moss, Fontinalis antipyretica*, Chemosphere, vol. 66(3), p. 444-451, 2007.

[42]. Moreno-Casas P. A., *et al.*, *Environmental Impact and Toxicology of Sulphate*, Enviromine, 2009.

[43]. Wu D., *et al.*, *Review of Chloride Ion Detection Technology in Water*, Applied. Sciences, vol. 11(23), p. 11137, 2021.

[44]. Szklarek S., *et al.*, *The effects of road salt on freshwater ecosystems and solutions for mitigating chloride pollution—A review*, Sci. Total Environ, vol. 805, 2022.

[45]. Enyoh E. C., *et al.*, *pH Variations and Chemometric Assessment of Borehole Water in Orji, Owerri Imo State, Nigeria*, Journal of Environmental Analytical Chemistry, vol. 5(2), p. 2380-2391, 2019.

[46]. Wojnárovits L., *et al.*, *Wastewater Characterization: Chemical Oxygen Demand or Total Organic Carbon Content Measurement?*, Molecules, vol. 29(2), p. 405, 2024.

STATIC ANALYSIS OF A THERMAL SUPPORT

Ionel PETREA, Marian-Iulian NEACȘU

"Dunarea de Jos" University of Galati, Romania

e-mail: ionel.petrea@ugal.ro, marian.neacsu@ugal.ro

ABSTRACT

In this paper, a simulation is performed using CATIA software and the finite element method, regarding the static analysis of a thermally stressed support. The simulations were performed for several temperatures: 20 ºC, 100 ºC, 200 ºC, and 300 ºC, in order to observe the behavior of the support made of different materials at these temperatures.

KEYWORDS: modeling, simulation, support, constraints, thermal stress

1. Introduction

Engineering activity, in general, has as its outcome the creation of technical objects, which materialize as a result of complex production processes. The main stages of the creation of a technical product are: defining a general concept of the product, creating the technical project, establishing the manufacturing technology, creating the experimental model and product approval, and the actual manufacturing [1].

In the design of these structures, an integrated CAD/CAM/CAE software may be used, which incorporates the finite element analysis module FEM [2].

Support-type structures have the role of supporting components, being made of metal profiles. Thermal fields appear in these structures during their operation or during heat treatment processes. Stresses and deformations due to thermal fields are important parameters that must be taken into account in the product design stage.

CATIA (Computer Aided Three Dimensional Interactive Applications), a product of the Dassault Systems company, is one of the most widely used integrated CAD/CAM/CAE systems worldwide, with applications in various fields, including: the machine-building industry, aeronautics, naval, automotive, robotics, agricultural machinery, chemical and food industries, and many others.

The Finite Element Method (FEM) is one of the best existing methods for performing various calculations and simulations in the field of engineering. This method has become a basic component of modern computer-aided design systems.

Analyses performed using FEM are indispensable in all high-performance engineering activities.

FEM involves dividing the part into finite elements, a process called discretization. The result is a network of nodes and elements, called a mesh. At the nodes of the mesh, the program calculates the stresses and deformations that occur in the part, depending on the demands to which it is subjected. Essentially, the system of equilibrium equations between external forces and the stresses that occur is numerically solved.

Calculations performed using FEM represent a very important stage of the design, but can generally be performed only after clarifying other aspects, such as: the beneficiary's requirements, imposed costs, delivery times, available materials and technologies, product durability, production volume, ecological requirements, etc. [3, 5].

Thus, for a given product, some restrictions can be taken into account: the number and maximum value of static and/or dynamic loads, maximum values of deformations, different safety coefficients (for buckling, rupture or fatigue), minimum sensitivity to imperfections in execution, assembly or operation, vibration frequencies, deformation speed in stationary plastic flow, product life, weight, material and its moments of inertia, rigidity under different stresses, static and/or dynamic stability, behavior under different simultaneous loads, etc.

It should be noted that in the CAD-FEM-CAM sequence there is an iterative process of design-calculation-execution. In this process, synthesis and analysis operations of the prototype and the model for finite element calculation are successively performed.

At each iteration of the process, improvements are made to the prototype or computational model until the desired performance is achieved.

The finite element analysis of a structural model is, in fact, a numerical verification process. Thus, for a given, dimensionally defined geometry, for a given load and clearly specified support conditions (restrictions), the values of displacements, stresses, support reactions, natural frequencies, etc. are obtained [5, 6].

2. Finite Element Analysis Steps

One of the major advantages of the finite element analysis method is the simplicity of the basic concepts. It is very important for the user of a FEM program to understand and correctly apply these concepts because they include certain assumptions, simplifications and generalizations.

Finite element analysis involves going through the following steps [3]:

I. Geometric modeling of the part or component assembly. The Sketcher and Part Design modules, as well as the Assembly Design module, are used.

II. Applying a material, using the Apply Material icon.

The CATIA material library has a wide variety of materials.

In the practice of finite element analysis, the model material can be homogeneous and isotropic or anisotropic in nature. Also, the elastic and physical constants of the material may depend on temperature and/or stress.

Among the mechanical properties of the applied material, the most important is the admissible resistance, Yield Strength, expressed in MPa. The maximum stresses that occur in the part, calculated by the program, must not exceed the allowable resistance. Otherwise, it is necessary to return to the design stage and apply another material or resize the part.

III. Accessing the finite element analysis module, which includes the following steps:

1. Discretization of the part. By default, in CATIA, the part is discretized (divided into finite elements), but the designer has the possibility of modifying the size and type of the finite elements. Thus, from the command tree, access Finite Element Model/Nodes and Elements/Octree Tetrahedron Mesh, Figure 1.
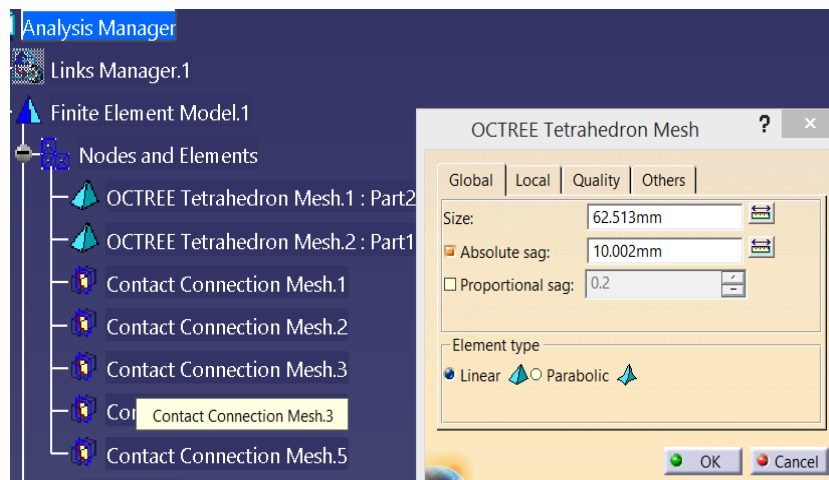
Fig. 1. *Determining the dimensions of finite elements*

2. Specifying restraints and constraints, using the tools on the Restraints toolbar.

Constraints represent an interface between the analysed model and the subassembly or assembly of which it is a part. If the model is not correctly constrained, the finite element analysis will give significant errors. Some examples of constraints include:

Clamp - constrains all degrees of freedom for a curve or surface.

Surface Slider - allows points on a deformable surface to slide along a rigid surface.

Slider - creates a prismatic joint constraint.

Sliding Pivot - creates a cylindrical joint constraint.

Pivot - are conical joint constraints.

User defined - creates generic constraints, allowing any combination of nodal degrees of freedom to be set.

3. Defining the loads to which the part is subjected, using the Loads toolbar.

The Loads tools add various loads to models that are analysed with FEM. Examples of loads include:

Pressure - this load, expressed in MPa, creates a uniform pressure, applied to a certain surface.

Distributed Force - distributed forces are, in fact, systems of forces statically equivalent to a resultant of a real force.

Moment - moments are systems of forces equivalent to a resultant torque (Nxm).

Bearing Load - simulates a contact load applied to surfaces of revolution.

Acceleration - represents concentrated loads of the acceleration field type (N/kg or m/s^2).

Line Force Density - represents concentrated loads (N/m) of the linear traction force field type.

Temperature Field - creates temperature fields, in degrees Kelvin (K) on the bodies of the analysed models.

4. The calculation stage, using the Adaptivity and Compute toolbars.

The Compute tool triggers the finite element analysis process, but only for the fully constrained and loaded model. It can perform static analysis, frequency analysis and free frequency analysis (Figure 2).
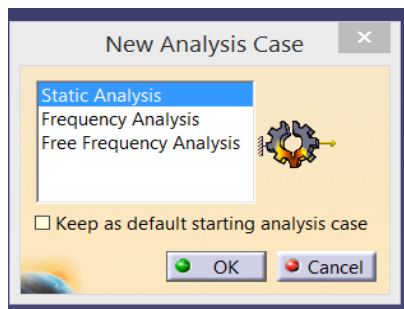
Fig. 2. Types of analysis with FEM

The calculator specifies the resources required for the calculation (Figure 3).
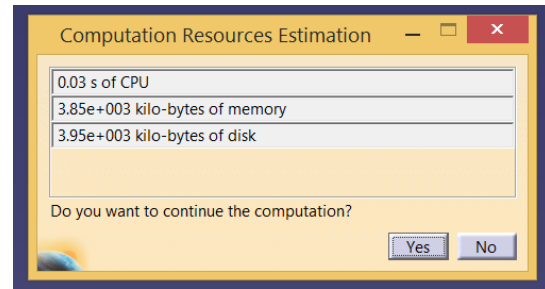
Fig. 3. Estimated resources for calculation

With the help of the New Adaptivity Entity tool, the user can refine the network of nodes and elements (mesh), so as to obtain the required precision of the mesh.

In industrial practice, it is considered that the model is correctly solved if it meets an error percentage of approximately 10%.

5. Processing the results - using the tools on the Image bar

3. Static analysis of a thermally stressed support

Thermal fields appear in structures during their operation or during various heat treatment processes. Stresses and deformations due to thermal fields are important parameters that must be taken into account during the product design stage.

The design of mechanical structures subjected to thermal fields and/or mechanical loads requires solving problems by also taking into account the influence of the thermal field on their resistance and deformation, which can be decisive in certain cases.

Figure 4 shows the diagram of a mechanical support-type structure, used to support parts subjected to heat treatments. The model can also be used to cool continuously cast slabs.
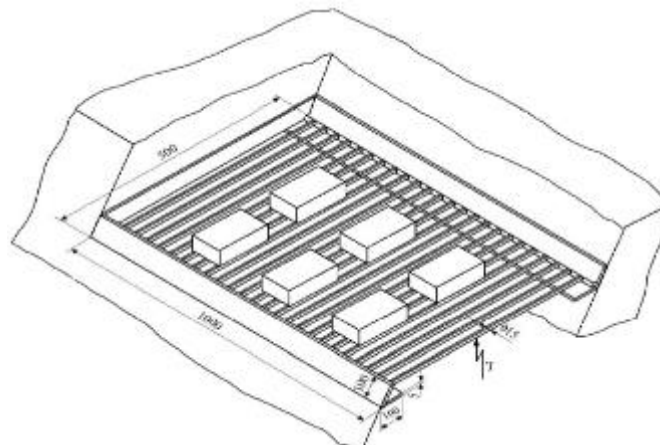

Fig. 4. Mechanical support structure

The application aims to determine the maximum values of the von Mises equivalent stress and, respectively, the displacement, produced by the thermal field acting on the support system at a temperature of t = 300 ºC and by the weight of the parts subjected to heat treatments, G = 2000 N.

The analysed structure is made of OL37 steel, with the following mechanical characteristics:

$E = 2.1 \cdot 10^5$ N/mm², where E is the longitudinal modulus of elasticity;

$\rho = 7800$ kg/m³ represents the density;

Transverse shrinkage coefficient (Poisson) = 0.3.
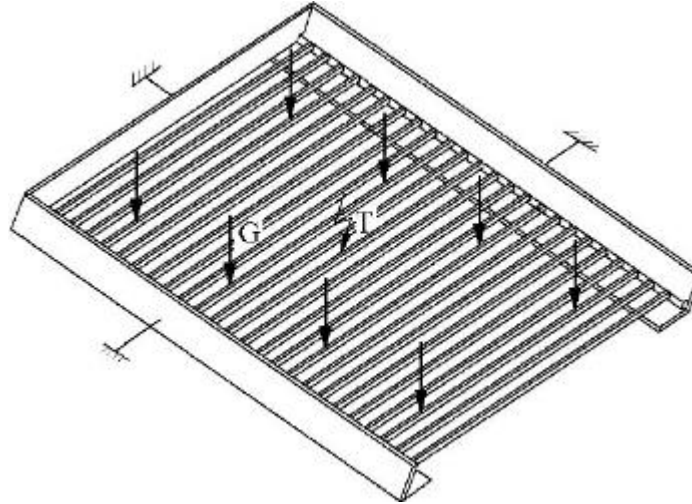
Fig. 5. *The analysis model*
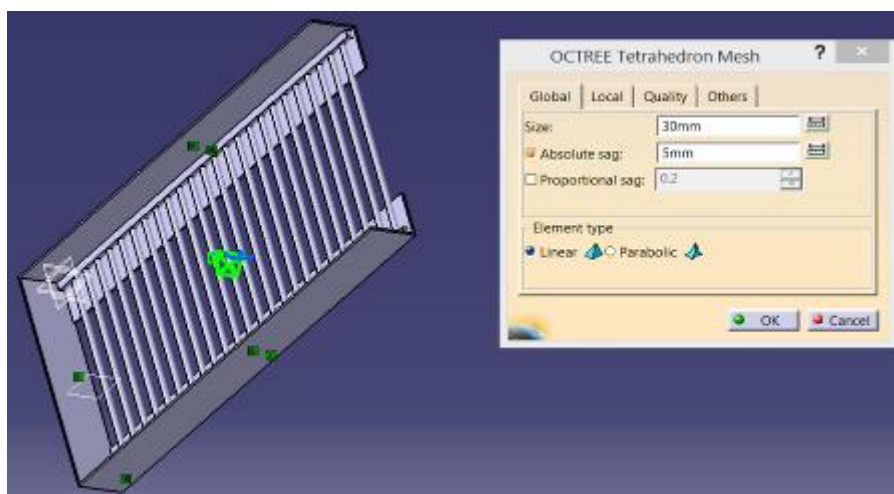
4. Finite element modeling

The main condition for a model to be analysed using the finite element method is that the user assigns a material for it that corresponds to its functional role.

To generate the finite element model, the commands Start ⇒ Analysis & Simulation ⇒ Generative Structural Analysis ⇒ New Analysis Case ⇒ Static Analysis ⇒ OK are followed, which enables the static analysis of the assembly under the conditions of imposed constraints and time-independent loading conditions.

For the component elements of the mechanism, the finite element size and the maximum permissible deviation for geometric modeling sag are chosen according to the figure (the menu being activated by double-clicking on OCTREE Tetrahedron Mesh.1: the part-type elements are successively selected from the specification tree).

Dimensions of 30 mm are imposed for the finite elements, with a maximum deviation of 5 mm, using linear elements (Figure 6).


Fig. 6. *Determining the dimensions of finite elements*

4.1. Constraint Modeling

In general, constraints can be applied to a single element (Length, Fix, Horizontal, Vertical) or between two elements (Distance, Angle, Coincidence, Parallelism, Perpendicular). Often, constraints are applied to selections consisting of several sketch elements.

A constrained profile does not allow its dimensions to be modified except by editing the component constraints individually. Editing the value of a constraint is done by double-clicking the mouse on the respective constraint, resulting in the appearance of the dialog window (Constraint Definition), which allows the modification of the respective value.

Modeling the connections between the support surface and the frame is done by selecting the geometric contact connections using the Contact Connection command between the frame and the support surface (Figure 7).
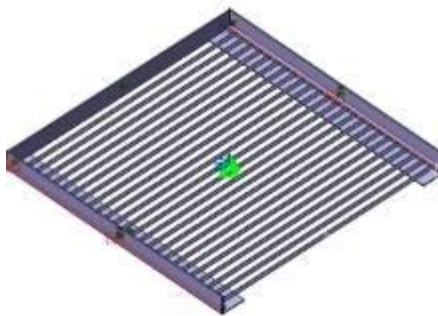
**Fig. 7.** *Modeling the connections between the support surface and the frame*

The connection with the base imposed on the side surfaces of the frame is defined by cancelling the 6 degrees of freedom associated with the surfaces: (Clamp), Clamp Name: Clamp.1, Supports: two faces selecting the side surfaces of the frame, OK (Figure 8).
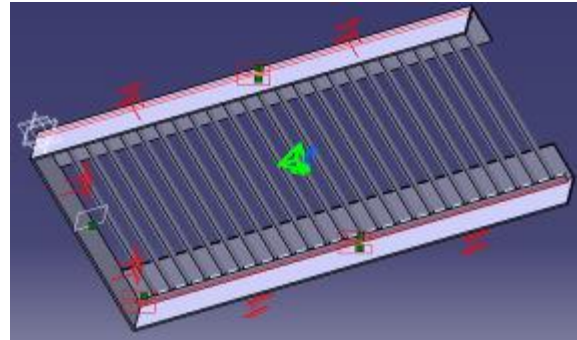
Fig. 8. *Applying restrictions*

4.2. Load Modeling

The loads are modeled in the form of a distributed force acting on the frame (Distributed Force), with Supports: 24 faces, selected as the upper faces of the frame profiles; Force vector: X = 0 N, Y = –2000 N, Z = 0 N, and in the form of a thermal field acting on the support (Temperature Field), applied by selecting the frame; temperature: 573 K, OK (300 ºC = 573 K) (Figure 9).
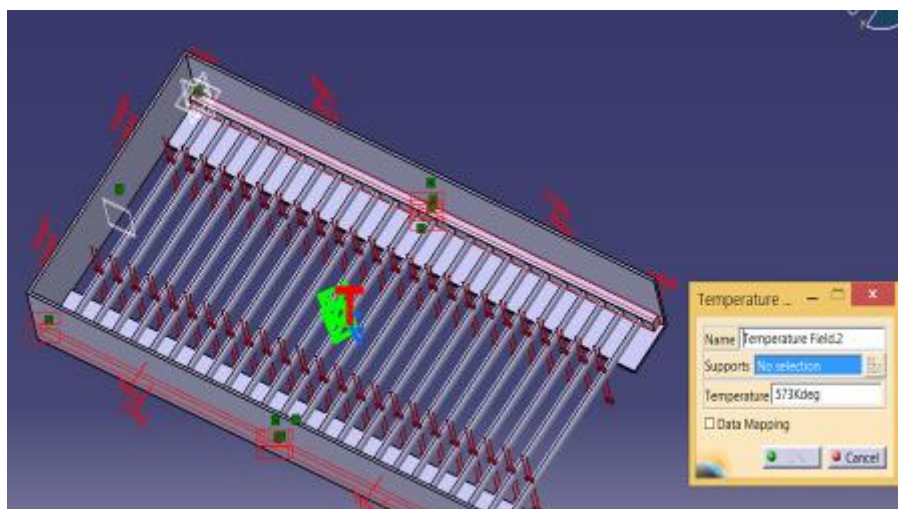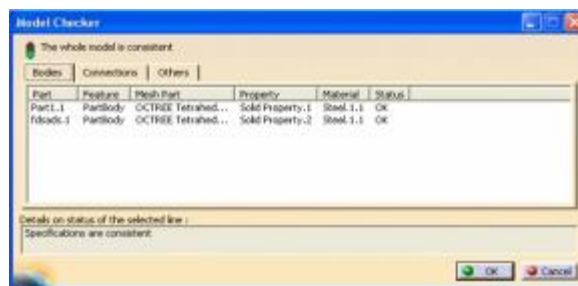

Fig. 9. *Application requests*
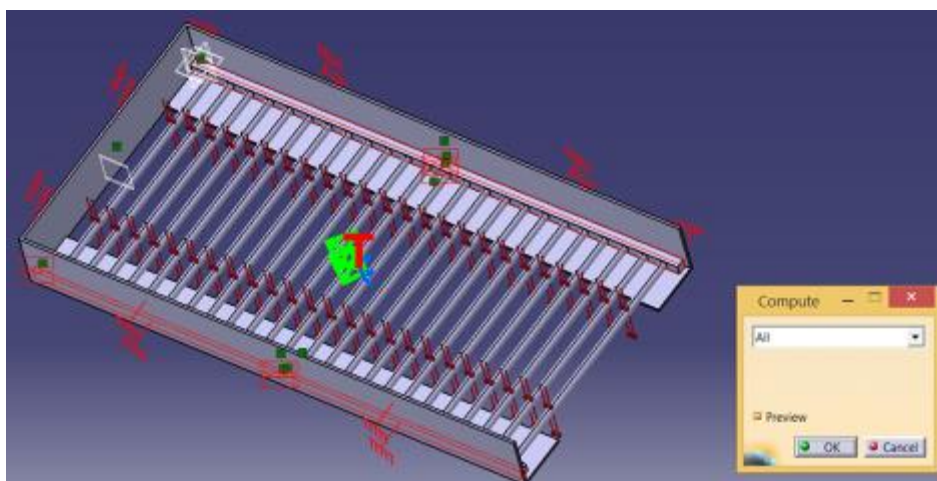
4.3. Model Checking

In the model checking stage, information is obtained about the correctness of the generated model: (Model Checker), OK; the green LED is lit and is accompanied by a message confirming the correctness of the model preparation.
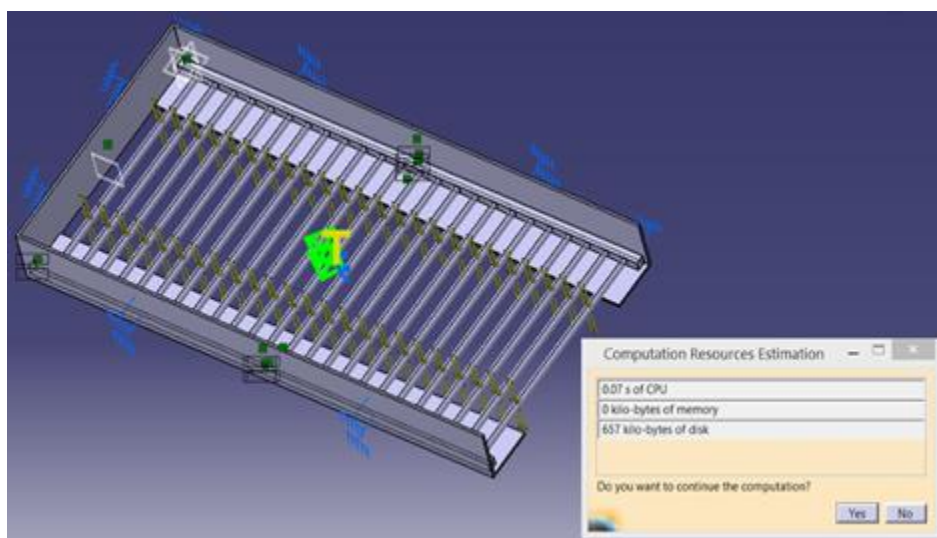

Fig. 10. *Model check*

4.4. Model Solving

The model is solved automatically by the software: (Compute) ⇒ Compute ↓All (Figure 11).

Fig. 11. *Calculation step*


Fig. 12. *Computing resources*

5. Processing the results

CATIA provides the results of the finite element analysis in the form of images. There are five such results:
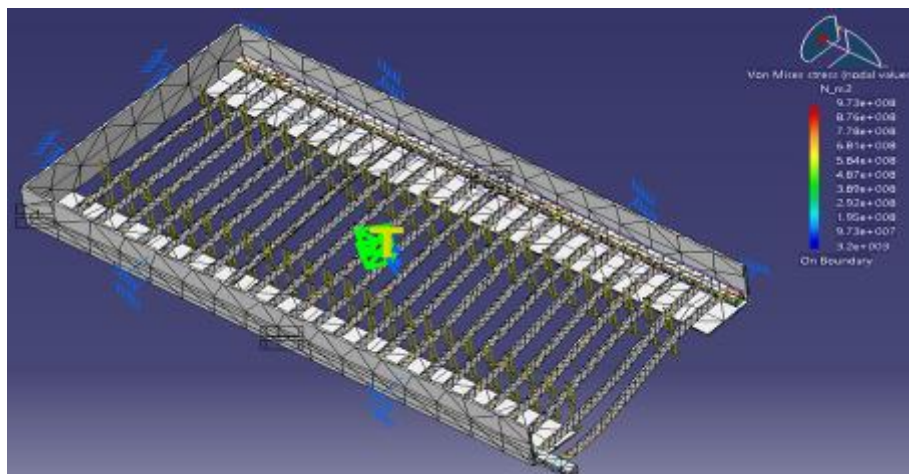
The deformed state of the model is visualized by activating the Deformation command.

The scale factor is modified by activating the Deformation Scale Factor icon, Figure 13.

Von Mises equivalent stresses are obtained using Stress Von Mises command, Figure 14.
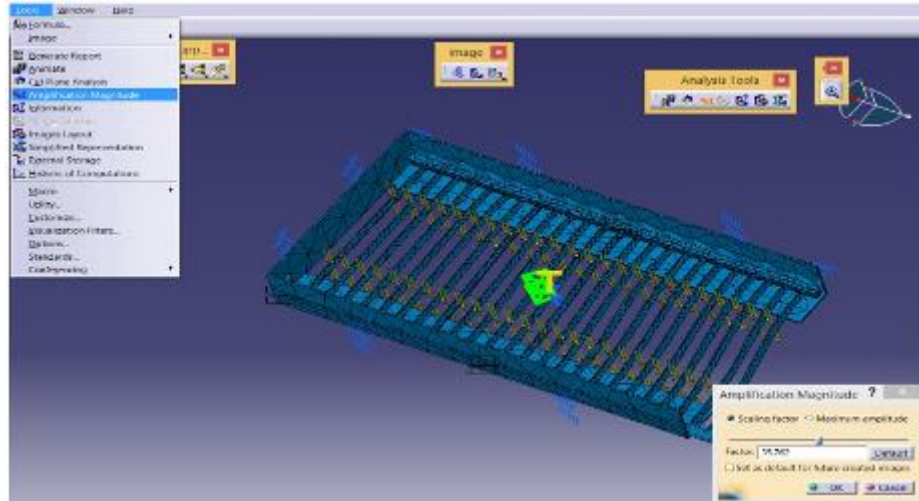
Fig. 13. *Deformed state of the model*

Fig. 14. *Von Mises equivalent stresses*

The maximum of the Von Mises equivalent stresses is found in the support elements and has a value of approximately 973 MPa.

To reduce these stresses, constructive and/or technological measures are adopted, such as increasing the support profile or using materials with superior mechanical properties.

The displacement field is visualized by the command (Displacement), Figure 15, where the maximum displacement reaches 3.38 mm.

The principal stress tensor is presented in Figure 16.

The maximum principal stresses are approximately 329 MPa. These stresses are lower than the von Mises equivalents. However, in the design of the support, the von Mises equivalents must be taken into account, as these stresses are correlated with the yield strength of the steel.

Calculation accuracy and the information window are presented in Figure 17.

The estimated global error rate is about 21%, a value that is unacceptable in the design and simulation process.

To reduce these errors, the simulation is repeated after mesh refinement, considering that the

repetition of the analysis in order to reduce the global error value is done by applying the New Adaptivity Entity tool.

Thus, in the "Global Adaptivity" dialog window, in the "Supports" field, the "OCTREE Tetraltedron Mesh" element is selected, then in the "Objective Error (%)" field, the target value of 13% is entered.
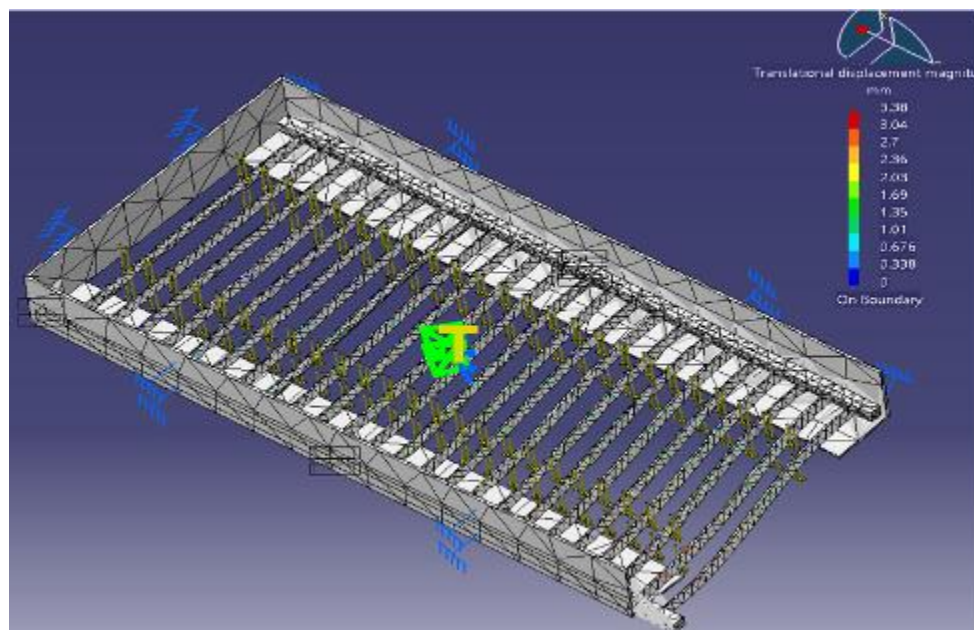
Fig. 15. *The field of displacements*
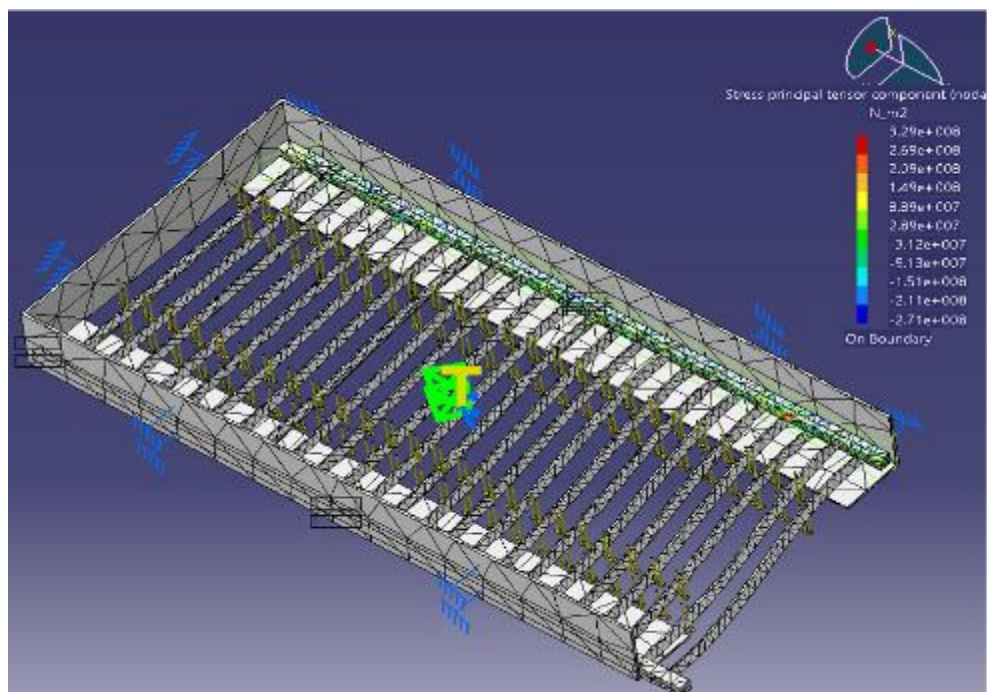
Fig. 16. *Principal stress tensor*

Fig. 17. *Estimated calculation error rate*

6. Conclusions

The simulations were performed for several temperatures: 20 ºC, 100 ºC, 200 ºC and 300 ºC.

The values for the von Mises equivalent stresses, principal stresses and displacements are presented in Table 2.

Table 2. *Stress and strain values*

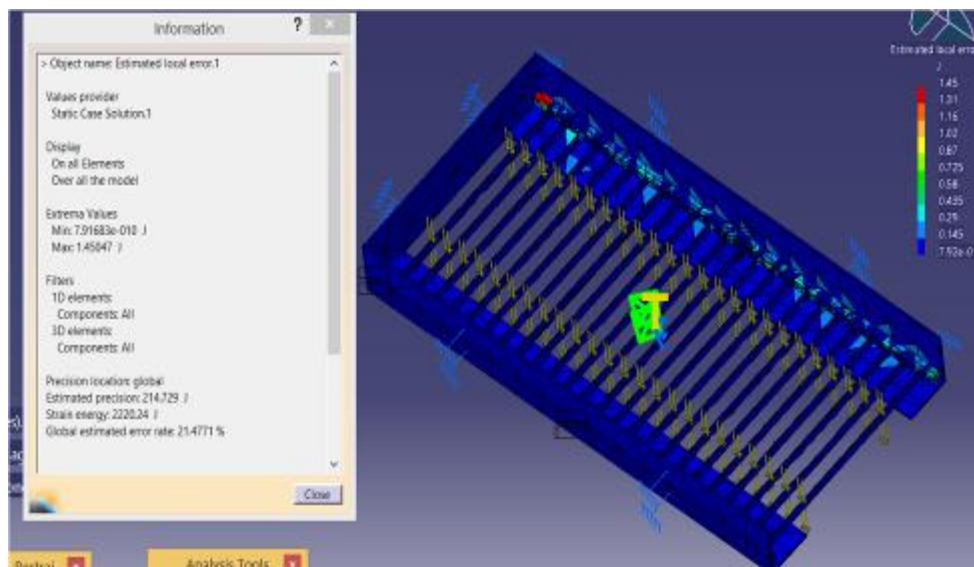| Temperature	20 ºC	100 ºC	200 ºC	300 ºC
Von Mises stress - MPa	8	278	626	973
Stress principal tensor component - MPa	6.2	94	212	329
Translational displacement magnitude - mm	0.04	0.96	2.17	3.38

Table 3. *Yield strength for structural steels*

Steel	OL37	OL44	OL50	OL60
Yield strength $R_{p0,2}$	240	260	290	330

Thus, with an applied force of 2000 N, the maximum stress is 973 MPa at a temperature of 300 ºC. These values indicate that none of the steels are suitable for manufacturing the support. Larger dimensions and thicknesses of the support, or a steel with superior mechanical properties, are required.

When simulating with an applied force of 500 N, at a temperature of 300 ºC, the maximum stress is 220 MPa. From these values, it follows that all four steels can be used to make the support.

References

[1]. **Ghionea I.**, *CATIA Knowlegle Advisor. Utilizarea regulilor, formulelor şi reacţiilor pentru parametrizarea completă a unui motor hidraulic linear*, Tehnică şi Tehnologie, nr. 3, Editura Tehnic Media, Bucureşti, 2003.
[2]. **Ghionea I.**, *Module de proiectare asistată în CATIA V5 cu aplicaţii în construcţia de maşini*, Editura BREN, Bucureşti, 2004.
[3]. **Marin C., *et al.***, *Modelarea cu elemente finite a structurilor mecanice*, Editura Academiei Române, Bucureşti, 2002.
[4]. **Tache V., *et al.***, *Elemente de proiectare a dispozitivelor pentru maşini-unelte*. Editura Tehnică, Bucureşti, 1985.
[5]. **Trebaol G.**, *Designing parametric spur gears with Catia V5*, 2007.
[6]. *****, *CATIA V5R15*, Documentaţie de firmă. Dassault System, 2005.

EVALUATION OF EDGE DETECTION AND FUSION METHODS FOR ANGIOGRAPHIC IMAGE PROCESSING

Cristian-Dragoș OBREJA

Department of Materials and Environmental Engineering, Faculty of Engineering, "Dunarea de Jos" University
of Galati, 47 Domneasca, 800008 Galati, Romania
e-mail: cristian.obreja@ugal.ro

ABSTRACT

This study explores the application of digital image processing techniques to improve the diagnostic accuracy of coronary artery disease through enhanced analysis of angiographic images. A curated dataset of 40 grayscale, single-vessel angiograms was used to evaluate the effectiveness of various preprocessing and edge detection methods. Preprocessing steps included noise reduction, histogram equalization, and morphological operations aimed at improving image clarity and highlighting vascular structures. Three edge detection algorithms, Otsu, Canny, and Roberts, were applied, and their outputs were further combined using the Dempster-Shafer fusion theory. Performance was assessed using edge-based structural similarity (ESSIM) and the percentage error in vessel diameter measurements. The Canny algorithm demonstrated the highest individual accuracy, while the fusion of Canny and Roberts yielded superior results, achieving the lowest error and the highest similarity index.

KEYWORDS: medical image analysis, coronary artery disease, edge detection, image fusion, structural similarity

1. Introduction

The human ability to interpret the surrounding environment relies largely on visual information, but natural perception is often limited in identifying subtle details in images. Medical imaging, addresses these limitations through a set of methods dedicated to the acquisition, processing and analysis of digital images obtained using various specialized devices [1]. The process begins with image generation using medical equipment, followed by preprocessing steps that include noise removal, contrast correction, and contour enhancement; segmentation also enables the automatic delineation of anatomical structures of interest based on homogeneity criteria. The choice of this research direction is justified by its transdisciplinary nature, combining principles from physics, mathematics, and computer science to support medical analysis [1-3].

This paper explores the role of digital image processing in supporting the assessment of cardiovascular conditions, focusing on coronary pathology, a major cause of mortality associated with heart disease. The methodology involves applying a set of algorithms in successive stages to medical images, with the aim of examining how these techniques can detect vascular structures relevant to diagnosis [4]. Additionally, the integration of results is tested using a fusion algorithm, to determine whether combining different methods can lead to a more accurate vascular map. The impact of the results is analysed in comparison with the original images, using indicators such as structural difference measurement and percentage error calculation, to assess accuracy [5-11].

2. Materials and methods

2.1. Database

The dataset used in this study consists of 40 angiographic images from patients diagnosed with single-vessel coronary artery disease, examined using Coroscop (Siemens) and Innova (GE Healthcare) equipment at the Research Institute for Complex Cardiovascular Problems (Kemerovo, Russia). Out of the total set of images (ranging in size from 512×512 to 1000×1000 pixels), 40 relevant ones were manually selected, each containing contrast-enhanced passages through stenotic vessels.
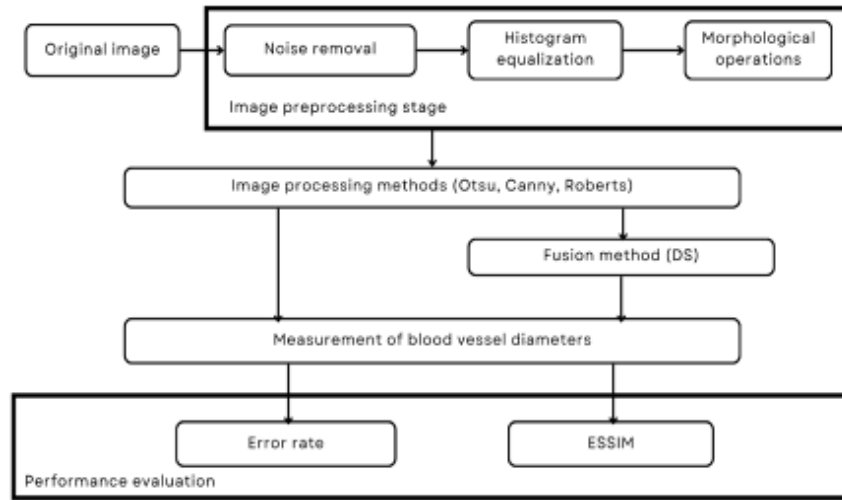
Fig. 1. *Flow chart of the proposed method*

2.2. Image preprocessing

The preprocessing stage plays a central role in image analysis, aiming to improve visual quality by reducing noise and eliminating irrelevant information. It also contributes to increased processing efficiency by reducing execution time and enhancing important details, such as edges. Noise filtering is essential because digital images can be affected by various types of noise introduced during acquisition, causing pixel intensity variations that do not reflect reality [12, 13]. Histogram equalization is frequently used to improve contrast by redistributing grey tones to highlight subtle details; an extension of this, CLAHE, allows for the enhancement of local contrast in poorly defined areas. Contrast adjustment involves transforming pixel values into an optimal range, increasing the visibility of relevant features [9]. Morphological operations, such as dilation, erosion, or contour and skeleton extraction, modify the structure of objects in the image and are applied using a structuring element [13].

2.3. Image processing algorithms

The Otsu method is an automatic technique used for determining the optimal threshold for binarizing grayscale images, based on the distribution of values in the histogram. The algorithm assumes the existence of two classes of pixels and determines the threshold that separates these classes by minimizing intra-class variance, ensuring a clear distinction between different regions of interest. Furthermore, the method iteratively evaluates all possible threshold values and selects the one for which the difference between the classes is maximized, meaning that pixels with values below the threshold are considered

background, while those with values equal to or above represent the image foreground [14, 15].

The Canny edge detection method is considered one of the most effective techniques for detecting edges in images. The method aims to achieve accurate detection by minimizing errors, ensuring correct localization of edge points, and generating a single response for each real edge. It unfolds in five steps: applying a Gaussian filter to reduce noise, calculating the intensity gradient, eliminating false responses through non-maximum suppression, using a double threshold to identify potential edges, and retaining only the strong edges [16].

The Roberts edge detection method offers a fast and efficient approach for estimating the two-dimensional spatial gradient of an image, in order to highlight regions with abrupt intensity changes. The Roberts operator is typically applied to grayscale images and produces an output image in which each pixel reflects the magnitude of the local spatial gradient, which enables clear outlining of the vessel edges [17].

2.4. Dempster-Shafer Fusion for Edge Detection

The Dempster-Shafer theory is a mathematical method for evidence analysis, used to combine information from independent sources in order to estimate the probability of an event. It is based on belief functions and plausible reasoning, allowing uncertainty to be managed by gradually narrowing down a set of competing hypotheses as new evidence becomes available [18].

In image processing, the Dempster-Shafer method has been used to combine the results obtained through the Otsu, Canny, and Roberts methods in

pairs of two methods, with each filter treated as a source of evidence. Their results are interpreted as fusion events, representing the classification of pixels into either "edge" (E) or "non-edge" (N) classes. The combination rule integrates the belief functions of each method, weighting their respective contributions through a coefficient w to obtain an optimal confidence level for edge detection [18, 19].

2.5. Image Processing Evaluation

The performance of the image processing methods was evaluated by calculating the percentage error and analysing structural similarity based on edge detection. The percentage error of the blood vessel diameters was calculated using the formula: $e = \frac{|M_R - M_i|}{M_R} \times 100\%$, where M_R represents the ground truth diameter values from the original images, and M_i corresponds to the diameter value measured after applying classical methods and the fusion algorithm [18].

ESSIM enables the evaluation of the degree of structural similarity between the original and processed images, in order to determine the accuracy of edge detection. However, ESSIM requires careful parameter tuning, as its performance can vary depending on the structure and complexity of the analysed images [20-22].

3. Results and discussion

To assess the impact of image processing on the diagnosis of coronary conditions, a workflow was implemented, consisting of preprocessing, edge detection and evaluation. The preprocessing stage included noise reduction, histogram equalization, and morphological operations, aiming to enhance clarity and highlight regions of interest. Three processing algorithms were applied to a set of 40 angiographic images to identify the optimal method for highlighting vascular structures, and the results generated were combined using a fusion method. The accuracy of each technique was analysed through measurements of vessel diameter. The quality of the results was quantified using the ESSIM algorithm, which estimates structural similarity between fused and processed images and the original image.
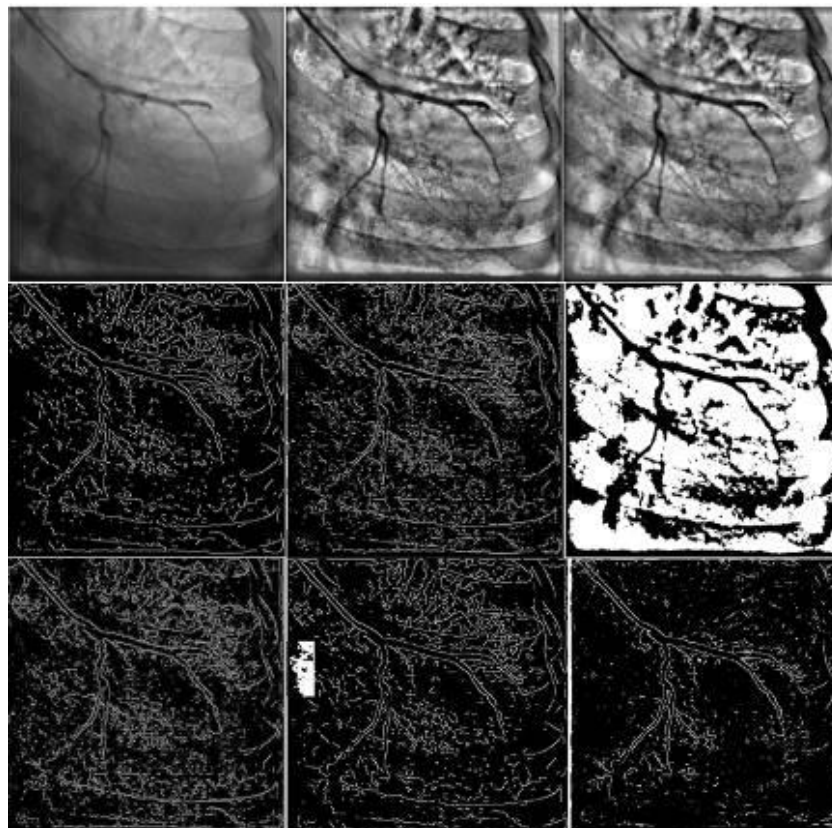
Fig. 2. Examples of vascular map. (a) Original input image; (b) CLAHE; (c) Morphological operation; (d) Canny filter; (e) Roberts filter; (f) Otsu filter; (g) Canny-Roberts fusion; (h) Roberts-Otsu fusion; (i) Canny-Otsu fusion

***Table 1.** Average blood vessel diameter values and mean percentage error*

	Ground truth	Otsu Method	Canny Method	Roberts Method
Average values	18.721	17.099	18.129	17.699
% error	-	*8.560*	*3.121*	*5.392*

	Ground truth	Otsu-Roberts Fusion	Otsu-Canny Fusion	Canny-Roberts Fusion
Average values	18.721	17.337	17.943	18.383
% error	-	*7.361*	*4.149*	*1.851*

***Table 2.** Structural similarity index (ESSIM) calculated between the processed images and the original image*

	ESSIM values
Otsu Method	0.973335
Canny Method	0.967023
Roberts Method	0.974530
Otsu-Roberts Fusion	0.98801
Otsu-Canny Fusion	0.983434
Canny-Roberts Fusion	0.994312

The analysis of image preprocessing methods highlights the efficiency and limitations of each algorithm used. The noise reduction filter, although it does not produce visually noticeable changes, significantly contributes to improving the results of subsequent processing by eliminating noise. Although its values deviate from those of the original image, the main purpose of this filter is to clean the raw data. In contrast, histogram equalization proved to be the most effective preprocessing method, offering strong contrast and clearly highlighting the region of interest. The morphological operation further enhanced vascular structures and contributed to the improvement of visual quality, although with a smaller quantitative impact compared to histogram equalization.

In the processing stage, three methods were applied: Otsu, Canny, and Roberts. The Otsu method showed limitations, either causing loss of relevant information or false identification of areas of interest, while the Canny edge detection algorithm delivered the best results, both visually and in measured values, preserving essential edges without significantly affecting the region of interest. The Roberts algorithm resulted in less clear segmentation, with weak separation between useful and redundant information.

Evaluating the results of the fusion method indicates a clear advantage in terms of accuracy, as it generates lower error rates than any of the individual classical edge detection techniques. Examination of Figure 2 further highlights certain limitations of traditional filters like Otsu, Canny and Roberts, which frequently introduce artifacts such as duplicated or incomplete edges. In contrast, the fusion-based approach demonstrates enhanced reliability, producing more accurate vascular maps and minimizing segmentation errors, with percentage error as low as 1.85% in the case of Canny-Roberts fusion, while the smallest error among the classical algorithms is 3.12% when using the Canny algorithm.

Performance evaluation using the structural similarity coefficient (ESSIM) confirmed the superiority of the Canny method (among the three classical methods), although all three methods fell within the similarity range of 0.95–0.97 when compared to the original image. Finally, the application of the Dempster-Shafer fusion method demonstrated that integrating information from the Otsu-Canny and Otsu-Roberts pairs yields satisfactory results, better than each method on its own, while the Canny-Roberts fusion outperformed both the individual performance of the Canny method and the other two paired fusions, according to the values in Table 2.

4. Conclusions

The main objective of this paper was to identify the most effective image processing techniques for optimizing the diagnosis of coronary artery disease. Based on experimental values, the Canny method stood out for its superior performance in image segmentation, delivering the best results among the three analysed algorithms. The Roberts algorithm achieved comparable results, according to the evaluation using the structural similarity coefficient (ESSIM), while the Otsu method, although less effective in terms of quality, still recorded an acceptable level of fidelity. The application of these methods revealed a significant improvement in image

quality, directly contributing to the facilitation of the medical diagnosis process.

Moreover, the use of the fusion algorithm based on Dempster-Shafer theory demonstrated greater robustness against variations in illumination and noise, and the low mean error in vascular diameter measurements supports the potential of this method as a viable alternative to conventional techniques. The most promising results were obtained from the fusion of the Canny and Roberts methods.

References

[1]. Chellappa R., Rosenfeld A., *Image Processing*, Encyclopedia of Physical Science and Technology, p. 595-630, 2003.

[2]. Ekstrom M. P., *Digital Image Processing Techniques*, Academic Press, Orlando, FL, 1984.

[3]. Abràmoff M. D., *et al.*, *Pivotal trial of an autonomous AI-based diagnostic system for detection of diabetic retinopathy in primary care offices*, Digital Medicine, 1(1), p. 1-8. https://doi.org/10.1038/s41746-018-0040-6, 2018.

[4]. Riaz T., *et al.*, *The analysis of retinal blood vessels and systemic diseases includes the relationship between retinal blood vessels and myocardial infarction (heart disease), and retinal blood vessels and cerebrovascular diseases*, IAIM, 10(11), p. 61-68, 2023.

[5]. Zhang L., Zhang J., *A New Saliency-Driven Fusion Method Based on Complex Wavelet Transform for Remote Sensing Images*, in IEEE Geoscience and Remote Sensing Letters, vol. 14, no. 12, p. 2433-2437, doi: 10.1109/LGRS.2017.2768070, Dec. 2017.

[6]. Li R., *et al.*, *A survey of multi-source image fusion*, Multimed Tools Appl, 83, p. 18573-18605, https://doi.org/10.1007/s11042-023-16071-9, 2024.

[7]. Acharya and Ray, *Image Processing Principles and Applications*, Wiley-Interscience, ISBN 0-471-71998-6, 2005.

[8]. Buades A., *et al.*, *Efficient joint noise removal and multi exposure fusion*, PloS One, 17(3), e0265464, doi: 10.1371/journal.pone.0265464, 2022.

[9]. Haddadi Y. R., *et al.*, *A novel medical image enhancement algorithm based on CLAHE and pelican optimization*, Multimed Tools Appl, https://doi.org/10.1007/s11042-024-19070-6, 2024.

[10]. Russ, *The Processing Handbook*, Fourth Edition, CRC 2002 ISBN 0-8493-2532-3.

[11]. Hanan Saleh S. Ahmed, J. Nordin, *Improving Diagnostic Viewing of Medical Images using Enhancement Algorithms*, Journal of Computer Science, 7(12), p. 1831-1838, 2011.

[12]. Budai A., *et al.*, *Robust vessel segmentation in fundus images*, International Journal of Biomedical Imaging, Article 154860, https://doi.org/10.1155/2013/154860, 2013.

[13]. Klein R., *et al.*, *Changes in retinal vessel diameter and incidence and progression of diabetic retinopathy*, Arch Ophthalmol, 130, p. 749-755, PMID: 22332203, 2012.

[14]. Fielding S., *Segmentation and Focus. Digital Video Processing for Engineers*, p. 181-190, doi:10.1016/b978-0-12-415760-6.00019-2, 2013.

[15]. Otsu N., *A Threshold Selection Method from Gray-Level Histograms*, IEEE Transactions on Systems, Man, and Cybernetics, vol. 9, no. 1, p. 62-66, doi: 10.1109/TSMC.1979.4310076, 1979.

[16]. Canny J., *A Computational Approach to Edge Detection*, IEEE Transactions on Pattern Analysis and Machine Intelligence, vol. PAMI-8, no. 6, p. 679-698, doi: 10.1109/TPAMI.1986.4767851, 1986.

[17]. Mogos G., *Quantum Image Processing Using Edge Detection Based on Roberts Cross Operators*, Lecture Notes in Networks and Systems, vol 945, Springer, Singapore, https://doi.org/10.1007/978-981-97-1320-2_13, 2024.

[18]. Moraru L., Obreja C. D., *Retinal vessel enhancement based on the Gaussian function and image fusion*, AIP Conf. Proc., 1796 (1), 040007, https://doi.org/10.1063/1.4972385, 2017.

[19]. Qiu S., *et al.*, *Fortino, Multi-sensor information fusion based on machine learning for real applications in human activity recognition: State-of-the-art and research challenges*, Information Fusion, vol. 80, p. 241-265, doi.org/10.1016/j.inffus.2021.11.006, 2022.

[20]. Betrabet S., Bhogayta C. K., *Structural Similarity based Image Quality Assessment using full reference method*, International Journal of Scientific Engineering and Technology, 4(4), p. 252-255, 2015.

[21]. Li Cui, Alastair R. Allen, *An image quality metric based on corner, edge and symmetry maps*, In BMVC, p. 1-10, 2008.

[22]. Cheng J., Wang Z., *Improved structural similarity index for image quality assessment*, Journal of Computer Science, 10(2), p. 353-360, 2014.

MATHEMATICAL MODELING
OF THE CARBONITRIDING PROCESS FOR OLC 25 STEEL

Marian-Iulian NEACȘU

"Dunarea de Jos" University of Galati

e-mail: mneacsu@ugal.ro

ABSTRACT

The paper is based on research on several experimental carbonitriding regimes of OLC25 steel samples.

Following the experiment for each regime, the HV microhardness values of the treated samples were measured at various points (identical for all samples) along the depth of the carbonitrided layer. The results of these measurements were compiled into a database that was used to create a mathematical model of the carbonitriding process.

The paper presents the results of mathematical modeling based on an active experimental study of the carbonitriding process applied to OLC25 steel samples.

KEYWORDS: steel, carbonitriding, mathematical modeling, simulation

1. Introduction

Thermochemical treatments are technological processes applied to metallic materials, especially steels, with the main objective of modifying the chemical composition of the surface layers of the parts. These treatments consist of introducing active chemical elements (such as carbon, nitrogen, boron, etc.) into the surface layer of the material, by diffusion, at high temperatures. Thus, unlike thermophysical treatments, which produce only internal structural changes without altering the chemical composition, thermochemical treatments simultaneously induce structural and chemical transformations in the surface region of the part [1].

The clear differentiation between the characteristics of the treated layer and the core represents the essence and fundamental purpose of applying thermochemical treatments in industry [2].

For thermochemical treatments to be effective and to lead to the formation of a surface layer with desired properties, it is essential that the three fundamental stages of the process - dissociation of the active substance (Ds), adsorption of active atoms on the surface of the part (A) and their diffusion into the material (D) - are correctly balanced [2].

Carbonitriding is a complex thermochemical treatment aimed at simultaneously enriching the surface layer of metal parts with carbon and nitrogen atoms, thus combining the advantages offered by carburizing (increased hardness through carbon

addition) and nitriding (high resistance to wear and corrosion through nitrogen addition). Basically, this process brings together in a single step the effects of the two treatments, resulting in a surface layer that benefits from superior mechanical and chemical characteristics [3, 4].

The treatment is carried out in special environments (solid, liquid or gaseous), which have the capacity to provide active carbon and nitrogen atoms. The temperature at which the process takes place is intermediate between that specific to nitriding (500-550 °C) and that of carburizing (900-950 °C), which allows for an efficient diffusion of both elements into the base material [5].

In the carbonitriding process, a thermochemical treatment used to improve the mechanical properties of metal parts, a gas mixture consisting predominantly of methane (CH_4) in proportions ranging from 65% to 75%, and ammonia (NH_3) in proportions ranging from 25% to 35% is frequently used. The treatment is carried out at temperatures between 600 and 750 °C [3, 6, 7].

To ensure efficient treatment, the gas composition is precisely controlled, using special autonomous installations. These allow maintaining a constant composition of the gas mixture in the retort (the container where the treatment takes place), and regulating the degree of ammonia dissociation, an essential parameter for controlling the nitrogen diffusion process in the steel.

The duration of keeping the parts in the active atmosphere depends directly on the depth of the

desired layer, but is generally shorter than in the case of classical nitriding. In practice, this duration is not fixed, but is determined experimentally, by testing representative samples until the desired characteristics of the layer are achieved [8].

Process modeling is an essential tool both in the design stage of metallurgical installations and in the analysis of their operation under real conditions. By using mathematical models, in combination with the advantages offered by modern information technology, it becomes possible to identify and establish optimal operating regimes for various metallurgical processes. Progress in the development of the specific mathematical apparatus, as well as in the development and application of advanced statistical methods, has allowed the optimization problem to be approached as not only possible, but also extremely efficient from a technical and economic point of view [9].

The mathematical models resulting from these methods not only allow the determination of extreme (optimal) operating conditions, but also constitute a valuable source of useful information for the real-time management and regulation of metallurgical processes. Although several works on mathematical optimization methods have been published in the Romanian technical literature in recent times, few of them deal in an applied manner with the particularities of processes specific to the metallurgical industry [10].

The process of developing a mathematical model based on statistical methods involves two main stages. In the first stage, called the preliminary experiment, essential issues related to the identification and selection of the main factors influencing the analysed process, as well as the possible interactions between them, are resolved. The second stage, known as the basic experiment, consists of the actual construction of the mathematical model and the performance of a detailed statistical analysis thereof [10].

The modeling process itself usually involves two fundamental steps:
• in the first step, the form of expression of the model is established, this can be, for example, in the form of a system of equations, an algorithm or a set of logical rules.
• in the second step, the model is used to make a series of predictions on the behavior of the system, to simulate possible scenarios or to identify the optimal solution to a given problem [9].

An essential aspect of mathematical models is the use of concise and rigorous notations, which allow a clear representation of the possible states of a system and the way in which these states evolve over time, depending on the modification of certain variables. This approach provides a solid basis for making predictions and simulations, as the model can be mathematically manipulated to highlight the behavior of the system in various scenarios [11].

For a mathematical model to be correct and useful, it is necessary to define a formal structure, based on axioms (basic principles accepted as true), theorems (propositions proven based on these axioms), and standardized mathematical procedures. The choice of these elements constitutes a fundamental step in the construction of the model, as they determine the limits of applicability and the degree of precision of the predictions it can generate [11].

An important advantage of mathematical models is the relatively low cost of their use, especially compared to physical models. Once formulated, they can be quickly implemented on a computer, and the analysis can be easily repeated for different data sets or conditions. Additionally, their structure allows for general conclusions to be obtained about the behavior of the system, without the need for expensive physical experiments [10].

2. Experimental conditions and obtained results

In this paper, we developed a mathematical model of the thermochemical carbonitriding treatment process applied to OLC25 steel, using statistical methods, namely regression analysis through an active experiment [12].

This approach to the problem involves experimental programming, that is:
• establishing the necessary and sufficient experiments, as well as the conditions for their implementation.
• determining by statistical methods the regression equation, which represents with a calculable degree of approximation, the process model.
• determining the conditions for achieving the optimal value, i.e., the performance of the analysed process [18].

In the paper, several experimental regimes of carbonitriding of OLC25 samples were studied (researched).

The experimental regimes were the following:

Ammonia/methane ratio = 0.25% at temperatures $T_1 = 550$ °C, $T_2 = 650$ °C, $T_3 = 750$ °C, with a holding time of 150 minutes.

Ammonia/methane ratio = 0.15% at temperatures $T_1 = 550$ °C, $T_2 = 650$ °C, $T_3 = 750$ °C, with a holding time of 150 minutes.

Ammonia/methane ratio = 0.05% at temperatures $T_1 = 550$ °C, $T_2 = 650$ °C, $T_3 = 750$ °C, with a holding time of 150 minutes.

After carrying out the experiment for each regime, the HV microhardness of the treated samples was measured at various points (identical for all measurements) along the depth of the carbonitrided layer.

The results of these measurements were organized into a database that we used to create a mathematical model of the carbonitriding process.

We considered the following technological parameters as the main influencing factors (independent variables):

- temperature of the thermochemical treatment – t, °C;
- ammonia percentage – NH_3, %;
- depth of the carbonitrided layer – As, mm.

The parameter to be optimized is the HV microhardness.

To establish the base level and the variation range of the influencing factors, we used data from the specialized literature [13].

To establish the base level and the variation range of the influencing factors, we also used values obtained from HV microhardness tests.

In order to encode the experimental design, the following notations and symbols were used:

Independent variables:

x1 - temperature of thermochemical treatment;
x2 - ammonia percentage;
x3 - depth of the carbonitrided layer.

Dependent variables (parameters to be optimized):

Y – HV microhardness, [MPa];

There are the following relationships between the natural and coded values of the factors x_i: $x_1 = (t-t_0)/\Delta t$; $x_2 = (NH_3-NH_{30})/\Delta NH_3$; $x_3 = (As-As_0)/(\Delta As)$.

The Yi values are expressed in natural units.

In order to create the mathematical model for the carbonitriding process under investigation, we considered as process parameters: treatment temperature (t1, t2, t3), ammonia/methane ratio and carbonitrided layer depth with the following values:

As = 0.09; 0.17; 0.25; 0.33; 0.47; 0.49; 0.57, for all variants, the treatment time was 150 minutes.

According to this method, the number of experiments taken into account is 2k.

The equation of the mathematical model has the general form: y = f(x_1,x_2,….x_k) where k represents the number of parameters taken into account. In the case of the present work, we considered the equation:

Y = f(x_1,x_2,x_3,x_4=ct), where x_1 is the encoded quantity for temperature, x_2 is the encoded quantity for the ammonia/methane ratio, x_3 is the encoded quantity for the layer depth, x_4=ct is the encoded quantity for the treatment time.

The modeling variant performed shows the dependence of the HV size depending on the three parameters (temperature, ammonia percentage and layer depth).

Before drawing up the experiment matrix, it is necessary to establish the minimum, maximum and base values for the process parameters (Table 1).

Table 1. *Minimum, maximum and baseline values for process parameters*

Coded variable	Maximum value (+1)	Base value (0)	Minimum value (-1)
$x_1 \rightarrow t$	750 °C	650 °C	550 °C
$x_2 \rightarrow NH_3$	25%	15%	5%
$x_3 \rightarrow A_s$	0.57 mm	0.33 mm	0.09 mm
$x_4 \rightarrow \tau$	150 min	150 min	150 min

The relationships between the coded quantities (x_1, x_2, x_3, x_4) and the natural quantities (temperature, ammonia/methane ratio, layer depth and time) are given by the following:

$$x_1 = \frac{t - t_0}{\Delta_t}; \quad x_2 = \frac{NH_3 - NH_{30}}{\Delta_{NH_3}}; \quad x_3 = \frac{A_s - A_{s0}}{\Delta A_s}$$

$$x_4 = \text{treatment time} = \text{ct}.$$

For temperature, the minimum value is 550 °C and will be coded with (-1), the maximum is 750 °C and will be coded with (+1), and the value of 650 °C will be considered the "base value", coded with (0).

Δ_t = 650-550 = 750-650 $\Rightarrow$ Δ_t = 100 °C, which is called the range of variation of the temperature parameter.

For NH_3, the minimum value = 5%, coded with (-1), the maximum value = 25%, coded with (+1), and the "base value" = 15%, coded with (0).

The interval $\Delta_{NH_3} = 15 - 5 = 25 - 15 \Rightarrow \Delta_{NH_3} = 10\%$, is called the variation interval of the NH_3 parameter.

For the layer depth (A_s), the minimum value is 0.09 mm, coded with (-1), the maximum value is 0.57 mm, coded with (+1), and the value of 0.33 will be considered the "base value", marked with (0).

The time for each experiment had a fixed value of 150 min.

The equation of the mathematical model has the form: $y=f(t°,NH\_3,A\_s)$

Codified we will make the association:

$$x_1 \rightarrow t°C; x_2 \rightarrow NH_3, x_3 \rightarrow A_s; y \rightarrow HV$$

$$y = C_0 + C_1X_1 + C_2X_2 + C_3X_3 + C_{12}X_1X_2 + C_{13}X_1X_3 + C_{23}X_2X_3$$

$$y = -122{,}591 + 0{,}678t - 1633{,}269A + 578{,}039A_s - 1{,}38tA_s + 3{,}637tA - 1119{,}791AA_s$$

Following the application of mathematical modeling, when the dependence of the HV microhardness on three parameters of the carbonitriding process is shown, namely carbonitriding temperature, ammonia percentage, and layer depth - it is found that there are minor differences between the values obtained from the mathematical model calculations and the values measured under the same conditions. The graphical representation of these differences is shown in Figures from 1 to 8.
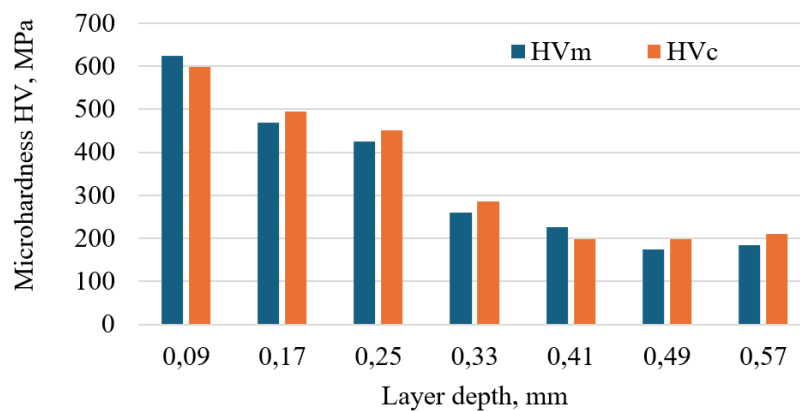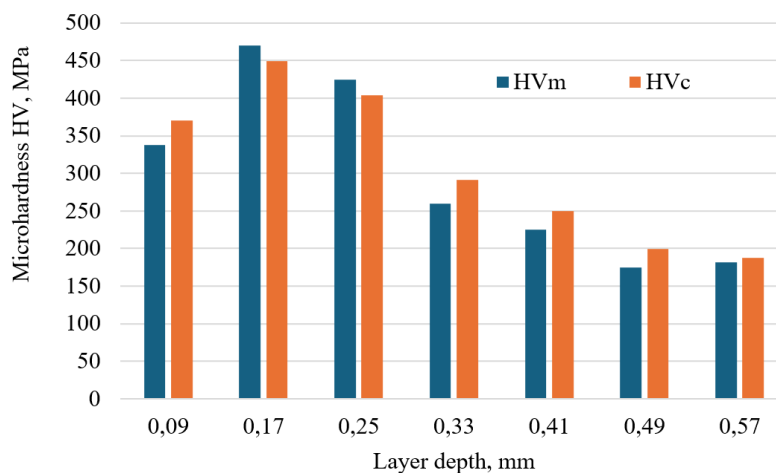

Fig. 1. *Comparison of measured values with those calculated at a temperature of 750 °C, for an ammonia concentration of 25%, HVm = Measured HV, HVc = Calculated HV*
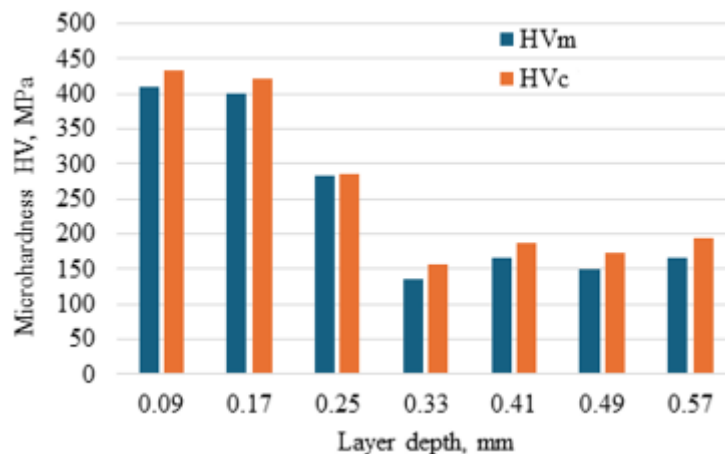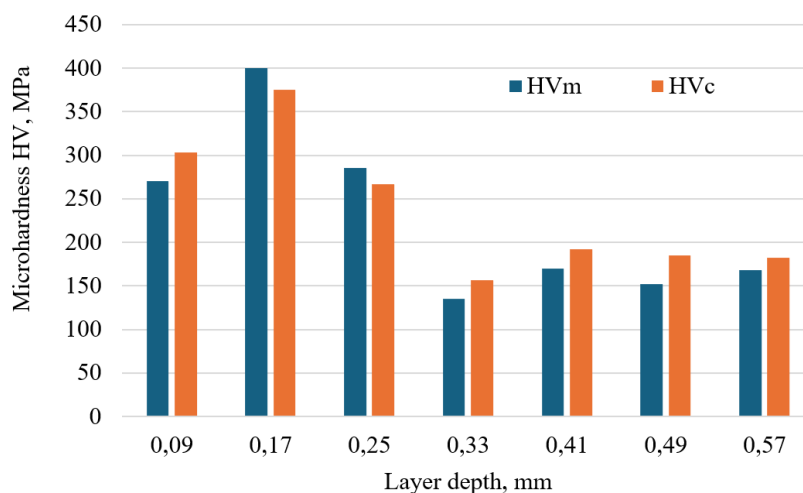

Fig. 2. *Comparison of measured values with those calculated at a temperature of 750 °C, for an ammonia concentration of 15%, HVm = Measured HV, HVc = Calculated HV*
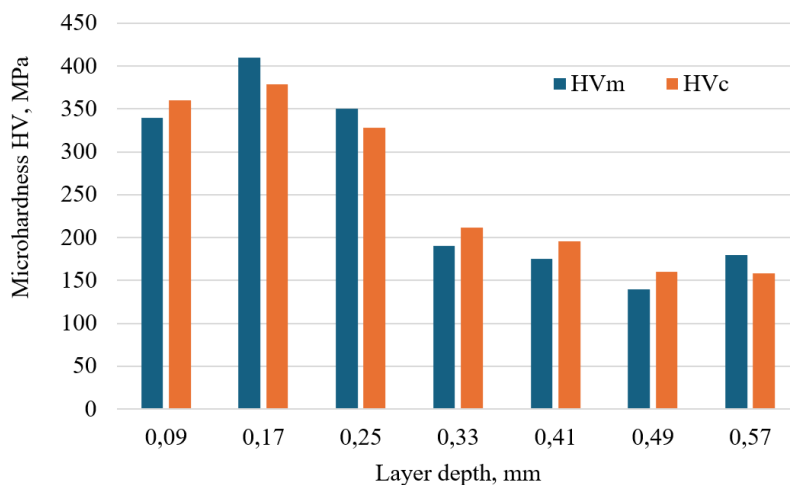
Fig. 3. *Comparison of measured values with those calculated at a temperature of 750 °C, for an ammonia concentration of 5%, HVm = Measured HV, HVc = Calculated HV*
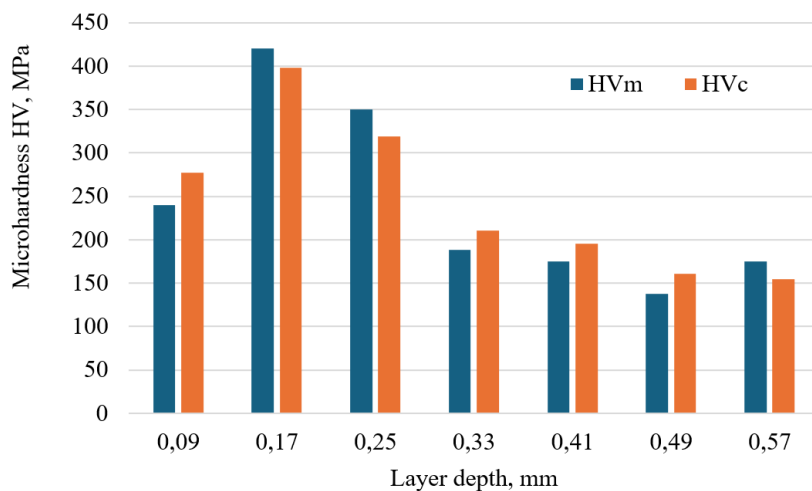

Fig. 4. *Comparison of measured values with those calculated at a temperature of 650 °C, for an ammonia concentration of 25%, HVm = Measured HV, HVc = Calculated HV*
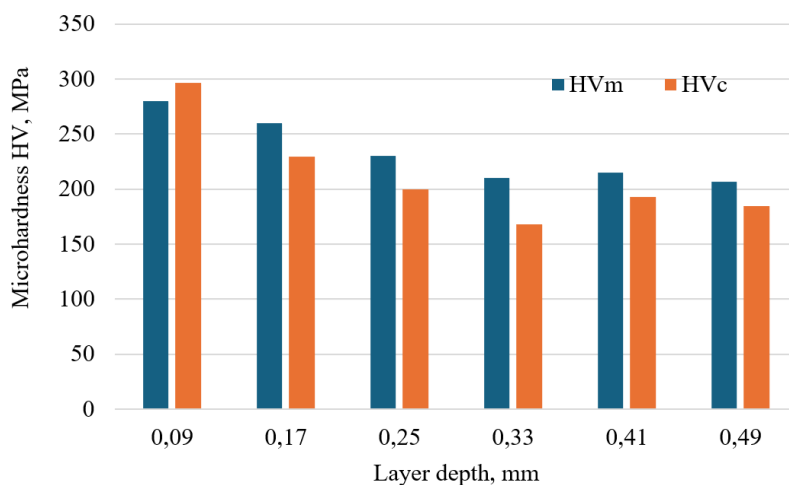

Fig. 5. *Comparison of measured values with those calculated at a temperature of 650 °C, for an ammonia concentration of 15%, HVm = Measured HV, HVc = Calculated HV*

Fig. 6. Comparison of measured values with those calculated at a temperature of 650 °C, for an ammonia concentration of 5%, HVm = Measured HV, HVc = Calculated HV
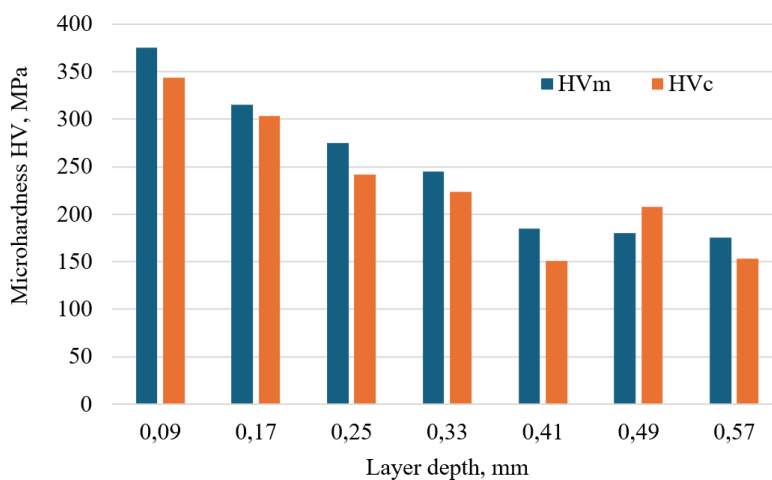

Fig. 7. Comparison of measured values with those calculated at a temperature of 550 °C, for an ammonia concentration of 25%, HVm = Measured HV, HVc = Calculated HV

Fig. 8. Comparison of measured values with those calculated at a temperature of 550 °C, for an ammonia concentration of 5%, HVm = Measured HV, HVc = Calculated HV

3. Conclusions

The objective of this work was to develop a mathematical model capable of describing the carbonitriding process applied to OLC25 steel, more precisely to show the dependence of the HV microhardness on the process parameters.

During the work, the following main conclusions were highlighted:

• Importance of the carbonitriding treatment: By combining the diffusion of carbon and nitrogen at controlled temperatures, carbonitriding allows the achievement of a hard and wear-resistant surface layer, without negatively affecting the toughness of the core. This is particularly valuable in the case of low-alloy steels, such as OLC25.

• Mathematical modelling: A model was developed based on an active experiment that assumed a finite number of experiments with the variation of the carbonitriding process parameters. Four variants of specific mathematical equations were developed, which show the dependence of the HV microhardness as a function of the values of the carbonitriding process parameters. The model allows the estimation of HV microhardness values depending on the treatment temperature, ammonia concentration and carbonitrided layer depth.

• Model validation: The results obtained through numerical simulation were compared with experimental data obtained during the experiments performed and showed a good correlation, which confirms the validity of the theoretical approach.

• Process optimization: The use of the mathematical model allows rapid testing and optimization of technological parameters (temperature and ammonia concentration) without resorting to expensive experiments. Thus, efficient treatments can be obtained, tailored to the functional requirements of the part.

• Industrial applications: The proposed model has a high potential for application in industry, especially in digitally assisted thermochemical treatment processes, contributing to improved precision and reduced material losses.

In conclusion, the mathematical modelling of the carbonitriding process for OLC25 steel represents a valuable tool both theoretically and practically, providing support for efficient technological decisions, based on rigorous predictive calculations. The present work represents a step towards the integration of mathematical methods in the control and optimization of modern thermochemical treatments.

References

[1]. Crainic N., *Tratamente termochimice*, Editura MatrixRom, București, 2007.
[2]. Gîrbea I. D., *Tratamente termice şi termochimice – Ghid de laborator*, Editura Universității Tehnice din Cluj-Napoca, 2018.
[3]. Țugui A., *Oțeluri şi tratamente termice*, Editura Didactică şi Pedagogică, București, 2002.
[4]. Allen J. Fuller Jr., *Introduction to Carburizing and Carbonitriding*, in ASM Handbook, 2013.
[5]. Mitelea I., Tîțu I., Giurgiu L., *Tratamente termice – Teorie şi aplicații*, Editura Universității „Lucian Blaga" din Sibiu, 2016.
[6]. Marin N., *Tratamente termice ale oțelurilor aliate*, Editura Universitaria, Craiova, 2014.
[7]. Popescu L. G., *Modificări structurale în oțeluri supuse tratamentelor termice*, Editura Politehnica, Timișoara, 2011.
[8]. Totten G. E., *Tratamentul termic al oțelului: Metalurgie şi tehnologii*, CRC Press, Taylor & Francis, 2007.
[9]. Crainic N., *Tratamente termochimice*, Editura MatrixRom, București, 2007.
[10]. Ionescu V., *Bazele modelării matematice în inginerie*, Editura Politehnica Press, București, 2007.
[11]. Bălan C., *Modelare matematică şi simulare numerică în inginerie*, Editura MatrixRom, București, 2009.
[12]. Dowden John M., *The Mathematics of Thermal Modeling: An Introduction to the Theory of Laser Material Processing*, Editura: CRC Press, 2001.

MANUSCRISELE, CĂRŢILE ŞI REVISTELE PENTRU SCHIMB, PRECUM ŞI ORICE
CORESPONDENŢE SE VOR TRIMITE PE ADRESA:

MANUSCRIPTS, REVIEWS AND BOOKS FOR EXCHANGE COOPERATION,
AS WELL AS ANY CORRESPONDANCE WILL BE MAILED TO:

LES MANUSCRIPTS, LES REVUES ET LES LIVRES POUR L'ECHANGE, TOUT AUSSI
QUE LA CORRESPONDANCE SERONT ENVOYES A L'ADRESSE:

MANUSCKRIPTEN, ZIETSCHRITFTEN UND BUCHER FUR AUSTAUCH SOWIE DIE
KORRESPONDENZ SID AN FOLGENDE ANSCHRIFT ZU SEDEN:

After the latest evaluation of the journals by the National Center for Science Policy and Scientometrics (**CENAPOSS**), in recognition of its quality and impact at national level, the journal will be included in the B^+ category, 215 code (http://cncsis.gov.ro/userfiles/file/CENAPOSS/Bplus_2011.pdf).

The journal is already indexed in:
DOAJ: https://doaj.org/
SCIPIO-RO: http://www.scipio.ro/web/182206
EBSCO: http://www.ebscohost.com/titleLists/a9h-journals.pdf
Google Academic: https://scholar.google.ro
Index Copernicus: https://journals.indexcopernicus.com
Crossref: https://search.crossref.org/

The papers published in this journal can be viewed on the website:
http://www.gup.ugal.ro/ugaljournals/index.php/mms

Name and Address of Publisher:
Contact person: Prof. Dr. Eng. Elena MEREUŢĂ
Galati University Press - GUP
47 Domneasca St., 800008 - Galati, Romania
Phone: +40 336 130139
Fax: +40 236 461353
Email: gup@ugal.ro

Name and Address of Editor:
Ş. L. Dr. Eng. Marius BODOR
"Dunarea de Jos" University of Galati, Faculty of Engineering
111 Domneasca St., 800201 - Galati, Romania
Phone: +40 336 130208
Phone/Fax: +40 336 130283
Email: marius.bodor@ugal.ro

AFFILIATED WITH:
- **THE ROMANIAN SOCIETY FOR METALLURGY**
- **THE ROMANIAN SOCIETY FOR CHEMISTRY**
- **THE ROMANIAN SOCIETY FOR BIOMATERIALS**
- **THE ROMANIAN TECHNICAL FOUNDRY SOCIETY**
- **THE MATERIALS INFORMATION SOCIETY**
(ASM INTERNATIONAL)

Edited under the care of
the FACULTY OF ENGINEERING
Annual subscription (4 issues per year)